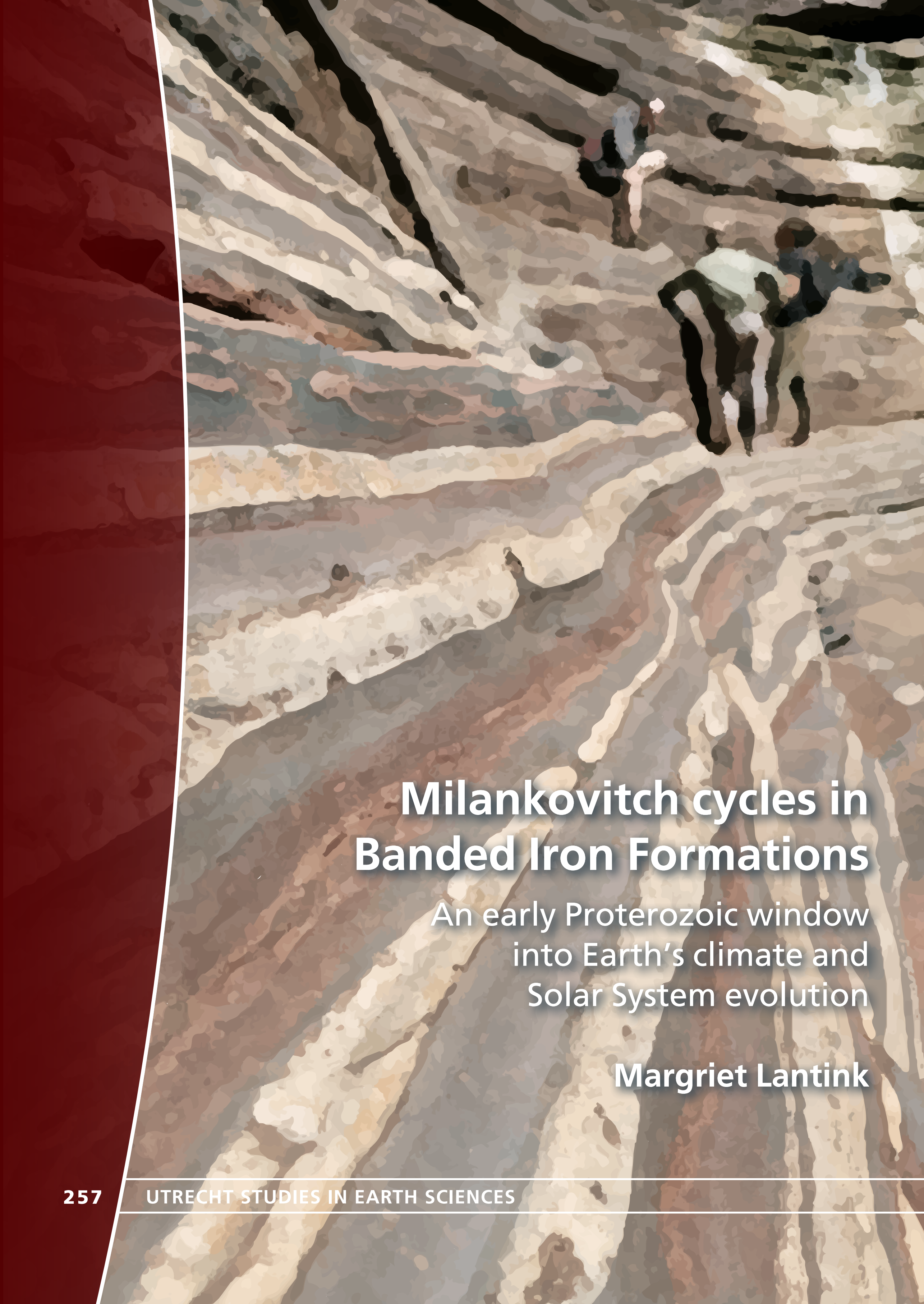

Milankovitch cycles in Banded Iron Formations

An early Proterozoic window into Earth's climate and Solar System evolution

Margriet Lantink

257 UTRECHT STUDIES IN EARTH SCIENCES

Members of the dissertation committee:

Prof. dr. Linda Hinnov
George Mason University, USA

Prof. dr. Jacques Laskar
IMCCE, Paris Observatory, France

Prof. dr. Jack Middelburg
Utrecht University, The Netherlands

Prof. dr. Ronny Schönberg
University of Tübingen, Germany

Dr. Harilaos Tsikos
University of Patras, Greece

ISBN: 978-90-6266-625-6

USES no. 257

Cover design by Margriet Lantink and Margot Stoete
Photographs for cover and page 5 by Gregory Jack

Copyright © 2022 M.L. Lantink. All rights reserved. No part of this publication may be reproduced in any form, by print or photo print, microfilm or any other means, without written permission by the author.

Printed in the Netherlands by Ipskamp

Milankovitch cycles in Banded Iron Formations

An early Proterozoic window into Earth's climate and Solar System evolution

Milankovitch-cycli in gestreepte ijzerformaties
Een vroeg-Proterozoïsch venster op de geschiedenis
van het Aardse klimaatsysteem en Zonnestelsel
(met een samenvatting in het Nederlands)

Proefschrift

ter verkrijging van de graad van doctor aan de Universiteit Utrecht
op gezag van de rector magnificus, prof.dr. H.R.B.M. Kummeling,
ingevolge het besluit van het college voor promoties
in het openbaar te verdedigen op

vrijdag 3 juni 2022 des ochtends te 10.15 uur

door

Margriet Louise Lantink

geboren op 16 maart 1992
te Leiden

Promotoren: Prof. dr. L.J. Lourens
Prof. dr. P.R.D. Mason

Copromotor: Dr. F.J. Hilgen

This study was financially supported by the Netherlands Organization for Scientific Research (NWO-ALWOP grant no. 192)

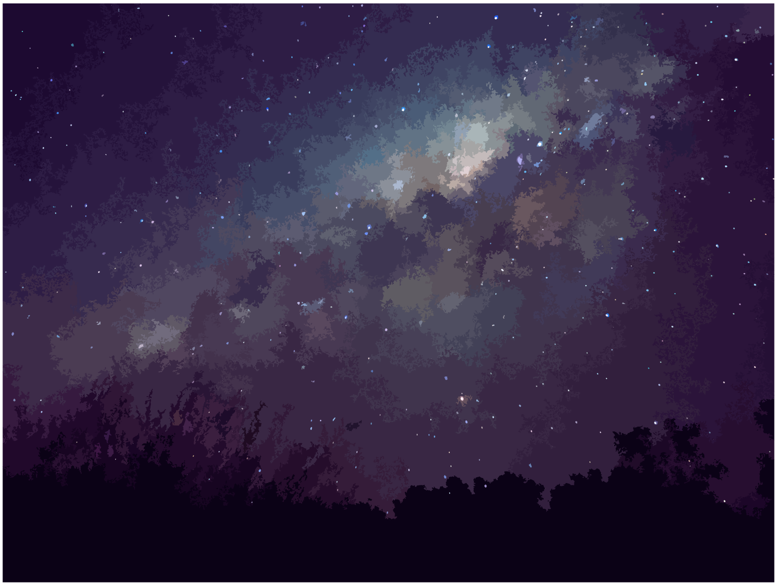

Karijini night sky

Contents

Acknowledgements 8

Chapter 1 **Introduction, summary and outlook** 11

Chapter 2 **Climate control on banded iron formations linked to orbital eccentricity** 31
M.L. Lantink, J.H.F.L. Davies, P.R.D. Mason, U. Schaltegger and F.J. Hilgen (2019). *Nature geoscience 12(5),* 369-374.

Chapter 3 **Precession as the pacemaker of early Earth's oxygenation** 63
M.L. Lantink, W.K. Lenstra, J.H.F.L. Davies, R. Hennekam, D. McB. Martin, P.R.D. Mason, M. Ovtcharova, G.J. Reichart, C.P. Slomp and F.J. Hilgen.

Chapter 4 **Milankovitch cycles and the Earth-Moon distance 2.46 billion years ago** 105
M.L. Lantink, J.H.F.L. Davies and F.J. Hilgen (*in review)*

Chapter 5 **Towards and astrochronological framework for the early Paleoproterozoic and origin of very long-period astronomical-induced cyclicity** 163
M.L. Lantink, J.H.F.L. Davies, R. Hennekam, D. McB. Martin, P.R.D. Mason, G.J. Reichart and F.J. Hilgen.

References 225

Samenvatting in het Nederlands 245

Curriculum vitae and publications 250

Acknowledgements (Dankwoord)

The completion of this thesis became possible thanks to the help of many people. By far the most thanks I owe, of course, to Frits Hilgen, who, as the founder and driving force behind the research project, provided me with the opportunity to embark on this adventure in 2017. In the more than five years since then, I have come to know Frits as a relentlessly enthousiastic and committed supervisor, pleasant discussion partner, motivator and source of inspiration; someone with an admirable dedication to science, intuition for new paths to be taken and razor-sharp insight - and who also likes to repeat these insights very much and often so that it continues to echo in your mind for a long time.... In short, without whom this dissertation would never have existed.

Secondly, I would like to thank my promotors Lucas Lourens and Paul Mason for their support, commitment, interesting ideas and discussions; I really appreciate that you were always available for (independent) advice or a listening ear. And Paul, thank you for introducing me to the fascinating world of banded iron formations.

I am grateful to all my scientific colleagues for their contribution to this thesis and/or research. First and foremost, special thanks go to Joshua Davies, who has been closely involved from the beginning of the project and has been invaluable for its success; not only because of his U-Pb dating efforts (or hopeless attempts), but also because of his good company during fieldwork in particular. Josh has an admirable ability to be genuinely interested in a variety of research topics/areas, and indeed he may now consider himself a proper cyclostratigrapher. In addition, I would specifically like to thank Nic Beukes and Hari Tsikos for their help with the UUBH-1 drilling project (and Hari also for lively discussions); David Martin for organising fieldwork and access to drill core; Gert-Jan Reichart and Rick Hennekam for the wonderful XRF data; Wytze Lenstra and Caroline Slomp for their resolute action on the modelling; and Jacques Laskar, Mohammad Farhat, Nam Hoang, Pierre Auclair-Desrotour and Federico Mogavero for their patient efforts to make me a little less ignorant about astronomy. I am indebted to the members of the dissertation committee for reading and evaluating the thesis.

Similarly am I indebted to all those who were additionally important to the study in terms of fieldwork, measurements, data sharing and/or interpretation. Concerning our activities in South Africa: thanks in particular to Clive Albutt and Murphy for kindly providing us access to sections Woodstock and Daniëlskuil, to the landowners of Fairholt farm, and to those that made the drilling possible (Okker, Bernard, Wanda c.s.), as well as Maarten Roeterink and Sander Hilgen for their assistence during the fieldwork and/or the drilling. Greg Jack, I think I can say also on behalf of Frits and Josh that you have made our trips to the Hamersley Range and Coral Bay an unforgettable experience. In addition, many thanks to the people of the GSWA and Perth core library, in particular Monique Brouxhon, Paul Stephenson, Michael Wawryck and Lena Hancock, for so generously providing us with drill core material and mineral reflectance data. I also much appreciate the help I received from Marcel van Maarsseenveen, Timothy Baars and Jakob Steiner with regards to the GPS measurements, drone flying and photogrammetry. Richard Ray and David Waltham are acknowledged for sharing their model curves for the lunar recession history. For discrete sample analyses: thanks to all the people involved from the GeoLab Utrecht, in particular Leonard Bik, Jan van Tongeren, Coen Mulder, Helen de Waard, Arnold van Dijk, Natasja Welters, Giovanni Dammers, Thom Claessen and Bernadette Marchand, and Roel van Elsas from the VU Amsterdam. To the students of Team BIF, Tian Schuurmans, Appie Haddouzi, Ewald van Dael, Lea de Vries, Rea Vaz and Sander Hoogendoorn: thank you for your enthousiasm, hard work, and the fact that you were the (only?) ones that I could really talk to about (the details of) the research. In addition, I should like to mention Appy Sluijs and Jack Middelburg for pleasant conversations on biogeochemically related topics. Special thanks go to the late Rineke Gieles for her dedication with regards to the XRF measurements and who sadly passed away in 2020.

Then there is a large group of people whom I would like to thank in a more general sense for their pleasant company and (moral) support over the past years, and whom I unfortunately cannot mention all by name. In ieder geval bedankt aan kamergenootjes en paranimfen Ilja en Inigo voor de speciale band die we toch wel hebben opgebouwd, en voor het mij aansporen tot sociaal-maatschappelijk engagement (Ilja) danwel mountainbiken (Inigo). In addition, thanks to the people of the Stratigraphy & Paleontology group, o.a. Niels, Martin, Wilma, Tjitske, Emilia, for interesting discussions about the state of the (academic) world; the Petrology group (sorry for not being around that often); the people on the 3rd floor; Marjolein en Jan-Willem; and the Ocean Systems group at the NIOZ. Merci to Matthias and the non-geologists from the Observatoire de Paris for their relaxing influence on me during the final writing stages of the thesis. (Oud-) roei- en andere sportgenootjes: dank voor jullie (gespeelde?) interesse bij het aanhoren van mijn verhalen over het onderzoek en leven van een PhD-student.

Ten slotte wil ik mijn (schoon)familieleden, in het bijzonder mijn ouders en natuurlijk Freek, bedanken voor alles. En ik denk aan Jos, die ons te vroeg vaarwel heeft moeten zeggen, maar dit vast en zeker prachtig had gevonden.

Chapter 1

Introduction, summary and outlook

1. Introduction

1.1 Astronomical forcing and its cyclostratigraphic applications during the Phanerozoic

The Milankovitch cycles

Quasi-periodic changes in the geometry of Earth's orbit and inclination axis occur on timescales of many thousands (kyr) to millions of years (Myr) as a consequence of gravitational interactions of Earth with other bodies in the Solar System. These changes give rise to cyclical variations in the amount and distribution of sunlight reaching Earth (i.e., solar insolation), and are called "Milankovitch cycles" after Milutin Milankovitch, who presented the first complete mathematical computation of the insolation variations in 1920 and in his magnum opus *Kanon der Erdbestrahlung* in 1941.

Three different parameters are distinguished, namely orbital eccentricity, axial inclination or obliquity, and climatic precession, with at present main periods of ~100 and 405 kyr, 41 kyr, and 23 and 19 kyr, respectively (Fig. 1a). Climatic precession is the combined effect of Earth's axial precession ("wobble") and the precession of the perihelion, and controls the drift of the seasons along the Earth's elliptical orbit leading to variations in summer-winter contrast (Fig. 1b). Obliquity determines the angle of incidence of solar insolation, leading to changes in seasonal and latitudinal distribution which mainly affect high latitudes. Eccentricity has a very small effect on global annual insolation (0.25%), but principally acts as amplitude modulator of climatic precession.

Importantly, these secular insolation variations, which amount up to 20-25% change in monthly insolation, influence Earth's climate, a phenomenon that is referred to as astronomical forcing or Milankovitch (climate) forcing.

Evidence for the astronomical theory of climate change

Studies of the Phanerozoic (last ~540 Myr) have exposed a key control of astronomical forcing on Earth's climate history, and the so-called astronomical theory of climate (changes) is now widely accepted (Hinnov, 2013; Hilgen et al., 2015). This theory was initially formulated in the 19th century to explain the Pleistocene ice ages (Adhémar, 1842; Croll, 1864). With the recovery of long, continuous deep-sea cores and associated climate proxy records (Emiliani, 1955; Shackleton and Opdyke, 1973), combined with improved magneto-chronostratigraphy (Ericson and Wollin, 1968), the final confirmation of the theory came from the milestone publication of Hays et al. in 1976. In the decades following, the evidence for astronomically induced climate changes has been extended to progressively older time intervals and to both high- and low-latitude parts of the climate system.

Astronomical forcing is equally held responsible for the great ice ages of the Quaternary and Carboniferous (Imbrie et al., 1984; Heckel, 1986; Davydov et al., 2010; Liebrand et al., 2017), the hyperthermals of the Eocene (Zachos et al., 2010; Littler et al., 2014; Westerhold et al., 2020), monsoonal intensification and the deposition of organic-rich mudstones known as black shales during the Cretaceous (Herbert and Fischer,

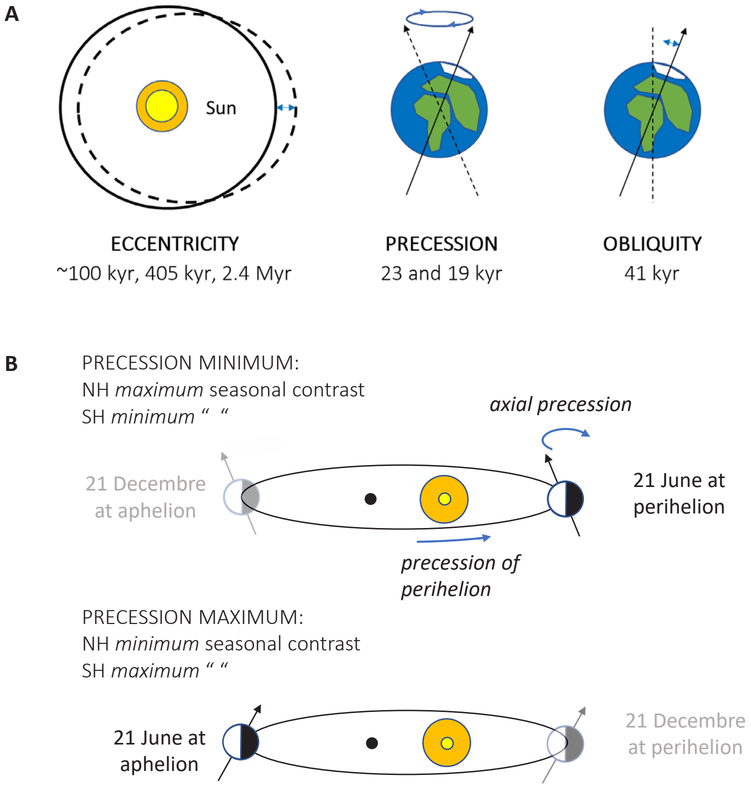
A
Sun
ECCENTRICITY
~100 kyr, 405 kyr, 2.4 Myr
PRECESSION
23 and 19 kyr
OBLIQUITY
41 kyr
B
PRECESSION MINIMUM:
NH *maximum* seasonal contrast
SH *minimum* " "
axial precession
21 Decembre at aphelion
21 June at perihelion
precession of perihelion
PRECESSION MAXIMUM:
NH *minimum* seasonal contrast
SH *maximum* " "
21 June at aphelion
21 Decembre at perihelion

Figure 1. Schematic representation of (**A**) the three Milankovitch cycle parameters with present-day main periodicities (Laskar et al., 2004), and of (**B**) the climatic precession cycle, causing changes in summer-winter contrast. The upper panel indicates the configuration defined as "precession minimum", which is when the northern hemisphere (NH) summer solstice occurs at perihelion (position closest to the Sun). The lower panel indicates the situation half a climatic precession cycle later ("precession maximum"), when the NH summer solstice occurs at aphelion (position furthest away from the Sun). Note that due to the slow opposite motion of the Earth's orbital plane (i.e., precession of perihelion) with respect to the axial precession motion, aphelion is reached at a slightly earlier point in time/position in space than the time/position corresponding to exactly half a rotation of the axis. Note further that the changes in seasonality on the southern hemisphere (SH) occur 180° out of phase with those on the NH.

1986; Mitchell et al., 2008; Batenburg et al., 2016) and sapropels in the Mediterranean Quaternary and Neogene (Rossignol-Strick, 1983; Hilgen, 1991; Röhling et al., 2015), representing periods of extensive marine bottom water anoxia/dysoxia (Figs. 2 and 3). These advances went hand in hand with improvements in integrated stratigraphic approaches including radio-isotopic dating (Kuiper et al., 2008; Meyers et al., 2012a) and astronomical models (Berger, 1978; Laskar et al., 1993; 2004) and are independently corroborated by climate modelling experiments (e.g. Kutzbach 1981; Crowley and

Baum, 1992; Imbrie et al., 1993; Pollard and DeConto, 2009; Bosmans et al., 2015). Astronomically induced paleoclimate and environmental changes have also influenced the distribution and evolution of floral and faunal species (e.g. Van Dam et al., 2006; Timmerman and Friedrich, 2016; Crampton et al., 2018) and are ubiquitously recorded in a wide range of sedimentary environments, including the terrestrial realm (e.g. Olsen and Kent, 1996; Petit et al., 1999; Ding et al., 2002; Tzedakis et al., 2006; Abels et al., 2013; van Noorbergen et al., 2018).

Investigating Earth System's response using climate proxy analysis

In order to document, portray and reconstruct the response of Earth System to astronomical forcing, astronomical-induced cycle patterns expressed in stratigraphic sequences ("cyclostratigraphy") have been subjected to detailed and numerous types of proxy analysis, i.e., the collection and study of stratigraphic variations in physical, chemical and/or biogenic signatures of climatic or climate-related processes. Deep-sea oxygen and carbon isotopes are key examples of such paleoclimate proxies, the data of which have been compiled to provide a global record of Cenozoic variations in deep-sea temperature/ice volume ($\delta^{18}O$) and atmospheric CO_2/ocean circulation ($\delta^{13}C$), respectively (Lisecki and Raymo, 2005; Zachos et al., 2010; Barnet et al., 2019; Westerhold et al., 2020).

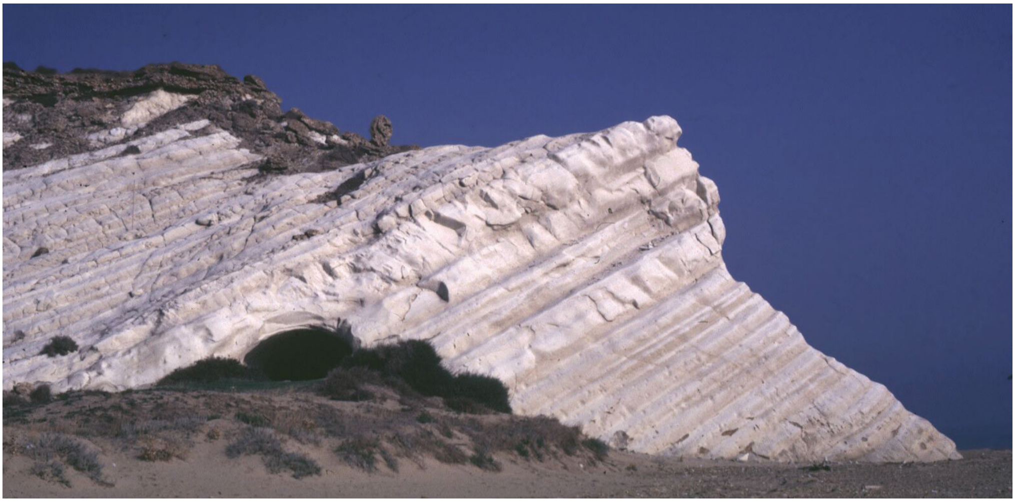

Figure 2. Deep-marine marl successions of the Pliocene Trubi Formation at Capo di Bianco on Sicily (Italy), showing rhythmic Milankovitch-forced alternations and bundling patterns. Small-scale (i.e. precession-related) cycles are of quadripartite structure, consisting of successive grey, white, beige and white marl (see also Fig. 3), and represent changes in bottom-water paleoredox conditions (e.g. Van Hoof et al., 1993; Van Os et al., 1994). This section forms part of the Capo Rossello composite, which underlies the Pliocene part of the astronomical and geologic time scale (Hilgen and Langereis, 1989). Photo by Frits Hilgen.

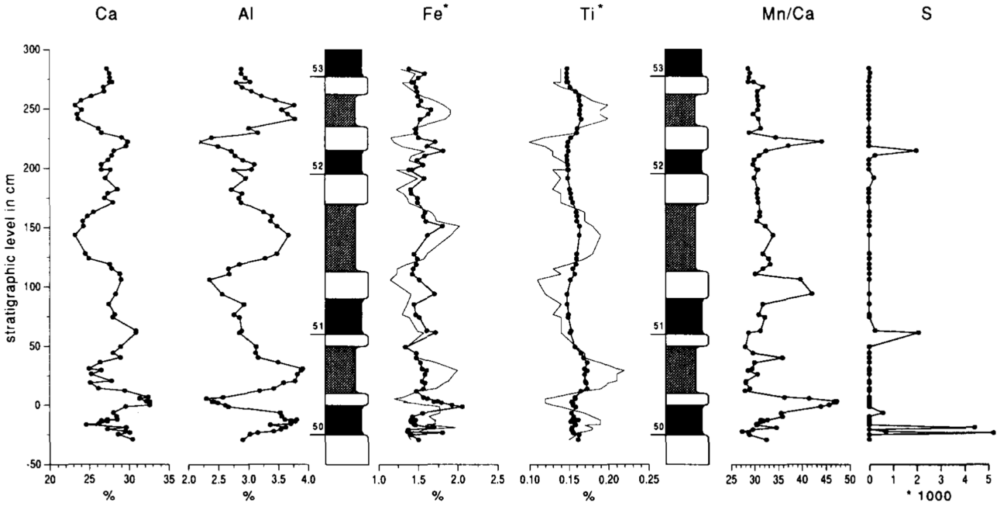

Figure 3. Lithology and high-resolution geochemical analysis of the precession-related quadruplet cycles of the Pliocene Trubi Formation as presented in Van Hoof et al. (1993; their Figure 5). Grey-coloured marls are shown in black, white marls in white and beige marl are shaded. The abundances of Ca, AI, Fe (thin line), Fe* (Fe/AI, thick line), Ti (thin line), Ti* (Ti/AI, thick line), Mn/Ca and S are indicated. The alternating sequence of beige (carbonate-poor with detrital iron (hydro)oxides), white (carbonate-rich and containing authigenic Fe and Mn enrichments) and grey layers (rich in organic matter with sharp sulphide peaks at the base and/or top) suggests that the diagenetic conditions changed from oxic via suboxic to anoxic for the respective layers. Beige layers are linked to enhanced terrigenous (dust) input associated with a weak monsoon during precession maxima. Grey marls are linked to increased water-column productivity and/or stagnation associated with a larger freshwater input from the river Nile, due to intensification of the African (summer) monsoon during precession minima.

In shelf area and pelagic sediments, mineralogical and trace-elemental properties such as Ti/Al ratio, Fe content and magnetic susceptibility have proven diagnostic for tracking astronomical-induced changes in eolian or fluvial input (e.g. Wehausen and Brumsack, 2000; Lourens et al., 2005; van der Laan et al., 2012). In addition, (calcium) carbonate content, organic carbon chemistry and redox-sensitive (trace) metal distributions are commonly applied to track regular variations in biological productivity and paleoredox conditions, i.e. periodic development of dysoxic or euxinic conditions in the water column and/or below the sediment-water interface. Such variations have often been linked to astronomical induced and monsoonal-related changes in continental precipitation, wind patterns, ocean circulation/water column overturn and nutrient input/upwelling (e.g. Herbert and Fischer, 1986; Van Hoof et al., 1993; Van Os et al., 1994; Reichart et al., 1998; Kuypers et al., 2004; Röhling et al., 2015; Hennekam et al., 2014; see also Fig. 3). However, also more generic sediment parameters such as lithofacies descriptions (e.g. Olsen and Kent, 1996) and colour (e.g. Lourens et al., 2005; van der Laan et al., 2012) have proven highly informative for documenting and interpreting astronomical-induced paleoclimate signals.

Importantly, these proxy data provide a numerical record which can be used to quantitatively determine periodicity using time series analysis techniques (e.g. Weedon, 2003), and further allow statistical evaluation of the astronomical theory by comparison with stochastic noise models (e.g. Meyers et al., 2008).

Cyclostratigraphy as precise geochronometer and archive of planetary orbital evolution

The study of cyclostratigraphy not only offers insight into Earth System's intricate response to astronomical forcing (some might say its primary task), but it has also proven a powerful method for establishing high-resolution temporal frameworks for reconstructing Earth history. Precise correlation of cyclostratigraphic patterns to computed astronomical and/or insolation time series (Laskar et al., 1993; 2004) has led to the establishment of numerically dated frameworks ("astrochronologies") at the level of precession to short (~100 kyr) eccentricity, which currently form the backbone of the Geologic Time Scale for the Cenozoic (Fig. 2; Hinnov and Hilgen, 2012; Gradstein et al., 2020). In turn, such frameworks have enabled distinguishing between volcanic or tectonic influences and the contribution of very long-period (i.e., multi-million-year) orbital cycles (e.g. Boulila, 2012; Barnet et al., 2019).

However, due to the fundamentally chaotic nature of orbital motion in the Solar System, which mainly originates from the inner Solar System bodies (Laskar, 1989; 1990), the ability to construct a precise orbital solution from the present is limited to about ~60

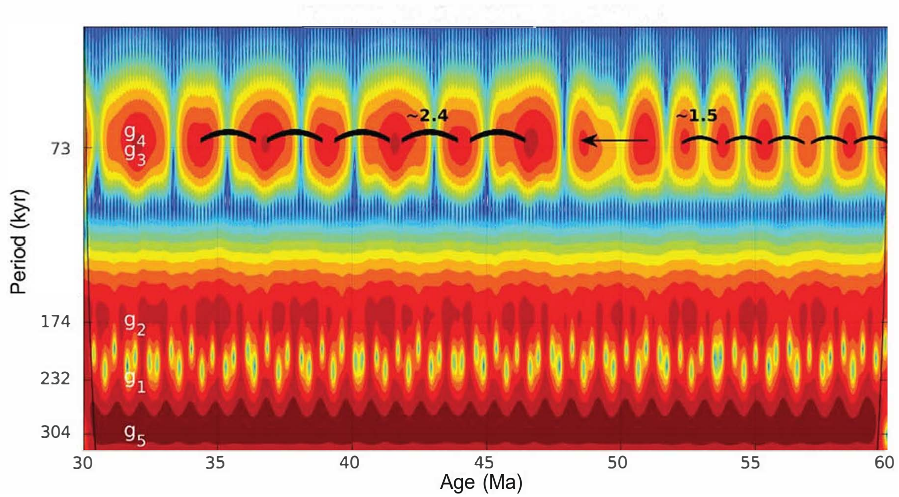

Figure 4. Wavelet analysis of the ZB18a astronomical solution ($h = e*\sin\varpi$, where e and ϖ are the eccentricity and longitude of perihelion of Earth's orbit, respectively) of Zeebe and Lourens (2019; their Figure 2). In this solution, a chaotic resonance transition occurs around 50 Ma as represented by a shift in the period of g4 – g3 from ~1.6 Myr to ~2.4 Myr (see arrow).

million years ago (Ma) (Laskar et al, 2011). On the other hand, the orbits of the outer Solar System planets, notably of Jupiter, are considered much more stable (Laskar et al., 2010; Hoang et al., 2021). Likewise, the strong 405-kyr eccentricity cycle is considered relatively stable in deep time, originating from interactions between the orbital perihelia of Venus and Jupiter described by $g_2 - g_5$ (g_i terms indicating the fundamental frequencies of the rotation of the planetary orbits on their orbital plane, i.e. precession of perihelion, for the planets i = 1, 2, . . . , 8). As such, calibration of pre-50 Ma sediment sequences to this 405-kyr "metronome" has been employed for developing astrochronostratigraphic frameworks or "floating" astrochronologies, where possible anchored with high-precision uranium-lead (U-Pb) zircon ages and/or magnetostratigraphy, for intervals of the Mesozoic and Paleozoic (Huang et al., 2018; Wu et al., 2013). In turn, such cycle frameworks have been examined for the (chaotic) evolution of planetary orbital cycles, notably of the ~2.4 Myr Mars-Earth eccentricity cycle $g_4 - g_3$ (e.g. Olsen and Kent 1999; Ma et al., 2017; Zeebe and Lourens, 2019; Ikeda and Tada, 2020; see also Fig. 4). Recently, they have even been used for retrieving values of individual planetary frequencies g_1 to g_5 during the Late Triassic – Early Jurassic (Olsen et al., 2019).

Cyclostratigraphic potential for reconstructing the history of the Earth-Moon system

Another valuable application of cyclostratigraphy is its potential for reconstructing the past evolution of the Earth-Moon system. While variations in Earth's orbital eccentricity result from interplanetary gravitational interactions in the Solar System (i.e., from combinations of two or more g_i frequencies), the climatic precession and obliquity cycles arise in addition from Earth-Moon system dynamics. More specifically, these cycles derive from the combination of the precession frequency of Earth's axis (p) and the fundamental Solar System frequencies g_i (i.e., $p + g_i$), and s_i (i.e., $p + s_i$), respectively (s_i terms referring to the precession of the orbital nodes). Earth's precession frequency p is

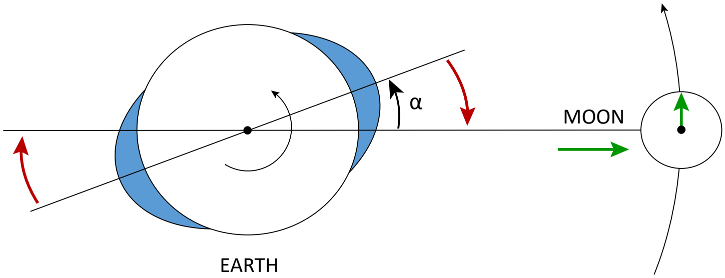

Figure 5. Tidal evolution of the Earth-Moon system. Due to the much faster Earth's spin rate relative to the Moon's orbital period, the tidal bulge raised by the gravitational pull of the Moon is pushed ahead with respect to the line connecting their centres of mass (which is possible because of friction). This excess mass creates a torque (α) in the direction opposite of Earth's spin, leading to a gradual deceleration. To conserve angular momentum, the Moon is accelerated into a higher orbit, i.e., gaining potential energy.

directly coupled to Earth's spin rate and the Earth-Moon distance (see also Hinnov, 2013). From both theory and observations we know that these two parameters were different in the past as a consequence of tidal dissipation, which predicts a gradual deceleration of Earth's rotation with time coupled to a gradual recession of the Moon (Fig. 5; Darwin, 1879). Correspondingly, a decrease in the value of *p* and of the associated precession and obliquity periods is expected back in time and is implemented in astronomical models (Fig. 6; Berger et al., 1992; Laskar et al., 2004).

However, while these models assume a constant tidal dissipation, it is evident from lunar laser ranging (LLR) measurements (Dickey et al., 1994; Williams and Boggs, 2016) that this value must have varied significantly over Earth's history. In particular, the LLR-derived rate at which the Moon is presently receding from Earth implies a close encounter within less than 2 Gyrs, when the corresponding tidal dissipation rate is extrapolated backwards (Gerstenkorn, 1967). This is obviously not compatible with the dated ~4.5 Ga age of the Moon (Kleine et al., 2005; Barboni et al., 2017). To empirically reconstruct this past evolution, the geological record of fossil growth bands and tidal laminae has been employed (Lambeck, 1980), yet these estimates suffer from relatively large uncertainties given that it is difficult to count the exact number of laminae per solar year or lunar month, respectively (Williams, 2005). Therefore, the cyclostratigraphic record of changing precessional and obliquity periods may provide a more robust and independent method. For example, the exceptional quality of Neogene cyclostratigraphic successions has allowed for an evaluation of short-term changes in tidal dissipation as well as dynamical ellipticity, based on observed differences in the phasing of precession and obliquity with respect to astronomical solutions employing certain Earth-Moon parameters (Lourens et al., 2001; Pälicke and Shackleton, 2000; Zeeden et al., 2014), although potential discrepancies with

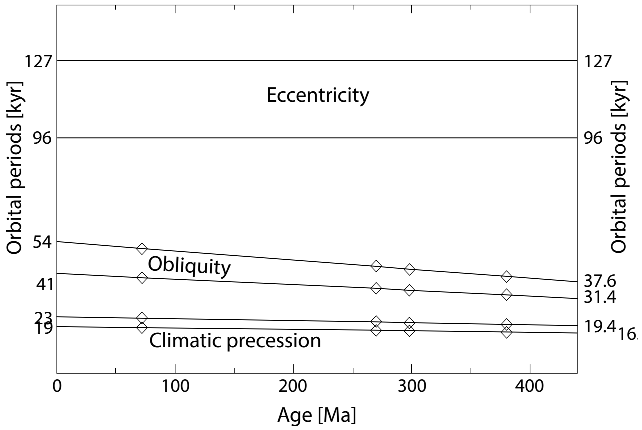

Figure 6. A shorter period of the climatic precession and obliquity cycles is expected in the past as a result of the tidal evolution of the Earth-Moon system. Accordingly, the ratio of the precession periods with respect to the periods of the eccentricity cycles would have been larger. Figure from Berger and Loutre (1994).

modeling efforts need to be solved (Green et al., 2017). On the longer term, a progressive shift in the ratio of the climatic precession- and obliquity-related spectral peaks with respect to their respective eccentricity and inclination amplitude modulating cycles is expected, as has been noted in several Mesozoic and Paleozoic sequences (e.g. Huang et al., 2010; Wu et al., 2013; Sørensen et al., 2020).

1.2 Extension of the astronomical theory into the Precambrian

In stark contrast to the Phanerozoic, research into the influence of astronomical forcing and its many cyclostratigraphic applications in the Precambrian is still in its infancy. In this period covering the oldest 85% of Earth's history, the Earth System was operating in fundamentally different ways than today or during the more recent geologic past. Notably, it witnessed the origin of life and transition to complex life forms (e.g., Dodd et al., 2017; Zhu et al., 2016; Spang et al., 2019), the birth of continents and plate tectonics (e.g. Næraa et al., 2012), extreme glacial Snowball Earth events (Hoffman et al., 1998; Rooney et al., 2015) and the oxygenation of the atmosphere and oceans (e.g., Holland, 2002; Lyons et al., 2014), laying the foundations for our modern oxygen-rich biosphere. Although there is no reason to assume that astronomical forcing did not exert a significant influence on the early Earth climate system, extension of the astronomical theory into the Precambrian has long been hampered by a lack of sufficient independent time control (i.e. radio-isotopic ages), as well as the increasing theoretical uncertainty in the Milankovitch cycle periods in deep time. Another major limitation which has often been put forward, is the increasing scarcity of continuous, well-preserved and sufficiently long sequences the further one goes back in the stratigraphic rock record (e.g. Waltham, 2015).

However, sediment sequences exhibiting regular bedding and hierarchical stacking patterns that are reminiscent of the superposition of Milankovitch cycles have been reported from a number of different Precambrian records (Knoll and Swett, 1990; Grotzinger, 1986; Le Roux, 1997; Hofman et al., 2004; Mingxiang and Tucker, 2013). And in recent years, the first couple of cyclostratigraphic studies have been published for intervals of the Neo- and Mesoproterozoic presenting radio-isotopic and/or statistical evidence in support of a Milankovitch origin (Zhang et al., 2015; Gong et al., 2017; Bao et al., 2018; Meyers and Malinverno, 2018; Mitchell et al., 2021a; Mitchell et al., 2021b). Particularly noteworthy are the regular chert-shale couplets in the ~1.4 Ga Xiamaling Formation of the North China Craton analysed by Zhang et al. (2015), whose proposed astronomical origin is consistent with results of high-precision chemical abrasion (CA-) TIMS U-Pb dating of ash layers. Based on geochemical multi-proxy analysis and by drawing an analogy to Cretaceous black shale rhythms, the authors proposed a model of astronomical-forced variations in marine primary productivity and organic matter accumulation linked to shifts in the position of the Intertropical Convergence Zone (i.e., monsoonal forcing). More recently, this record was re-analysed by Meyers and Malinverno (2018), who derived an estimate of the shorter precession frequency p, Earth-Moon distance and day length, using a Bayesian inversion approach.

Yet, if it is our main purpose to investigate how astronomical forcing influenced the early Earth System when conditions were truly different from today or in the Phanerozoic, then we need to also, or especially, search for Milankovitch signals in much older portions of the geological record. In particular, the period before the Great Oxidation Event (GOE) around 2.4 – 2.2 Ga (Fig. 7; Holland, 2002; Bekker et al., 2004; Gumsley et al., 2017; Warke et al., 2020) is of great interest, given that the GOE demarcates a fundamental transition (i.e. irreversible shift) in the biochemical and redox evolution of Earth's near-surface environment, between an essentially anoxic older part and oxic younger part of the history of Earth's atmosphere and surface ocean. An additional argument for looking this far back in time is that for the reconstruction of the Earth-Moon system, reliable constraints from the oldest 50% part of geologic history are thus far lacking, while these would obviously be very welcome.

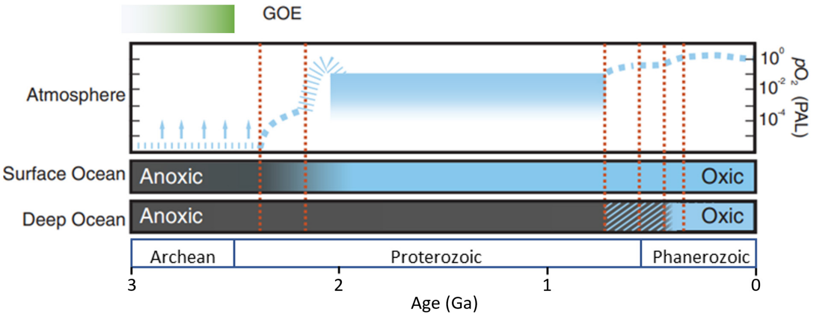

Figure 7. Redox history of Earth's ocean-atmosphere system. Green shading indicates the period when oxygenic photosynthesis may have evolved. Arrows denote possible O_2 'whiffs' prior to the GOE. PAL = present atmospheric level. Figure adapted from Alcott et al. (2019).

1.3 Early Paleoproterozoic banded iron formations as promising target/ case study

The standard BIF model

At this point, a distinctively layered rock type of exclusively Precambrian occurrence called 'banded iron formation' comes into view. BIFs are defined as marine chemical sedimentary deposits rich in iron (15 – 40 wt%) and silica (40 – 60 wt%) and showing a conspicuous centimetre-scale alternation of iron-rich and iron-poor bands, although such banding occurs in fact at a variety of thickness scales ranging from the micrometre to metre level (Trendall and Blockley, 1970; Ewers and Morris, 1981; Morris, 1993; Trendall 2002). They are widely distributed, albeit episodically, within the Precambrian stratigraphic record between 3.8 - 1.8 Ga (Fig. 8; Klein and Beukes, 1989; Isley et al., 1995; Trendall, 2002; Klein, 2005; Bekker et al., 2010), the majority of which is found across the Archean - Proterozoic boundary at 2.5 Ga.

Of these, the BIFs of the ~2.6 – 2.4 Ga Hamersley basin on the Pilbara craton in Western Australia and the Griqualand West basin on the Kaapvaal craton in South Africa

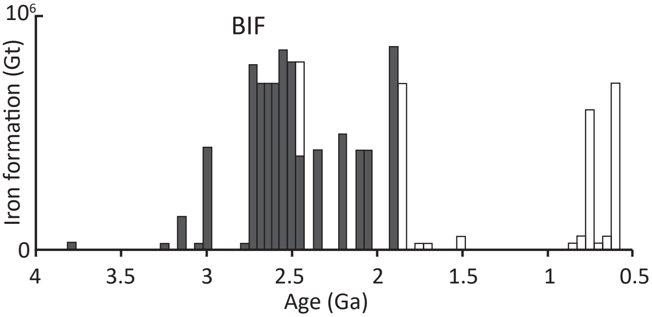

Figure 8. Precambrian distribution of marine Fe deposits. Occurrences of BIF are indicated in dark grey. Adapted from Bekker et al. (2010).

are arguably the most well-preserved (i.e., little metamorphosed and deformed) and largest known examples in terms of volume, thickness and areal extent (Trendall and Blockley, 1970; Beukes, 1983; Trendall, 2002). Consequently, these Australian and South African BIF successions, particularly the roughly coeval Brockman and Kuruman Iron Formations (IFs), respectively, have been regarded as archetypes and the main subject of extensive sedimentological, mineralogical and geochemical study, experiment and modelling over the past 70 years (e.g. James, 1954; Trendall and Blockley, 1970; Ewers and Morris, 1981; Beukes, 1983; Morris, 1993; Krapež et al., 2003; Posth et al., 2008; Robbins et al., 2019; Schad et al., 2019). As there are no good analogues to BIF on the present-day Earth, these collective efforts have been of great value to our understanding of BIF genesis and their paleoenvironmental significance, particularly with regards to the redox, biochemical and tectono-volcanic evolution of the early Earth leading up to the GOE (e.g. Trendall, 2002; Klein and Beukes, 1989; Beukes and Gutzmer, 2008; Bekker et al., 2010; Konhauser et al., 2017).

In brief, the now standard accepted model for the Archean and early Proterozoic occurrence of BIF (Fig. 9) is that of a globally anoxic deep ocean enriched in dissolved ferrous iron (Fe^{2+}) and primarily sourced from hydrothermal plumes (Holland, 1973; Klein and Beukes, 1989; Derry and Jacobsen, 1990; Isley et al., 1995; Poulton and Canfield, 2011). Subsequent Fe^{2+}oxidation took place in photic-zone continental margin waters of the first emerging proto-continents, either via anoxygenic photoferrotrophy or/and through reaction with O_2 produced by early evolved cyanobacteria (Cloud, 1973; Konhauser, 2002; Trendall, 2002; Buick, 2008), leading to precipitation of iron (oxyhydr) oxide particles. During later rock dehydration, these were converted to hematite (Ayres, 1972; Ahn and Buseck, 1990; Sun et al., 2015), while co-deposited silica originating from hydrothermally-sourced supersaturated waters formed microcrystalline quartz i.e. chert (Siever, 1992; Fischer and Knoll, 2009; Rasmussen et al., 2015). Co-accumulation of organic matter led to dissimilatory iron reduction (Baur, 1985; Heimann et al., 2010), producing magnetite and iron carbonate (i.e., ankerite, siderite) minerals. The variable occurrence of fine-grained iron-rich clays (stilpnomelane) and silicates (greenalite, minnesotaite, riebeckite) has been linked to both distal input of terrigenous/partly volcanogenic material, hemipelagic and/or authigenic origins (Trendall and Blockley, 1970; Klein and Beukes, 1989; Alibert and McGulloch, 1993; Pickard, 2003; Rasmussen et al., 2013).

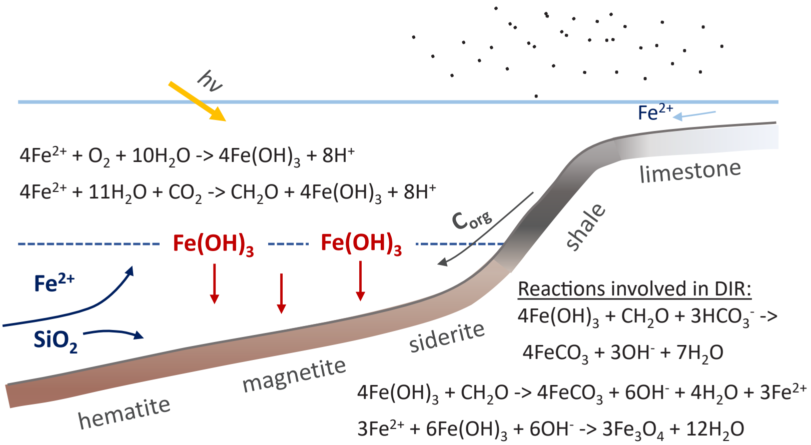
hν
Fe^{2+}
$4Fe^{2+} + O_2 + 10H_2O \rightarrow 4Fe(OH)_3 + 8H^+$
$4Fe^{2+} + 11H_2O + CO_2 \rightarrow CH_2O + 4Fe(OH)_3 + 8H^+$
limestone
C_{org}
shale
$Fe(OH)_3$
$Fe(OH)_3$
Fe^{2+}
SiO_2
Reactions involved in DIR:
$4Fe(OH)_3 + CH_2O + 3HCO_3^- \rightarrow$
$4FeCO_3 + 3OH^- + 7H_2O$
siderite
magnetite
hematite
$4Fe(OH)_3 + CH_2O \rightarrow 4FeCO_3 + 6OH^- + 4H_2O + 3Fe^{2+}$
$3Fe^{2+} + 6Fe(OH)_3 + 6OH^- \rightarrow 3Fe_3O_4 + 12H_2O$

Figure 9. The standard model for early Paleoproterozoic (B)IF deposition. This figure is based on a combination of the models of Klein and Beukes (1989) and Konhauser et al. (2017). DIR reactions are from Heimann et al. (2010).

Possible Milankovitch origin of the banding

Meanwhile, seemingly cyclic banding patterns at multiple scales (centimetre to metre) that are suggestive of an astronomical forcing control have been described from the Brockman as well as Kuruman IFs dating back to the late 60's to early 80's (Trendall and Blockley, 1970; Beukes, 1980). In particular, remarkable observations were made and documented by Alec Trendall (Trendall, 1969; 1972; 1973; Trendall and Blockley, 1968; 1970) from the Dales Gorge Member and to a lesser extent the Joffre Member BIF units of the Brockman IF (Fig. 10). While Trendall mainly focused on the regular millimetre-scale laminae patterns, which he interpreted as being controlled by annual-scale seasonal or solar sunspot cyclicity (the "Basic Hypothesis"; Trendall and Blockley, 1970; Trendall, 1973), he further hypothesized about the effect of a "superimposed longer climatic cycle" explaining the presence of a strikingly regular ~10 -15 cm scale variation of specific mesoband types called the Calamina and Knox cyclothem. Even more so, in his 1972 Presidential Address publication titled *Revolution in Earth history*, Trendall explicitly mentioned the possible causal connection with the Earth's precessional, obliquity and eccentricity cycles, concluding with "…continued attention to the history of the Earth's revolution around the Sun ..(..).. since it left its mark so indelibly on the Hamersley Group, is a topic to which simple and patient observations of the rocks still has much to contribute." Moreover, he remarked that, in turn, "stratigraphy can and should supply information on …. paleogeophysics".

Remarkably, since Trendall's revolutionary comments almost 50 years ago, the inferred astronomical forcing and potential cyclostratigraphic/ astrophysical applications of regular stratigraphic/ banding patterns in the lower Paleoproterozoic BIFs of Western Australia and South Africa have never been systematically investigated any further. At the time, a major limitation to testing the Milankovitch hypothesis was a lack of sufficiently accurate and precise radio-isotopic ages. So to estimate depositional rates, Trendall was reliant on making rather crude assumptions about average sedimentation rates based on interpreted varve thickness. With the appearance of multigrain SHRIMP U-Pb zircon ages during the late 1990s and early 2000s, age constraints improved considerably, but still remained of insufficient quality to make any reasonably precise determination of the depositional rate, leading to estimates that differed by two orders of magnitude (e.g. Pickard, 2002 versus Trendall et al., 2004; J. Davies pers. comm.).

Maybe partly because of this time scale uncertainty, general interest for BIF stratigraphic cyclicity and their possible astroclimatic implications seems to have largely

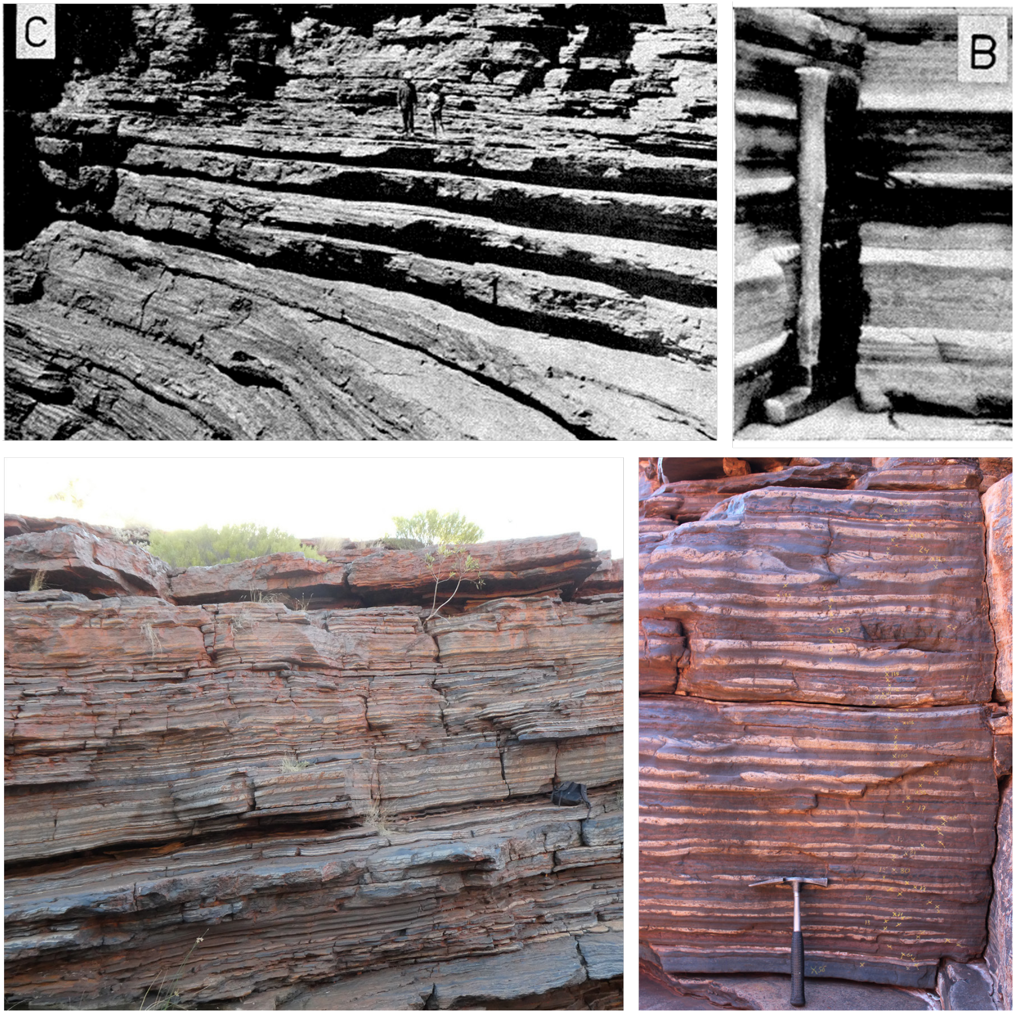

Figure 10. Regular stratigraphic cyclicity observed in field exposures of the Joffre Member in Joffre Gorge. The upper photographs are from Trendall & Blockley (1970; their Figure 19) and the lower pictures were taken during our own fieldwork in 2018 – 2019 (from the same location, but of different intervals). In the original figure caption of Fig. 19C in Trendall & Blockley (1970), the regular ~85 cm cycles are indicated as "four 21/2-foot repetitions of thin stilpnomelane-rich tuffs ... well displayed on the east side of Joffre Falls below the ledge on which the boys are standing." In addition, they write that "In the lower left-hand corner of the picture the much thinner Knox cyclothem may be discerned as a white striping; each stripe consists of a double white chert, in contrast with the single white chert of B."

been ignored over recent years, and the term 'Milankovitch' has only been mentioned in a few subsequent publications (Walker and Zahnle, 1986; Simonson and Hassler, 1996; Pickard et al., 2004; Rasmussen et al., 2015). This diminished attention or awareness is also illustrated by the lack of BIF stratigraphic proxy studies providing sufficiently long, continuous and high-resolution records to allow the detection of Milankovitch-related signals (e.g. Heimann et al., 2010; Busigny et al., 2013; Li et al., 2015; Haugaard et al., 2016). Moreover, in the search for primary biogeochemical and oceanic redox signals, it has become a commonly adopted strategy to deliberately exclude one lithological endmember of BIF, i.e. its characteristically - and often regularly! - intercalated stilpnomelane-rich layers, from sampling (e.g. Planavsky et al., 2010; Konhauser et al., 2011; Oonk et al., 2017).

It is thus evident that a marked knowledge gap remains with regards to the 'Milankovitch hypothesis' for BIF deposition during the early Paleoproterozoic. Testing this hypothesis, and exploring the wider implications for the early Earth, lunar recession and Solar System planetary dynamics, has been the primary motivation and objective of this thesis.

2. Objectives, progress and summary of the thesis research

In this thesis, I present the results of a multi-proxy cyclostratigraphic study integrated with high-precision CA-ID-TIMS zircon dating, and geochemical modelling, of the early Paleoproterozoic (~2.49 – 2.45 Ga) Kuruman IF in South Africa and the Dales Gorge and Joffre Members of the Brockman IF in Western Australia. The study, conducted between 2017 and 2020, had two main research questions/objectives, which are addressed in the next four chapters:

- 1) to determine the potential influence of astronomical climate forcing on BIF deposition and Earth System during the early Paleoproterozoic (**Chapters 2** and **3**). Due to the progress of the research, **Chapter 3** is focused especially on the link between astronomical climate forcing and (cyclical changes in) paleoenvironmental redox conditions;

- 2) to use BIF cyclostratigraphy for reconstructing the history of the Earth-Moon system (**Chapter 4**) and the development of astrochronological frameworks (**Chapter 5**) for the early Paleoproterozoic.

At the start of the project, research was logically aimed at answering the first question, i.e. whether astronomical climate forcing is indeed recorded in early Paleoproterozoic BIFs. For this purpose, the Kuruman IF was selected, since regular sequences (macrocycles of "1 to 10 m") had been previously described from drill-core (Beukes, 1980) and inspection of satellite photos (Google Earth) revealed promising regularity at a similar scale in outcrop. During a subsequent reconnaissance fieldtrip to the Griqualand West basin (spring '17), existing drill-cores of the Kuruman IF stored at the Hotazel core repository were examined first. However, given the visually overwhelming presence of - often irregular - centimeter-scale banding that we encountered, starting from cores seemed a less promising strategy for testing the Milankovitch hypothesis at that time. Moreover, the stratigraphic order of the inspected GASESA-1 core was found to be incorrect in several places.

Instead, switching to the natural outcrops of the Kuruman IF yielded much more promising results. As outlined in **Chapter 2**, a prominent hierarchical stacking ("bundling") pattern was identified in its weathering profile and laterally traced over a distance of 250 km from Kuruman Kop in the north to Prieska in the south. Cyclostratigraphic analysis indicated that the pattern could be largely explained by the presence of two prominent cycles with thicknesses of ~4 - 6 and ~16 - 22 m. Lithological facies analysis showed that the indurated parts ("ridges") of these cycles were relatively richer in iron oxides, and alternated with intervals relatively richer in iron carbonate. By integrating the cyclostratigraphic observations with much-improved U-Pb geochronology, a Milankovitch origin for the cycles was established, linking the ~5m cycle to the long 405-kyr eccentricity cycle, and the ~16 – 22 m cycle to the very long ($g_4 - g_3$) eccentricity cycle with reduced period of ~1.2 - 1.6 Myr. Three of the four shale intervals that were sampled for CA-ID-TIMS U-Pb zircon dating came from a new core of the Kuruman IF, which we decided to drill during that same year (autumn '17). This core (UUBH-1) allowed for a more high-resolution and multi-proxy survey of the Kuruman IF during a later stage of the research (i.e., using X-ray fluorescence (XRF) core scanning), the results of which are included in **Chapter 5**.

Based on the results of **Chapter 2**, a very preliminary (conceptual) climate model was formulated, in which the long-eccentricity-related alternations in the Kuruman IF were attributed to a dominant control of the climatic precession cycle on variations in monsoonal intensity, marine productivity and ferric (oxyhydr)oxide and/or organic matter accumulation. However, the actual investigation of our precession hypothesis and of the associated paleoclimatic and -environmental consequences was hampered by the fact that the stratigraphic expression of the climatic precession in the Kuruman IF was not obvious (based on our relatively rudimentary field observations), nor was that of short (~100 kyr) eccentricity. A clear and continuous expression of these cycles was also required if we wanted to determine the precession period (and hence Earth-Moon distance) from its ratio with eccentricity.

To address these problems, we shifted our focus to the Joffre Member of the Brockman IF in **Chapters 3** and **4**. Field exposures of the Joffre Member within the gorges of the Karijini National Park at Joffre Falls, encountered during a reconnaissance visit to the Hamersley Range (summer ’18), revealed a remarkably continuous expression of a regular ~5 - 15 cm alternation grouped into larger ~85 cm thick bundles, indicative of the modulation of precession by short eccentricity. The cycles correspond to the characteristic “Knox cyclothem” of the Joffre Member, and a regular “65 – 150 cm” alternation between BIF and stilpnomelane mudrock, respectively, which was previously described from that same locality (Plate 28D in Trendall 1969; Fig. 19c in Trendall and Blockley, 1970). The Knox cyclothems in the field were generally distinguished by a conspicuous double white chert band (nicknamed “tramrails”). Upon subsequent inspection of an existing core (DD98SGP001) drilled ~150 km west of Joffre Falls and stored at the Perth core library, various lithologically different types of Knox cyclothems were identified, the most conspicuous of which consist of a regularly intercalated ~1cm greenish mudrock layer alternating with chert and iron oxide. Close examination revealed the occurrence of thin, shiny “fluid-like” magnetite laminae, as well as distinct carbonate and pyrite laminae, at the upper and lower boundary of the green mudrock layers. These features are strongly reminiscent of relict chemical reaction fronts as previously described from Pliocene-Pleistocene ‘redox cycles’ (Van Hoof et al., 1993; Fig. 3) and formed as a result of early diagenetic breakdown of cyclically deposited organic matter-rich layers. Accordingly, we decided to proceed in two ways, namely i) to conduct a more geochemically-focused study on the paleoenvironmental significance of the cyclothems based on selected intervals from the DD98SGP001 core (**Chapter 3**), and ii) concentrate our cyclostratigraphic reconstruction of the precession period and Earth-Moon distance at Joffre Falls (**Chapter 4**).

In **Chapter 3**, intriguing patterns in Fe and S concentration, revealed by mm-scale (calibrated) XRF core scanning of selected Knox cyclothem alternations, could be quantitively simulated using a reactive-transport model. Based on these results and new U-Pb zircon ages obtained from core DD98SGP001, these alternations were interpreted in terms of cyclical changes in organic matter accumulation, Fe^{2+} content and production of O_2 in the overlying water column that could be ascribed to precession-forced changes in monsoonal-induced runoff and associated nutrient input. Our results and model indicate a highly dynamic redox evolution of the Earth’s pre-oxygenated ocean and atmosphere in response to Milankovitch forcing. In fact, the astronomically-induced climate changes may have played an important role in the oxygenation of the ocean and atmosphere just prior to the GOE at 2.4 Ga.

In **Chapter 4**, the cyclostratigraphy of the Joffre Member at Joffre Falls proved consistent with the Milankovitch interpretation of the same member in **Chapter 3**, i.e., a short eccentricity origin for the ~85 cm cycles and climatic precession origin for the Knox cyclothem, based on the sedimentation rates obtained from the DD98SGP001 core.

Due to the complex structure of the Knox cyclothem and marked differences in local thickness of the cycle (i.e., varying from less than 5 to more than 20 cm within one short eccentricity-related bundle), we adopted a cycle counting approach (instead of the spectral peak ratio method), to determine the average number of climatic precession-related cycles per short eccentricity-related bundle. Based on the established 9:1 cycle ratio, a value of the axial precession frequency, Earth-Moon distance and daylength could subsequently be obtained and was compared to other empirical estimates and lunar recession models from the literature. Our result and the trajectory of lunar recession that is indicated together with two previous cyclostratigraphy-based estimates of the Mesoproterozoic (Meyers and Malinverno, 2018) and Cambrian (Sørensen et al., 2020) shows a close agreement with the model of Webb (1982), implying a dominant influence of long-term changes in the Earth's rotation rate on the power dissipated by the ocean tides.

Finally, in **Chapter 5** we explored the cyclostratigraphic correlation potential between the Kuruman IF and the roughly age-equivalent Dales Gorge Member of the Brockman IF. Metre-scale alternations suggestive of the same long-period eccentricity control as demonstrated for the Kuruman IF (in **Chapter 2**) were also described from the Dales Gorge Member ("BIF-S macrobanding"; Trendall and Blockley, 1970; de Oliveira Carvalho Rodriguez et al., 2019). As such, these two BIF units presented an interesting case study for establishing a 405 kyr cycle-based astrochronological framework for the lower Paleoproterozoic sequences of Western Australia and South Africa. In addition, such an exercise could provide more precise and/or robust information on the period of the inferred $g_4 - g_3$ cycle (of **Chapter 2**), as well as on the presence of other long-period Milankovitch cycles.

To this end, a combined cyclostratigraphic study of the Dales Gorge Member and Kuruman IF was carried out using various high-resolution proxy records (e.g., verticality profiles of field outcrops using drone-based photogrammetric models, drill-core mineral reflectance data, elemental records from XRF core scanning, downhole magnetic susceptibility) integrated again with U-Pb zircon dating. The results turned out to be in overall agreement, though slightly different from those in **Chapter 2**: apart from a ~5 m cycle related to $g_2 - g_5$, a ~16 m cycle was found to be the dominant component responsible for the characteristic hierarchical stacking / bundling seen in both BIF units; this cycle is now tentatively linked to $g_4 - g_3$ at a much-reduced period of ~1.3 Myr.

Despite the inferred astronomical forcing and the fact that the cycles in each of the units could be traced over hundreds of kilometres within their respective basins, it proved not possible to correlate the Dales Gorge Member and Kuruman IF cyclostratigraphically in a high-resolution (i.e., at the 405-kyr level) convincing way. The main reason for this is likely the difference in depositional environment in which these units were deposited, resulting in a different expression and/or amplitude of certain cycles whose astronomical origin also remains uncertain. Thus, while considerable progress has been made, *much more remains to be investigated regarding the astronomical theory for early Paleoproterozoic banded iron formations*.

In summary, looking at chapters of my thesis in relation to the originally formulated research objectives, it is clear that the overall results are very positive. Firstly, we demonstrated that astronomical climate forcing is recorded in the ~2.49 – 2.45 Ga old BIFs of the early Paleoproterozoic. Secondly, we established a depositional model for these cycles by combining high-resolution proxy and reactive transport modeling efforts. Thirdly, we calculated the Earth-Moon distance and length of day at 2.46 Ga, providing a critical tie-point for the reconstruction of the long-term history of the Earth-Moon system. Fourthly, we established an integrated (cyclo)stratigraphic framework for the Kuruman IF and Dales Gorge Member. Unfortunately, the final correlation scheme remains uncertain due to a difference in the registration/expression of the astronomical forcing/cycles between these two stratigraphic units. This also hampered the study of the chaotic behavior of the Solar System. However, there is considerable evidence that the current 2.4 Myr eccentricity cycle may have been significantly shorter at that time.

3. Outlook

Overall, our results point to a very bright future for cyclostratigraphic studies of the Precambrian. The depositional model for the BIF cycles needs to be refined and expanded to include both the time interval well before and across the GOE. Similar studies should be carried out in other critical time intervals of the Precambrian, focusing especially on the potential relationship with ice ages and the evolution and mode of distribution of early life. Promisingly, an increasing number of Precambrian cyclostratigraphic studies has already been published over the last years (see section 1.2). Our determination of the Earth-Moon distance at 321.8 ± 6.5 thousand kilometres at 2.46 Ga should be verified, for which the Dales Gorge Member is a potential target (de Oliveira Carvalho Rodriguez et al., 2019). New data from other time intervals must be incorporated to better constrain the uninterrupted evolution of the Earth-Moon system, needed for comparison with more sophisticated models currently being developed (e.g., Daher et al., 2021). Furthermore, the complex cyclostratigraphy of the investigated BIFs needs to be studied in more detail and further disentangled, possibly by adding other high-resolution proxy records such as stable isotopes. This may solve our current problems in establishing an integrated cyclostratigraphic BIF framework, and shed new light on the chaotic nature of the Solar System during a much earlier stage in its evolution than hitherto explored. Finally, improved independent age constraints from U-Pb zircon dating must be generated to convince other (skeptical?) Earth scientists and solve remaining fundamental problems in BIF cyclostratigraphy. Such an integrated effort will be very challenging but worthwhile, not only for our understanding of BIF, but for the entire Precambrian.

Chapter 2

Climate control on banded iron formations linked to orbital eccentricity

Climate control on banded iron formations linked to orbital eccentricity

Margriet L. Lantink, Joshua H.F.L. Davies, Paul R.D. Mason, Urs Schaltegger and Frederik J. Hilgen

Abstract

Astronomical forcing associated with Earth's orbital and inclination parameters (Milankovitch forcing) exerts a major control on climate as recorded in the sedimentary rock record, but its influence in deep time is largely unknown. Banded iron formations, iron-rich marine sediments older than 1.8 billion years, offer unique insight into the early Earth's environment. Their origin and distinctive layering have been explained by various mechanisms, including hydrothermal plume activity, the redox evolution of the oceans, microbial and diagenetic processes, sea-level fluctuations, and seasonal or tidal forcing. However, their potential link to past climate oscillations remains unexplored. Here we use cyclostratigraphic analysis combined with high precision uranium–lead dating to investigate the potential influence of Milankovitch forcing on their deposition. Field exposures of the 2.48-billion-year-old Kuruman Banded Iron Formation reveal a well-defined hierarchical cycle pattern in the weathering profile that is laterally continuous over at least 250 km. The isotopic ages constrain the sedimentation rate at 10 m Myr^{-1} and link the observed cycles to known eccentricity oscillations with periods of 405 thousand and about 1.4 to 1.6 million years. We conclude that long-period, Milankovitch-forced climate cycles exerted a primary control on large-scale compositional variations in banded iron formations.

Introduction

Banded iron formations (BIFs) are iron-rich (~30wt%) and distinctively layered chemical sediments that were widely deposited in the Neoarchean to early Paleoproterozoic oceans, between 2.8 and 2.4 billion years ago (Klein, 2005; Bekker et al., 2010). So far, they have been mainly related to hydrothermal plume activity (Morris, 1993; Isley, 1995; Krapež et al., 2003; Viehmann et al., 2015), the evolution of continental shelves (Trendall, 2002; Barley et al., 2005), diagenetic and microbial iron cycling (Konhauser et al., 2002; Heimann et al., 2010; Fischer and Knoll, 2009) and the rise of oxygen in the oceans and atmosphere (Cloud, 1973; Konhauser et al., 2017). In contrast, very little is known about the possible link between climate variability and BIFs.

Here we focus on the potential influence of Milankovitch forcing on the formation of BIFs. Secular climate variations (10^4 –10^6 yr scale) induced by cyclic changes in the Earth's orbit and inclination axis must have been operating at that time (Laskar et al., 2004) and may explain the rhythmic layering observed in BIFs (Trendall and Blockley, 1970; Beukes, 1980). However, evidence for Milankovitch cyclicity in BIFs has never been conclusively presented, despite claims for the presence of seasonal (Morris, 1993; Trendall., 1973; Posth et al., 2009) or tidal (Walker and Zahnle, 1986) laminations and eustatic sea level

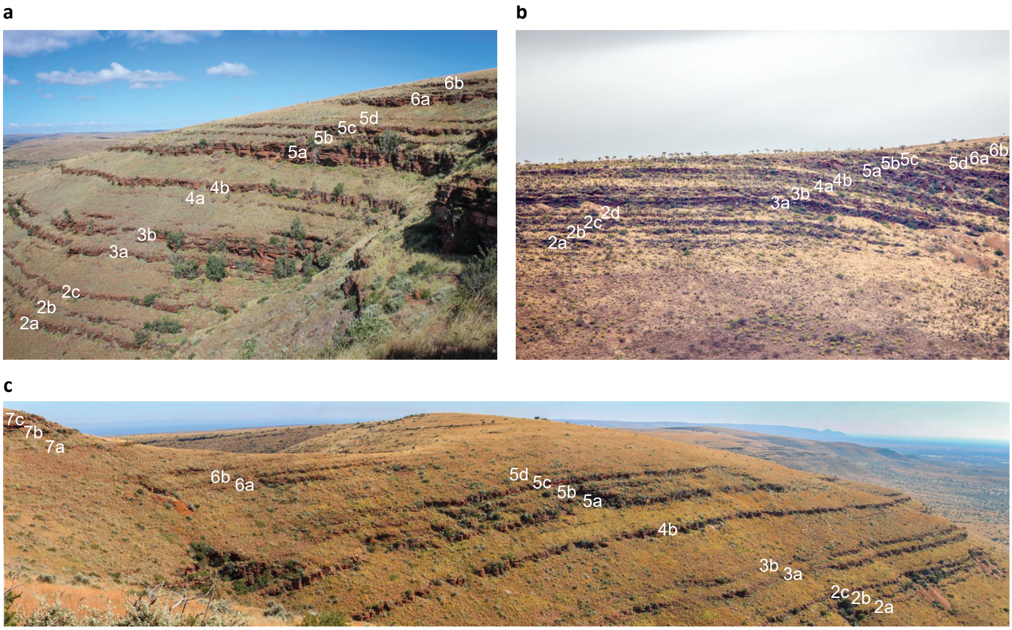

Figure 1 | Rhythmic alternations in the weathering profile of the Kuruman BIF. The alternations show a consistent pattern between different sections in the Griqualand West basin. Photos are from sections Whitebank (**a**), Prieska (**b**) and Woodstock (**c**).

alternations (Morris, 1993; Simonson and Hassler, 1996) suggesting climate control. A key problem is the uncertainty in BIF depositional rates due to the lack of high-quality radioisotopic ages. Currently available U–Pb SHRIMP ages (Trendall et al., 2004; Pickard, 2003) are insufficiently precise and accurate to independently test a potential Milankovitch origin for stratigraphic rhythms in BIFs.

For this reason, we carried out a cyclostratigraphic study combined with high-precision chemical-abrasion isotope-dilution thermal ionization mass spectrometry (CA-ID-TIMS) U–Pb zircon dating of the early Paleoproterozoic Kuruman Formation in the Griqualand West Basin, South Africa (Supplementary Text 1). This 200m thick BIF succession is a suitable target for exploring our Milankovitch working hypothesis, because it contains several volcanic ash layers (Pickard, 2003), which can be dated with high accuracy and precision using U–Pb high-precision isotope-dilution techniques, and shows rhythmic bedding on multiple scales (Beukes, 1984; Beukes and Gutzmer, 2008). Previous observations from the Kuruman BIF were solely based on drill cores (Beukes, 1980; Klein and Beukes, 1989). Instead, we concentrated on field exposures, as stratigraphic changes in composition are often visually enhanced by the effects of weathering.

Cycle hierarchy and possible origin

Field exposures of the Kuruman BIF show clearly defined, regular alternations in the weathering profile (Fig. 1, Supplementary Figs. 1 and 2). More specifically, a rhythmic alternation is visible between well-exposed, protruding BIF, and deeply weathered, poorly exposed intervals. The weathering-resistant intervals tend to form steep cliffs, whereas the unexposed sections form gentle slopes, thus causing variations in relief. These alternations occur on two distinct scales, namely at about 5m and 20m, producing a hierarchical stacking pattern with typically two to four indurated ridges grouped together into larger scale bundles. Lithological observations indicate higher concentrations of iron oxide-rich beds in the indurated and iron carbonate-rich beds in the soft intervals (Supplementary Fig. 3–5). This is supported by X-ray fluorescence (XRF) data (Supplementary Table 1).

The alternations form a characteristic pattern that is laterally continuous over 250 km. Starting in the Kuruman Hills at Kuruman Kop, we identified a characteristic succession of alternations, which we could trace southwards over more than 60 km (along the road from Kuruman towards Daniëlskuil). We subsequently recognized the same pattern near Prieska, 250km towards the south. In total, we logged eight characteristic bundles (labelled 1–8), each made up of a number of exposed intervals (labelled a–d) with a typical weathering profile expressed in terms of 'relief ' (Supplementary Text 2). Proposed correlations are shown in Fig. 2.

Spectral analysis results suggest a cyclic origin for the two scales of alternations observed in the Kuruman BIF weathering profile. Multitaper method (MTM) spectra with classical AR1 and LOWSPEC (Meyers, 2012) noise model confidence levels show concentration of power at two spatial wavelengths for the five different logs, that is around 4.3–6.3m and 16–22m (Fig. 3a, Supplementary Fig. 6), with peaks often but not always exceeding 90–95% (Supplementary Text 3, Supplementary Table 2). Bandpass filtering confirms the link between the 4.3–6.3m and 16–22m periods and the characteristic alternations observed in the field: maxima in the corresponding filter outputs coincide with the occurrence of the individual ridges (a–d) and bundles 1–8 (Fig. 2), respectively, with some exceptions (Supplementary Text 4). The two filtered signals reveal a 1:3 to 1:4 cycle ratio, with the longer-period waveform following the amplitude modulation of the shorter-period cycle. Additional filtering (Supplementary Fig. 8) and evolutive harmonic analysis (Fig. 3b) indicate that the pronounced peak splitting (double peaks) in the two main frequency bands (Fig. 3a) are due to time-depth distortion. In Fig. 3b, the two high-amplitude peaks in the lower portion of the stratigraphy show a systematic shift towards higher frequencies between cycles 3b and 5a, suggesting an upward decrease in depositional rate.

Our cyclostratigraphic results strongly argue for a Milankovitch influence on the formation of the Kuruman BIF. The discovery of rhythmic alternations that are continuous over 250 km forms direct evidence for widespread, cyclic palaeoenvironmental changes affecting the deposition. Astronomical climate forcing is the only mechanism that can explain the cyclic nature and hierarchical ordering of the characteristic alternations. Moreover, the systematic shift of the two dominant wavelengths with stratigraphic height (Fig. 3b) and the observed amplitude-modulating relation in their bandpassfiltered signals (Fig. 2) cannot be attributed to an autoregressive noise source and therefore provide strong supporting evidence for an astronomical origin of both cycles. A possible argument

Figure 2 | Weathering profile logs and cyclostratigraphic correlations. a, Logs of the Kuruman BIF weathering profile in sections Kuruman Kop (KK), Whitebank (WB), Woodstock (WS), Daniëlskuil (DK) and Prieska (PK). The relief ranges from 0 (deeply weathered, unexposed) to 5 (very much protuding). Blue zones mark our proposed correlations of the characteristic ridges (labelled a–d) and bundles (labelled 1–8) between the sections. Bandpass filter outputs are indicated on the right-hand side of each

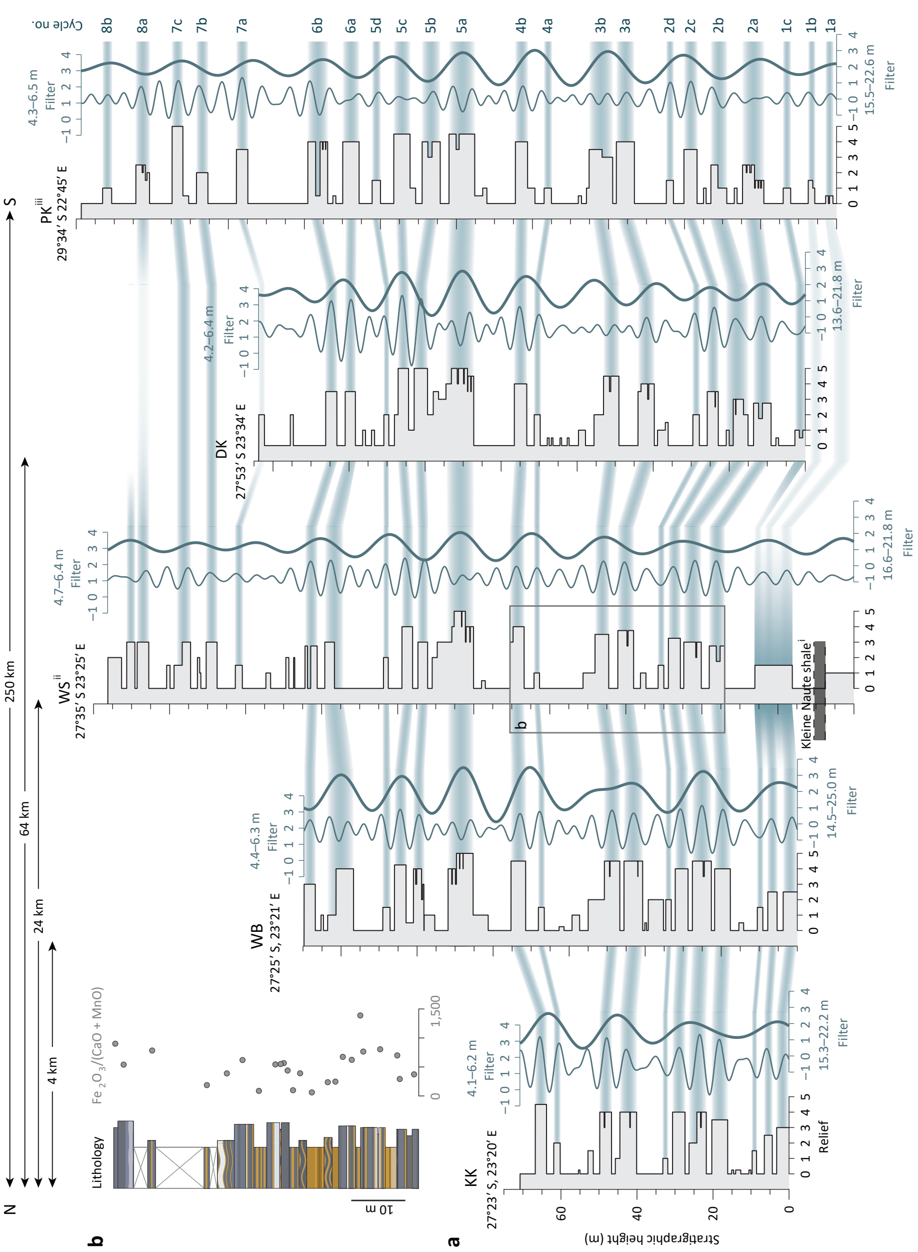

log. ^{i}The Kleine Naute shale marks the bottom of the Kuruman Formation. However, its stratigraphic position with respect to our characteristic cycles is inferred from correlations with drill core, because it does not crop out in the field. ^{ii}Bundles 7 and 8 are part of the uppermost Ouplaas Member of the Kuruman Formation in the Daniëlskuil–Kuruman area (Supplementary Fig. 4). ^{iii}The Prieska log only captures the bottom 200 m of the Kuruman Formation in this region (Supplementary Figs. 2 and 4). **b**, Detail of cycles 2–4 in section WS showing lithological observations (left) and XRF results (right). Yellow colours indicate carbonate-dominated intervals, blue colours the oxide-dominated intervals (see Supplementary Fig. 4 for a complete legend).

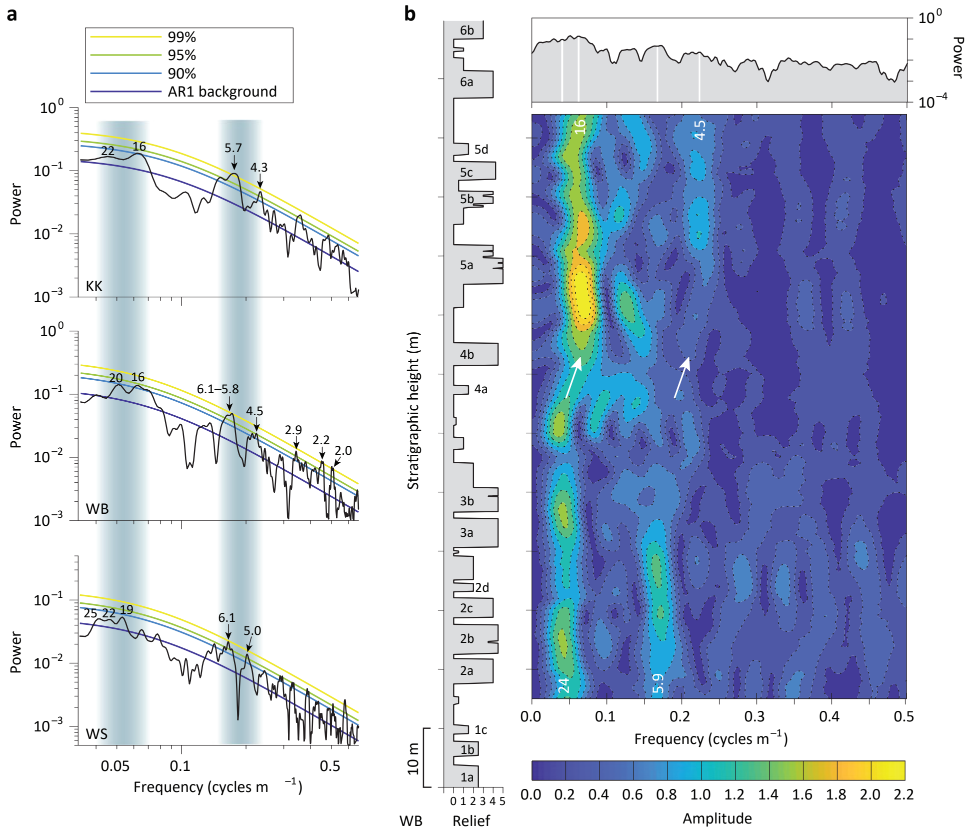

Figure 3 | Spectral analysis results. **a**, MTM power spectra (three 2π prolate tapers) for the logs from sections KK, WB and WS (10 cm linear interpolated; detrended) with AR1 background, 90, 95 and 99% confidence levels and peak labels in metres. Blue zones indicate the two areas of enhanced spectral power that are linked to the characteristic alternations and bundles. The peaks at 1–3 m are considered artefactual harmonics (Supplementary Fig. 7). **b**, EHA amplitude (three 2π; 30 m window) and MTM power spectrum (top) for the log of section WB (left). White arrows mark the frequency shift of the two main high-amplitude components between cycles 3b and 5a (mean periods are indicated in metres).

against our Milankovitch interpretation is the somewhat lower confidence levels of the 16–22m components (Supplementary Table 2), but this can be explained in a number of ways (Supplementary Text 5).

From a cyclostratigraphic Milankovitch perspective, there are a few ways to interpret the distinct 1:3 to 1:4 cycle ratio that we observe in the Kuruman BIF. The most logical candidate is the combination of the Earth's short (100 kyr) and long (405 kyr) eccentricity cycles (Hypothesis 1). Both cycles are known to have a strong stratigraphic imprint as amplitude modulators of the climatic precession cycle (Hilgen et al., 2015). Moreover, their periods are thought to be relatively robust in deep time. In particular the 405 kyr cycle is considered very stable, resulting from the combination of the precessional motions of the perihelia of Venus and Jupiter ($g_2 - g_5$) (Lasker et al., 2011). Alternatively, the pattern could be linked to the superposition of the 405 kyr and moderately strong, very long (now 2.4 Myr) eccentricity cycle (Hypothesis 2). In contrast to the 405 kyr cycle, the very long 2.4 Myr eccentricity cycle related to $g_4 - g_3$ is unstable, because of the chaotic secular resonance associated with $(s_4 - s_3) - 2(g_4 - g_3)$ (Pälike et al., 2004; Laskar et al., 2004); this resonance involves the fundamental planetary frequencies of the precessional motions of the perihelia and nodes of Earth (g_3 and s_3) and Mars (g_4 and s_4). As a consequence, its period may become shorter than 2.4 Myr, possibly down to 1.2 Myr (Laskar, 1990, Ma et al., 2017). In this case, a shorter period around 1.2–1.6 Myr would fit the observed 1:3 to 1:4 ratio in the Kuruman BIF. Other Milankovitch options that include precession or obliquity are unlikely since they do not match the observed ratio between the two cycles (Supplementary Text 6). Precise and accurate U–Pb geochronology should be able to distinguish between options 1 and 2.

Uranium–lead ages and link to long-period eccentricity

To obtain such high-precision U–Pb ages, we sampled different shale levels within the Kuruman BIF. Euhedral ash fall zircon crystals were extracted from four stilpnomelane lutite intervals from the GASESA-1 and UUBH-1 drill cores, spanning the entire stratigraphy (see Methods). All of the extracted zircon crystals were chemically abraded to remove the effect of decay-damage-related Pb loss and dated using CA-ID-TIMS techniques. However, since the grains were small (100–50 µm) and metamict, only moderate chemical abrasion was possible to avoid complete dissolution. Therefore, significant Pb loss is still observed in most grains. Fortunately, at least one grain from each sample gave concordant results (where both U–Pb geochronometers agree within uncertainty), which provides a high level of confidence in the calculated age. Only concordant analyses were used to calculate the ^{207}Pb/^{206}Pb ages, either through a weighted mean in the case of multiple concordant analyses or of a single grain. This gives an age of 2,484.6 ± 0.34 Ma (2σ) for the base and 2464.0 ± 1.3 Ma for the lutite closest to the top of the Kuruman BIF (Fig. 4a).

Our new high-precision ages are in general agreement with previously published ages (Pickard, 2003), although they are about 10–20 times more precise, allowing a significantly better estimation of the depositional rate. The depositional rate was estimated using the Bayesian model Bchron (Parnell et al., 2008) and suggests an extremely consistent average rate of 10 ± 10 mMyr^{-1} for the 200m of Kuruman BIF deposition (Fig. 4b and Supplementary Fig. 10). The average accumulation rate of 10 ± 10mMyr^{-1} for the Kuruman BIF yields periods of 430–630 kyr and 1.6–2.2 Myr for the characteristic alternations and bundles, respectively. These periods are very close to and within the uncertainty of the Earth's long (405 kyr) and very long (between 1.2 and 2.4 Myr) eccentricity cycles. In contrast, all other Milankovitch hypotheses are in conflict with the U–Pb results since they require depositional rates above the 20mMyr^{-1} upper limit. Therefore, the consistency between the U–Pb and the cyclostratigraphic results strongly argues for Hypothesis 2.

Tying the small-scale alternations to the stable 405 kyr cycle, a 1:3 to 1:4 cycle ratio would suggests a period between 1.2 and 1.6 Myr for the very long eccentricity cycle. This is shorter but within uncertainty consistent with the average 1.6–2.2 Myr period constrained by the U–Pb results. Bandpass filtering (Supplementary Fig. 8) suggests that

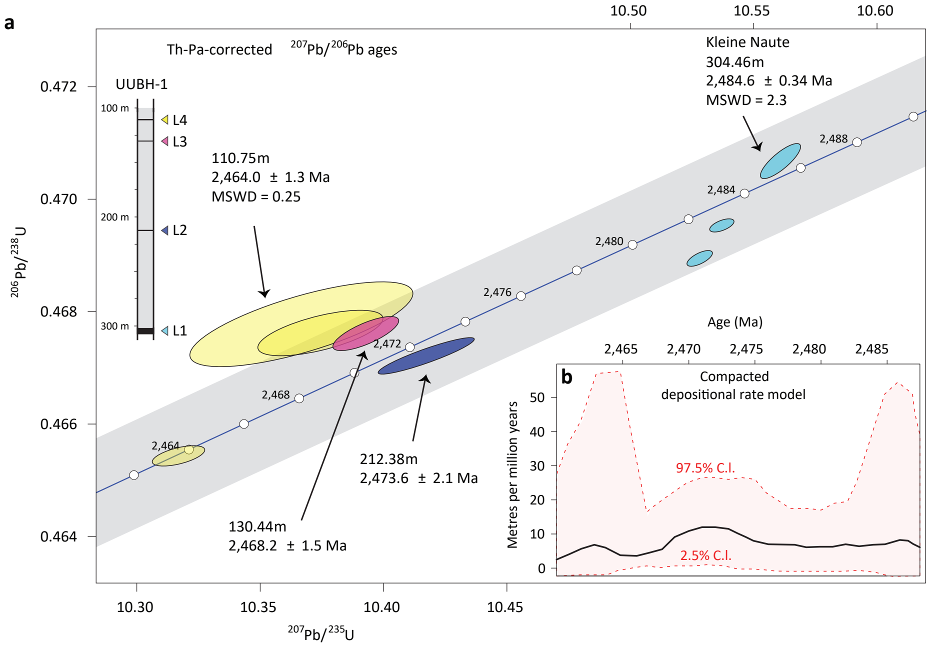

Figure 4 | U–Pb zircon ages and depositional rate. a, Concordia diagram showing the concordant high-precision U–Pb TIMS results and the calculated ages. The grey band represents the uncertainty on the Concordia curve due to the decay constant uncertainties. The ellipses represent the U–Pb isotopic data and 2σ uncertainty for individual chemically abraded zircon fragments, and the colours represent the different samples. The ^{207}Pb/^{206}Pb ages are given for each sample, either as a weighted mean or from an individual analysis, along with the depth in the UUBH-1 core. MSWD, mean square of the weighted deviates. Left: schematic representation of sample depth (stilpnomelane lutite L1–L4) and extent of the Kuruman Formation (in grey) in the UUBH-1 drill core (see Methods). **b**, Depositional rate model for the Kuruman BIF with 97.5% confidence intervals indicated.

the actual cycle ratio lies between 1:3.5 and 1:4, implying periods between 1.4 and 1.6 Myr for $g_4 - g_3$. Tuning the 4.5–6.1m wavelengths in the Whitebank spectrum to the 405 kyr cycle (Supplementary Fig. 9), we similarly obtain values between 1.4 and 1.6 Myr. The fact that bundle 2 contains four exposed ridges (2a–d) may even suggest a minimum ratio of 1:4 and a period of 1.6 Myr for very long eccentricity, since a fourth alternation should then be present in each bundle but is simply not exposed (that is, it is hidden in the softer intervals in between the bundles). Irrespectively, it is clear that $g_4 - g_3$ has a period smaller than the present-day 2.4 Myr and probably larger than 1.2 Myr. Similarly reduced periods around 1.6 Myr for the $g_4 - g_3$ cycle have been found in other cyclostratigraphic studies on Mesozoic to Palaeozoic strata (Olsen and Kent, 1999; Fang et al., 2015) indicating chaotic planetary behaviour.

In contrast to the long and very long eccentricity cycles, the expression of the climatic precession and short eccentricity cycle is not clear from our weathering profile logs and may point to a significant nonlinear response (Ripepe and Fischer, 1991). Nevertheless, short eccentricity might be represented by some of the splitting up we encountered in specific horizons, such as 2b, 3a, 3b, 5a, 6a, and 6b. Our logs are not detailed enough to resolve the precession-related cycles, with an expected thickness of approximately 10–15 cm (Supplementary Text 6).

Link to basin history, Australian BIF and climate

We are not the first to discover metre-scale variability in the Kuruman BIF. Our 405 kyr-related alternations share parallels with Beukes's (Beukes, 1980; Beukes and Gutzmer, 2008) macrocycles previously identified in drill core. These comprise a vertical sequence of stilpnomelane lutite, siderite- and subsequently magnetite–haematite-facies BIF occurring "on the order of 1–10m". In addition, the superposed megacycles that were distinguished (Fig. 5 in Beukes, 1980) show a striking resemblance to our characteristic bundles. Yet Beukes's macro- and megacycles hinge on the occurrence of thin stilpnomelane lutite beds and are linked to volcanic activity. In contrast, our cycles are determined by relative alternations in iron oxide versus iron carbonate content and are linked to eccentricity forcing. According to Beukes's observations, the stilpnomelane lutite intervals predominantly occur in the iron carbonate-rich intervals; however, we were unable to incorporate the lutites in our current lithofacies model due to their poor field exposure.

Our cyclostratigraphic correlations (Fig. 2) further have direct consequences for the Griqualand West basin history. Previous studies (Beukes, 1980; Beukes and Gutzmer, 2008) have temporally linked 200m of Kuruman BIF stratigraphy (and its characteristic megacycles) in the Kuruman–Daniëlskuil platform area to more than 600m of Kuruman BIF in the southern basinal part (for example Figs. 10 and 11 in Beukes, 1980). However, we observed the same cycle thicknesses and characteristic pattern in the lower 200m of Kuruman BIF in the southern Prieska section, implying that (1) accumulation rates were essentially the same as in the northern Kuruman–Daniëlskuil region and that (2) the much larger thickness in the south is likely due to prolonged sedimentation of Kuruman BIF in that area or, alternatively, by condensation or erosion in the northern platform region.

The 140m thick and roughly time-equivalent (Cheney, 1996; Pickard, 2003) Dales Gorge Member BIF (Hamersley Basin, Western Australia) exhibits similar lithological variations24 for which a Milankovitch origin has now become a plausible scenario. Its characteristic 17 BIF–S macrobands comprise iron oxide-dominated (BIF) and silicate- and carbonatedominated (S) or shale bands (Trendall and Blockley, 1970; Ewers and Morris, 1981; Krapež et al., 2003; Pickard et al., 2004) between 2.3 and 15m and between 0.6 and 5.5m thick, respectively, and have been correlated over the entire outcrop area. Moreover, wavelet analysis on magnetic susceptibility drill-hole data (Cowan and Cooper, 2003) has revealed clear periodic signals in the 5–6m and 15–20m ranges associated with the macrobanding. These results hint at the presence of cycles similar to those observed in the Kuruman BIF. If interpreted in the same way, the very regular, 15 cm thick Calamina cyclothem (Trendall and Blockley, 1970) in the Dales Gorge Member has the expected thickness of a precession-related cycle. This may be an important extra argument for our preferred interpretation of the Kuruman BIF cyclostratigraphy.

At this stage, we can only speculate about potential climate mechanisms for Milankovitch forcing of BIF. The dominance of eccentricity hints at a low-latitude climate control. Monsoonal systems are known to respond strongly to precession-eccentricity forcing (Kutzbach et al., 2008), with eccentricity modulating the precession amplitude, and were probably present during the Phanerozoic (Kutzbach, 1994; Reinhardt and Ricken, 2000) and Proterozoic (Zhang et al., 2015; Meyers and Malinverno, 2018) as well. Recently, approximately 5m scale variations in Fe–Nd isotopes from the Dales Gorge Member were linked to oscillations in riverine versus hydrothermal (marine) iron (Li et al., 2015), parallel to the S–BIF alternations, respectively. Continental runoff and ocean circulation are both mechanisms that can be strongly dependent on monsoonal intensity. Going one step further, monsoonal-enhanced iron or nutrient supply could have triggered photosynthetic or photoferrotrophic activity in the ocean's photic zone, leading to increased iron oxide production and accumulation on the seafloor. Alternatively, nutrient availability could have stimulated biological productivity, organic carbon production and subsequent formation of iron carbonates in the sediment via dissimilatory iron reduction (Heimann et al., 2010). However, the phase relations between precession, eccentricity and the chemical alternations in the Kuruman BIF are still unknown, yet they are crucial for any first-order climate interpretation.

We have demonstrated that Milankovitch-induced climate cycles exerted a major control on the deposition of the early Paleoproterozoic Kuruman BIF. The fact that this primary signal is still present within the stratigraphy has direct implications for BIF depositional models, and encourages the use of BIFs as a climate proxy for the early Earth's pre- and syn-oxygenated environment. We have further shown that our cyclostratigraphy combined with highprecision U–Pb dating allows for basin-scale correlations for this time period with a much higher temporal resolution (10^5 yr instead of 10^6 yr), which may facilitate future basin analysis. Moreover, the identification of 405 kyr and approximately 1.4–1.6 Myr eccentricity cycles provides new geological constraints on Solar system planetary behaviour in deep time.

Methods

Sections and logging. During a three-week reconnaissance field study, we selected five suitable outcrops for logging the observed regular alternations in the weathering profile of the Kuruman BIF. To demonstrate the lateral continuity of the pattern, we distributed them spatially over a distance of 250 km, along a N–S transect between the towns of Kuruman and Prieska. In each section, logging was done along trajectories (subsections) where the alternations were most clearly expressed, that is on hill slopes that were neither too steep (for example vertical walls created by streams) nor too gentle (for example at the very bottom or top part of a hill, where the exposure is typically poor). Thickness measurements of the different intervals were made with a Jacob staff and at a decimetre to metre resolution, yet some distinct features at the centimetre scale were reported as well if they were laterally consistent over 50m or more. Note that there was some ambiguity in defining the boundary between subsequent beds, because the changes in relief were often gradual rather than sharp. Individual logs of the subsections were subsequently combined into a composite log representative for an entire section.

Relief grading. For each composite section, we subsequently ranked the logged intervals in terms of their relief. The most deeply weathered, soft intervals were given a value of 0 and the most prominent, well-exposed ridges a value of 5. We did the ranking visually at a location where we had a good overview of the entire section. For the Prieska section this was not possible because its four subsections were relatively widely spaced, so here the grading was done three times: for a bottom, top and overlapping section. First, ranking was done independently by three people using only whole numbers (0, 1, 2, 3, 4 or 5), and these rankings were subsequently compared. Although this method comes with a level of subjectivity, individual results turned out to be in close agreement with one another, with a maximum difference of 1. We subsequently discussed the intervals about which there was some ambiguity in the grading, and decided to introduce 0.5 and in some cases 0.25 points to account for more subtle variations in relief, which were causing the disagreement in the individual rankings. Slight modifications were additionally made based on inspection of photos from each section.

Lithological analysis. For three sections (Whitebank, Woodstock and Prieska) we added textural and mineralogical observations by taking representative samples from each interval (if possible). This was generally done at a coarse resolution, that is metre scale, and samples usually covered 5 to 15 cm of stratigraphy. Samples of a smaller size would be biased too much by the micro- and mesobanding (highfrequency chert–iron alternations) and thus not representative of the large-scale changes in composition associated with the alternations in weathering. Twentyfour representative samples from section Woodstock, covering bundles 2 to 4, were subsequently prepared for XRF analysis using a Retsch tungsten carbide jaw crusher, Herzog mill and Leco thermogravimetric analyser. Approximately 0.6 g of dry sample was fused into glass beads at 1,200 °C and analysed with an ARL Perform'X sequential XRF spectrometer at Utrecht University. Based on our field observations and the XRF results (Supplementary Table 1) we developed a lithological facies model (Supplementary Fig. 5).

Spectral analysis. Time-series analysis was carried out on the five composite rank series (that is, relief listed versus depth), which were detrended and linearly interpolated at 10 cm. We used MTM spectral analysis (Thomson, 1982) as implemented in the R package astrochron (Meyers, 2014) using three 2π prolate tapers. AR1 and LOWSPEC (Meyers., 2012) confidence levels were determined using the functions mtm and lowspec. Astrochron was further used for rectangular bandpass filtering (bandpass) and evolutive harmonic analysis (eha) to evaluate spatial frequency changes (that is, time-depth distortion). In addition, we applied frequency domain minimal tuning (Meyers et al., 2001) to the Whitebank log (Supplementary Fig. 9) using the functions traceFreq, freqs2sedrate, sedrate2time and tune.

TIMS U–Pb geochronology. Four stilpnomelane lutite shales were sampled from the GASESA-1 and UUBH-1 drill cores (see Supplementary Fig. 1 for drill-hole information) for zircon extraction. The Kleine Naute shale, a distinct marker bed at the top of the Gamohaan Formation, was sampled from the GASESA-1 core close to the boundary with the Kuruman Formation. Since many other lutites in the GASESA-1 core were highly weathered and their stratigraphic height with respect to the Kleine Naute was not perfectly clear, the three other shales were sampled from the new UUBH-1 core at 212.18–212.57m, 130.35–130.54m and 110.60–110.90m core depths. The depth of the Kleine Naute shale in UUBH-1 was established at 302.19–306.73m and was used for calculating the depositional rate. All samples were subsequently crushed in a tungsten mill and sieved to less than 250µm before zircon concentration using the Wilfley table method (Söderlund and Johansson, 2002) and zircon picking under a binocular microscope. Once prismatic euhedral zircon grains had been extracted from the samples, these grains were annealed in a muffle furnace at 900 °C for 48h. The annealed grains were then subjected to chemical abrasion (Mattinson, 2005) at 210 °C for 2×3h in concentrated HF in 3ml Savillex beakers placed in a Parr digestion vessel. After 3h the zircon grains were inspected and the remaining fragments deemed large enough to survive another 3h partial dissolution. The grain fragments remaining after chemical abrasion were cleaned on a hotplate at 80 °C in 6N HCL overnight. The grain fragments were then further cleaned in four rounds of 3N HNO_3 combined with ultrasonication. The zircon crystals were then loaded into individual 200µl Savillex microcapsules, spiked with about 5mg of the EARTHTIME $^{202}Pb+^{205}Pb+^{233}U+^{235}U$ tracer solution (calibration version 3, Condon et al., 2015; McLean et al., 2015) and dissolved with about 70µl HF and trace HNO_3 in a Parr digestion vessel at 210 °C for 48h. Following dissolution, the samples were dried down and converted to a chloride by placing them back in the oven overnight in 6N HCl. The samples were then dried down again before being re-dissolved in 3N HCl and loaded into columns for anion exchange chromatography to purify and separate the U and Pb fractions (Krogh, 1973).

Once purified, the U and Pb fractions were combined in cleaned 7ml Savillex beakers and dried down with trace H_3PO_4 before loading on outgassed zone-refined Re ribbon filaments with a Si-gel emitter. U and Pb measurements were made on either a Thermo TRITON thermal ionization mass spectrometer or a Isotopx Phoenix TIMS machine, both housed at the University of Geneva. On the TRITON Pb was measured in dynamic mode using an axial MasCom, whereas for Phoenix measurements Pb was measured in dynamic mode using a Daly photomultiplier system. U was measured as an oxide on both machines, either in static mode using Faraday cups coupled to 1012Ω resistors or on the same ion counting system as used to measure Pb when the signal on $^{238}U^{16}O_2$ was not high enough for Faraday measurements. The $^{18}O/^{16}O$ oxygen isotope ratio in uranium oxide was assumed to be 0.00205. Mass fractionation of Pb and U was corrected for using a $^{202}Pb/^{205}Pb$ ratio of 0.99506 and a $^{238}U/^{235}U$ ratio of 137.818 ± 0.045 (2σ) (Hiess et al., 2012). All common Pb was considered laboratory blank and was corrected using the long-term isotopic composition of the Pb blank at the University of Geneva (see footnote in Supplementary Table 3). All data were processed with the Tripoli and Redux U–Pb software packages using the algorithms of McLean et al. (2011). The weighted mean ages presented here are reported without the additional uncertainty associated with the spike calibration and also the decay constant uncertainties, since these were unnecessary for our purposes; see Supplementary Table 3 for ages including these sources of uncertainty. All ages were corrected for initial ^{230}Th disequilibrium in the melt using a U/Th ratio of the magma of 3.5 and an initial $^{231}Pa/^{235}U$ ratio of 1.1, although adding or removing these corrections makes no difference to our results.

Depositional rate model. The stilpnomelane lutites contain a significant component of felsic volcanic material (Pickard, 2003), whereas the surrounding BIF contains almost no traces of this (Oonk, 2016). Although there is uncertainty on the origin of the stilpnomelane lutites, the zircons within the lutites must originate from relatively instantaneous volcanic eruption events. We therefore modelled the depositional rate of the Kuruman BIF assuming that the zircons originated from 1 cm thick, tuff-rich layers, which formed instantaneously within the lutites. This assumption has almost no impact on our calculated depositional rate; the same rate is obtained by treating the whole lutite as an instantaneous event (similar to a tuff deposit).

Acknowledgements

We thank C. Albutt and Murphy for providing us with access to sections Woodstock and Daniëlskuil; S. Hilgen for help with the logging; H. Tsikos for arranging access to drill core Gasesa-1; N. Beukes for help with organizing the drilling and lutite sampling of drill core UUBH-1, which was drilled by OB Mining & Drilling Pty Ltd; and S. Meyers for advice on the spectral analysis. This study was supported by the Dutch National Science Foundation (grant NWO ALWOP.192), the Swiss National Science Foundation (grant 200021_169086) and the Foundation Stichting Dr. Schürmannfonds (grant 2017-126).

Supplementary Information

Supplementary Text 1

The Kuruman Iron Formation crops out along the entire N-S stretch of the Griqualand West Basin, over a distance of some 500 km. It is part of the lower Ghaap Group of the Transvaal Supergroup, deposited on the Kaapvaal craton in Southern Africa between ca 2.6 – 2.4 Ga (Supplementary Fig. 1). The iron formations of the Transvaal Supergroup are considered time-equivalent to those of the Hamersley Group, deposited on the Pilbara craton in Western Australia (Pickard, 2003; Cheney, 1996), and which together embody one of the world's best preserved and laterally extensive BIFs (Beukes and Gutzmer, 2008).

In the centre of the Griqualand West Basin, deposition of the Ghaap Group started with a thick (> 2 km) stromatolitic carbonate platform succession of the Campbellrand Subgroup representing relatively shallow-marine conditions (Beukes, 1987). A major transgression ultimately led to the drowning of the carbonate platform and the deposition of the rhythmically microbanded Kuruman BIF (approximately 200 m thick). An open-shelf environment is inferred from the absence of wave-agitated structures and very low aluminosilicate content (Klein and Beukes, 1989). The Campbellrand-Kuruman transition is marked by the Tsineng Member at the top of the Gamohaan Formation, and comprises chert-rich BIF alternating with carbonaceous black shales. The uppermost Kleine Naute shale forms a distinct marker bed at the boundary with the Kuruman Formation. A transition towards clastic-textured BIF at the top of the Kuruman Formation (the Ouplaas Member) and in the overlying Griquatown Formation indicates a gradual change towards a shallower-water, storm-dominated depositional environment (Beukes and Klein, 1990).

In the Prieska area in the south of the Basin (at the Kaapvaal craton margin), the Campbellrand Subgroup is much thinner (<400 m) and comprises more shaly and thinly laminated carbonate iron formation facies, implying more deep-marine conditions57. In contrast, the overlying Kuruman BIF is much thicker here (500 – 600 m) and is directly overlain by the Griquatown Formation (the brecciated Ouplaas Member is absent; Beukes, 1980; Beukes and Klein, 1990).

Supplementary Text 2

The two scales of rhythmic alternations observed in the weathering profile of the Kuruman BIF produce a very characteristic pattern that forms the basis of our correlations presented in Figure 2. Bundle number 1 at the base consists of three (1a - c) rather thin and poorly developed ridges. In contrast, bundle number 2 is made up of three well-exposed intervals (2a - c), with a much fainter one on top (2d), and is overlain by two thick, protruding intervals of bundle 3 (3a - b). Bundle 4 is relatively isolated and contains a single, prominent ridge (4b) with a very faint one below (4a). Number 5 comprises four indurated intervals (5a – d) of which the bottom three, especially 5a, are very thick and tend to form steep cliffs. Bundle number 6 is again made up of two thinner ridges (6a – b) and has a comparable relief as bundles 2 - 4. Correlations for cycles 7a-c and 8 are more tentative since they were only recorded in two sections (Woodstock and Prieska), and show brecciation textures (Supplementary Fig. 3) hinting at irregular sedimentation. Note that the Kuruman Formation is significantly thicker at Prieska (more than 500 m) than in the Daniëlskuil – Kuruman area (ca 200 m; Beukes, 1980), and that our Prieska log in Figure 2 only represents the bottom 200 m of the Formation (see also Supplementary Figs. 2 and 4).

Supplementary Text 3

MTM spectra were calculated using both the classical AR1 and LOWSPEC approach to compute the null-spectrum and associated significance levels. The 4.3 – 6.3 m peaks always exceed the 90 %, often 95 % and sometimes 99 % confidence level, while the 16 – 22 m components only reach the 90 % using the classical AR1 noise model (Supplementary Table 2). In addition, highly significant peaks (above 95 % or even 99% confidence) occur in the higher frequency range (< 3 m) of the spectra, but these at least partly represent artefactual harmonics due to applying Fourier spectral techniques to a square wave record (Supplementary Fig. 7). Generally speaking, the LOWSPEC confidence levels are considered more reliable for cycles in the lower frequency (i.e. eccentricity) band of the spectrum (Meyers, 2012). Note that we did not apply a 'multiple testing' correction on the AR1 and LOWSPEC results (with the aim to reduce the number of potential false positives; Vaughan et al., 2011), because this correction is considered unreliable for application in the stratigraphic domain (instead of time domain; Meyers, 2012).

Supplementary Text 4

The results of the bandpass filtering show a clear correspondence between the 4.3 – 6.3 and 16 – 22 m components in the MTM spectra (Fig. 3a; Supplementary Fig. 6) and the alternations and bundles identified in the field. However, two notable exceptions are (1) ridge 5a, which is recognised in each of the five weathering profile records as a double 4.3 – 6.3 m cycle; and (2) bundles 5 and 7, which are recognised as two 16 – 22 m cycles (Fig. 2a).

Supplementary Text 5

The 16 – 22 m spectral components do not reach the preferred 95 % confidence level (AR1 and LOWSPEC) to reject the 'null hypothesis' (i.e. a non-cyclic, stochastic origin) with a high degree of confidence (Supplementary Table 2). However, the reduced power could in the first place be due to the fact that the records are relatively short and therefore contain only a limited number of cycles for Fourier analysis. Secondly, changes in the sedimentation not only cause peak defocusing, but also reduction of power (Herbert, 1994). Moreover, long-period Milankovitch cycles invariably result from the amplitude modulation of either precession or obliquity and therefore, by definition, do not appear in the power spectra of precession, obliquity or insolation time series. They only show up in the spectra of paleoclimate records due to non-linear responses to the initial astronomical (insolation) forcing (Ripepe and Fischer, 1991). Therefore, we can state that it is not the exact level of significance that is important here, but the consistent concentration of spectral power at two spatial wavelengths, linked to the cycle hierarchy observed in the field.

Supplementary Text 6

As a third option, the two cycles might be related to precession (now 21 kyr) and short eccentricity (Hypothesis 3). However, the precession period is assumed to be much shorter during the Paleoproterozoic due to a reduced Earth-Moon distance, possibly around 11 - 12 kyr at 2.48 Ga (Waltham, 2015). This would raise the precession - short eccentricity ratio to 1:8 and therefore this scenario is unlikely. Similar to precession, the period of obliquity (now 41 kyr) must have been very short (16 kyr at 2.48 Ga, according to the model of Waltham, 2015), resulting in a 1:10 ratio with the weaker 176 kyr obliquity beat and a 1:8 ratio between the 176 kyr and 1.2 Myr obliquity beat cycle. We therefore consider either of these two obliquity scenarios (Hypothesis 4) unlikely as well.

Supplementary Figures

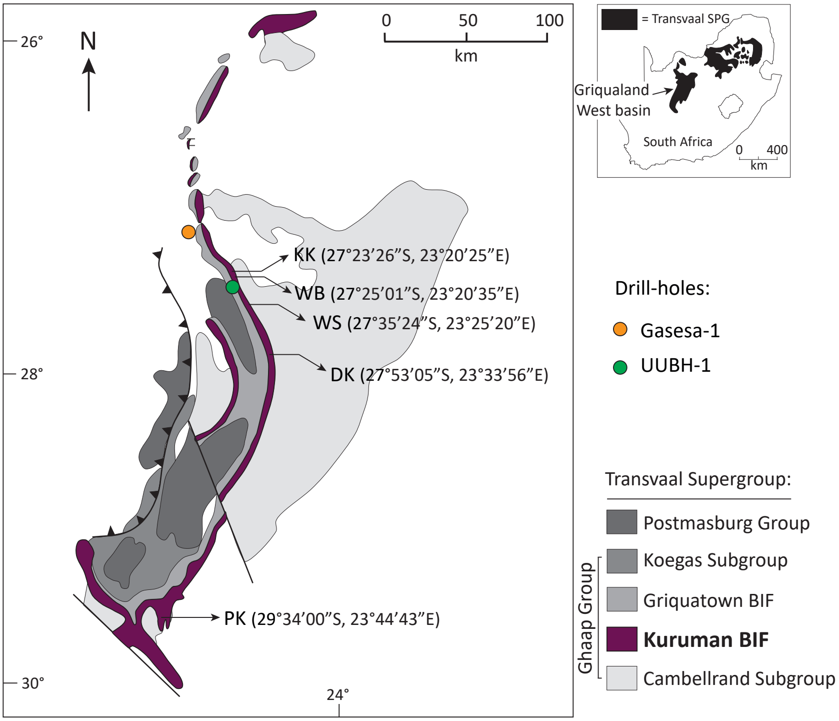
26°
N
0 50 100
km
= Transvaal SPG
Griqualand West basin
South Africa
0 400
km
KK (27°23'26"S, 23°20'25"E)
WB (27°25'01"S, 23°20'35"E)
WS (27°35'24"S, 23°25'20"E)
28°
DK (27°53'05"S, 23°33'56"E)
Drill-holes:
Gasesa-1
UUBH-1
Transvaal Supergroup:
Postmasburg Group
Koegas Subgroup
Griquatown BIF
Kuruman BIF
Cambellrand Subgroup
Ghaap Group
PK (29°34'00"S, 23°44'43"E)
30°
24°

Supplementary Figure 1. Simplified geological map of the Griqualand West basin (modified from Tsikos et al., 2010) showing the location of the five field sections of the Kuruman Formation and the two drill-cores used for sampling the stilpnomelane lutite shales. The Gasesa-1 core was drilled as part of a water exploration program in the mid-1990's near the town of Hotazel, and captures most of the Griquatown Formation, the entire Kuruman Formation and the top of the underlying (continues next page)

Gamohaan Formation. The UUBH-1 core was drilled in 2017, ca 10 km west of the town of Kuruman (S27° 28’ 44.4” E23° 19’ 13.0”). The primary goal of this scientific drill-core was to obtain a new (fresh) and stratigraphically complete record through the entire Kuruman Formation.

Supplementary Figure 2. Characteristic alternations in the Kuruman BIF weathering profile. Images are from Google Earth and pictures taken in the field. Coordinates refer to Google Earth image midpoints. **a** – **e** correspond to main sections KK, WB, WS, DK and PK. Labels X, Y, Z denote individual subsections, which were used to provide a continuous log of the stratigraphy. White labels 1a, 1b, 1c etc. (referring to the characteristic alternations) indicate the approximate logging trajectory. Note that there are more alternations present above 8b in the Prieska section (see subsections Zi and Zii in Supplementary Figure 2e).

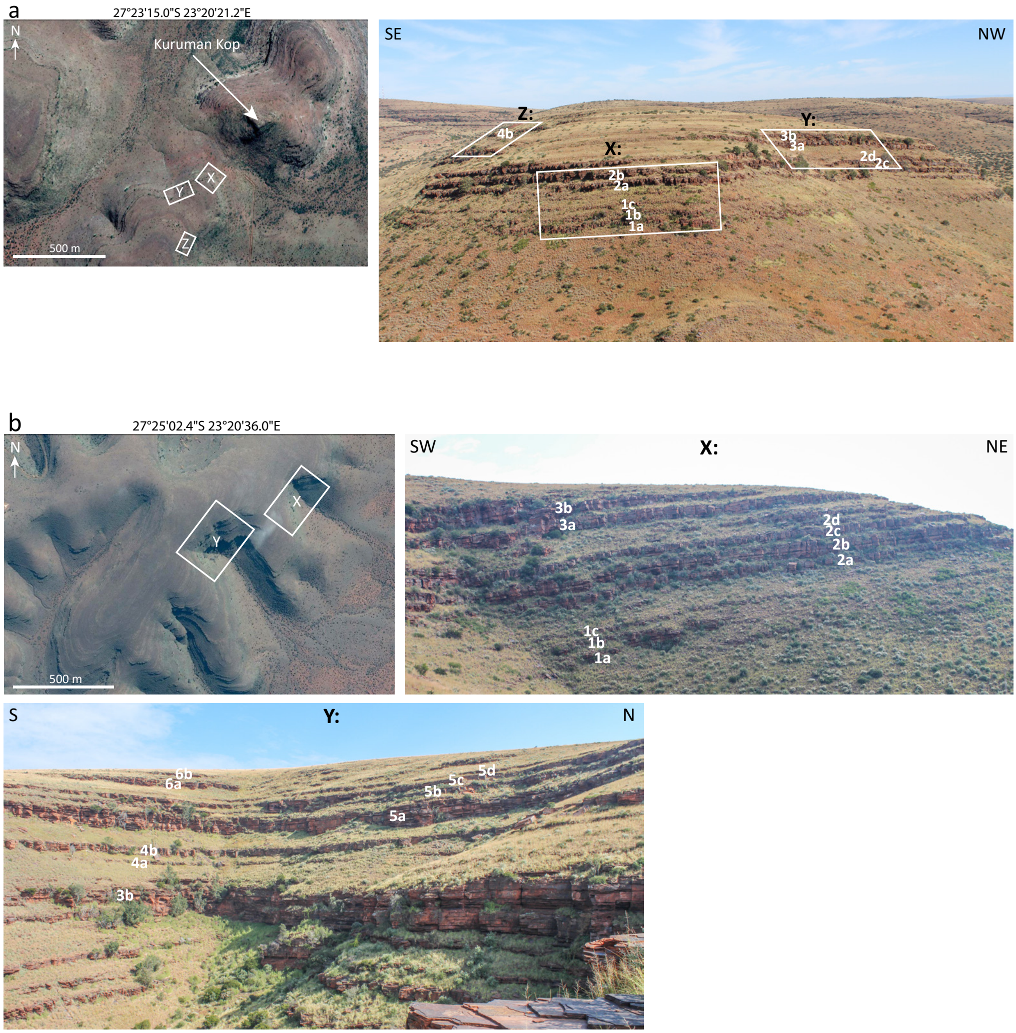
a
27°23'15.0"S 23°20'21.2"E
N
Kuruman Kop
X
Y
Z
500 m
SE
NW
Z:
4b
X:
2b
2a
1c
1b
1a
Y:
3b
3a
2d
2c
b
27°25'02.4"S 23°20'36.0"E
N
X
Y
500 m
SW
X:
NE
3b
3a
2d
2c
2b
2a
1c
1b
1a
S
Y:
N
6b
6a
5d
5c
5b
5a
4b
4a
3b

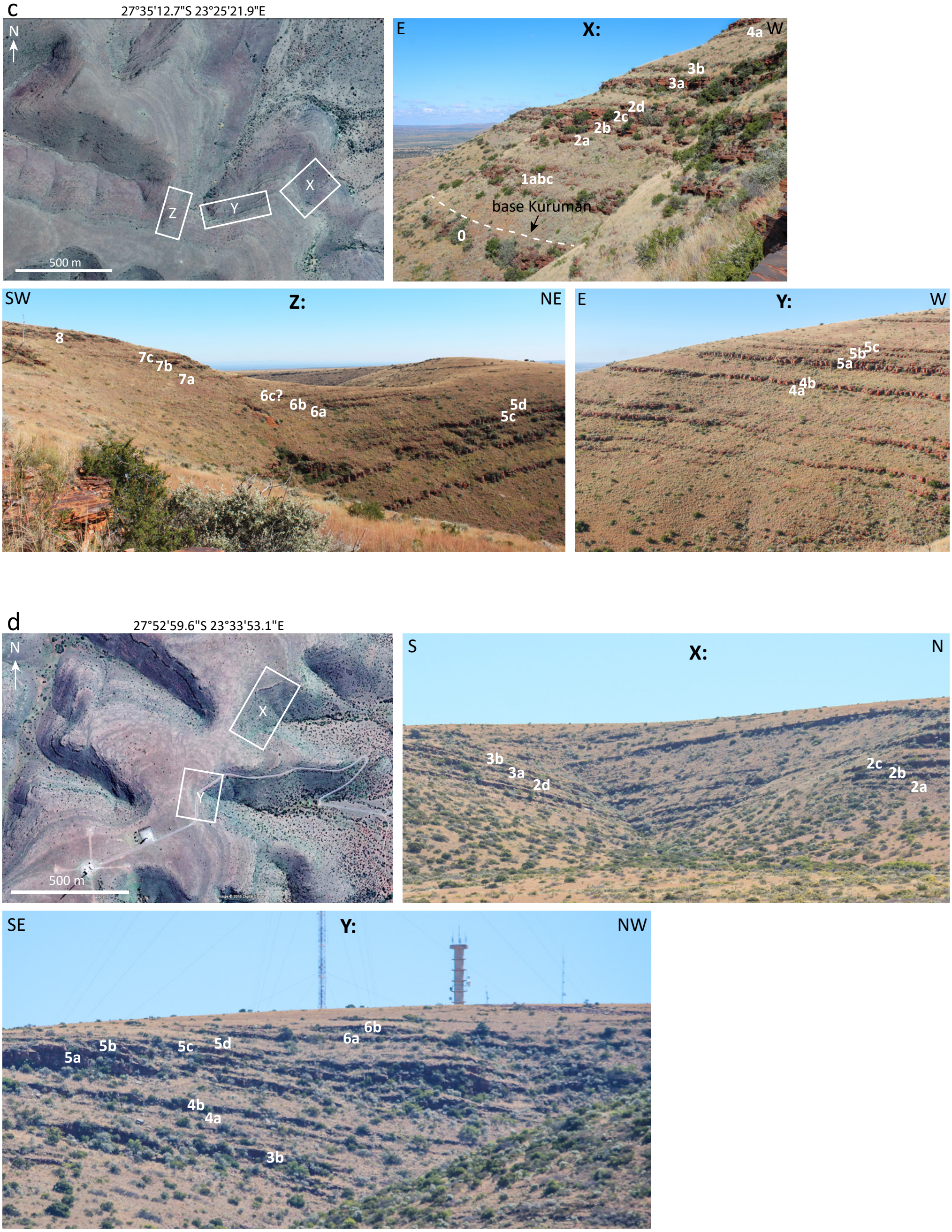
c
27°35'12.7"S 23°25'21.9"E
N
500 m
Z
Y
X
E
X:
W
4a
3b
3a
2d
2c
2b
2a
1abc
base Kuruman
0
SW
Z:
NE
8
7c
7b
7a
6c?
6b
6a
5d
5c
E
Y:
W
5c
5b
5a
4b
4a
d
27°52'59.6"S 23°33'53.1"E
N
X
Y
500 m
S
X:
N
3b
3a
2d
2c
2b
2a
SE
Y:
NW
5a
5b
5c
5d
6a
6b
4b
4a
3b

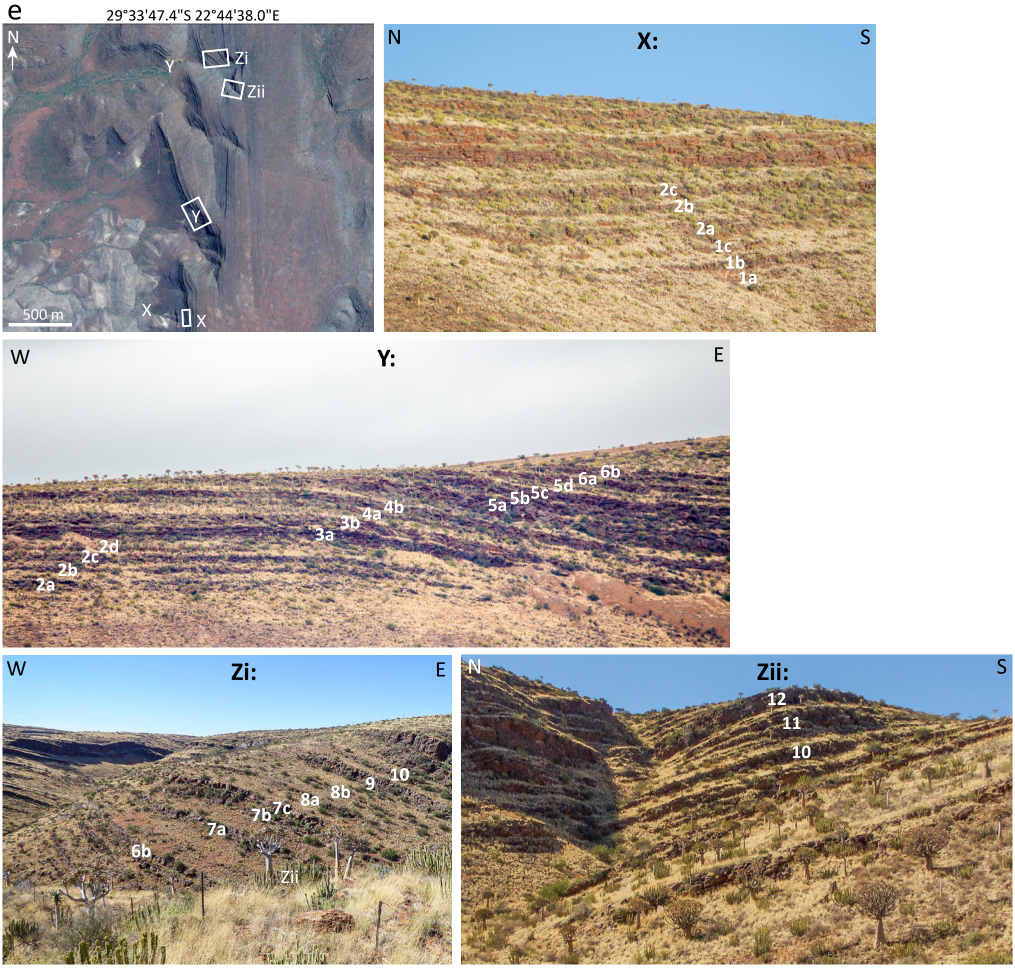
e
29°33'47.4"S 22°44'38.0"E
N
Y
Zi
Zii
Y
500 m
X
X
N
X:
S
2c
2b
2a
1c
1b
1a
W
Y:
E
2a
2b
2c
2d
3a
3b
4a
4b
5a
5b
5c
5d
6a
6b
W
Zi:
E
6b
7a
7b
7c
8a
8b
9
10
Zii
N
Zii:
S
12
11
10

Supplementary Figure 3 (next page). Examples of lithologies and textures encountered in the field. These observations were used to develop a lithological facies model (see Supplementary Figs. 4 and 5). **a**, "Blocky" intervals (cycles 2c and 3a) which have a high degree of protrusion versus a lower-relief interval (cycle 2d), which has a more "platy" and "wavy" appearance. **b**, Platy carbonate-oxide BIF. **c**, Oxide-carbonate-chert BIF. **d**, Oxide-dominated BIF. **e**, Very chert-rich (chert bands > 10 cm) BIF in cycle 7a. **f**, Very thick chert pods between cycle 7b and 7c. **g**, In-situ brecciation in the top of cycle 7c. **h**, Ferruginous limestone (pale grey) and ferruginous chert (blue) in the top of the Gamohaan Formation in section WS.

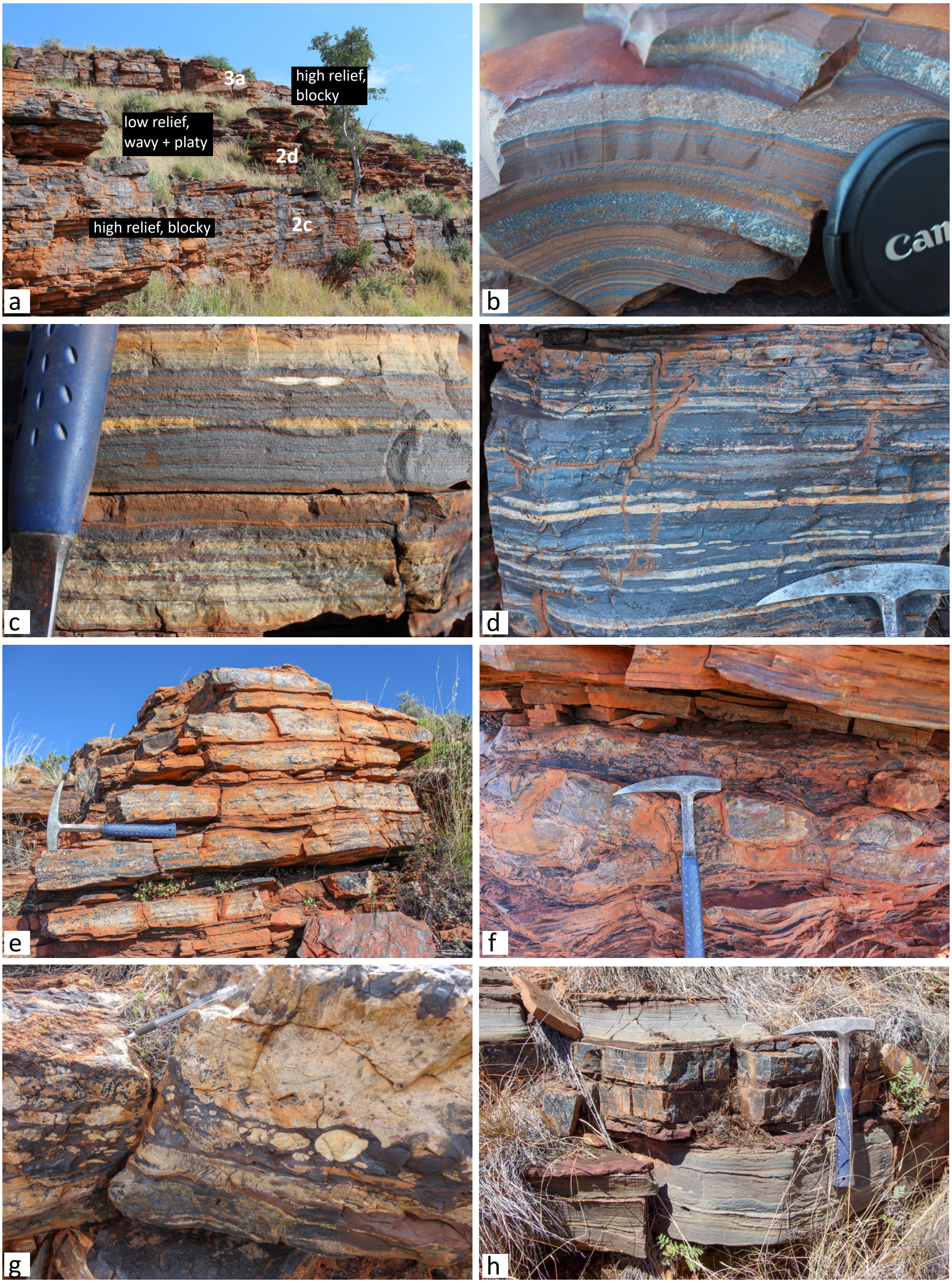
3a
high relief, blocky
low relief, wavy + platy
2d
high relief, blocky
2c
a
b
Can
c
d
e
f
g
h

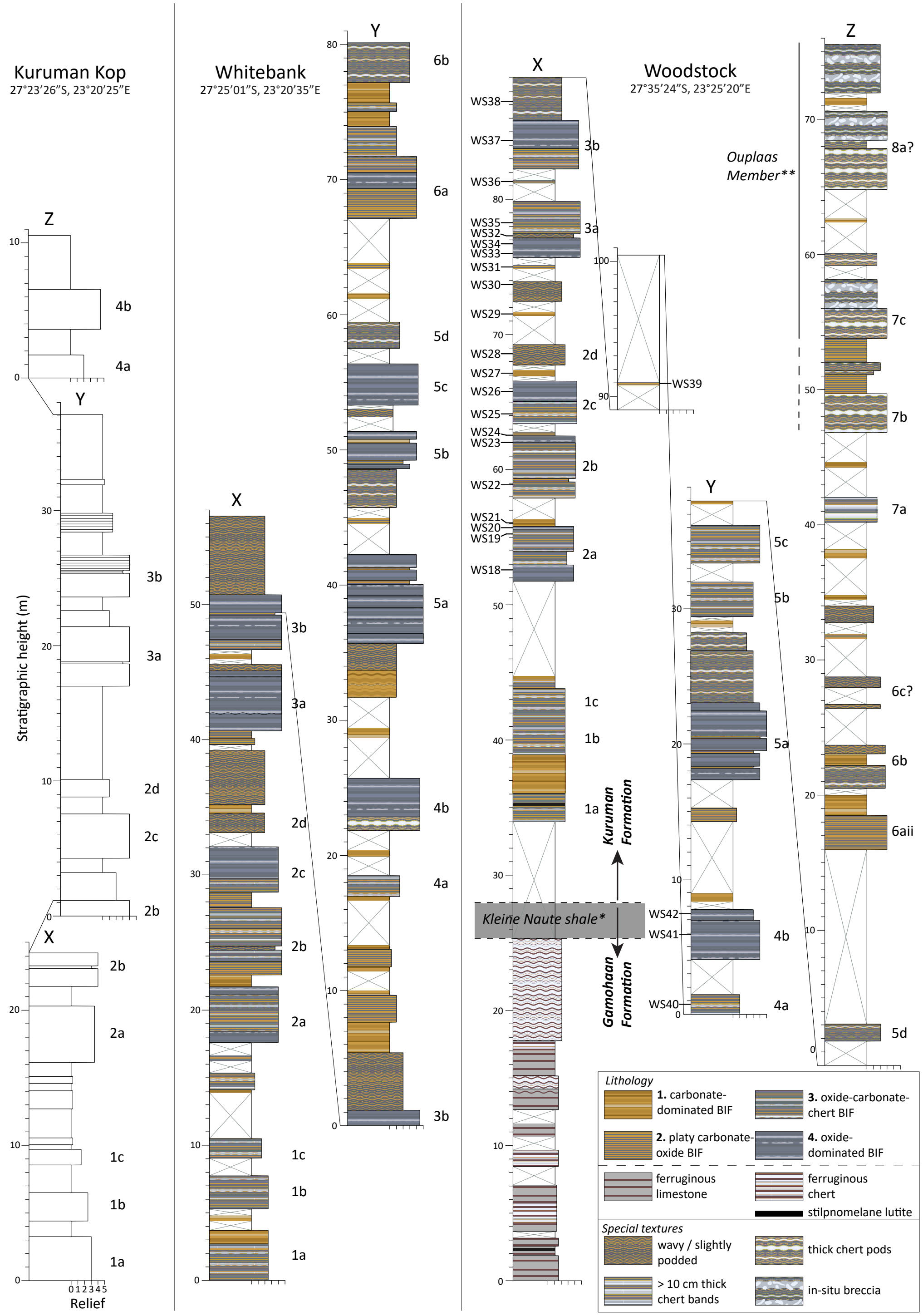
Kuruman Kop
27°23'26"S, 23°20'25"E
Whitebank
27°25'01"S, 23°20'35"E
Woodstock
27°35'24"S, 23°25'20"E
Stratigraphic height (m)
Relief
0 1 2 3 4 5
X
Y
Z
1a
1b
1c
2a
2b
2c
2d
3a
3b
4a
4b
5a
5b
5c
5d
6a
6b
6aii
6c?
7a
7b
7c
8a?
Ouplaas Member**
Kleine Naute shale*
Kuruman Formation
Gamohaan Formation
WS18
WS19
WS20
WS21
WS22
WS23
WS24
WS25
WS26
WS27
WS28
WS29
WS30
WS31
WS32
WS33
WS34
WS35
WS36
WS37
WS38
WS39
WS40
WS41
WS42
Lithology
1. carbonate-dominated BIF
2. platy carbonate-oxide BIF
3. oxide-carbonate-chert BIF
4. oxide-dominated BIF
ferruginous limestone
ferruginous chert
stilpnomelane lutite
Special textures
wavy / slightly podded
thick chert pods
> 10 cm thick chert bands
in-situ breccia

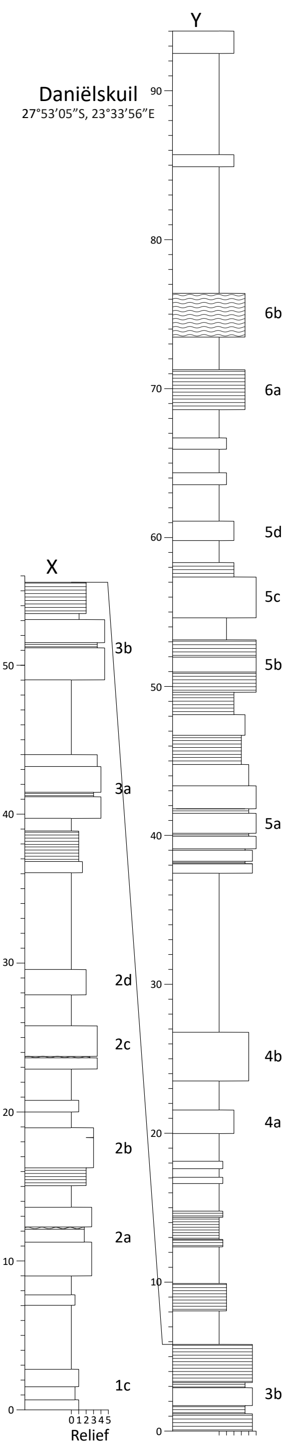
Daniëlskuil
27°53’05”S, 23°33’56”E
X
Y
1c
2a
2b
2c
2d
3a
3b
3b
4a
4b
5a
5b
5c
5d
6a
6b
0
10
20
30
40
50
60
70
80
90
0 1 2 3 4 5
Relief

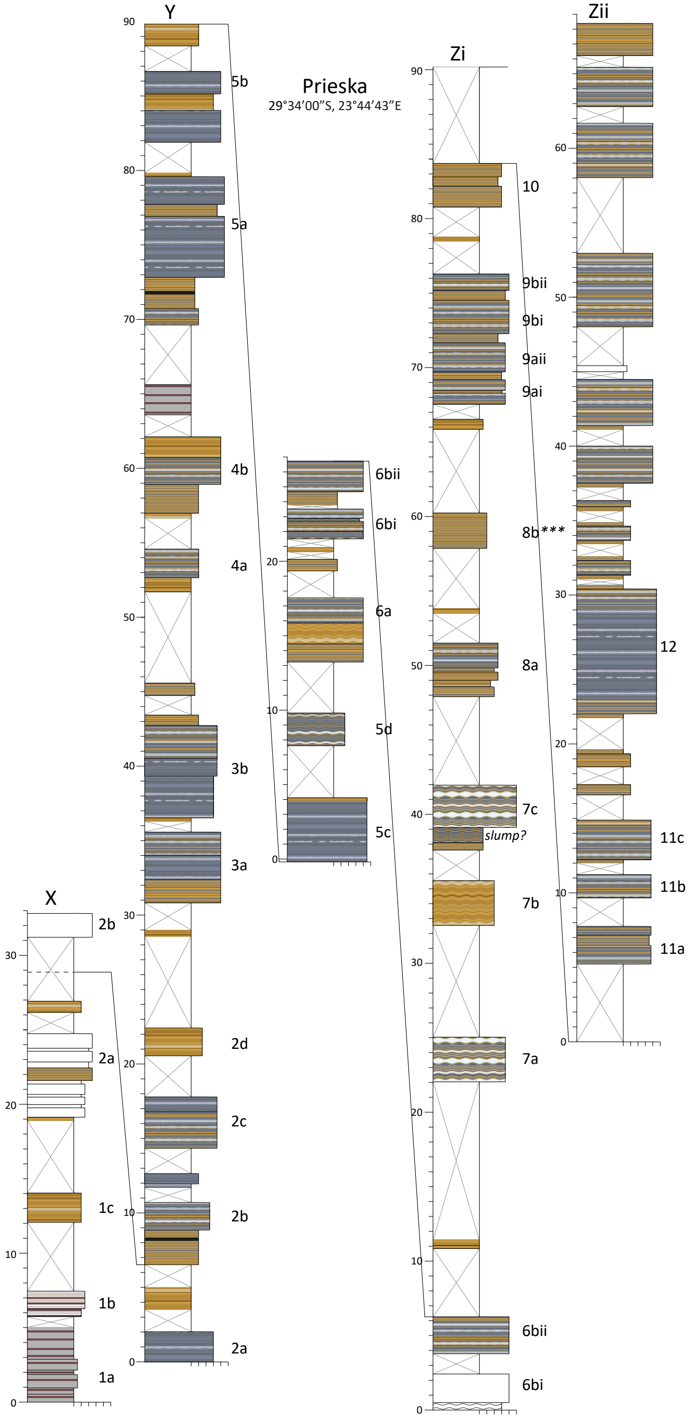
Prieska
29°34’00”S, 23°44’43”E
X
Y
Zi
Zii
1a
1b
1c
2a
2b
2a
2b
2c
2d
3a
3b
4a
4b
5a
5b
5c
5d
6a
6bi
6bii
6bi
6bii
7a
7b
7c
slump?
8a
8b***
9ai
9aii
9bi
9bii
10
11a
11b
11c
12
0
10
20
30
40
50
60
70
80
90

Supplementary Figure 4 (previous page). Detailed logs of the weathering profile in the five Kuruman BIF sections. Individual subsections are labelled X, Y, Z. Black connection lines mark the parts of the subsections used for creating the composite logs (in Fig. 2). Lithological information is included for three sections (WB, WS and PK) and was obtained by regular sampling (to create a fresh surface for description). Labels WS18 – 42 indicate the position of the representative samples used for XRF analysis (see Supplementary Table 1). Unexposed intervals are marked by faint crosses.

*The position of the Kleine Naute shale is inferred from stratigraphic correlations with drill-core UUBH1, because it does not crop out in the field.

** Brecciation textures and relative height with respect to the Kleine Naute shale suggest cycles 7c – 8 are part of the Ouplaas Member, the uppermost member of the Kuruman Formation.

*** Note that we logged more alternations above 8b in the Prieska section, but we did not reach the boundary with the Griquatown Formation, which is presumably another 200 - 300 metres higher up in the stratigraphy.

Supplementary Figure 5. Lithological facies model for the alternations in the weathering profile. Facies numbers 1 and 2 have a relatively high iron-carbonate content and typically occur in the low-relief intervals, while numbers 3 and 4 are magnetite-dominated and typically occur in the high-relief intervals. Note that within rank number 3 the relative iron content increases from sample WS34 to WS25. Photos are from sliced field samples that were subsequently powdered and analysed with XRF.

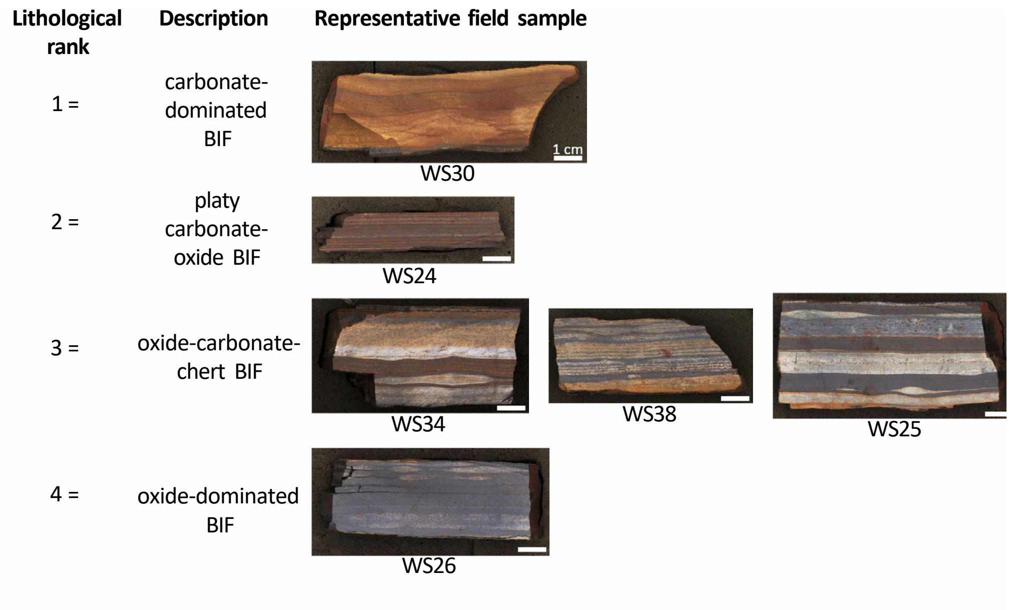
Lithological rank
Description
Representative field sample
1 =
carbonate-dominated BIF
1 cm
WS30
2 =
platy carbonate-oxide BIF
WS24
3 =
oxide-carbonate-chert BIF
WS34
WS38
WS25
4 =
oxide-dominated BIF
WS26

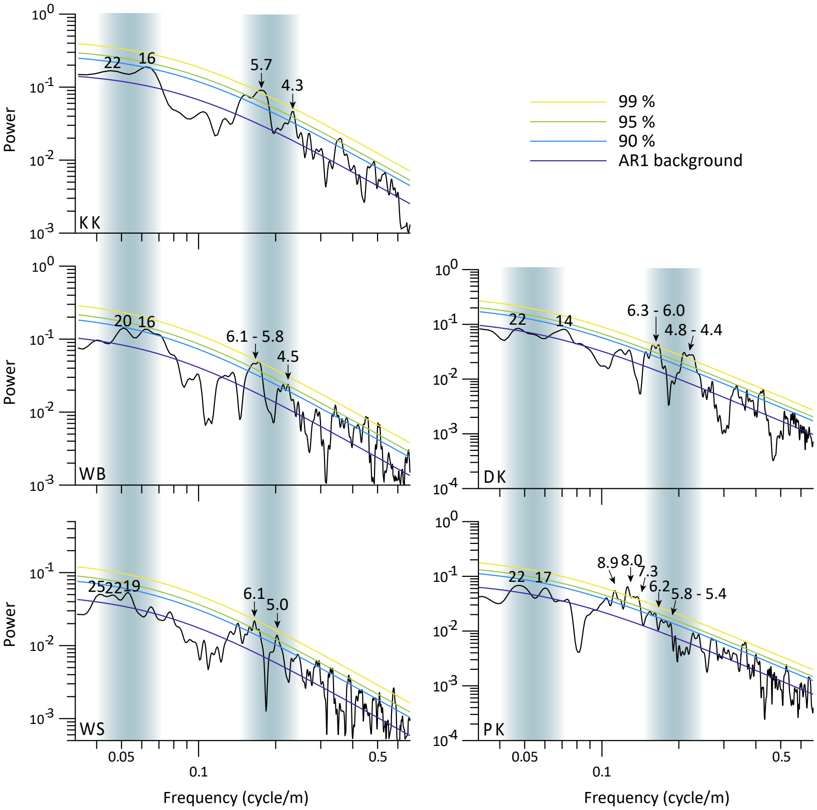

Supplementary Figure 6. MTM AR1 spectra for the five different weathering profile logs. MTM power spectra (three 2π prolate tapers) with classical AR1 background estimation conducted on 10-cm-interpolated, detrended weathering profile logs for the five Kuruman BIF sections. Peak labels are in metres. Blue zones indicate the two areas of enhanced spectral power that are linked to the characteristic alternations and bundles. The significant wavelengths at 1 – 3 m and at 7.3 – 8.9 m (in the PK spectrum) are considered artefacts (Supplementary Figs. 7 and 11).

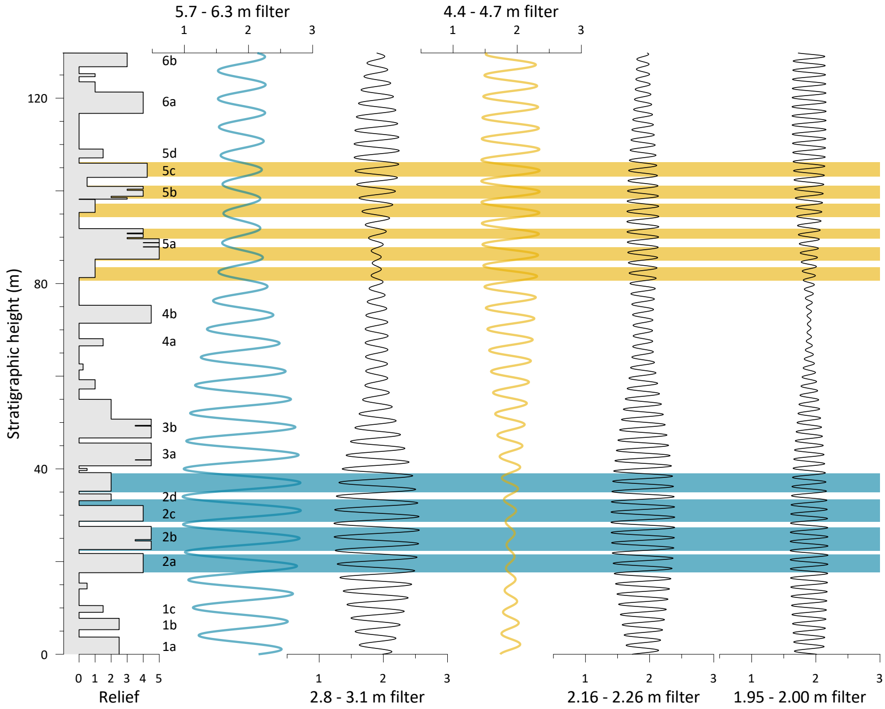

Supplementary Figure 7. The origin of the higher-frequency peaks (< 3 m). Blue and orange bands highlight maximum amplitude for the bandpass filtered 5.7 – 6.3 m and 4.4 – 4.7 m cycles (from the Whitebank spectrum) corresponding to the abc-alternations. The amplitude variation of the filtered 2.9 m signal perfectly mimics that of the ~6 m cycle. Moreover, its maxima coincide with the upper and lower edges of the protruding ridges. This suggests that the 2.9 m cycle is a spectral artefact (i.e. 1st harmonic of the ~6 m cycle) and results from using Fourier spectral techniques to evaluate a square wave (the logs have a rectangular shape). The amplitude variation of the filtered 2.2 m and 2.0 m cycles similarly indicates artefactual harmonic behaviour, i.e. they are the 2nd harmonic of the ~6 m and the 1st harmonic of the ~4.5 m cycle, respectively.

Supplementary Figure 8 (next page). The origin of the peak splitting in Figure 3a. Bandpass filters of individual spectral peaks of the 4.3 – 6.3 and 16 – 22 m cycle indicate a shift to lower sedimentation rates above bundle 3, and a 1:3.5 - 1:4 ratio between the alternations and bundles. Blue horizontal bands highlight intervals of highest amplitude. **a**, Section Woodstock. The amplitude of the filtered ~5 m and ~19 m cycles increases towards the top half of the Kuruman Formation, while the amplitude of the filtered ~6 m and ~22 m cycle is highest in the bottom half. In both cases, four small-scale cycles occur within one larger-scale cycle (at maximum amplitude), i.e. they show a 1:4 ratio in thickness. **b**, Section Whitebank. Again, there is a positive correlation between the amplitude of the filtered ~4.5 m and ~16 m cycles (higher towards the top), as well as for the amplitude of the ~6 m and ~20 m cycle (higher towards the base). At their maximum amplitude, the filtered ~6 and ~20 m cycle show a 1:4 ratio, yet for the ~4.5 and ~16 m cycles this ratio varies between 1:3 and 1:4.

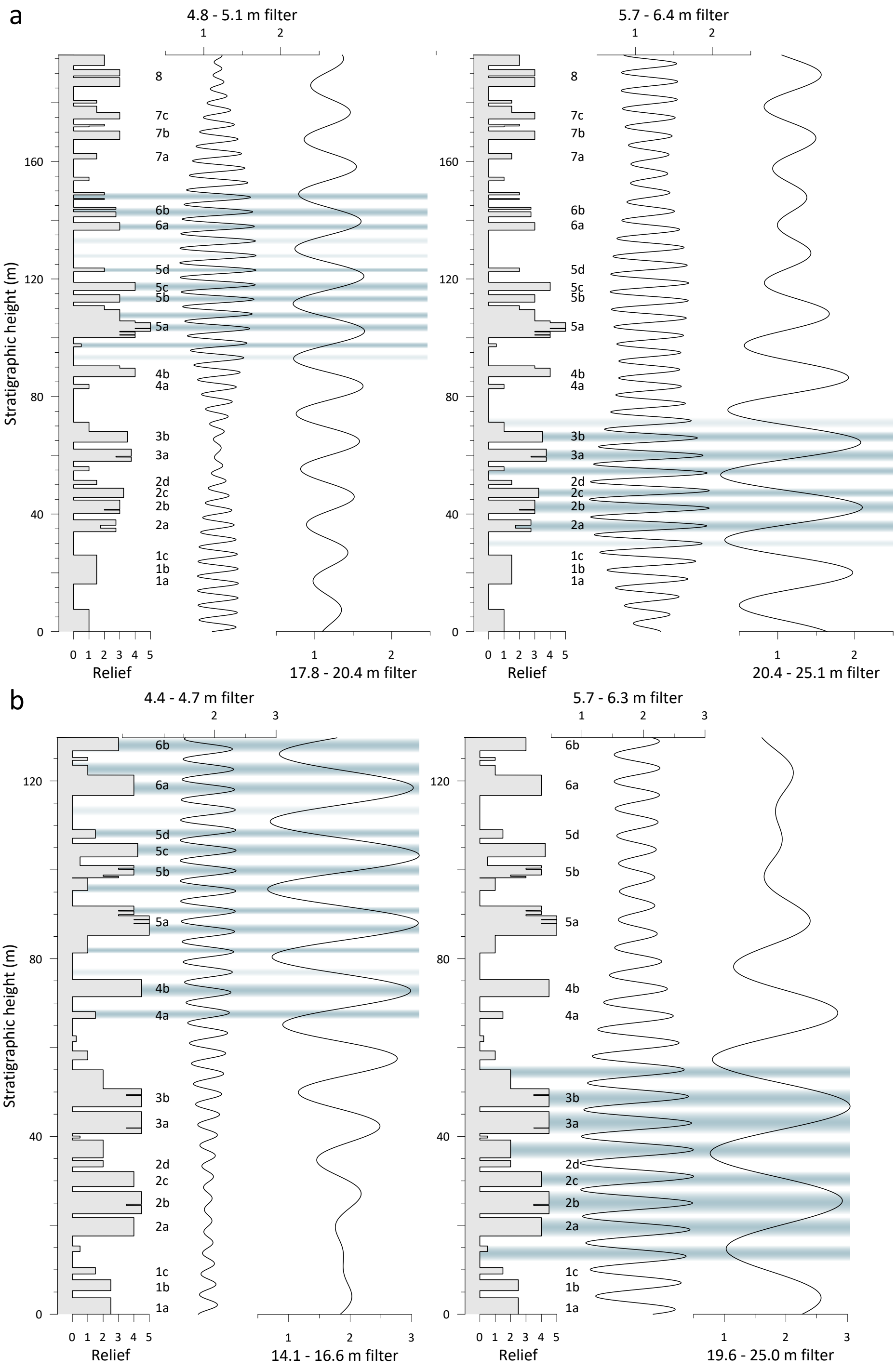
a
4.8 - 5.1 m filter
5.7 - 6.4 m filter
Stratigraphic height (m)
0
40
80
120
160
8
7c
7b
7a
6b
6a
5d
5c
5b
5a
4b
4a
3b
3a
2d
2c
2b
2a
1c
1b
1a
Relief
0 1 2 3 4 5
17.8 - 20.4 m filter
20.4 - 25.1 m filter
1
2
b
4.4 - 4.7 m filter
5.7 - 6.3 m filter
3
14.1 - 16.6 m filter
19.6 - 25.0 m filter

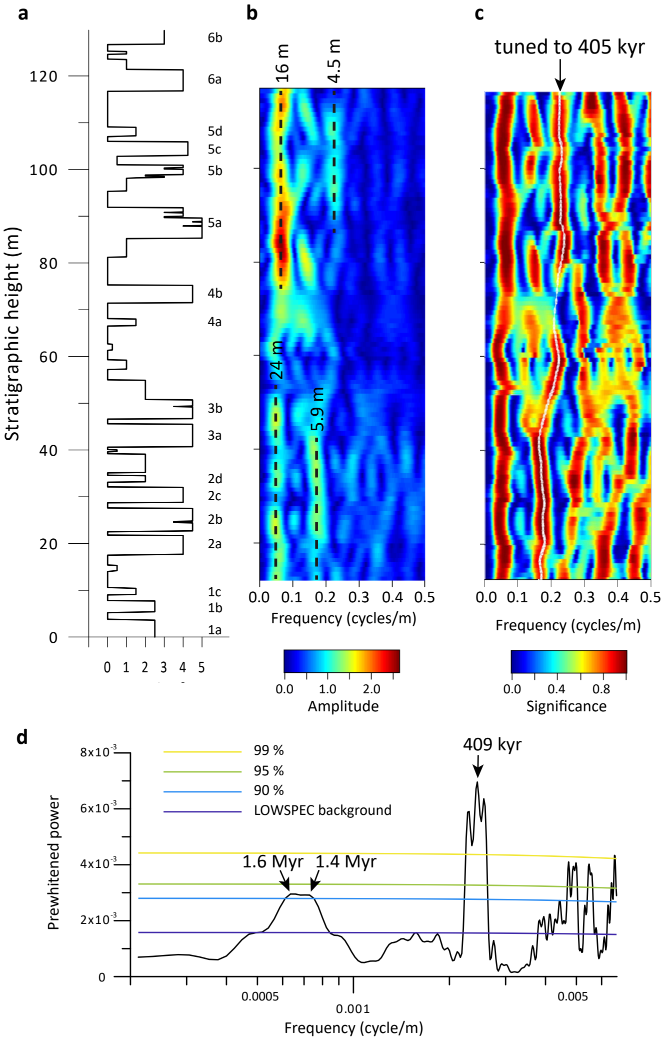

Supplementary Figure 9. Frequency domain minimal tuning. **a**, 10-cm-interpolated weathering profile log of section Whitebank. **b**, EHA amplitude and c, significance spectra (MTM three 2π prolate tapers, window size of 25 m). The two main high-amplitude bands show a general shift towards higher frequencies between bundles 3 and 5, indicating a decrease in the depositional rate. Moreover, both bands reveal cyclic frequency variations at approximately 5 and 20 m scale, where the highest frequencies occur at bundle midpoints. We applied frequency domain minimal tuning (see Methods) to tune the 4.5 – 6.1 m component to 405 kyr. In **c**, The tuning line is indicated in white. **d**, Spectral analysis results (MTM three 2π prolate tapers) of the 405-kyr-tuned record (20 kyr time steps) with LOWSPEC background estimation. Now that we have corrected for changes in the depositional rate, the spectrum reveals a single instead of double peaks of the two main cycles. According to the tuning, the larger-scale cycle has a period of around 1.4 – 1.6 Myr and reaches the 90 % confidence level.

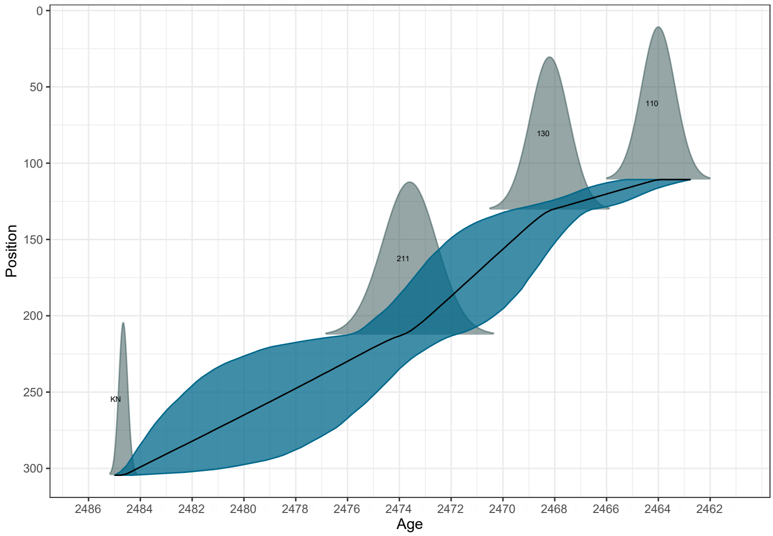

Supplementary Figure 10. U-Pb ages with analytical uncertainties of the 4 lutite samples plotted against depth within the UUBH-1 drill-core. Bchron 97.5% confidence zone is indicated in blue.

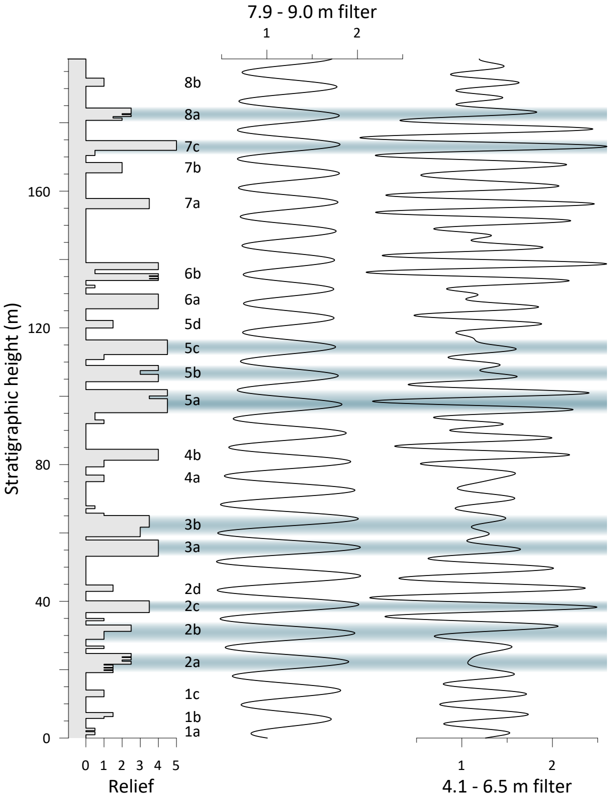

Supplementary Figure 11. The origin of the 8 - 9 m peaks in the MTM spectrum of section Prieska. The amplitude of the bandpass filtered 8 – 9 m cycle is highest in the bottom part of the log, where it follows the stratigraphy better than the filtered 4.1 – 6.5 m cycle (i.e. each of its maxima coincide with the characteristic abc-alternations). This demonstrates that the 8 – 9 m peaks are the effect of lateral thickness variations between the sections, and that the alternations in the bottom part of section PK are relatively thicker.

Supplementary Tables

Supplementary Table 1. LOI-corrected XRF results and lithological rank of the representative 230 field samples from section Woodstock. *Sample WS21 was lost during preparation for XRF.

Sample	Strat. height m	Al_2O_3 ‰	Ba ‰	CaO ‰	Cr ‰	Fe_2O_3 ‰	K_2O ‰	MgO ‰	MnO ‰	Ni ppm	P_2O_5 ‰	SiO_2 ‰	Sr ppm	Zr ‰	Lithological rank
WS18	52.6	BDL	0.01	1.4	0.01	511.1	BDL	BDL	BDL	BDL	0.49	478.6	BDL	BDL	4
WS19	55.2	BDL	0.00	0.8	0.01	346.0	BDL	0.3	0.4	5	0.20	647.2	BDL	BDL	3
WS20	55.7	BDL	0.00	0.6	0.01	484.1	BDL	BDL	0.1	1	0.20	515.1	BDL	BDL	4
WS21*	56.0	-	-	-	-		-	-	-	-	-		-	-	1
WS22	58.9	0.2	0.01	0.5	0.01	479.1	0.1	0.3	0.1	11	0.40	522.8	2	0.00	4
WS23	62.0	BDL	0.01	0.6	0.01	455.0	0.1	BDL	BDL	2	0.70	542.4	1	BDL	2
WS24	62.6	3.6	BDL	0.4	BDL	804.7	BDL	BDL	0.2	BDL	1.75	164.8	BDL	BDL	4
WS25	64.1	BDL	0.01	0.5	0.01	495.0	0.1	0.1	0.3	1	0.40	507.3	BDL	BDL	3/4
WS26	65.8	BDL	0.01	0.9	0.01	602.3	0.1	0.2	BDL	BDL	0.20	399.8	BDL	BDL	4
WS27	67.2	BDL	BDL	0.6	0.01	215.4	0.1	0.3	0.3	4	0.68	756.4	BDL	0.01	1
WS28	68.6	0.4	0.01	0.5	0.01	233.1	0.2	0.4	0.5	4	0.40	751.9	BDL	0.00	2
WS29	71.5	BDL	BDL	0.5	0.01	36.2	0.4	0.3	0.1	8	0.10	951.6	BDL	0.01	1
WS30	73.7	BDL	0.00	0.5	0.01	264.9	0.1	0.8	0.2	3	0.49	706.6	1	0.01	1
WS31	75.0	0.2	0.01	0.5	0.01	106.9	0.3	0.5	0.6	6	0.30	879.2	BDL	BDL	1
WS33	76.0	0.3	0.05	0.5	0.01	475.2	0.3	0.4	0.6	BDL	0.40	519.3	3	BDL	3
WS34	76.7	0.1	0.01	0.5	0.01	389.6	0.1	0.2	0.2	7	0.30	601.5	1	BDL	2/3
WS32	77.3	0.3	0.02	0.8	0.01	435.0	0.2	0.4	BDL	8	0.60	559.7	3	BDL	3
WS35	78.3	0.1	BDL	0.5	0.01	268.6	0.4	0.4	BDL	5	0.10	724.6	BDL	BDL	3
WS36	81.3	0.4	0.03	0.8	0.01	222.6	0.7	1.1	1.8	4	0.40	761.5	2	0.00	3
WS37	84.4	BDL	0.02	0.7	0.01	549.5	0.2	0.1	0.2	BDL	0.20	448.4	BDL	BDL	4
WS38	87.3	BDL	0.06	0.7	0.01	345.4	0.4	0.2	0.2	7	0.40	647.4	7	BDL	3
WS39	91.0	BDL	0.00	0.9	0.01	182.9	0.3	0.3	0.1	3	0.20	797.8	BDL	BDL	2
WS40	101.2	BDL	0.00	0.4	0.01	386.5	0.2	0.2	0.1	BDL	0.40	607.5	BDL	BDL	3
WS41	106.4	BDL	0.02	0.6	0.01	427.0	0.1	0.3	0.2	1	0.50	571.5	1	BDL	3/4
WS42	107.9	BDL	0.02	0.5	0.01	444.6	0.2	BDL	BDL	5	0.20	550.3	1	BDL	3/4
ISE921a		106.8	0.59	60.4	0.14	45.3	23.1	18.6	1.6	44	3.12	581	165	0.24	
ISE921b		108.2	0.60	60.5	0.14	46.1	23.3	19.0	1.6	51	3.12	581	164	0.29	
ISE921 acc. value		107.3	0.56	60.2	0.13	45.6	23.0	18.4	1.5	42	3.21	-	165	0.25	
Max. bias (%)		0.8	6.5	0.6	10.6	1.0	1.3	3.0	7.1	20.5	2.8	-	0.8	18.1	

Supplementary Table 2. MTM power spectral peaks associated with the alternations (4.3 – 6.3 m) and bundles (16 -22 m) versus their AR1 and LOWSPEC noise model confidence level. Peak wavelengths (in metres) represent "local" maximum power (for MTM AR1) and local maximum prewhitened power (for LOWSPEC). Note that the peaks in the 16 – 22 m range only reach the 90 % confidence level in the MTM AR1 spectra for sections Kuruman Kop and Whitebank.

Section	MTM Peak wavelength m	AR1 Confid. level %	MTM Peak wavelength m	LOWSPEC Confid. level %
Kuruman Kop	22.1	76.1	22.1	69.6
	16.1	90.8	15.4	83.9
	5.7	99.4	5.7	98.4
	4.3	98.1	4.3	96.8
Whitebank	19.7	88.9	19.1	79.9
	16.2	92.9	15.8	88.9
	6.1	97.8	6.1	95.0
	5.8	99.0	5.8	96.4
	4.5	95.8	4.5	91.2
Woodstock	24.5	73.6	23.9	66.1
	21.8	76.2	21.8	68.8
	18.9	85.7	18.9	76.5
	6.1	98.7	6.1	97.4
	5.0	97.5	4.9	95.6
Daniëlskuil	21.1	64.5	21.1	55.0
	14.1	85.5	13.8	79.3
	6.3	99.1	6.3	98.2
	6.0	99.5	6.0	98.3
	4.8	99.7	4.8	99.5
	4.4	99.8	4.4	99.5
Prieska	21.0	76.7	21.0	71.0
	16.6	81.7	16.6	74.0
	6.2	95.3	6.2	92.1
	5.9	88.4	5.8	83.8
	5.6	89.3	5.6	83.7
	5.4	88.2	5.4	83.0

Confidence level:
░ > 99 %
▒ > 95 %
▓ > 90 %
█ < 90 %

Chapter 3

Precession as the pacemaker of early Earth's oxygenation

Precession as the pacemaker of early Earth's oxygenation

Margriet L. Lantink, Wytze K. Lenstra, Joshua H.F.L. Davies, Rick Hennekam, David McB. Martin, Paul R.D. Mason, Maria Ovtcharova, Gert-Jan Reichart, Caroline P. Slomp and Frederik J. Hilgen

Abstract

Fundamental changes occurred in the redox structure of Earth's ferruginous ocean prior to the Paleoproterozoic Great Oxidation Event (GOE), yet the exact processes and associated time scales of oxygenation in relation to oxygen production remain unclear. Here we present evidence from 2.469 - 2.454 billion-year-old marine deposits of the Joffre Member, NW Australia, for high-frequency, cyclical redox variations induced by astronomical climate forcing (precession). Characteristic patterns in iron, sulfur and phosphorus indicate vertical oscillations in the iron chemocline that periodically reached the seabed, as a consequence of enhanced productivity and oxygen production in surface waters when nutrient runoff peaked. We propose that precession, via its control on monsoonal intensity, provided a key pacing mechanism for the oxygenation of the shallow ocean, likely enabling the cyclic release of oxygen into the atmosphere before the GOE onset.

Introduction

The redox state of the ocean-atmosphere system has experienced dramatic changes over Earth history, profoundly shaping past surface environments and the biosphere across geological timescales (Lyons et al., 2014; Reinhard and Planavsky, 2020). Regular large amplitude swings in dissolved oxygen concentrations of oceanic and marine basins have occurred throughout various intervals of the Phanerozoic against a backdrop of a well-oxygenated atmosphere. These redox cycles, manifested as periodic deep-water anoxia, have been attributed to astronomical induced climate changes that originate from quasi-periodic variations in the Earth's orbital and inclination parameters (Milankovitch forcing on 10^4 – 10^6 year scale) (Rossignol-Strick, 1983; Herbert and Fischer, 1986; Röhling et al., 2014; Mitchell et al., 2008; Meyers et al., 2012b; Jin et al., 2020). In many instances, their occurrence has been explained by periodically increased productivity and/or stratification-induced burial of organic carbon as a consequence of variations in monsoonal intensity, driven by the precession and eccentricity cycles (Kutzbach, 1994; Kutzbach et al., 2008; Bosmans et al., 2015; Beckman et al., 2005). These two cycles are directly coupled, where eccentricity acts as amplitude modulator of climatic precession that is the principal insolation driver.

Recently, evidence has been found for Milankovitch-related stratigraphic variability in ~2.47 billion year old (Ga) banded iron formations (BIFs) (Lantink et al., 2019; de Oliveira Carvalho Rodriguez et al., 2019). More specifically, these Precambrian marine sedimentary rocks, indicating periods of anoxic and ferrous iron (Fe^{2+})-rich ocean water

(Poulton and Canfield, 2011; Konhauser et al., 2017), show regular meter-scale alternations between iron(III) oxide-rich 'BIF' versus iron(II) silicate- and carbonate-rich 'shale' lithology which were linked to long-period eccentricity (13). This raises the intriguing question whether precession also exerted a control on redox variability in the Earth's early oceans before atmospheric oxygenation ~2.4 – 2.2 Ga (the "GOE" Great Oxidation Event (Holland, 2002; Bekker et al., 2004) or Episode (Poulton et al., 2021)), when boundary conditions were fundamentally different from those during the Phanerozoic. Thus far, several studies have found geochemical indications for redox fluctuations over very long time scales (tens of millions of years), in the form of transient surface-ocean oxygen build-up and atmospheric escape ("whiffs of oxygen") prior to and during the GOE (Anbar et al., 2007; Frei et al., 2009; Kendall et al., 2015; Koehler et al., 2018). However, the precise trajectory and pacing mechanisms of this potentially more dynamic evolution of the Earth's oxygenation history remain elusive and the links with redox processes at the well-understood much shorter timescales of the Milankovitch cycles, are currently unknown.

Here we present high resolution stratigraphic and geochemical analysis from regular 'Knox cyclothem' (Trendall, 1969; Trendall and Blockley, 1970) alternations of the early Paleoproterozoic Joffre Member BIF of the Brockman Iron Formation (IF), as exposed in the Hamersley Range in NW Australia (Supplementary text S1; fig. S1). Recently established depositional rates from the correlative Kuruman IF in South Africa suggested a precession origin (Lantink et al., 2019) for the cyclothems of the Brockman IF. Thus, these cyclothems provide a promising opportunity to i) test our precession hypothesis and ii) gain direct insight into the Earth System response to the inferred precession forcing.

Results and Discussion

In outcrops of the Joffre Member at Joffre Falls (Trendall, 1969; Trendall and Blockley, 1970) we found that Knox cyclothems (~10 cm) are typically arranged into distinct ~85 cm thick bundles of alternating 'BIF' and more weathering-prone 'shale' (text S2). This cycle hierarchy is consistent with the combined influence of precession and short eccentricity, if a reduced precession period, due to the shorter Earth-Moon distance, is taken into account (Waltham, 2015). In core DD98SGP001 (DD98), which intersects the Joffre ~150 km west of the Falls, we observed a similar regular and continuous expression of unweathered cyclothems, characterized by a greenish mudrock layer (~0.5 – 1 cm thick) with an iron oxide-rich band above and/or below, alternating with chert (text S3; fig. S2). From this core, chemical abrasion (CA-)ID-TIMS U-Pb zircon dating was carried out on 4 different horizons spanning 200 m and two short segments of representative Knox cyclothems (J45de and J60d) were selected for calibrated X-ray fluorescence (XRF) core scanning (Fig. 1a; Methods 1-3; figs. S4-7; tables S1-2). Time series analysis results based on high (1 mm) resolution elemental (K weight %) and spectroscopic mineral (ferric oxide) abundance records (Methods 4) demonstrate the same cycle hierarchy in DD98 as observed at Joffre Falls (Fig. 1b-c; fig. S8). Crucially, our new high-precision ages for the Joffre yield a mean accumulation rate of ~10 m/Myr (Fig. 1a; fig. S9), which matches the average rate determined for the Kuruman IF (Lantink et al., 2019), and places the alternations in the precession and short eccentricity time domain (text S4). Thus, the combination of the cyclostratigraphic and independently consistent U-Pb ages presented here, provides robust direct support for our Milankovitch forcing hypothesis for BIF and a precession origin of the cyclothems.

Distinctive patterns in redox-sensitive elements revealed by our analyses of the Knox cyclothems (Fig. 1d-e; fig. S7) indicate significant changes in the redox conditions during deposition that vary with precession. At or close to the bottom and top of the regular mudrock layers, we noted the presence of thin conspicuous laminae of magnetite and pyrite, recognizable by sharp, often double, peaks in Fe and S respectively, as well as distinct laminae of beige-white carbonate (Ca) and phosphorus (P) enrichments (text S3). The sharply defined yet wavy ("fluid-looking") nature of the horizons, cross-cutting the primary bedding (figs. S2-3), is strongly reminiscent of in-situ redistribution and reaction processes arising from breakdown of organic matter (OM) during early diagenesis (Berner, 1981; Kasten et al., 2003). Such authigenic mineral laminae, which can be preserved on geological time scales, point towards nonsteady-state diagenesis (Berner, 1969; de Lange et al., 1987; Van Hoof et al., 1993; Passier et al., 1996; Kasten et al., 2003). The symmetrical

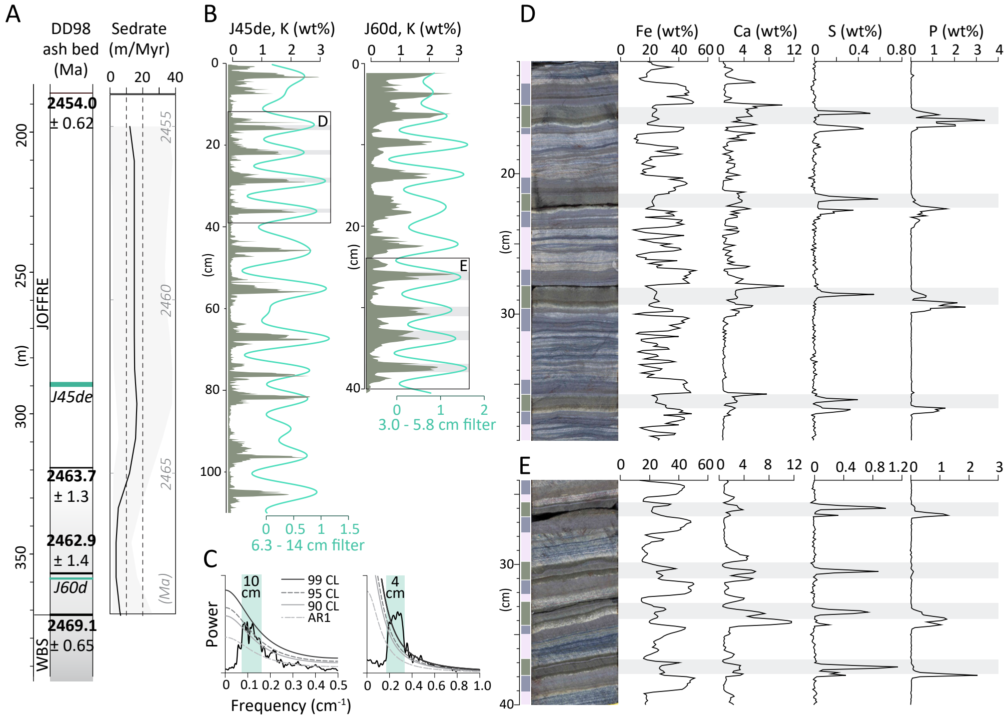

Figure 1. U-Pb and geochemical profiles for core DD98SGP001 (continues next page)

(**A**) Left: schematic column indicating sample depth and calculated $^{207}Pb/^{206}Pb$ ages. Dark grey to white coloring indicates a transition from shale-carbonate to cherty BIF. Right: depositional rate model for the targeted stratigraphic interval of the Joffre Member with 97.5% confidence intervals indicated in light grey (see also fig. S9). (**B**) Regular alternations in K weight % of sections J45de and J60d and bandpass filters. (**C**) Multitaper method (MTM) power spectra of the K wt% records in B with autoregressive noise (AR1), 90, 95 and 99% confidence levels (CL). Turquoise shaded zones indicate the area of enhanced spectral power (frequency window) that corresponds to the filter output in **B**. (**D**, **E**) Detail of four Knox cyclothem alternations from section J45de (**D**) and J60d (**E**) showing lithology (left) and Fe, Ca, S and P wt% records (right). Grey horizontal bands mark the position of the peaks in K wt% as visible in B. Vertical bars to the left of the core: green = stilpnomelane-carbonate mudrock layers; dark blue-purple = iron oxide-dominated zones; light beige = microbanded chert or "zebra" intervals (text S3).

arrangement of the Fe and S horizons (fig. S10) is best explained by a marked increase in the net arrival of organic matter at the seafloor during the mudrock phase of the precession cycle, as detailed below.

The systematic positioning of the double pyrite laminae (S peaks) on the inner side of iron oxide bands and/or magnetite laminae (Fe plateaus and peaks, respectively) suggest a specific nonsteady-state situation (Berner, 1969) involving the development of sulfide (H_2S) in the mudrock porewaters, as a consequence of organic matter oxidation with SO_4^{2-}. Similar (multiple) iron sulfide and -oxide enrichments have been described for Plio-Pleistocene sapropel alternations, where they reflect the formation of 'redox fronts' involving diffusion of H_2S, Fe^{2+} and O_2 during burial (Van Hoof et al., 1993; Passier et al., 1996). During the early Paleoproterozoic, however, seawater SO_4^{2-} concentrations have been estimated to be three orders of magnitude lower and iron (hydr)oxides, precipitated from the photic zone, are considered the dominant primary oxidants for organic matter on the seabed during BIF formation (Konhauser et al., 2017; Robbins et al., 2019). Thus, understanding how these observed patterns can be generated and translated to precession-induced processes in the early Paleoproterozoic water column, requires further examination.

We applied a reactive-transport model (RTM) to evaluate how variations in the flux of organic matter (OM) versus iron (hydr)oxides (FeOx) and bottom water Fe^{2+} concentrations are able to quantitatively reproduce the characteristic Fe and S profiles on the timescales of precession (Methods 5). Bottom water SO_4^{2-} was set at 20 μmol/L, whilst assuming a permanently anoxic sediment-water interface (tables S3-8). To represent the formation of the chert and iron oxide layers of the Knox cyclothem, we assumed a constant high FeOx flux of 0.11 mol m^{-2} yr^{-1} based on the total Fe concentration of the iron oxide layers. Deposition of the mudrock layers was simulated by imposing an abrupt increase in the OM flux from zero to 0.04 mol m^{-2} yr^{-1} (~1.8 weight % organic C) for a period of 4 kyr (~1/3rd of the precession cycle).

The outcome of our data-model comparison exercise (Fig. 2; figs. S11-14) demonstrates that, in addition to an increase in OM, a strong decline in FeOx input and

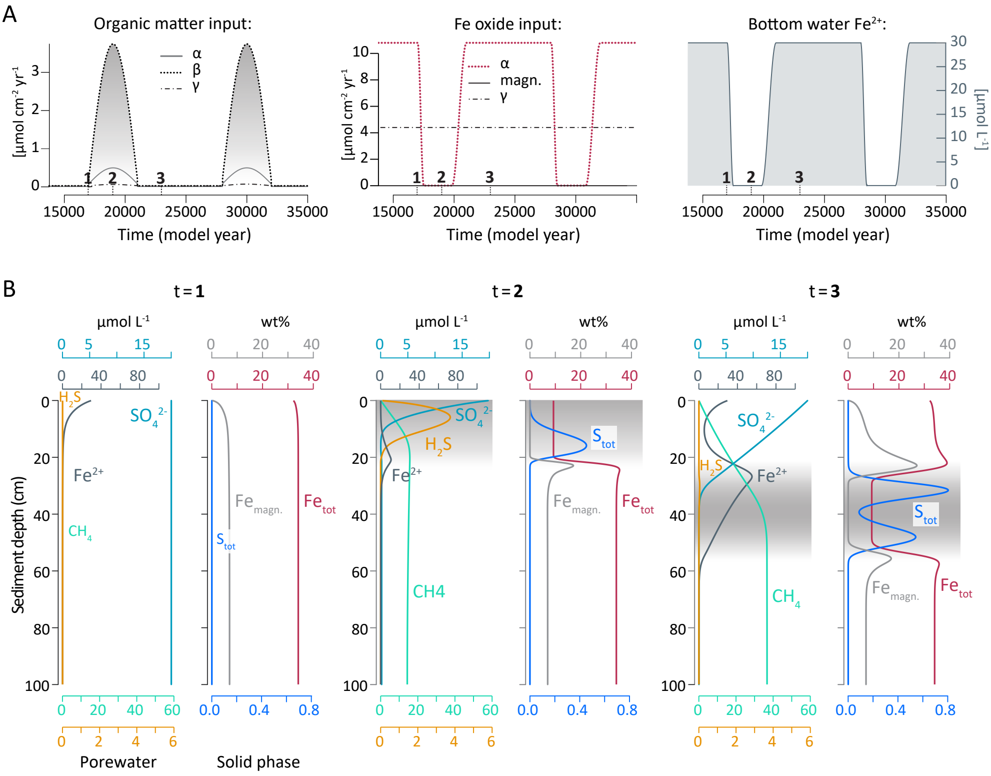

Figure 2. Model scenario with variable organic matter and iron input Results of the RTM demonstrating formation of diagenetic magnetite and pyrite laminae (two Fe and S maxima). (**A**) Transient scenario for the input of organic matter and Fe oxides to the sediment-water interface and bottom water Fe^{2+} for two successive precession cycles. The different types of organic matter are denoted as α (highly reactive), β (less reactive) and γ (refractory); different types of Fe oxides as α (highly reactive), magnetite and γ (refractory). 1, 2 and 3 indicate the time points shown in **B**. Note that the width of the OM peak is larger than that of the Fe oxide and bottom water Fe^{2+} minimum. (**B**) Modelled porewater (Fe^{2+}, SO$_4^{2-}$, H$_2$S and CH$_4$) and solid phase depth profiles (total Fe oxides, magnetite and total S) for three time points indicated in **A**: before (t = 1), during (t = 2) and after (t = 3) deposition of the organic matter-rich layer. The grey shaded zones indicate the depth interval of enhanced organic matter deposition.

porewater Fe^{2+} during deposition of the OM-rich mudrock layer is a prerequisite for the accurate reproduction of both observed S and Fe records. More specifically, our model calculations imply that an episode of near-complete cessation in FeOx deposition (less than 1% of its original flux) and bottom water Fe^{2+} concentrations close to zero during the OM-rich phase, is essential for the build-up of porewater H$_2$S which leads to double S peaks (Methods 5.4). In the model, these double peaks arise from precipitation of iron sulfides (FeS$_x$) at two separate reaction fronts, involving H$_2$S and Fe^{2+}, in the basal and upper part of the OM-rich sediment interval. In addition, two narrow Fe peaks in the form of magnetite are developed around the FeS_x laminae due to the reaction of FeOx with Fe^{2+} liberated from FeOx reduction in the sediment immediately above or below the sulfidic zone in the sediment.

The double S peaks do not occur when we prescribe a more moderate decline or continuous high FeOx flux over the modelled Knox cyclothem, even when the rate of OM input is sufficient for a switch from FeOx to SO_4^{2-} reduction (Methods 5.3; fig. S11). This is because the low amounts of H_2S that are produced in the OM-rich depth interval, once Fe oxides become depleted, are directly precipitated as FeS_x due to the high abundance of Fe^{2+}. As a result, only a single broad horizon of FeS_x is formed in the middle of the OM-rich depth interval (fig. S12), contrary to the observed narrow, often double S peaks and their more outward, closer position to the base and top of the Fe minimum (Fig. 1d-e; fig. S10). Fundamentally, these characteristic patterns can only be explained when H_2S produced in the OM-rich layer diffuses upwards and downwards to meet Fe^{2+} liberated from FeOx reduction in the surrounding sediment (text S5). This implies that during deposition of the OM-rich mudrock layer the flux of FeOx and porewater Fe^{2+} must have been very low.

These findings indicate that, over the precession cycle, dramatic changes must have occurred in the redox conditions of the overlying water column resulting from changes in primary productivity. The combination of low bottom water Fe^{2+} concentrations and limited FeOx flux, required by the RTM, indicates that the water column periodically became low in dissolved Fe^{2+} over its entire vertical extent, from the sea surface to sediment-water interface. This suggests that large-amplitude oscillations occurred in the vertical and lateral position of the Fe^{2+}-poor / Fe^{2+}-rich gradient or redox boundary (iron chemocline), assuming this boundary was originally positioned within the photic zone of more proximal shelf waters (Lyons et al., 2014; Poulton and Canfield, 2011; Kendall et al., 2010; Zerkle et al., 2017; Ostrander et al., 2019). Such periodic downward shifts, reflecting a net increase in Fe^{2+} oxidation (removal) versus Fe^{2+} supply, must have resulted either directly or indirectly from increased O_2 production via oxygenic photosynthesis, in order to explain the simultaneous increase in the flux of OM as interpreted here. While increased photoferrotroph activity likely contributed to the initial lowering of the iron chemocline, a further deepening beyond the photic limit and the strong decoupling between OM and Fe input (increase vs. decline, respectively) can only be logically explained by cyanobacterial growth and associated OM export. The iron oxide-rich zones that occur systematically below the mudrock layers may directly result from – and provide evidence for – the net Fe^{2+} oxidation and "raining out" of iron (hydr)oxides during iron chemocline lowering.

The distinct P enrichment patterns provide a potential key to understand how the variations in O_2 production and chemocline oscillations may have been brought about by precessional forcing. Their high concentrations (1-3 weight %) cannot be explained only by input of OM, given a C:P ratio of the OM of 106:1 (Redfield ratio). This suggests an additional input of phosphate originating directly or indirectly from the water column (text S5). Considering also the significantly higher proportion of aluminosilicate clay in the mudrock layers (text S3; fig. S7), indicating enhanced terrigenous input, this phosphate may have been periodically introduced via distal continental runoff during precession-induced wetter climatic conditions. As P is commonly considered the ultimate limiting nutrient for oxygenic photosynthesis on geological timescales (Tyrrel, 1999) such periodic riverine input could have acted as a critical primary productivity stimulant, in particular considering that it may have been quickly depleted in the intervening ferruginous periods (Bjerrum and Canfield, 2002; Jones et al., 2015; Reinhard et al., 2017).

Synthesizing our observations with knowledge from the Phanerozoic into a conceptual model for precession forcing of the Knox cyclothem (Fig. 3; text S6), we link the inferred variations in continental nutrient input, primary productivity and iron chemocline oscillations to precession-driven changes in (summer) monsoon intensity. Given the low- to mid-paleolatitude position of the Hamersley-Transvaal basin (de Kock et al., 2009; Gumsley et al., 2017) and dominant precession-eccentricity forcing of monsoonal systems, monsoonal activity would have intensified by 2.5 Ga with the emergence of large elevated landmasses (Bindeman et al., 2018). We envisage chert deposition at times of limited runoff and surface water oxygenation during overall dry climatic conditions, at

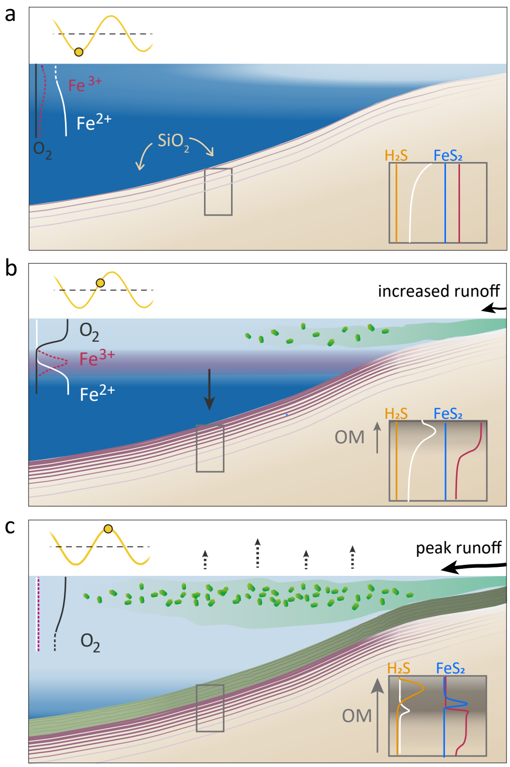

Figure 3. Conceptual climate model for redox oscillations during the early Paleoproterozoic. (**A**-**C**) show the progression from summer insolation minimum to maximum (position on yellow curve in the upper left) and the proposed monsoonal response. Middle left of each panel: interpreted water column redox structure. Bottom right inset: sedimentary redox profile (RTM summary – schematic of Fig. 2). Dark grey colors denote organic matter, green = cyanobacteria (water column) and terrigenous material (sediment floor), red purple = iron oxide, beige = chert. Black arrow (**B**) indicates downward movement of the iron chemocline, causing enhanced 'rain down' of iron (hydr)oxides. Dotted arrows (**C**) denote possible net O_2 diffusion to the atmosphere during periods of maximum water column oxygenation.

times of reduced seasonality (text S6). Towards the opposite phase of the precession cycle, monsoonal intensification and increased nutrient input stimulated marine productivity and led to chemocline lowering and deposition of the iron oxide bands. Maximum oxygenated conditions, lowest chemocline position and organic matter burial occurred during the peak 'wet' phase (at maximum seasonal contrast) represented by the green mudrock layers. Our monsoonal hypothesis also applies to the meter-scale eccentricity-related alternations characteristic for the Dales Gorge Member and Kuruman BIFs (Lantink et al., 2019). The dominant expression of these latter cycles points to a strong non-linear response to the initial precession-induced insolation forcing.

Our findings indicate a much more dynamic redox structure of Neoarchean to early Paleoproterozoic continental margins than previous reconstructions (Lyons et al., 2014; Poulton and Canfield, 2011; Kendall et al., 2010; Ostrander et al., 2019), in which variability on the Milankovitch scale was not included. In addition, our precession model links the regular variations between 'BIF' and 'shale' to laterally synchronous changes in water column biogeochemistry, as opposed to sea level-controlled changes in proximity to the (less ferruginous and more productive) shoreline and marine surface, that imply a stable chemocline position. The vertical amplitude of our proposed (iron) chemocline oscillations is difficult to estimate given the large uncertainty in the absolute depth of deposition and paleo-bathymetry (text S1). However, we suspect that the oscillations spanned at least several tens of meters given the downward shifts from well above to below the photic limit or even the sediment-water interface, based on the Joffre sequences studied here. The link with precession also makes it unlikely that the redox cycles record a secondary or local phenomenon only, or conversely, a purely turbiditic i.e. laterally transported signal (Krapež et al., 2003). Rather, these variations likely applied to the entire Hamersley-Transvaal region, and may be representative for other marine environments worldwide situated within the same mid- to low latitude climatic zone and in the vicinity of a large hinterland.

Conclusion and implications

We thus tentatively conclude that, as during the Phanerozoic, the redox balance of the pre-oxygenated Earth's oceanic margins was critically unstable with regards to astronomically-forced insolation variations and their associated climatic and productivity response. However, where periods of higher export productivity during the Phanerozoic effectively resulted in the periodic development of deep-water ocean anoxia, precession stimulation of photosynthesis during the early Paleoproterozoic led to periodic net removal of reducing Fe^{2+}, facilitating the possible build-up of oxygen in the shallowest ocean. In this respect, the mudrock layers of the Knox cyclothem would represent a high-frequency subtle version of the 'whiffs of oxygen' (Anbar et al., 2007; Koehler et al., 2018), with a much more regular occurrence (i.e. orbitally synchronized). Further research should explore whether these transient oxygenation signals have a tectonic or internal feedback origin as suggested earlier (Lyons et al., 2014; Kendall et al., 2015; Alcott et al., 2019; van de Velde, 2020), or whether they might alternatively be the manifestation of very long-period eccentricity maxima (Boulila et al., 2012), given their coincidence with prominent black (i.e. organic carbon- and pyrite-rich) shale intervals.

The precession-paced changes in iron and carbon drawdown in association with O_2 production may have important implications for how the early Earth's atmosphere became oxygenated. When considering the oscillations as superimposed on a gradually increasing trend, possibly related to the emergence of large landmasses and associated monsoonal intensification, we speculate that cyclically enhanced primary productivity in low-Fe^{2+} surface waters resulted in an earlier surpassing of the critical threshold for O_2 diffusion and build-up into the atmosphere (Figure 3c), than currently known. This certainly is conceivable given the timing of our targeted interval from the Joffre (2.47 – 2.45 Ga) with respect to the first reported evidence for atmospheric O_2 levels higher than 10^{-5} of their present value at ~2.43 Ga (Warke et al., 2020) marking the onset of the GOE (Poulton et al., 2021).

This raises the intriguing follow-up question whether Milankovitch forcing actively contributed to the Earth's long-term oxygenation itself, given the aforementioned nonlinear response of the System. It is conceivable that in the hypothetical case of a stable, average monsoon strength, rates of riverine nutrient supply and associated O_2 production would have been insufficient to outpace O_2 consumption by Fe^{2+} oxidation, and thus to reach the critical threshold for build-up of dissolved O_2 and atmospheric release. One can thus speculate how the oxygenation of the Earth would have occurred or proceeded in the case of a circular orbit, which would have effectively eliminated the precession forcing on climate.

Acknowledgements

We acknowledge the GSWA for providing field logistical support and core material; we thank L. Hancock and M. Wawryck for the Hylogger mineral extractions. This research was financially supported by the Dutch National Science Foundation, grant NWO ALWOP.190 (FJH, PRDM, MLL); the Swiss National Science Foundation grant 200021_169086 (JHFLD, MO); the Netherlands Earth System Science Centre Gravitation Grant 024.002.001 (WKL, CPS); and the Foundation Stiching Dr. Schürmannfonds, grant no. 2018-136 and 2019-145 (FJH, PRDM, MLL).

Supplementary Information

Materials and Methods

1. Sample selection

Our study focused on the Joffre Member in diamond drill-core DD98SGP001 (22°03’29.9”S 116°50’06.0”E) drilled at Silvergrass, which retrieved well-preserved strata of the Joffre, Whaleback Shale and Dales Gorge Member of the Brockman Iron Formation from 87.7 m to 450.5 m depth (Fig. S1). We started our investigation by visual inspection of the entire core, after which representative intervals were selected that showed a particular regular expression of the Knox cyclothem. The core sections J45de (box 45, rows no. d-e) and J60d (box 60, row no. d) presented in this paper come from 289.05 – 290.26 m depth, a cherty BIF interval, and from 358.34 – 358.73 m depth, a shaley carbonaceous BIF interval, respectively (Fig. S4). The selected intervals were subsequently cut in halves, generating a flat surface along the length of the sampled core. Specific intervals were in addition polished to facilitate detailed inspection of sedimentary textures and mineralogy using high magnification scans (Fig. S3).

2. XRF core scanning and calibration

X-ray fluorescence (XRF) core scanning was conducted with the Avaatech core scanner at the Royal Netherlands institute of Sea Research (NIOZ), which is equipped with a new generation XRF detector yielding improved spectral resolution (Hennekam et al., 2019). The tube energy settings (1–50 kV at a maximum of 2 mA), primary beam filters and measurement time were optimized for minor/trace elements while maintaining a dead time between 20 to 40 % (Table S1). The XRF analyses were carried out with a 12 x 1 mm slit, at 1 mm intervals, on freshly cut surfaces and covered with a 4-µm SPEXCerti Ultralene foil to prevent cross contamination. Prior to the analyses the cores were placed in split plastic tubes and supported from underneath with foam to create a stable and even surface. Data points associated with core breaks were removed if the total yield (sum intensities in 10 kV range) was significantly lower than that of the surroundings. Repeated analyses (N = 37) of reference sample SARM 4 in between runs indicate a precision (relative standard deviation) of < 1% for Fe; < 4% for Al, Ca, K, Mn; < 7% for S implying that the detector remained stable during the whole experiment. Spectral data (see example spectrum Fig. S5) were interpreted using bAxil spectrum analysis software developed by Brightspec.

ICP-OES analysis on 14 discrete samples was carried out to convert raw XRF intensities to approximate concentrations. Thin (3 – 5 mm) core slices were obtained from two additional scanned intervals (J36c and J57e). The slices were chosen such that they captured a range of different chemical compositions as indicated by the XRF data and they were sawed as bedding parallel as possible, although this could not always be achieved due to the curved nature of the layers. Homogenized rock powders (crushed with either tungsten carbide or corundum) underwent total digestion using a procedure with HF-$HClO_4$-HNO_3 acid mixtures (details in Hennekam et al., 2015). The ICP-OES measurements were performed with a Spectro Ciros Vision ICP-OES at Utrecht University. Reference samples (ISE921 and PACS-2) and duplicate measurements (N = 4) indicate an accuracy and precision (reported here as deviation from reference value; relative standard deviation) of: Al (7%; ± 1%), Ba (-; ± 1%), Ca (11%; ± 0.5%), Fe (13%; ± 3%), K (7%; ± 2%), Mn (6%; ± 0.2%), P (4%; ± 1%) and S (3%; ± 2%) (Table S2).

Comparison of XRF intensities to ICP-OES concentrations was done by visual alignment of the XRF slit positions and corresponding core slices. First, a calibration was attempted using common multivariate log-ratio calibration (Weltje et al., 2015). However, this led to inferior results (i.e. poor R^2 accuracy values in particular for Fe, and various discrepancies for the S and P records) compared to direct relation of counts versus concentrations. We suspect that this is because the XRF signal of the heavier elements comes from a slightly broader depth interval than for lighter elements (Potts et al., 1997), which in these thinly laminated sediments leads to compromised results when calibrating all elements together. Therefore, conversion to weight percentage was based on simple linear calibration (i.e. linear regressions in X-Y plots of intensity versus concentration). This yielded high R^2 values of the regression lines of the targeted elements: > 80% for Al and Mn; ≥ 90% for Ca, Fe, K; and ≥ 95% for Ba, P and S (Fig. S6).

3. TIMS U-Pb geochronology

Multiple shale intervals from the DD98SGP001 drill core were tested for their Zr content using a handheld XRF and four shales with the highest concentrations were chosen for zircon extraction. The shale intervals were at 186.1m, 319.43m, 356.88m and 371.55m in the core, and were between 10-30cm thick. The shale at 356.88m had previously been sampled and dated in Pickard (2002), i.e. sample 835. We cut the core in half for each sample, leaving half of the material behind. This resulted in either a half or quarter core for zircon extraction, depending on if the interval had been previously sampled. All samples were subsequently crushed in a tungsten mill and sieved to <250 µm in the mineral processing labs at the Université du Québec à Montréal. The powder was subsequently passed over a Wilfley table and zircon grains were hand-picked under a binocular microscope. Prismatic euhedral zircon grains were extracted from the samples and were subsequently annealed at 950°C for 48h. The grains from each sample were placed in 3ml Savillex vials and chemically abraded in concentrated HF for 6x3h at 180°C (Widmann et al., 2019). The grains were checked after 3h to make sure some fragments were still big enough to undergo further chemical abrasion. All samples were given 18h chemical abrasion apart from the sample from 319.43m, which was only given 12h chemical abrasion due to the very small sizes of the remaining grains. After chemical abrasion, the zircons were cleaned in 6N HCl at 80°C for 12h, before being cleaned in HNO_3 multiple times, followed by loading into microcapsules for dissolution at the high precision U-Pb geochronology lab at the University of Geneva using the techniques described in Lantink et al. (2019). Individual grain fragments were loaded into Savillex microcapsules with ~5 mg of the EARTHTIME ^{202}Pb + ^{205}Pb + ^{233}U + ^{235}U tracer solution (Condon et al., 2015;

McLean et al., 2015) and ~70 μl of concentrated HF and were dissolved in a Parr high pressure digestion vessel at 210°C for 48h. Following digestion, the samples were dried down on a hotplate and converted to chloride form by re-dissolving them in 6N HCl overnight in the Parr pressure vessel at 180°C. After chloride conversion, the samples were dried down again and re-dissolved in 3N HCl before loading onto pre-cleaned anion exchange columns for U and Pb purification. The concentrated U and Pb aliquots were loaded onto outgassed zone-refined Re filaments and measured with a Thermo Scientific TRITON or IsotopX PHOENIX thermal ionization mass spectrometer (TIMS). On the TRITON, Pb was measured in dynamic peak jumping mode using a MasCom discrete-dynode secondary electron multiplier, whereas UO_2 was measured in static mode using Faraday cups attached to either 10^{12} Ω or 1013 Ω resistors. When the UO_2 signal was not sufficient to be measured on the Faraday cups, the electron multiplier was used in dynamic peak jumping mode. Samples measured on the PHOENIX were measured in the same way. However, a daly detector was used instead of a secondary electron multiplier for Pb, and small UO_2 ion beams, and for larger UO_2 ion beams, Faraday cups with 10^{12} Ω were used in static mode. All common Pb was attributed to laboratory blank and was assigned the long term isotopic composition of the Geneva procedural blank. All U-Pb data processing was conducted using the Tripoli and Redux software packages, following the algorithms of McLean et al. (2011). Ages reported here are given without the additional uncertainty associated with the tracer calibration and uranium decay constants. All ages were corrected for initial ^{230}Th and ^{231}Pa disequilibrium in the melt using a U/Th ratio of the magma of 3.5 and an initial ^{231}Pa/^{235}U ratio of 1.1. Depositional rate modelling was conducted using the R package Bchron (Hasslet and Parnell, 2018) with concordant weighted mean ^{207}Pb/^{206}Pb ages or single grain ^{207}Pb/^{206}Pb ages depending on how many concordant analysis were found in the sample.

4. Time series analysis

Spectral analysis was carried out on the K records of J45de and J60d, which were detrended and linearly interpolated at 10 mm and 1 mm, respectively. In addition, 'ferric oxide abundance' records of two longer intervals were selected for the analysis of longer-period cycles (Fig. S8). These ferric oxide records are based on mineral reflectance data acquired by the GSWA Hylogger scanner and were extracted from The Spectral Geologist spectral interpretation software. We used multitaper method (MTM) spectral analysis (Thomson, 1982) as implemented in the R package astrochron (Meyers, 2014) using three 2π slepian tapers and a time-bandwidth product of 3. Classical AR1 and LOWSPEC (Meyers, 2012) confidence levels were determined using the functions 'mtm' and 'lowspec'. Astrochron was further used for rectangular bandpass filtering (bandpass).

5. Reactive transport modelling

5.1 Model description

To investigate the formation of the Fe and S enrichments in the selected core intervals of the Joffre Member (Fig. 1) a reactive transport model was applied. The model describes the mass balance of 6 dissolved and 7 particulate species (Table S3) and is a modified version of that of Lenstra et al. (2018) based on Wang and Van Capellen (1996), extended here to include the formation of magnetite (Fe_3O_4). The model domain consists of a one-dimensional grid of 1000 evenly distributed cells that captures the interval from the sediment-water interface to a depth of 100 cm. All chemical species are subject to biogeochemical reactions (Table S4). Solids and solutes are transported by sediment accumulation. Solutes are additionally transported by molecular diffusion (Wang and Van Capellen, 1996; Boudreau, 1997).

The generic mass conservation equations for solids and solutes are described by Eq. 1 and 2;

$$(1-\phi)\frac{\partial C_s}{\partial t} = -(1-\phi)\mathrm{v}\frac{\partial C_s}{\partial z} + \Sigma R_s \qquad \text{Eq. 1}$$

$$\phi\frac{\partial C_{aq}}{\partial t} = \phi \mathrm{D}'\frac{\partial^2 C_{aq}}{\partial z^2} - \phi \mathrm{u}\frac{\partial C_{aq}}{\partial z} + \sum R_{aq} \qquad \text{Eq. 2}$$

$$D' = \frac{D_m}{(1-2\ln\ )} \qquad \text{Eq. 3}$$

where C_s is the concentration of solid species (mol L^{-1}), C_{aq} is the concentration of dissolved species (mol L^{-1}), t is time (yr), ϕ is the sediment porosity, v and u are the advective velocities of solid and dissolved species (cm yr^{-1}), respectively. Variables v and u were described by a depth-dependent function to account for changes in porosity (Meysman et al., 2005). The distance from the sediment-water interface is z (cm). D' is the diffusion coefficient of dissolved species (cm^2 yr^{-1}), corrected for tortuosity in the porous medium (Eq. 3 in Boudreau, 1996a) and ambient temperature and salinity. ΣR_s and ΣR_{aq} are the net rates of each chemical reaction (Table S4) for solid and dissolved species.

Porosity (ϕ) is described by Eq. 4 to account for sediment compaction (Boudreau, 1996a),

$$\phi(z) = \phi_{\infty} + (\phi_0 - \phi_{\infty})e^{-\frac{z}{\gamma}} \qquad \text{Eq. 4}$$

where ϕ_0 is the porosity at the sediment-water interface, ϕ_{∞} is the porosity at depth and γ is the porosity attenuation factor/e-folding distance (Table S5).

The model code was written in R with the use of the marelac geochemical dataset package of Stoetaert et al. (2010). To calculate the transport, the R package Reactran was used (Stoetaert et al., 2012). The set of ordinary differential equations was solved numerically with the Lsode integrator algorithm (Petzhold, 1983).

Zero gradient boundary conditions were applied to the base of the model domain for all chemical species to avoid an influence of the lower boundary conditions. Reaction parameters were mostly taken from literature or estimated using existing parameter ranges (Table S6). If these were not available, or no fit to the data could be obtained with existing ranges, parameters were constrained by fitting the model to the measured data.

In the model, reactions are divided in primary redox reactions and other biogeochemical reactions (Table S4). The succession of oxidants during organic matter degradation (Froelich et al., 1979) is described by means of Monod kinetics (Boudreau, 1997) (Table S7). This means that the oxidant with the highest metabolic free energy yield is preferentially used until it becomes limiting and the oxidant with the next highest energy yield is used (Wang and Van Capellen, 1996; Boudreau, 1996b). Respiratory reactions occur where $Fe(OH)_3$ and SO_4^{2-} serve as electron acceptors and finally organic matter is subject to methanogenesis (Reed et al., 2001; Lenstra et al., 2018) (Table S7). In the model, oxidation of CH_4 is possible with $Fe(OH)_3$ and SO_4^{2-}. Dissolved inorganic carbon in the model is calculated as the sum of the carbon in CO_2 and HCO_3^{2-}, which is produced or consumed by modeled reactions (Table S7).

In the model, Fe oxides are assumed to consist of fractions with different crystallinities, which affect their reactivity towards organic matter, H_2S and CH_4 (Table S3). A highly reactive fraction (α), a less reactive fraction (magnetite) and a refractory fraction (γ) were included. Magnetite is resistant to microbial iron reduction (Lovely and Phillips, 1986; Kostka and Nealson, 1995) and has not been shown to be reactive towards CH_4. Therefore, only the α fraction of the Fe oxides is susceptible to reductive dissolution linked to degradation of OM and the oxidation of CH_4.

Magnetite can form both biotically and abiotically, where the biotic formation of magnetite has been shown to be coupled to microbial dissimilatory iron reduction (Lovley et al., 1987; Lovley, 1991). Magnetite formation in our model therefore occurs via two pathways. (1) the kinetic reaction between $Fe(OH)_3$ and Fe^{2+} (R14) and (2) the reaction between $Fe(OH)_3$ and Fe^{2+} coupled to the rate of dissimilatory Fe reduction in the sediment (R15).

5.2 Transient scenario

We based the sedimentation rate on the U/Pb results, which indicate an average compacted rate of ca. 1 cm/kyr (Fig. 1; Fig. S9), consistent with a precession origin (11 kyr) for the ca. 10 cm thick Knox cyclothems. Assuming a porosity of 0.95, the sedimentation rate at the sediment-water interface in the model is 0.02 cm yr^{-1} (Table S7). Bottom water concentrations of solutes are based on literature while fluxes of solids towards the sediment-water interface are constrained by the XRF records (Table S8). Prior to our transient scenarios, the model was run to steady state for 17.000 years with the boundary conditions at the sediment-water interface as given in Table S8.

5.3 First scenario: varying OM and constant high Fe input

In our first transient scenario, we tested whether the Fe and S profiles (Fig. 1), determined by XRF core scanning, could form by enhancing the organic matter deposition. In this scenario a constant flux of Fe oxides to the sediment water interface and constant bottom water Fe^{2+} is assumed (Table S8). The organic matter flux during the deposition of the green mudrock layer was increased to 4.3 μmol cm^{-2} yr^{-1} for a period of 4 kyr (Fig. S11). In this scenario, the total organic carbon content at the sediment water interface increased from ca. 0.03 to 1.8 wt%.

At T1, before the enhanced deposition of organic matter (Fig. S1), ca. 98% of organic matter is oxidized through Fe oxide and SO_4^{2-} reduction. Rates of methanogenesis are negligible. The low rates of Fe oxide reduction lead to low concentrations of Fe^{2+} in the porewater and there is no accumulation of H_2S and CH_4 in the porewater. The presence of dissolved Fe^{2+} leads to formation of magnetite in the sediment.

At T2, during the enhanced deposition of organic matter (Fig. S11), the relatively high organic matter input leads to enhanced sulfate reduction and methanogenesis and subsequent formation of H_2S and CH_4. The high deposition of organic matter and continued input of Fe oxides leads to high rates of Fe oxide reduction and high Fe^{2+} concentrations in the porewater (up to 400 μmol L^{-1}). The high porewater Fe^{2+} concentrations in the presence of H_2S production lead to the formation of Fe sulfides in the organic-rich layer (as shown as total S, S_{tot}, in Fig. S12). Additionally, there is enhanced magnetite formation on the edges of the green mudrock layer.

At T3, after the enhanced deposition of organic matter (Fig. S11), the organic-rich layer is buried until ca. 40-60 cm depth. The presence of organic matter in this layer leads to SO_4^{2-} reduction and the release of minor amounts of H_2S to the porewater (<0.02 μmol L^{-1}). Within the green mudrock layer, the formation of Fe sulfides is limited by the formation of H_2S and dissolved Fe^{2+} can diffusive upwards and downwards where it forms magnetite along the edges of the green mudrock layer.

In this first scenario, only a single broad peak of FeS_x (i.e. S_{tot} in Fig. S12) is formed in the middle of the organic matter-rich depth interval, which contrasts with the narrow double S peaks observed in the core record (Fig. 1). In the model, the high concentrations of Fe^{2+} in the porewater and bottom water do not allow H_2S to accumulate and form FeS_x on the upper and lower side of the green mudrock layer. Additionally, organic matter is mostly oxidized by Fe oxides, thereby limiting SO_4^{2-} reduction and subsequent H_2S production in the sediment. To form the observed characteristic S profile with two narrow peaks, it thus appears essential to impose a significant decline dissolved Fe^{2+} in the porewater. To reach low concentrations of dissolved Fe^{2+} in the porewater during the deposition of the green mudrock layer, both the Fe oxide deposition at the sediment water interface and the bottom water Fe^{2+} concentration need to strongly decline.

5.4 Second updated scenario: strong decoupling of Fe and OM

To test our hypothesis we applied a second transient scenario that included the same temporal trend in organic matter input (Fig. S1) but we now prescribed a lower Fe oxide input, which we set at ca. 1% of the baseline scenario, and decreased the bottom water Fe^{2+} concentrations to 0 μmol L^{-1} (Fig. S13).

At T1, before the enhanced deposition of organic matter (Fig. S13), the low organic matter content leads to low rates of Fe oxide reduction and low concentrations of Fe^{2+} in the porewater (Fig. S14). There is negligible SO_4^{2-} reduction and no accumulation of H_2S and CH_4 in the porewater. The presence of dissolved Fe^{2+} leads to the formation of magnetite.

At T2, during the enhanced deposition of organic matter (Fig. S13), the relatively high organic matter content leads to enhanced SO_4^{2-} reduction and subsequent production of H_2S. In contrast with the previous scenario, H_2S can accumulate in the porewater to concentrations of ca. 4 μmol L^{-1} and diffuse upwards and downwards. As a result, H_2S meets Fe oxides and dissolved Fe^{2+} released from Fe oxide reduction in the deeper sediment, which subsequently leads to the formation of Fe sulfides on the lower boundary of the green mudrock layer. In contrast with the previous scenario there is a strong enrichment of magnetite at the bottom of the green mudrock layer.

At T3, after the enhanced deposition of organic matter (Fig. S13), the organic-rich layer is buried until ca. 40-60 cm depth. The relatively high organic matter content in the green mudrock layer leads to sulfate reduction and continued production of H_2S. The upward and downward diffusion H_2S leads to the formation of a peak in total S (Fe sulfides) at the top and bottom of the green mudrock layer.

Supplementary Text

Text S1. Geological background

The Hamersley Basin extends over ca. 500 km in WNW-ESE direction on the Pilbara Craton in Western Australia (Fig. S1a). The late Neoarchean to early Paleoproterozoic Hamersley Group comprises a ~1.5 km thick continental margin sediment succession characterized by the abundance of (banded) iron formations interstratified by carbonate and shale units (Fig. S1b). The Joffre Member forms the second and thickest BIF unit (ca. 350 m average) of the Brockman Iron Formation (Fig. S1b). Our study focuses on the Joffre Member as exposed in diamond drill-core DD98SGP001 (22°03’29.9”S 116°50’06.0”E) drilled at Silvergrass (Fig. S1a), which intersects well-preserved strata of the Joffre, Whaleback Shale and Dales Gorge Member of the Brockman Iron Formation from 87.7 m to 450.5 m depth (Fig. S1c).

Depositional setting

The laterally extensive iron formations of the Hamersley Group are classically interpreted as being deposited in a continental shelf environment (Trendall and Blockley, 1970; Morris and Horwitz, 1983) during sea level high-stands (Simonson and Hassler, 1996), given their frequent interstratification with organic-rich shales and carbonates that are considered shallower water equivalents (Klein and Beukes, 1989; Beukes et al., 1990; Simonson and Hassler, 1996). However, a deeper-marine basin plain setting has later been proposed on the basis of high energy features (carbonate breccia and possible distal turbidite structures) in the shale 'S' macrobands of the Dales Gorge Member (Krapež et al., 2003; Pickard et al., 2004). Absence of current- or wave-generated structures in BIF indicates deposition below storm wave base (150 – 200m), but shallow enough for carbonate deposition and preservation (i.e. above the carbonate compensation depth). Thus, BIF are typically considered as relatively deep-marine and could have been deposited at several hundreds of meters depth.

No paleo-shoreline is preserved in the Hamersley area, but the presence of large carbonate olistoliths in the middle to upper Joffre Member in the Mindy area (Kepert, 2002) suggest deposition proximal to a slope (shelf-slope break) located in the north, and the presence of a carbonate reef along certain parts. A well-defined carbonate platform to basin transition is preserved in the time-equivalent Griqualand West-Transvaal Basin in South Africa, suggesting the Kuruman IF was deposited in a continuous succession from the shelf to deeper basin during platform drowning (Beukes and Klein, 1990; Beukes and Gutzmer, 2008). Striking litho- and cyclostratigraphic similarities between the Dales Gorge Member of the Brockman IF and the Kuruman IF (Cheney, 1996; Martin et al., 1998; Beukes and Gutzmer, 2008; Lantink et al., 2019) combined with paleomagnetic data (de Kock et al., 2009) suggest that these BIFs may have been deposited in a single large basin, or along a contiguous basin margin, connected to the open ocean.

Text S2. Cyclostratigraphic observations at Joffre Falls and in DD98

The Joffre Member is characterized by two main scales of regular bedding, which were first described in Trendall (1969) and Trendall and Blockley (1970) from the remarkable outcrops in Joffre Gorge and downstream of Joffre Falls in Karijini National Park (Fig. S1a). At this locality, Trendall noted a prominent "rhythmic appearance of thin stilpnomelane-rich shale bands at intervals of 2 to 5 foot" and a smaller-scale "cyclic alternation… just over 3 inches" within the interstitial BIF intervals. See also Figs. 19B-C in Trendall and Blockley (1970).

In a parallel study focused on Joffre Falls (*see Chapter 4*), we present results of time series analysis demonstrating a cyclical origin for these two scales of alternations described by Trendall, with periodicities / thicknesses around ~85 and ~10 cm. This cycle hierarchy (~1 : 8 – 1 : 9) is consistent with the expected ratio between the periods of the short eccentricity and climatic precession cycles around that time given that, due to a shorter Earth-Moon distance, the period of climatic precession must have been much shorter than the present-day ~21 kyr average, while the period of short eccentricity (~100 kyr average) is thought to have remained largely stable in deep time (Laskar et al., 2011). More specifically, the precession : short eccentricity ratio must have been larger than 1:7, given the empirical ~14 kyr average value estimated for climatic precession based on cyclostratigraphic analysis of 1.4 Gyr old sedimentary rocks (Meyers and Malinverno, 2018), and could have been ~1:9 given a precession period of ~11-12 kyr at 2.5 Ga as calculated by Berger and Loutre (1994) and Waltham (2015).

In core DD98SGP001 from Silvergrass, which is located 150 km to the west of Joffre Falls (Fig. S1a), we noted a similar regular expression of Knox cyclothems in large parts of the Joffre stratigraphy. These correspond to the rhythmical "chert-BIF" and "chert-mudrock" couplets mentioned in Pickard (2002). The Knox cyclothems in the DD98 core have a somewhat different lithological character than at Joffre Falls (see Fig. 19B in Trendall and Blockley, 1970) which may be partly due to the absence of surface weathering. In addition, a larger-scale variation is visible, manifested by the occurrence of thick stilpnomelane lutites (Fig. S4) and ferric oxide abundance (Fig. S8) that is equivalent to the 85 cm thick stilpnomelane-BIF cyclicity observed in the field.

Text S3. Lithological description Knox cyclothem

3.1 Basic alternation

The basic structure of the Knox cyclothems as manifested in the J45de and J60d core intervals consists of a 1) greenish mudrock layer (0.5 – 1 cm thick) with 2) laminated iron oxide either below (J60d) or on both sides (J45de), which together alternate with 3) laminated chert. In the XRF data, this basic alternation is indicated by regular prominent peaks in detrital elements (Al, Ti, Zr, Rb) and K wt% (Fig. 1b) that are preceded (or bound) by 'plateaus' of high Fe concentrations, alternating with Si (Fig. 1d-e; Fig. S7). The alternations in J45de are representative of cherty 'BIF-type' Knox cyclothems and are generally 2-3 times thicker than in the alternations in J60d, which are representative of 'shale carbonate-type' cyclothems, which contain much thinner chert layers.

1) Mudrock layers are composed mainly of ferrous aluminosilicates, including stilpnomelane (an Fe, Al, K-bearing metamorphic clay mineral), and carbonate as indicated by the peaks in Ca and Mn. They have a homogenous appearance, showing no obvious internal lamination or grading textures. In J60d, the mudrock layers are split into two parts by a distinct carbonate-rich band with a sharp magnetite layer at the top and pyrite laminae in the middle (see also Text S3.2). In J45de, this separation is less well developed, but the mudrock layers also show a darker greenish-brown base and a paler

grey, more carbonaceous top that appears equivalent to the carbonate-rich zone in the mudrock layers of J60d.

2) We have defined the iron oxide layers as the intervals composed of densely spaced magnetite and hematite laminae ("microbands") that immediately precede the mudrock layers. In the BIF-type cyclothems in J45de, a second iron oxide layer also occurs systematically on top of the mudrock layer. The iron oxide layers contain a fair amount of carbonate and aluminosilicate and typically reveal a minor extra K peak at the base of the lower iron oxide layer as well as one at the top in case an upper iron oxide layer is developed (Fig. 1d-e; Fig. S7).

3) The chert layers are predominantly composed of microcrystalline quartz and are carbonate-poor. Beige chert is composed of widely spaced microbands of dusty hematite; blue colours indicate a significant contribution of riebeckite (NaFe-silicate). "Zebra" chert constitutes microbanded chert alternating with relatively thin (< 0.5 cm) magnetite mesobands. The thicknesses of the chert layers may vary considerably between successive Knox cyclothems depending on the addition /absence of blue riebeckite chert (see for example Fig. S4b), or alternatively, chert layers may be completely absent (Figs. S4 and 7).

3.2 Thin laminae

Thin (< 1mm) shiny magnetite enrichments are systematically developed around the green mudrock layers: at the top (J45de) or within the upper part (J60d) and at the base (J45de and J60d). The horizons or laminae have a wavy, fluid-like appearance and may cross-cut the observed general bedding (Fig. 1d-e; Fig. S2-3, 10). In the Fe wt% record of J45de they are represented by narrow Fe enrichments at the base and top of the Fe minimum that corresponds to the mudrock layers; in J60d, the upper Fe peak is very prominent and sharp.

Secondly, thin bands of yellow to whiteish carbonate occur in between the magnetite laminae and mudrock layer, coinciding with sharp peaks in Ca, Mn and in J45de also in Ba. The horizons at the base are generally more diffuse and may show mottling textures (Fig. S2), whereas they are generally much thinner and more sharply defined in the top part of the mudrock layer, in particular in J60d.

Thirdly, narrow and often double pyrite horizons are noticeable: one in the upper part of the green mudrock layer, either below (J45de) or above (J60d) the white carbonate; and one at the base, in between the lower magnetite and carbonate bands. In the XRF data these pyrite layers are manifested as well-defined, double peaks in the S profile of 0.5 – 2 wt %. In the alternations of J60d the lower peak is generally much weaker.

Fourthly, distinct yet somewhat more irregularly distributed P enrichments are visible. The largest and sharpest P enrichments are typically located either just below or within the lowermost part of the mudrock layers, but more moderate and broader P enrichments are also observed in the middle part of the mudrock. The P peaks seem to follow the peaks in Ca, K and/or Fe.

Text S4. Extended discussion Milankovitch interpretation

The MTM spectra of the K wt% records of J45de and J60d reveal a dominant cyclicity at periodicities of approximately 10 (7 – 13) cm and 4.5 cm, respectively, exceeding 95 – 99 % confidence limits (Fig. 1c). Similar periodicities are found based on MTM analysis on the two ferric oxide abundance records (Fig. S8c-d) which span two longer intervals around the shorter intervals J45de and J60d, respectively (Fig. S8a-b). In addition, these longer records demonstrate the presence of a larger scale cycle, which modulates the amplitude of the Knox cyclothems, having an average wavelength of 88 cm and 41 cm, respectively (Figs. S8c-d). These results indicate a ~1:9 thickness ratio between the wavelengths of the small- and larger-scale cyclicity, for both the J45de and J60d intervals. This is the same cycle hierarchy that was observed at Joffre Falls (Text S2) and is consistent with a much-reduced climatic precession: short eccentricity ratio around 2.5 Ga due to a reduced Earth-Moon distance (26, 89). Specifically, these two model studies estimated a climatic precession period of 11-12 kyr, which equally corresponds to a ~1:9 period ratio with the stable short eccentricity cycle (~100 kyr).

Our new high-precision TIMS U-Pb ages allow for a significantly better estimation of the depositional rate of the Joffre Member than previous estimates (Pickard, 2002; Trendall et al., 2004). The depositional rate model suggests an upward increase in the average rate from 4 to 15 m/Myr for the lower 200 m of Joffre Member in the DD98 core (Fig. 1a; Fig. S9). The 4 m/Myr rate, which applies to the lowermost part from which interval J60 was selected, converts the ~4.5 cm thickness of the cyclothems in this interval to a period of ~11 kyr. The overall ~10 m/Myr average rate suggests a period of ~10 kyr for the ~10 cm thick Knox cyclothems in interval J45de. Again, these periodicities are very consistent with the precession period modelled by Berger and Loutre (1994) and Waltham (2015) for 2.5 Ga, i.e. 11-12 kyr. Therefore, the consistency between the cyclostratigraphic and the U-Pb results strongly argues for a climatic precession origin of the Knox cyclothems.

Text S5. Extended discussion early diagenetic interpretation

Strong decoupling of Fe and OM essential to explain the Fe and S patterns

The evaluation of the different RTM scenarios (Methods 5.3-5.4; Figs. S11-14) shows that a strong decoupling of Fe oxide and OM is essential to explain the formation of double S peaks, which require the build-up of dissolved H_2S within the buried OM-rich sediment. This subsequently leads to two separate horizons for FeS_x precipitation: one below and one above the OM-rich layer, at the reaction fronts between H_2S and Fe^{2+}. Consistent with the observations of J45de (Fig. 1d), our model scenario also shows how Fe enrichments in the form of magnetite are formed just below and above the FeS_x peaks and the resultant minimum in the total Fe profile. These magnetite laminae originate from the reaction between FeOx with Fe^{2+}, liberated from FeOx reduction in the sediment immediately above or below the sulfidic zone in the sediment (see also Methods 5.1).

We note that the scenario with the almost complete depletion of bottom water Fe^{2+} and Fe oxide deposition, which is required to form the double S peaks in the model, is an end-member scenario. For example, in J60d the lower S peaks are typically less well developed. This suggests a more gradual or asymmetric decline in the deposition of Fe oxides and bottom water Fe^{2+} concentrations, or a change in the amount and timing of organic matter deposition. In some cases, the lower S peak is even completely absent (Fig. S7). However, it is important to emphasize that also for these cyclothems exhibiting a single S peak, the peaks are still sharp and occur near the top of the minimum in the total Fe profile. This suggests that no reaction front was developed between Fe^{2+} and H_2S at the base and only at the top. Yet the diagenetic process did not fundamentally differ from that interpreted for the formation of double S peaks: it involved the build-up of porewater H_2S. We therefore argue that a periodic strong lowering of the Fe oxide deposition and bottom water Fe^{2+} concentrations was a consistent feature of the precession forcing, despite the variability in the development of double S peaks between successive cyclothems.

Preliminary interpretation of the Ca enrichments

In addition to the characteristic S patterns, the Ca enrichments (Fig. 1; Text S3) seem in further support of our interpretation of dissolved H_2S build-up within the mudrock porewaters during burial. Firstly, the systematic arrangement of the sharp, double Ca peaks in the cyclothems of J45de, either just below or above the S peaks (Fig. 1d), is compatible with preferential carbonate precipitation just outside the sulphidic zone, where much higher alkalinity production and carbonate saturation is expected in association with iron reduction (Coleman, 1993; Middelburg et al., 2020). Secondly, the high Ca concentrations associated with the carbonate laminae suggests the enhanced incorporation of Ca^{2+}, which is expected to occur in Fe^{2+}-poor waters (Sumner and Grotzinger, 1996).

Preliminary interpretation of the P enrichments

The P enrichments in Figure 1 (1-3 wt%) are difficult to explain by input of organic P only, when assuming an input of ~2 wt% Corg (Methods 4) and a C:P ratio of the organic matter of 106:1 (Redfield, 1934). This, combined with the sharpness of the peaks, suggests the additional input of non-organic and non-detrital i.e. reactive phosphate. For instance, such additional sources could have comprised the input of Fe(II) phosphate minerals (e.g. vivianite) and Fe (hydr)oxide-bound P from the seawater, prior to the establishment of an Fe^{2+}-depleted water column; or direct diffusive transport of dissolved HPO_4^{2-} from the water column into the sediment. However, the irregular distribution of the P peaks, exhibiting one or several sharp enrichments just below and/or within the mudrock layer, or the complete absence of a P peak (Fig. 1d-e; Fig. S7), indicates a rather complex early diagenetic history. Their variable coincidence with peaks in K, Ca and/or Fe suggests different degrees of diagenetic P release and incorporation into authigenic phases such as carbonate fluorapatite (Ruttenberg and Berner, 1993) or vivianite (Egger et al., 2015) and, possibly, re-adsorption onto Fe (hydr)oxides (Slomp et al., 1996) where these persisted. To properly determine the source of the P enrichments requires a more thorough evaluation, which will be discussed in a follow-up study.

Text S6. Extended discussion conceptual climate model

Monsoonal vs. glacio-eustatic control

Monsoons are low-latitude weather systems that are linked to the seasonal movement of the ITCZ and strongly respond to precession forcing, with eccentricity modulating the precession amplitude (Kutzbach et al., 2008; Ruddiman, 2001). The reason behind this precession and eccentricity dominance is that the (summer) monsoonal intensity is to a large part controlled by summer insolation, which at low- to mid-latitudes is dominated by precession. Maximum summer insolation, which occurs at times of precession minima for the NH and at times of precession maxima for the SH, results in the heating of continental landmasses, resulting in low pressure areas that attract moist-loaden air from the ocean, due to the atmospheric pressure difference between land and sea, resulting in an intensification of monsoonal precipitation (Kutzbach et al., 2008; Ruddiman, 2001). A similar hydrological response during deposition of the Joffre Member is therefore a logical first-order interpretation for the dominant imprint of precession- and eccentricity-related cycles, also because it is inferred that the Hamersley basin was located at relatively low southern latitudes around that time (Gumsley et al., 2017).

This monsoonal interpretation is in strong contrast with previous sea level models for the Hamersley BIFs (Bekker et al., 2010), which are based on density current structures identified in several ‘S’ bands of the regular BIF-S macroband alternations in the Dales Gorge Member (Krapež et al., 2003; Pickard et al., 2004). Although eustatic sea level variations may have been operative at the same time, the absence of a clear obliquity signal in the studied part of the Joffre Member does not provide support for a glacio-eustatic instead of monsoonal control. Moreover, density currents can equally develop due to increased continental runoff, by creating delta slope instability, in response to precession-forced climatic changes and enhanced terrigenous input (Postma et al., 1993). We also did not find any indication for a turbiditic origin of the thin mudrock layers of the Knox cyclothems (Text S3), while their elevated clay fraction, which we interpret as increased sediment-laden runoff, must indicate the lateral supply of terrigenous material. However, it is difficult to determine to what degree this terrigenous material may have originated from re-sedimentation of more proximal shelf settings, or settled directly from suspended river plumes introduced into the basin.

Phase relation

It is not possible to establish the phase relation between the precession-eccentricity forcing, the interpreted monsoonal response and the interpreted variations in primary productivity with any certainty in the absence of astronomical solutions and/or climate models at 2.5 Ga. However, a plausible scenario for the increase in continental discharge during deposition of the mudrock layers, which we inferred from the elevated clay and high P content, is that this was induced during periods of relatively 'wet' climatic conditions. Therefore, it seems logical to link the high productive periods to periods of intensified monsoonal circulation and summer monsoonal precipitation. Assuming that the Pilbara Craton was located on the southern hemisphere (41, 42), this would have occurred during precession maxima, and even more so during eccentricity maxima when the strength of the seasonal (summer) signal is enhanced. In this context, we hypothesize that the chert layers, which occur in the opposite part or phase of the Knox cyclothem, were deposited during relatively dry periods marked by low productivity during precession minima. Intriguingly, the sudden changes in thickness of the chert layers between successive cycles upon the addition of riebeckite-chert (Text S3.1; Fig. S3-4) could hint at an evaporative control.

Supplementary Figures

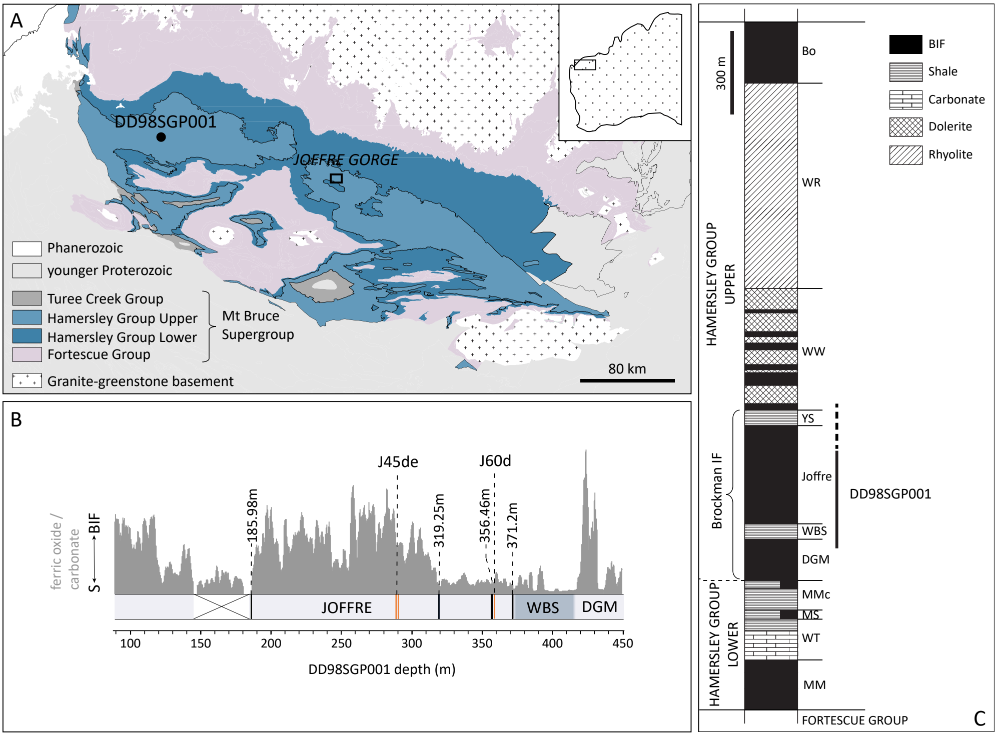
A
DD98SGP001
JOFFRE GORGE
Phanerozoic
younger Proterozoic
Turee Creek Group
Hamersley Group Upper
Hamersley Group Lower
Fortescue Group
Mt Bruce Supergroup
Granite-greenstone basement
80 km
B
ferric oxide / carbonate
S
BIF
185.98m
J45de
319.25m
J60d
356.46m
371.2m
JOFFRE
WBS
DGM
100
150
200
250
300
350
400
450
DD98SGP001 depth (m)
C
300 m
Bo
WR
WW
YS
Joffre
WBS
DGM
MMc
MS
WT
MM
FORTESCUE GROUP
HAMERSLEY GROUP UPPER
HAMERSLEY GROUP LOWER
Brockman IF
DD98SGP001
BIF
Shale
Carbonate
Dolerite
Rhyolite

Figure S1 (previous page). (**A**) Geological map of the Hamersley Basin on the Pilbara Craton in NW Australia with the location of core DD98SGP001 (22°03'29.9"S 116°50'06.0"E) and Joffre Gorge. Modified from the Geological Survey of Western Australia (GSWA) 2020, extracted from GeoVIEW.WA. (**B**) Generalized stratigraphy of the Hamersley Group and stratigraphic interval covered in DD98SGP001. It is not clear to what extent the top of the Joffre is included in the core (dotted line). MM: Marra (Mamba IF, WT: Wittenoom dolomite, MS: Mount Sylvia Formation, MMc: Mount McRae Shale, DGM: Dales Gorge Member, WBS: Whaleback Shale Member, Joffre: Joffre Member, YS: Yandicoogina Shale Member, WW: Weeli Wolli Formation, WR: Woongarra Rhyolite and Bo: Bolgeeda IF. Modified from Harmsworth et al. (1990). (C) Schematic overview of DD98SGP001 with positions of samples J45de and J60d and dated ash layers (this study) and Hylogger ferric oxide vs. carbonate abundance record. Note that there is fractured lithology in the 145 – 185 m depth interval leading to signal distortion. Stratigraphic boundaries are according to Pickard (2002).

Figure S2. Examples of regular Knox cyclothems in the D98SGP001 core. Arrows denote cross-cutting "fluid-like" laminae of magnetite, carbonate and pyrite pointing to early diagenetic reaction fronts.

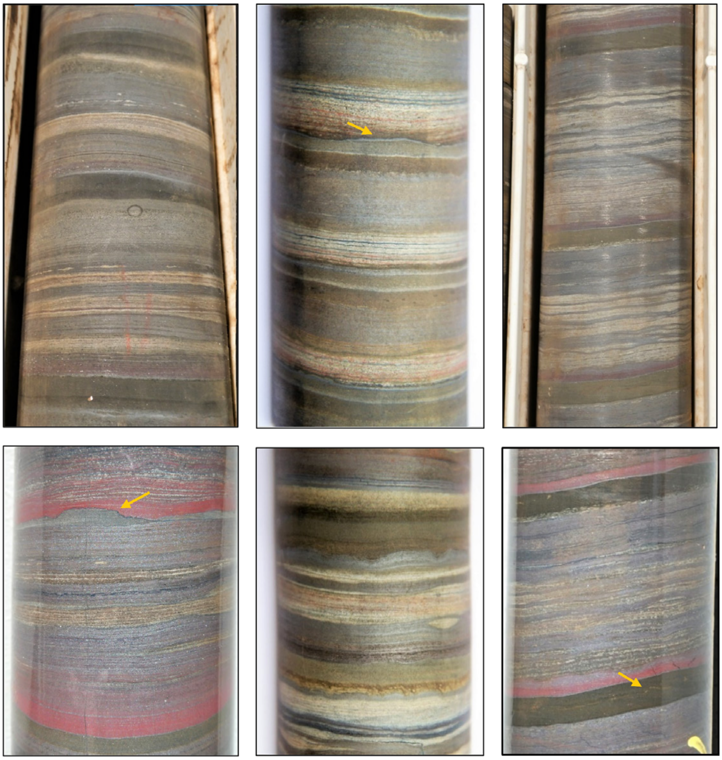

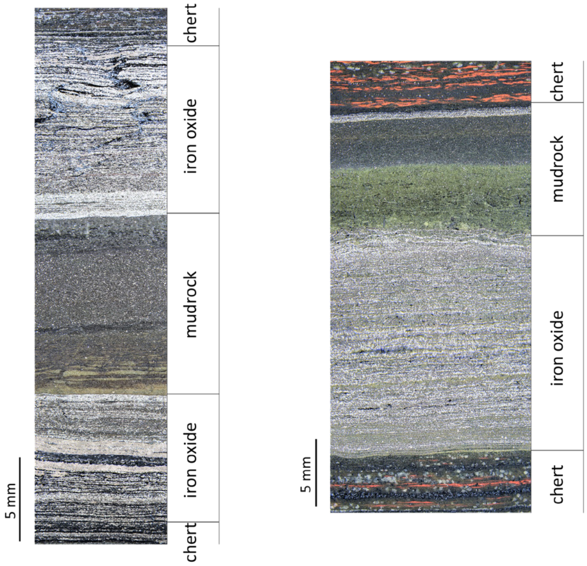
chert
iron oxide
mudrock
iron oxide
chert
5 mm
chert
mudrock
iron oxide
chert
5 mm

Figure S3. Polished half core sections showing the basic lithological structure of the Knox cyclothem for a cherty BIF-type (left) and shale carbonate-type (right).

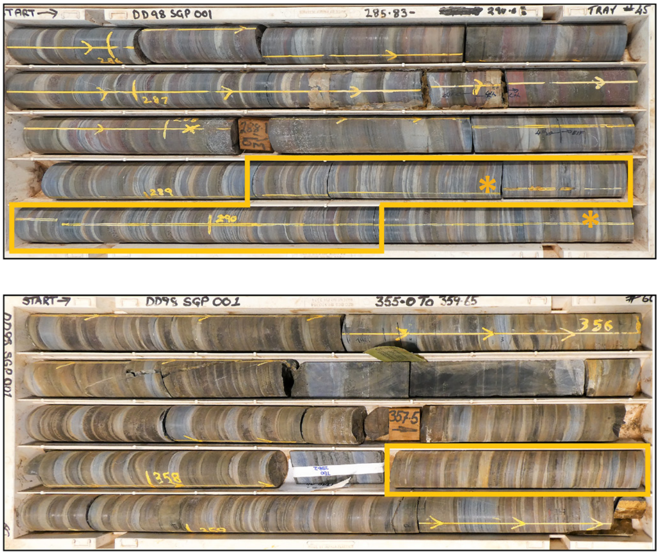
START
DD98 SGP 001
285.83
TRAY #45
287
289
290
START
DD98 SGP 001
355.0 TO 359.65
356
357.5
358

Figure S4. Photos of core boxes 45 (upper) and 60 (lower) with the selected intervals J45de and J60d, respectively, indicated by the orange rectangles. Asterixes in box 45 mark two succesive more prominent shales that represent the expression of the larger-scale ~88 cm cyclicity (see also Fig. S8a).

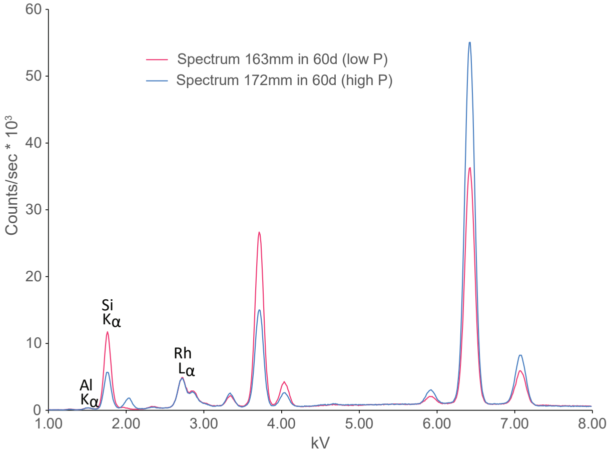

Figure S5. XRF spectra for a low- (red line) and high-phosphorus (blue line) sample from J60d at 10kV.

Figure S6. Comparison of the raw XRF intensity and ICP-OES concentration data for the target elements (K, Al, Fe, Ca, Mn, Ba, S and P). **Left**: direct comparison of the patterns to check visual alignment of the XRF slit positions and sawing lines. **Right**: x-y cross plots of intensity (counts per second) versus concentration with linear regression coefficient of determination (R^2) values. cps = counts per second.

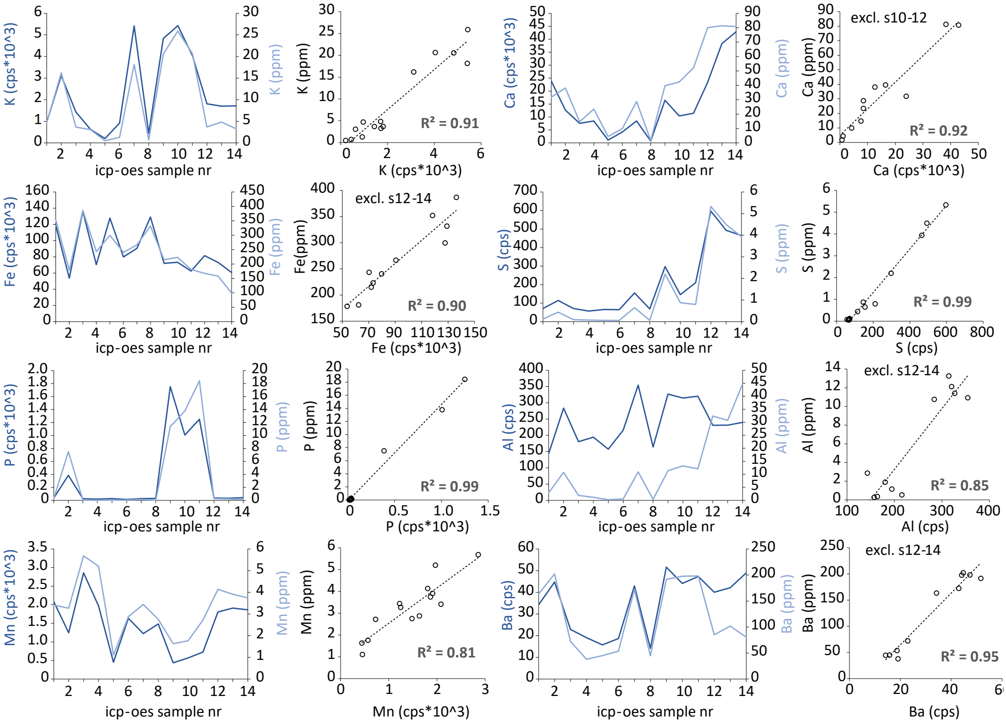

Figure S7. XRF records for core segments J45de and J60d. Concentration axes (calibrated weight %) are linearly scaled to the intensity axes (raw counts/sec). Green bands indicate the position of the K peaks.

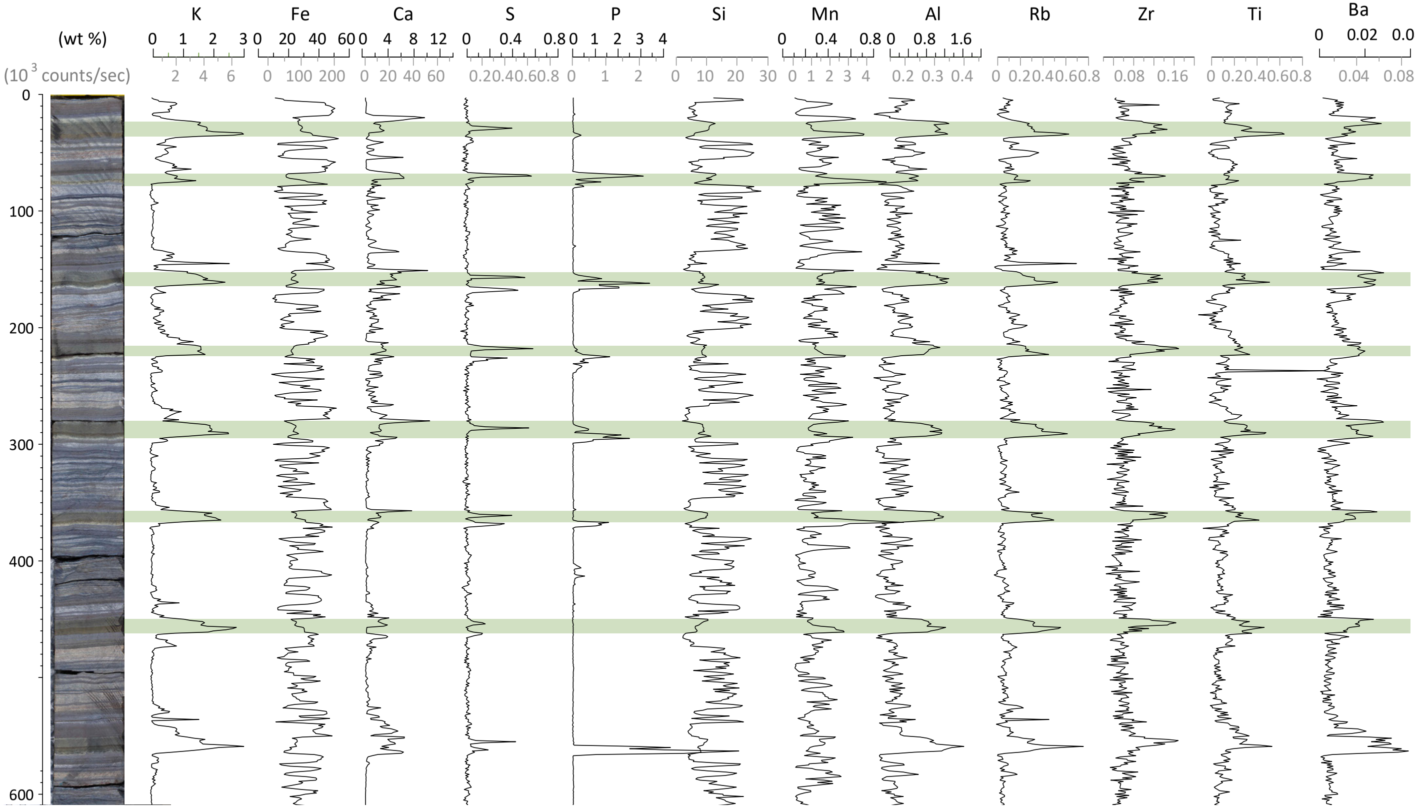

J45de 1/2

J45de 2/2

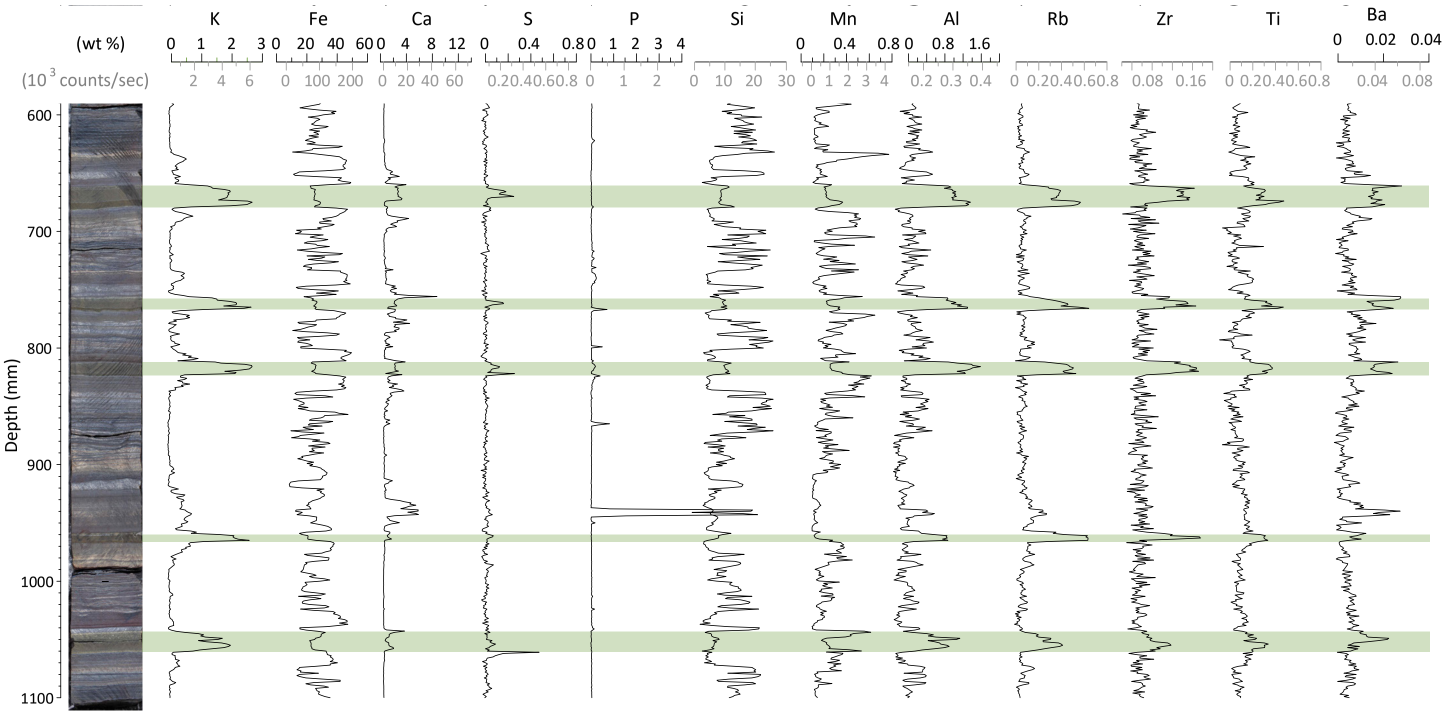
(wt %)
(10 3 counts/sec)
K
0 1 2 3
2 4 6
Fe
0 20 40 60
0 100 200
Ca
0 4 8 12
0 20 40 60
S
0 0.4 0.8
0.20.40.60.8
P
0 1 2 3 4
0 1 2
Si
0 10 20 30
Mn
0 0.4 0.8
0 1 2 3 4
Al
0 0.8 1.6
0.2 0.3 0.4
Rb
0 0.20.40.60.8
Zr
0.08 0.16
Ti
0 0.20.40.60.8
Ba
0 0.02 0.04
0.04 0.08
Depth (mm)
600
700
800
900
1000
1100

J60d

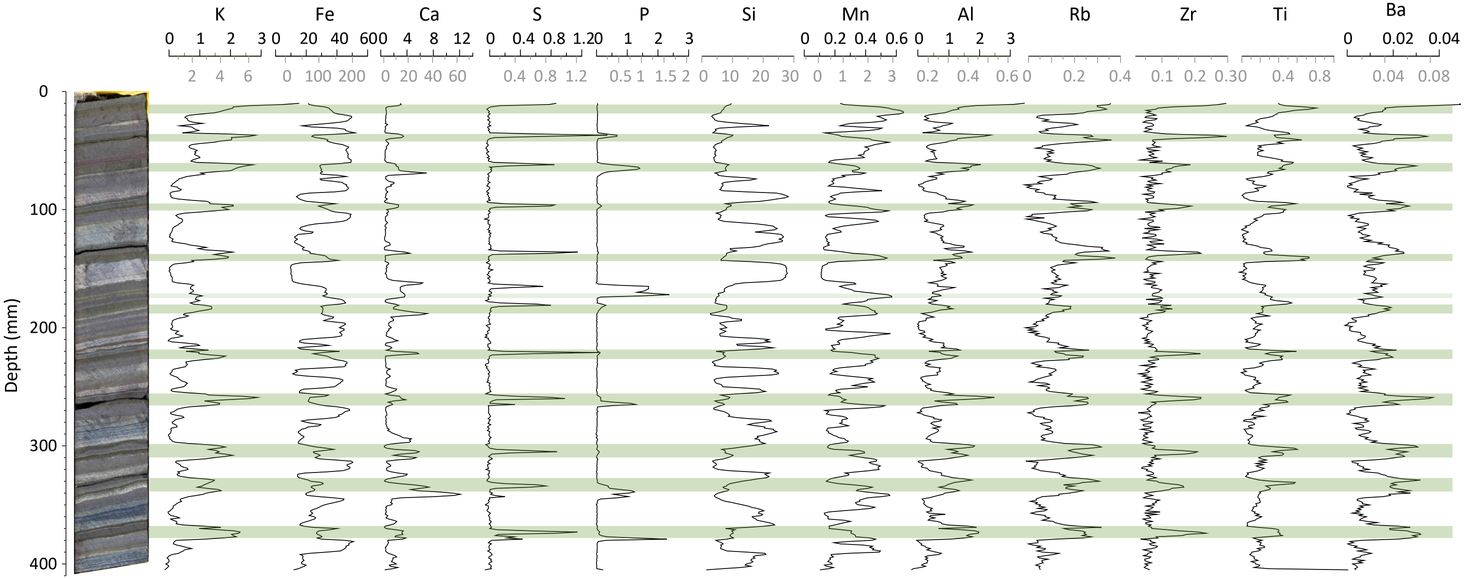
K
0 1 2 3
2 4 6
Fe
0 20 40 60
0 100 200
Ca
0 4 8 12
0 20 40 60
S
0 0.4 0.8 1.2
0.4 0.8 1.2
P
0 1 2 3
0.5 1 1.5 2
Si
0 10 20 30
Mn
0 0.2 0.4 0.6
0 1 2 3
Al
0 1 2 3
0.2 0.4 0.6
Rb
0 0.2 0.4
Zr
0 0.1 0.2 0.30
Ti
0.4 0.8
Ba
0 0.02 0.04
0.04 0.08
Depth (mm)
0
100
200
300
400

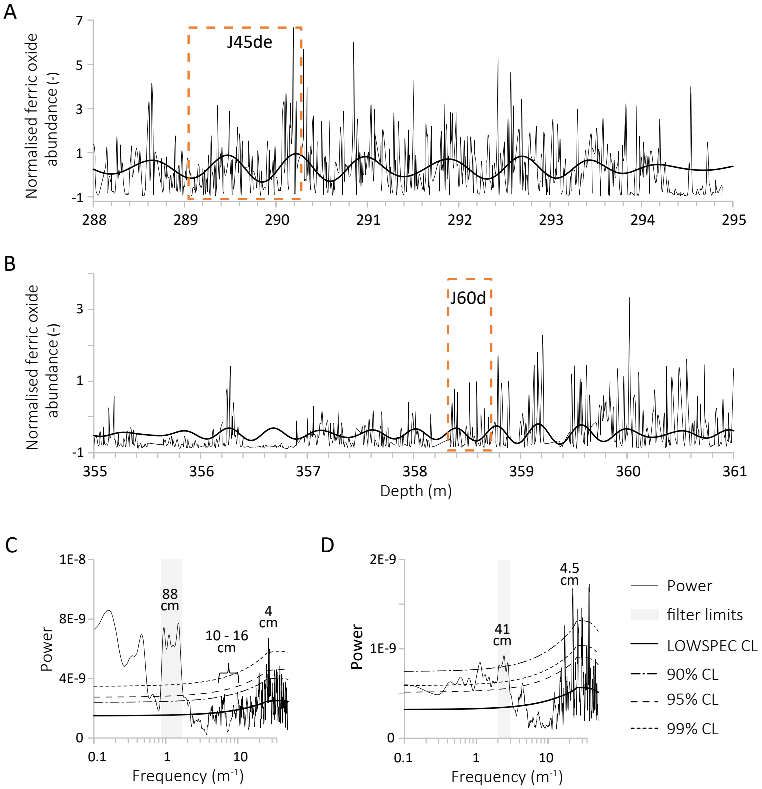

Figure S8. Time series analysis results for the Hylogger records from core DD98SGP001. (**A**, **B**) Normalized ferric oxide abundance (thin black line) showing the expression of both the small- (Knox) and larger-scale cycles. Bandpass filtered signals (thick black line) corresponding to the grey bands in (**C**, **D**), respectively. Orange dotted rectangles indicate the positions of intervals J45de and J60d. a, Depth interval 288 – 295 m; filter limits 0.6 – 1.167 m. (**B**) Depth interval 355 – 361 m; filter limits 0.35 - 0.5 m. (C, D) MTM power spectra of the records in (**A**, **B**)), respectively (1 cm interpolated; linear detrended) with LOWSPEC confidence levels. Peak labels 88 cm (**C**) and 41 cm (**D**) are the representative F-test peaks for the high power area that was targeted for bandpass filtering (in grey). The 10 - 16 and 4.5 cm peak labels indicate the approximate wavelengths of > 90 % significant peaks that are related to the small-scale (Knox) cycles. The strong 4 cm peak in c is a real harmonic resulting from the occurrence of double ferric oxide maxima per single Knox cyclothem, which is related to its quadripartite structure (i.e. chert - iron oxide – mudrock – iron oxide; Text S3).

Figure S9 (next page). U-Pb zircon ages and depositional rate. Upper panel: Concordia diagram showing the concordant high-precision U–Pb TIMS results and the calculated ages. The grey band represents the uncertainty on the Concordia curve due to the decay constant uncertainties. The ellipses represent the U–Pb isotopic data and 2σ uncertainty for individual chemically abraded zircon fragments, and the colours represent the different samples. The ^{207}Pb/^{206}Pb ages are given for each sample, either as a weighted mean or from an individual analysis, along with the depth in the DD98SGP001 core. MSWD, mean square of the weighted deviates. Lower panels: Depositional rate model with 97.5% confidence intervals, plotted as age versus depth in the DD98SGP001 core (left) and as depositional rate against age (right)

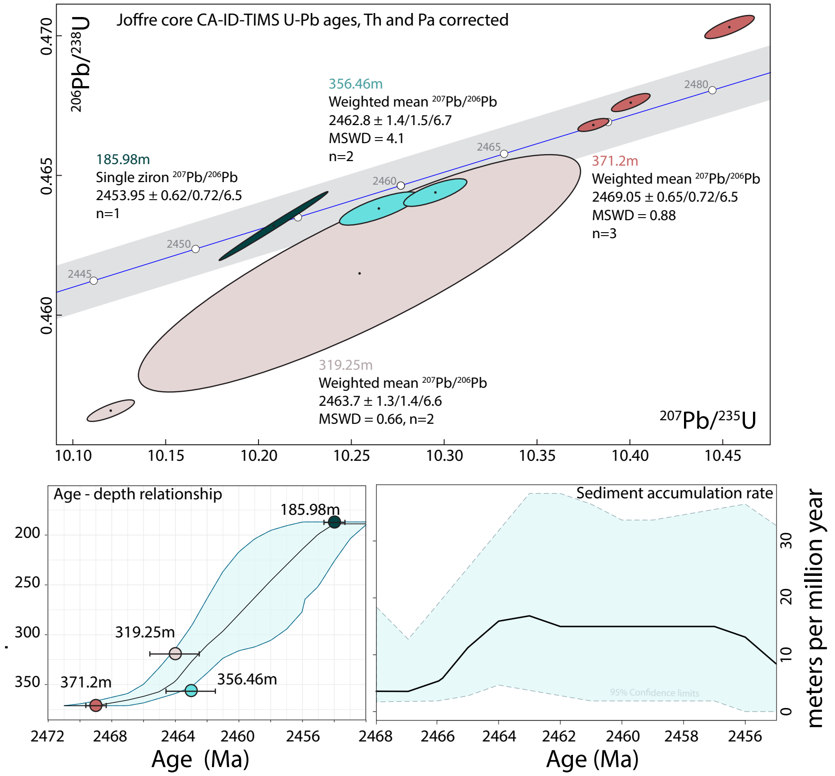

Figure S10. Close-ups of the mudrock layers from interval J60d and J45de (from Fig. 1d-e) with overlain records of Fe (grey lines) and S (white lines), respectively. Black horizontal bars denote the position and width (12 mm) of the XRF scanner.

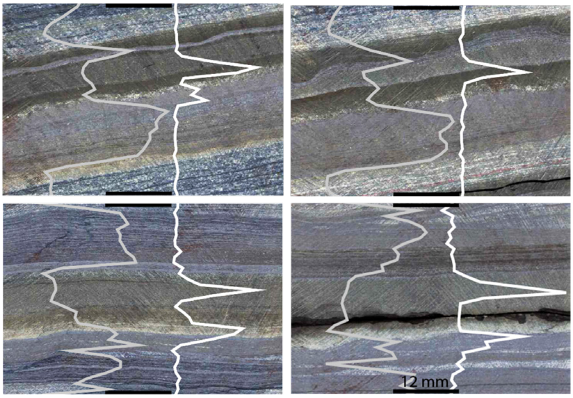

Figure S11. Transient scenario for organic matter input used in the reactive transport model in the first scenario. The different types of organic matter are denoted as α (highly reactive), β (less reactive) and γ (refractory). T1, T2 and T3 indicate the time points used in Fig. S12.

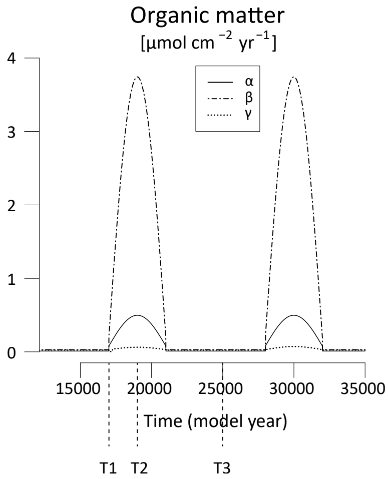

Figure S12. Modelled porewater (Fe^{2+}, SO_4^{2-}, H_2S and CH_4) and solid phase depth profiles (total Fe, magnetite and total S) for the first scenario for three time points during the modelled precession cycle: before (T1), during (T2) and after (T3) deposition of the organic matter-rich layer (Fig. S11). The grey shaded zones indicate the depth interval of enhanced organic matter deposition.

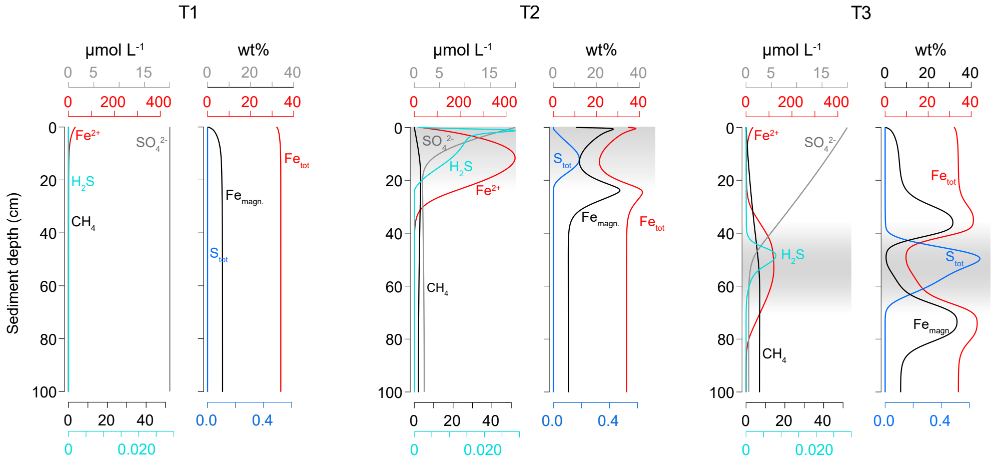

Figure S13. The transient scenario for input of organic matter and Fe oxides and the bottom water Fe^{2+} in reactive transport model in the second scenario. (**A**) The different types of organic matter are indicated as α (highly reactive), β (less reactive) and γ (refractory); (**B**) different types of Fe oxides α (highly reactive), magnetite and γ (refractory); and (**C**) bottom water Fe^{2+}. T1, T2 and T3 indicate the time points used in Fig. S14.

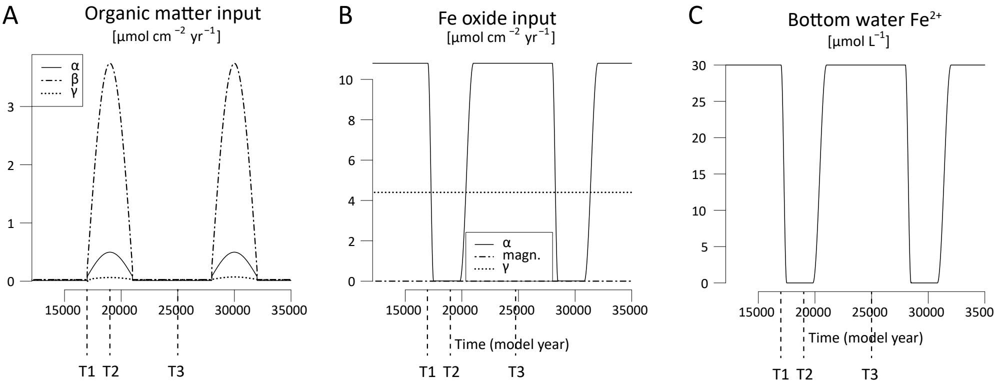

Figure S14. Modelled porewater (Fe^{2+}, SO_4^{2-}, H_2S and CH_4) and solid phase depth profiles (total Fe oxides, magnetite and total S) for the second scenario for three time points during the modelled precession cycle: before (T1), during (T2) and after (T3) deposition of the organic matter rich layer (Fig. S13). The grey shaded zones indicate the depth interval of enhanced organic matter deposition. From T1 to T2, the strong increase in sediment OM and decline in Fe oxides leads to build-up of H_2S from SO42- reduction in the porewater and the formation of an FeSx layer at the lower end of the OM-rich layer. Here, H_2S reacts with excess Fe^{2+} generated in the deeper sediment by ongoing reductive Fe oxide dissolution, in particular from the zone for which the initial Fe oxide input was still high while the OM flux had already increased, as well as with Fe oxides directly. In addition, excess Fe^{2+} generated in this transitional interval forms magnetite just below the FeSx layer, via a reaction with Fe oxides. When the deposition of Fe oxides and porewater Fe^{2+} increases again from T2 to T3, a second set of iron sulphide and magnetite layers is formed at the upper anoxic (sulphidic) – suboxic front.

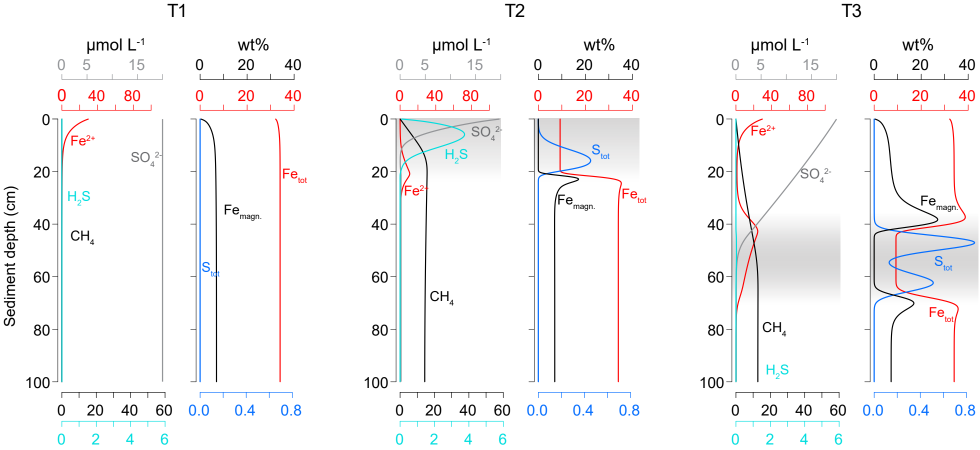

Supplementary Tables

Table S1. XRF core scanning settings.

Tube voltage	Current	Time analyzed	Filter	Element analyzed
10 kV	1.2 mA	15 sec	-	Mg(12) – Mn(25)
30 kV	0.9 mA	20 sec	Pd-thin filter	Fe(26) – U(92)
50 kV	1.0 mA	60 sec	Cu filter	Ba(56)

Table S2. ICP-OES data of the totally digested samples and reference materials. Values are reported in parts per million and represent the dry rock concentration. Values in grey italic are below the detection limit. The analytical accuracy is indicated by the bias (%) calculated from the deviation from the reference values of PACS-2 (high sulfur standard) and ISE921.

Sample	Al	Ba	Ca	Fe	K	Mn	P	S
J36c.27	2859	163	31783	351941	4711	3414	258	123
J36c.25	10754	202	38140	178523	16194	3271	7505	439
J36c.21	1900	72	14723	386664	3673	5683	*12*	89
J36c.20	1150	38	23502	243419	3077	5203	*13*	74
J36c.17	263	45	4461	299603	497	1109	*19*	59
J36c.13	538	54	9990	240578	1302	2879	*27*	57
J36c.8	10932	173	28742	266506	18150	3443	137	648
J36c.3	364	45	1751	331784	708	2752	*7*	63
J36c.43	11493	193	39687	210513	20794	1633	11441	2230
J36c.43 -duplo	11311	190	39586	219434	20335	1629	11323	2169
J36c.42	13258	198	42328	223016	25901	1764	13783	875
J36c.24	12128	198	52127	181088	20641	2722	18441	796
J57e.30	32210	85	80273	168284	3695	4143	270	5319
J57e.30 -duplo	32614	85	79741	167101	3677	4134	268	5351
J57e.19	30761	102	81333	158154	4837	3912	216	4495
J57e.8	44745	81	80763	98575	3269	3746	126	3937
PACS2	63042	951	21715	46042	12165	464	986	12975
ISE921	52974	545	43836	32843	17833	1197	1337	721
PACS2 acc. value	66200	-	19600	40900	12400	440	960	12900
ISE921 acc. value	56800	563	43000	31900	19100	1190	1400	702
RSD (± %)	1	1	0.5	3	2	0.2	1	2
Bias (%)	7	-	11	13	7	6	4	3

Table S3. Chemical species included in the model.

Species	Notation
Solid	
Organic matter [a]	$OM^{\alpha,\beta,\gamma}$
Iron oxide[b]	$Fe(OH)_3^{\alpha,\gamma}$
Magnetite	Fe_3O_4
Elemental sulfur	S^0
Iron monosulfide	FeS
Pyrite	FeS_2
Siderite	$FeCO_3$
Solute	
Sulfate	SO_4^{2-}
Methane	CH_4
Iron	Fe^{2+}
Hydrogen sulfide[c]	ΣH_2S
Dissolved inorganic matter	DIC

a: Chemical species consist of 3 types: reactive (α), less reactive (β) and refractory (γ)

b: Chemical species consist of 2 types: reactive (α) and refractory (γ)

c: Σ denotes that all species are included

Table S4. Reaction pathways and stoichiometry implemented in the model.

Primary redox reactions	
$OM^{\alpha,\beta} + 4a\ Fe(OH)_3^{\alpha} + 12a\ H^+ -> a\ CO_2 + 13a\ H_2O + 4a\ Fe^{2+}$	R1
$OM^{\alpha,\beta} + 0.5a\ SO_4^{2-} + a\ H^+ -> a\ CO_2 + 0.5a\ H_2S + a\ H_2O$	R2
$OM^{\alpha,\beta} -> 0.5a\ CO_2 + 0.5\ CH_4$	R3
Secondary and other reactions	
$2\ Fe(OH)_3^{\alpha} + H_2S + 4\ CO_2 -> 2\ Fe^{2+} + S^0 + 4\ HCO_3^- + 2\ H_2O$	R4
$2\ Fe_3O_4 + H_2S + 4\ CO_2 -> 6\ Fe^{2+} + S^0 + 4\ HCO_3^- + 2\ H_2O$	R5
$Fe^{2+} + H_2S -> FeS + 2\ H^+$	R6
$FeS + H_2S -> FeS_2 + 2\ H^+$	R7
$4\ S^0 + 4\ H_2S -> 3\ H_2S + SO_4^{2-} + 2\ H^+$	R8
$FeS + S^0 -> FeS_2$	R9
$SO_4^{2-} + CH_4 + CO_2 -> 2\ HCO_3^{2-} + H_2S$	R10
$CH_4 + 8\ Fe(OH)_3^{\alpha} + 15\ H^+ -> HCO_3^- + 8\ Fe^{2+} + 21\ H_2O$	R11
$Fe^{2+} + HCO_3^- -> FeCO_3 + H^+$	R12
$FeCO_3 + H_2S -> FeS + HCO_3^-$	R13
$2\ Fe(OH)_3^{\alpha} + Fe^{2+} + 2\ OH^- -> Fe_3O_4 + 4\ H_2O$	R14

Organic matter is in the form of $(CH_2O)a$.

α,β denote different fractions (i.e. highly reactive and less reactive).

Table S5. Environmental parameters used in the model.

Description	Symbol	Value or expression	Unit	Source
Porosity at the surface	ϕ_0	0.95	vol vol^{-1}	a
Porosity at depth	ϕ_∞	0.85	vol vol^{-1}	a
Porosity e-folding distance	γ	25	cm	a
Sediment density	ρ	2.65	g cm^{-3}	b
Temperature	T	4	°C	a
Salinity	S	35		a
Pressure	p	41.2	bar	a
Advective velocity of solids at depth	v	$\frac{F}{\rho(1-\phi_\infty)}$		-

Sources: (a) Model constrained; (b) Burdige (2006)

Table S6. Reaction parameters used in the model.

Parameter	Value	Unit	Source	Values in literature
k_α	0.03	yr^{-1}	b, c	0.05-1.62
K_β	0.0005	yr^{-1}	b	0.002-0.0086
$K_{Fe(OH)_3}$	65	µmol g^{-1}	b	65-100
$K_{SO_4^{2-}}$	1.6	mmol L^{-1}	b	1.6
K_1 (E4)	55	mmol^{-1} L yr^{-1}	b	55
K_2 (E5)	44	mmol^{-1} L yr^{-1}	a	
K_3 (E6)	4000	mmol^{-1} L yr^{-1}	b, c	100-14800
K_4 (E7)	3.15	mmol^{-1} L yr^{-1}	d	0.0003-3.15
K_5 (E8)	3	yr^{-1}	e	3
K_6 (E9)	0.0025	mmol^{-1} L yr^{-1}	d	0.001-7
K_7 (E10)	17	mmol^{-1} L yr^{-1}	e	10-120
K_8 (E11)	$2.1*10^{-6}$	mmol^{-1} L yr^{-1}	e	0-0.0074
K_9 (E12)	10	mmol^{-1} L yr^{-1}	a	
K_{10} (E13)	0.0004	mmol^{-1} L yr^{-1}	a	
K_{11} (E14)	0.01	mmol^{-1} L yr^{-1}	a	
K_{12} (E15)	100000	mmol^{-1} L yr^{-1}	a	

Sources: (a) Model constrained; (b) Wang and Van Capellen (1996); (c) Reed et al. (2011); (d) Egger et al. (2016); (e) Lenstra et al. (2018)

Table S7. Reaction equations implemented in the model.

Primary redox reaction equations	
$R_1 = K_{\alpha,\beta}\, OM^{\alpha,\beta} \left(\frac{[Fe(OH)_3]}{K_{Fe(OH)_3} + [Fe(OH)_3]} \right)$	E1
$R_2 = K_{\alpha,\beta}\, OM^{\alpha,\beta} \left(\frac{[SO_4^{2-}]}{K_{SO_4^{2-}} + [SO_4^{2-}]} \right) \left(\frac{K_{Fe(OH)_3}}{K_{Fe(OH)_3} + [Fe(OH)_3]} \right)$	E2
$R_3 = K_{\alpha,\beta}\, OM^{\alpha,\beta} \left(\frac{K_{SO_4^{2-}}}{K_{SO_4^{2-}} + [SO_4^{2-}]} \right) \left(\frac{K_{Fe(OH)_3}}{K_{Fe(OH)_3} + [Fe(OH)_3]} \right)$	E3
Secondary redox and other reaction equations	
$R_4 = k_1[Fe(OH)_3^{\alpha}][H_2S]$	E4
$R_5 = k_2[Fe^{3+}{}_2Fe^{2+}O_4][H_2S]$	E5
$R_6 = k_3[Fe^{2+}][H_2S]$	E6
$R_7 = k_4[FeS][H_2S]$	E7
$R_8 = k_5[S_0]$	E8
$R_9 = k_6[FeS][S_0]$	E9
$R_{10} = k_7[SO_4^{2-}][CH_4]$	E10
$R_{11} = k_8[CH_4][Fe(OH)_3^{\alpha}]$	E11
$R_{12} = k_9[Fe^{2+}][HCO_3^{-}]$	E12
$R_{13} = k_{10}[FeCO_3][H_2S]$	E13
$R_{14} = k_{11}[Fe(OH)_3^{\alpha}][Fe^{2+}]$	E14
$R_{15} = k_{12}[Fe(OH)_3^{\alpha}][Fe^{2+}][R_1]$	E15

Table S8. Boundary conditions of solids and solutes at the sediment-water interface in the model. Time dependent fluxes of OMα,β, and Fe(OH)3α,γ and bottom water Fe2+ concentration at the sediment water interface are shown in Figs. S11 and 13. For all chemical species a zero-gradient boundary condition was specified at the bottom of the model domain.

Solids	**Fluxes at sediment-water interface**	**unit**	**Source**
Sedimentation rate	0.02	cm yr^{-1}	U/Pb data
Flux of OM^{α}	0.01	µmol cm^{-2} yr^{-1}	a
F OM^{β}	0.03	µmol cm^{-2} yr^{-1}	a
F OM^{γ}	0.02	µmol cm^{-2} yr^{-1}	a
F $Fe(OH)_3^{\alpha}$	10.8	µmol cm^{-2} yr^{-1}	a
F $Fe(OH)_3^{\gamma}$	4.4	µmol cm^{-2} yr^{-1}	a
F $Fe^{3+}{}_2Fe^{2+}O_4$	0	µmol cm^{-2} yr^{-1}	a
F FeS	0	µmol cm^{-2} yr^{-1}	a
F FeS_x	0	µmol cm^{-2} yr^{-1}	a
F S^0	0	µmol cm^{-2} yr^{-1}	a
F $FeCO_3$	0	µmol cm^{-2} yr^{-1}	a
Solutes	**Bottom water concentration**	**unit**	**Source (range)**
O_2	0	µmol L^{-1}	b
NO_3^-	0	µmol L^{-1}	b
SO_4^{2-}	20	µmol L^{-1}	c-e (1 – <200)
Fe^{2+}	30	µmol L^{-1}	b, d (30-500)
H_2S	0	µmol L^{-1}	b
DIC	20	µmol L^{-1}	e

Sources: (a) Model constrained; (b) Konhauser et al. (2017); (c) Crowe et al., 2014; (d) Zhelezinskaia et al. (2014); (e) Habicht et al. (2002); (f) Holland (1984).

Chapter 4

Milankovitch cycles and the Earth-Moon distance 2.46 billion years ago

Milankovitch cycles and the Earth-Moon distance 2.46 billion years ago

Margriet L. Lantink, Joshua H.F.L. Davies and F.J. Hilgen

Abstract

The long-term history of the Earth-Moon system as reconstructed from the geological record remains unclear when based on fossil growth bands and tidal laminations. A possibly more robust method employs the period ratio between the axial precession and orbital eccentricity components of the Milankovitch climate cycles, which increases with decreasing Earth-Moon distance. However, sedimentary successions in which these cycles are recorded are essentially unknown from the older majority of Earth history. Here we present results of cyclostratigraphic analysis and high-precision uranium-lead dating of early Paleoproterozoic banded iron formation from the Joffre Member, NW Australia, showing that precession- and eccentricity-related alternations are, in certain intervals, well preserved in these ancient marine deposits. Combining visual and statistical tools to determine their hierarchical relation, we arrive at an average climatic precession duration of 10.9 ± 0.8 thousand years, corresponding to an Earth-Moon distance of 321.8 ± 6.5 thousand kilometers and 16.9 ± 0.2 hour daylength at 2459.2 ± 1.3 Ma. Our reconstruction, providing the oldest reliable data point so far, confirms lower mean dissipation rates in deep time, consistent with an early Moon origin. Remarkable agreement with ocean tide models hints at a principal influence of Earth's slowing rotation on the long-term trajectory of lunar retreat.

Significance statement

Tidally-induced dissipation of energy within the ocean and Earth causes the Moon to gradually recede from Earth, however, back-projection of the present-day rate implies a lunar origin at 1.5 Ga that is incompatible with its 4.5 Ga age. To reconstruct the past evolution of lunar retreat, the sedimentary record of the changing Milankovitch cycle periods may be used, yet the existence of such archives has thus far remained elusive for the older part of geologic history. Here, we identified the excellent expression of the climatic precession and eccentricity cycles in 2.46 Ga banded iron formations, whose relative ratios provide a reconstruction of the shorter Earth-Moon distance and daylength. Our results extend cyclostratigraphic constraints on the Earth-Moon system by more than 1 Gyr further back in time.

Introduction

The past evolution of the Earth-Moon system is a major uncertainty in the history of our Solar system. Due to tidal-induced dissipation of energy within the Earth and ocean, the Moon is gradually reaching a higher orbit and the Earth rotation is gradually slowing down (Darwin, 1980). Extrapolating the current rate of the Moon recession back in time yields an Earth-Moon collision around 1.5 billion years ago (Gerstenkorn, 1969; Dickey et al., 1994). However, this is in direct conflict with the formation age of the Moon of around 4.5 billion years, based on radio-isotopic dating of lunar rocks (Kleine et al., 2015; Taboul et al., 2007; Barboni et al., 2017). This implies that, over Earth's history, the average rate of tidal dissipation must have been much lower, but the details of this past temporal evolution, and hence the corresponding trajectory of lunar recession, remain highly uncertain (Munk, 1968; Webb, 1982; Hansen, 1982; Berger et al., 1992; Berger and Loutre, 1994; Laskar et al., 2004; Waltham, 2015; Green et al., 2017).

To constrain models of the tidal evolution history we ultimately need empirical data from the geological record. So far, reconstructions have been mainly based on fossil growth bands (Lambeck, 1980 and references therein) and tidal laminations (Williams, 1989; 2000), but these have the disadvantage that it is challenging to count the exact number of laminations per lunar month or solar year. An alternative and potentially more robust method uses the sedimentary record of climate variations induced by quasi-periodic changes in the Earth's orbit and inclination parameters (Milankovitch cycles). The periods of the climatic precession and obliquity cycles (now ca. 21,000 and 41,000 year, respectively) partly depend on the precession frequency of the Earth's spin axis (*p*), which is in turn directly related to the Earth-Moon distance: p decreases with increasing Earth-Moon distance and day length. In contrast, the periods of the short and long eccentricity cycles of the Earth's orbit (~100,000 and 405,000 year) are independent of *p* and have remained largely stable (Laskar et al., 2011; Olsen et al., 2019). In theory, therefore, the evolution of the Earth-Moon system could be traced back in time from the shifting ratio between these Milankovitch cycle periods, provided that there are sedimentary successions available in which they are well recorded. Indeed, this technique and comparable cyclostratigraphic methods have already been applied to different intervals of the Phanerozoic (Lourens et al., 2001; Zeeden et al., 2013; Wu et al., 2013; Meyers and Malinverno, 2018; Sørensen et al., 2020). Unfortunately, high-quality records become increasingly rare further back in time and thus far, only one serious attempt has been made for the Precambrian at ~1.4 Ga based on a relatively short section (Zhang et al., 2015; Meyers and Malinverno, 2018), while robust data points from much older time intervals are essential for determining the longer-term evolution and earliest history of the Earth-Moon system and/or tidal dissipation.

Banded iron formations (BIFs), conspicuously layered marine deposits characterizing the oldest Precambrian sedimentary record (Klein, 2005), are a potentially suitable candidate for providing estimates of the changing Earth-Moon distance in deep time. Regular 5m-scale alternations in the ~2.47 Ga Kuruman Iron Formation (IF) in South Africa (Lantink et al., 2019) and the supposedly time-equivalent Dales Gorge Member of the Brockman IF in Western Australia were recently linked to the 405,000 year eccentricity cycle (Lantink et al., 2019; de Oliveira Carvalho Rodriguez et al., 2019). This implies the dominant influence of climatic precession, since the main effect of eccentricity on variations in solar insolation is through the amplitude modulation of the precession cycle. Accordingly, regular 15 cm-thick lithological alternations (the "Calamina cyclothem")

(Trendall and Blockley, 1970) in the Dales Gorge Member hint at the presence of climatic precession cyclicity in certain intervals (Lantink et al., 2019; de Oliveira Carvalho Rodriguez et al., 2019). Particularly promising, however, is the slightly younger Joffre Member of the Brockman IF, with distinct regular alternations on both the 10 cm (the "Knox cyclothem") and "65 - 150 cm" scale (Trendall, 1969; Trendall and Blockley, 1970), suggesting that both precession and short eccentricity, needed to properly examine the precession to eccentricity frequency ratio, have been recorded.

Here, we combine detailed cyclostratigraphic analysis with results of high-precision U-Pb dating of a ~47 m stratigraphic interval in the Joffre Member as exposed at Joffre Falls in the Karijini National Park, Hamersley Range, NW Australia (SI Appendix, Figs. S1-2). Our primary research objective is to determine whether (i.e. by testing the Milankovitch hypothesis) and how a reliable value can be obtained for the precession frequency *p*, lunar distance and length of day, by applying and evaluating different statistical- and visual-based approaches. Comparing our result with existing (younger) geological estimates and theoretical models, we discuss its significance for - and potential contribution to - an improved understanding of the long-term evolution of the Earth-Moon system.

Results

Regular large- and small-scale alternations

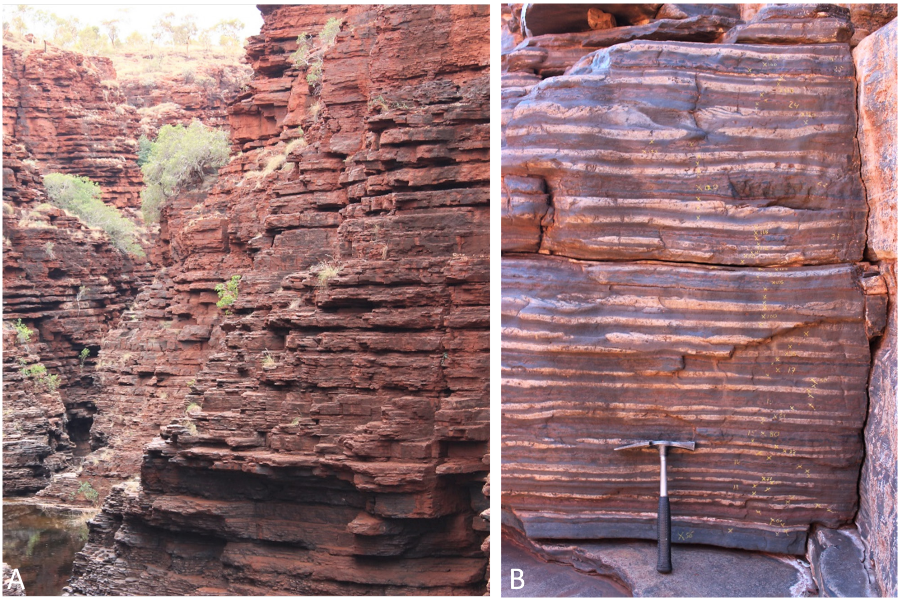

Figure 1. Regular alternations in the Joffre Member at Joffre Falls. (**A**) Large-scale shale-BIF alternations of ~85 cm; (**B**) small-scale alternations of ~10 cm.

The outcrops of the Joffre Member at Joffre Falls exhibit a distinct hierarchy of regular alternations at a number of scales (Fig. 1). Viewed from a relative distance, prominent alternations are visible between reddish brown, indurated BIF and weathering-prone, thinner shaley intervals with a thickness of ~85 cm (Fig. 1a). On a larger (meter) scale, variations can be recognized in the thickness and distinctness of the shaley intervals (SI Appendix). Combined, these form a characteristic (bundling) pattern that is laterally continuous at the outcrop scale. We have logged the observed changes in lithology and relief for a total of 57 shale-BIF alternations (Fig. 2; SI Appendix, Figs. S3-4).

Zooming in on the ~85 cm alternations, we identified the consistent expression of small-scale alternations of ~5 to 15 cm (Fig. 1b), matching Trendall's description of the Knox cyclothem (29). The alternations typically consist of (i) two white chert layers in a magnetite-rich matrix alternating with (ii) a red chert centered in dark greenish-grey softer ("mixed") lithology. However, their expression and thickness can vary significantly along their position within the larger-scale shale-BIF variability (Fig. 3a; SI Appendix). From a lower, middle and upper part of Joffre Falls, we selected three representative short intervals (Fig. 2a; Fig. S5) for detailed logging of the small-scale Knox cyclothems, complemented by handheld color and X-ray fluorescence analysis (SI Appendix, Figs. S6-7). Of the acquired dataset, the lightness pattern, Si/Fe ratio and K abundance (%) appear to most accurately reflect the Knox cyclothem structure (Fig. 3b), with the K (%) signal additionally showing a clear amplitude modulation pattern of the cyclothems, which follows the larger-scale shale-BIF cyclicity (Fig. S6d).

To statistically evaluate the periodic nature of the described scales of alternations and determine their wavelengths more precisely, we first applied time series analysis. Multitaper method (MTM) (Thomson, 1982) power spectra for the complete log show dominant peaks around 78 cm and 93 cm (Fig. 2b; Fig. S8a-b), exceeding 99% LOWSPEC confidence (Meyers, 2012), as well as concentration of power around 1.5 m, 3-4m, 5m, 8m and 11m corresponding to the observed bundling. The 78 cm and 93 cm cycles together define the basic ~85 cm shale-BIF alternations as demonstrated by the bandpass filtered (65-105 cm) signal (Fig. 2; Fig. S9). The amplitude modulation of this signal reveals a dominant ~3.3 m cycle (Fig. 2b; Fig. S8c).

Figure 2 (next page). (**A**) Composite log of the shale-BIF alternations at Joffre Falls and bandpass filtering. Cycle numbers mark individual shale-BIF alternations that occur on the ~85 cm scale; possible extra cycles that are relatively thinner are labelled 'b'. The shale-BIF record (relief) is indicated by the rectangular black curve. Bandpass filtered (65 – 105 cm) signal is indicated by the thick blue curve and the corresponding Hilbert transform is indicated by the thin blue curve. The brackets indicate the positions of the three short logs and bold numbers indicate minimum and maximum Knox cyclothem counts (see also Table 1). *CA-ID-TIMS zircon age from this study. (**B**) Spectral analysis results. Left: MTM power spectrum for the shale-BIF record with LOWSPEC background, 90, 95 and 99% confidence levels and peak labels in meters. Blue area indicates the 65 – 105 cm window for the bandpass filtering. Right: MTM power spectrum of the amplitude modulation signal (Hilbert transform) of the 65 – 105 cm filtered cycle.

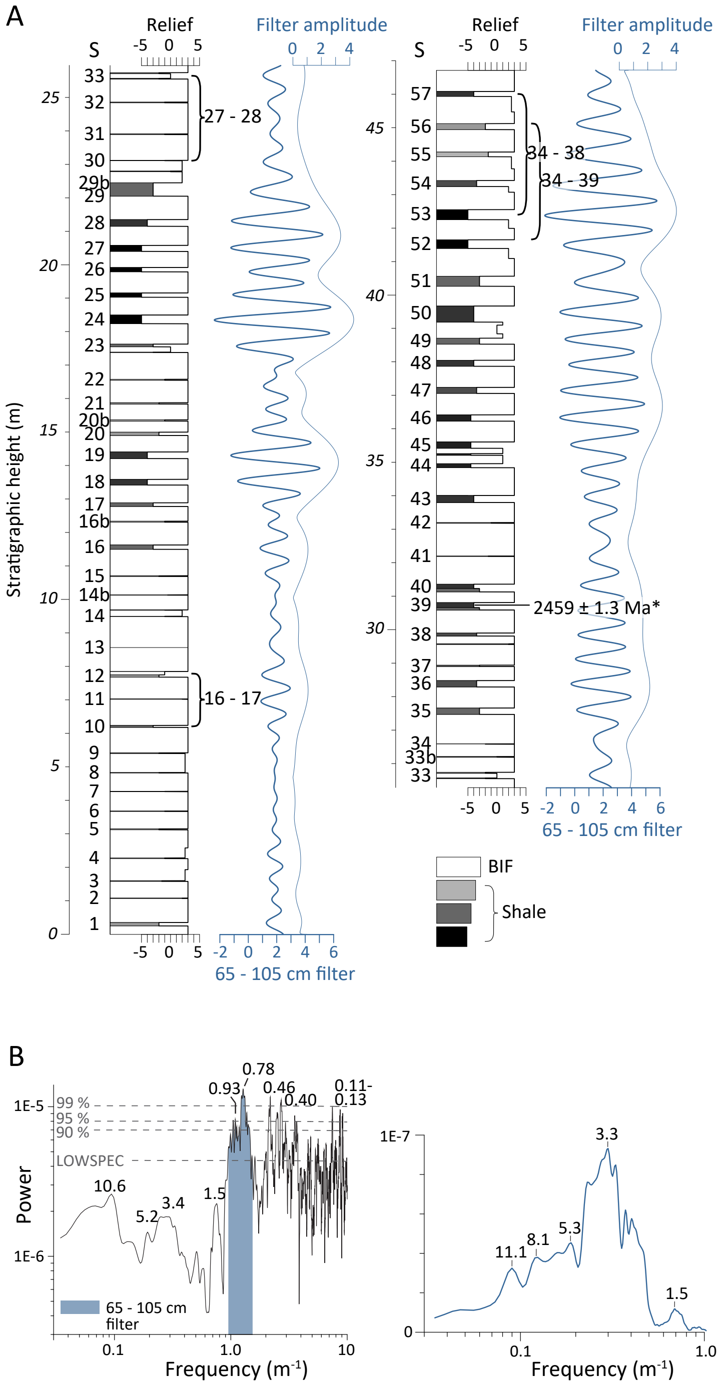
A
Relief
-5 0 5
Filter amplitude
0 2 4
S
Stratigraphic height (m)
0
5
10
15
20
25
1 2 3 4 5 6 7 8 9 10 11 12 13 14 14b 15 16 16b 17 18 19 20 20b 21 22 23 24 25 26 27 28 29 29b 30 31 32 33
27 - 28
16 - 17
-2 0 2 4 6
65 - 105 cm filter
30
35
40
45
33 33b 34 35 36 37 38 39 40 41 42 43 44 45 46 47 48 49 50 51 52 53 54 55 56 57
34 - 38
34 - 39
2459 ± 1.3 Ma*
BIF
Shale
B
Power
1E-5
1E-6
99 %
95 %
90 %
LOWSPEC
10.6
5.2
3.4
1.5
0.93
0.78
0.46
0.40
0.11-
0.13
65 - 105 cm
filter
0.1
1.0
10
Frequency (m⁻¹)
1E-7
0
11.1
8.1
5.3
3.3
1.5
0.1
1.0
Frequency (m⁻¹)

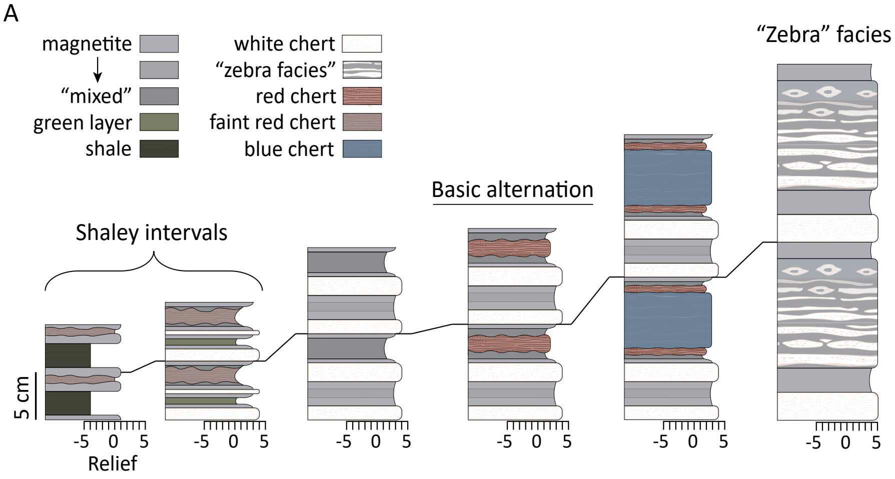
A
magnetite
"mixed"
green layer
shale
white chert
"zebra facies"
red chert
faint red chert
blue chert
"Zebra" facies
Basic alternation
Shaley intervals
5 cm
-5 0 5
Relief

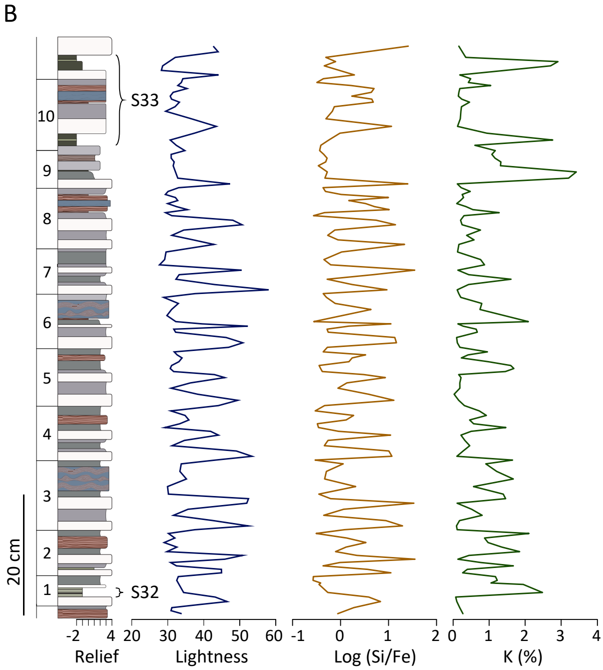

Figure 3. Characterization of the small-scale "Knox cyclothem" alternations. (**A**) Different expressions of the small-scale alternations. These are schematic 'idealized' representations of the different types of Knox cyclothems observed at Joffre Falls. Note the large range in their characteristic thickness. See main text and SI Appendix for a detailed description. (**B**) Detail of the lithological log and proxy data from the S32 to S33 interval of the middle interval (for complete record see Fig. S6). Cycle numbers are indicated on the left. Note the double or triple peaks per cycle in the lightness, Si/Fe and K (%) records.

Interval:	Number of cycles:	Average per bundle:	Subinterval:	Number of cycles:
S10 → S12 (2 bundles)	16 - 17	8.25 ± 0.25	S10 --> S12	16 - 17
S30 → S33 (3 bundles)	27 - 28	9.17 ± 0.17	S30 --> S31	10
			S31 --> S32	9
			S32 --> S33	9 - 10
S53 → S57 (4 bundles)	34 - 38	9.00 ± 0.50	S53 --> S54	8 - 10
Z52 → Z56* (4 bundles)	34 - 39	9.13 ± 0.63	S54 --> S56	17 - 18
			S56 --> S57	9 - 10
Total (9 bundles)	77 - 84	8.94 ± 0.39	Average per bundle:	9.00 ± 1.00

Table 1. Number of small-scale cycles per larger-scale shale-BIF alternation. Cycle counts are from shale midpoint to shale midpoint and are indicated per logged interval as well as per individual bundle (subinterval). ± indicates absolute uncertainty. *Z stands for "Zebra interval". For counting procedure and uncertainties see SI Appendix and Fig. S7.

Spectral analysis of the geochemical records (Si/Fe and K%) from the three short intervals however, produces very complex spectra, with multiple peaks in the 2 to 17 cm range (Fig. S10). This complexity results from the variable thickness and the two to three (Si/Fe and/or K%) maxima per small-scale cycle, reflecting the characteristic double to triple occurrence of chert and/or mixed beds of the Knox cyclothem structure (SI Appendix, Fig. S11). To avoid these statistical complications in determining their mean period and ratio with the larger-scale BIF-shale cyclicity, we switched to the visual approach of counting the number of small-scale alternations per larger scale cycle for each of the short sections (SI Appendix). Including absolute uncertainties for intervals where the cycle expression is relatively weak or condensed (SI Appendix, Fig. S7), we arrive at an average thickness of 8.9 ± 0.3 cm per Knox cyclothem and 8.9 ± 0.4 cyclothems per shale-BIF bundle, determined over a total of nine bundles (Table 1; Table S1).

Link to eccentricity and climatic precession

To establish a Milankovitch control and interpretation for the observed cycles at Joffre Falls, radio-isotopic ages of sufficient accuracy and precision are required for independent calculation of the depositional rate and cycle periods. In a parallel study, we present results of chemical abrasion (CA)-ID-TIMS U-Pb zircon dating of a 185 m interval of the Joffre Member in core DD98SGP001 (DD98), drilled ~150 km west of Joffre Falls, which indicate an average depositional rate between 5 - 15 m/Myr from 2.469 to 2.454 Ga (SI Appendix). This result is identical to the previously established 10 m/Myr rate for the Kuruman IF (Lantink et al., 2019) and the interpreted rate for the correlative Dales Gorge

Member lower in the Brockman IF stratigraphy. From Joffre Falls, we have produced a single concordant age for shale S39 of 2459.2 ± 1.3 Ma (SI Appendix, Fig. S12), which places our section within the well-dated time window of the Joffre Member in the core. Unfortunately, this correlation is in conflict with its estimated higher position within the general stratigraphy of the Joffre Member (SI Appendix) and previous lithostratigraphic correlations to core DD98 (Pickard, 2002). This implies that either these earlier correlations are incorrect, or that the zircons of S39 are xenocrystic or detrital in origin, in which case their established age reflects a maximum depositional age that is close to, but slightly older, than the expected age. Notwithstanding these uncertainties, we consider it entirely reasonable to invoke the depositional rate determined from the core for Joffre Falls, in particular given that the same cycle hierarchy and small-scale cycle thickness was observed in the core (SI Appendix).

Application of a 10 m/Myr mean rate yields a time period for the distinct 78 – 93 cm cycles and ~3.3 m amplitude modulating cycle at Joffre Falls that is closely consistent with that of the short (~100-kyr) and long (405-kyr) eccentricity cycles (SI Appendix). Moreover, linking the 3.3 m cycle to 405 kyr eccentricity converts the other weaker amplitude modulation terms to periods that closely approximate those of other existing long-period eccentricity cycles (Table S2). The prominent expression of eccentricity, and the amplitude modulation and hierarchical relationship with the small-scale Knox cyclothem alternations, implies that the latter represent the direct imprint of climatic precession with a much-reduced period (Webb, 1982; Berger and Loutre, 1994; Waltham, 2015; Meyers and Malinverno, 2018) compared to the modern ~21 kyr.

With these new data, we can now proceed with a more precise analysis of the precession period for determining the Earth-Moon distance, using the observed precession to eccentricity ratio.

Determining the Earth-Moon distance

The stratigraphic expression of precession does not reflect a single cycle, but the net effect or sum of individual climatic precession cycles, which together determine the precession-induced changes in insolation. These individual cycles are composed of combinations of Earth's axial (astronomical) precession frequency p, the value of which we are ultimately after, with one of the fundamental g_i frequencies of planet i, describing the rotation of the elliptical planetary orbits on the orbital plane. The four most important terms are related to Jupiter ($p + g_5$), Venus ($p + g_2$), Mars ($p + g_4$) and Earth ($p + g_3$); their differences yield the main eccentricity terms of the ~100-kyr ((g_4 - g_5), (g_3 - g_5), ($g_4 – g_2$) and ($g_3 – g_2$)) and 405-kyr ($g_2 – g_5$) cycles. Previous studies have employed the method of resolving the periods of these individual $p + g_i$ terms, and thereby the value of p, directly from the power spectral peak ratios of climate proxy records (Meyers and Malinverno, 2018; Olsen et al., 2019). However, in our case we consider such an approach not feasible given the large degree of stratigraphic distortion at the precession scale. Instead, we choose to first determine a duration (period) for the "average" climatic precession signal prior to extraction of p, for which we explore three different options.

The first option is to use and convert the previously established average Knox cyclothem thickness (8.9 ± 0.3 cm) to time by taking the mean wavelength of the stable long eccentricity cycle, determined by spectral analysis, as a reference. Considering that the average Knox cyclothem thickness has been determined over in total nine short eccentricity-related bundles, changes in sedimentation rate at the sub-eccentricity scale are in this way effectively eliminated. As such, the interpreted linkage between the 3.3 m cycle and 405 kyr eccentricity can be used for translating the mean precession-related cycle thickness to time. This approach (option 1) yields an overall average climatic precession cycle period of 10.9 ± 1.7 kyr (Table 2), which is consistent between the three separate short intervals. However, the disadvantage of this method is the relatively large uncertainty in the 3.3 m wavelength (Figs. S13-14).

Therefore, an alternative second option is to calculate the average climatic precession period from the average number of precession-related cycles per short eccentricity bundle (8.9 ± 0.4). For this we need to establish an average period for the short "100 kyr" eccentricity cycle, which can be estimated from the time differences between successive eccentricity maxima from e.g. the La2004 eccentricity solution (Laskar et al., 2004). This is unfortunately not straightforward as the time between two eccentricity cycle extremes may vary significantly (≥ 12 kyr) from one cycle to the next as a result of the interference (phase difference) between the individual short-eccentricity components (Fig. S15). However, this variability is significantly reduced bearing in mind the fact that we have logged three different intervals containing two, three and four successive short eccentricity bundles, which considerably reduces the chance that all nine logged eccentricity bundles will be very short or long. For this reason, we repeatedly made random selections of two, three and four successive cycles from the La2004 solution for the interval from 0 - 50 Ma, excluding anomalously short (< 80 kyr) or long intervals (> 115 kyr) (SI Appendix). This method (option 2a) yields an average duration of 96.2 kyr (Table S3, Fig. S16) and overall average climatic precession period of 10.8 ± 0.7 kyr (Table 2). The result is very similar to option 1, but it is much more precise.

	Option 1		Option 2a		Option 2b		2a & 2b	
	kyr	±	kyr	± 2σ	kyr	± 2σ	kyr	± 2σ
Lower	10.9	1.6	11.7	1.4	12.0	1.4		
Middle	11.0	1.3	10.5	0.8	10.7	0.9		
Upper	10.7*	1.9	10.7	0.8	10.9	1.0		
Total	10.9	1.7	10.8	0.7	11.0	0.7	10.9	0.8

Table 2. Calculated average climatic precession periods. Option 1: assuming an average small-scale cycle thickness and sedimentation rate using the average thickness of the 405 kyr-related cycle (i.e. 3.3 m). *based on a thickness correction (see main text, Table S1 and Fig. S13). ± represents estimated full uncertainty. Options 2a and b: based on the average number of small-scale cycles (Table 1) per average short eccentricity period derived from the La2004 (0 – 50 Ma) and ZB18a (50 – 80 Ma) solutions, respectively (Table S3).

Considering the chaotic nature of the solar system, the La2004 solution from 0 – 50 Ma might not correctly represent the orbital conditions at 2.46 Ga. One large source of uncertainty lies in the period of the inherently unstable long "2.4 Myr" eccentricity cycle which is related to the orbits of Earth and Mars (g_4 – g_3) and can be significantly reduced in period (Fig. S17). In fact, this was likely the case during deposition of the Kuruman IF and Dales Gorge Member, for which a shorter period of ~1.4 – 1.6 Myr was found (Lantink et al., 2019), which may have extended into the younger Joffre Member (Table S2). We therefore repeated our exercise of option 2a but instead used the ZB18a eccentricity solution (Zeebe and Lourens, 2019) between 50 – 80 Ma. This time interval includes a reduced period of ~1.6 Myr for the (g_4 – g_3) eccentricity cycle owing to a chaotic resonance transition between 45 - 50 Ma. This third approach (option 2b) produces only a slight (2 kyr) increase in the mean short eccentricity period (Table S3), resulting in a very similar mean precession period of 11.0 ± 0.7 kyr. The slightly longer short eccentricity period can be understood from the fact that, even though a reduction in the period of (g_4 – g_3) changes the individual frequencies of the four main ~100 kyr eccentricity terms, the frequency differences between its two main pairs changes symmetrically around their combined average (Fig. S17). Nevertheless, we prefer to incorporate this minor extra uncertainty to arrive at a final mean climatic precession period by combining the outcomes of option 2a and 2b, which gives 10.9 ± 0.8 kyr.

Finally, to isolate the astronomical precession frequency p from the average climatic precession period, we assume that each of the four major $p + g_i$ precession terms contributes to the total average precession signal with a factor that scales to their relative amplitude (strength) (SI Appendix). This assumption seems valid when tested on several different intervals of the La2004 solution (Table S4). For the calculation (eq. 1-2 in SI Appendix) we used the present-day g frequencies and their amplitudes (Table 4 in Laskar et al., 2004) rather than trying to reconstruct them from the inferred eccentricity-related cycles in the Joffre Falls record, again, because their exact frequencies i.e. peak positions are poorly constrained (Table S2). This approach results in a p frequency of 109 ± 9 "/yr and period of 11.9 ± 0.9 kyr for astronomical precession, corresponding to an Earth-Moon distance of 321.8 ± 6.5 thousand km and length-of-day of 16.9 ± 0.2 h (SI Appendix, Fig. S18).

Discussion

In Figure 4 we compare our reconstructed Earth-Moon distance at 2.46 Ga to previous geological estimates available from the Cambrian (Sørensen et al. 2020) to Proterozoic (Williams, 1989; Sonett et al., 1996; Sonett and Chan, 1998; Walker and Zahnle, 1986), and to a number of theoretical models for the lunar recession history (Webb, 1982; Bills and Ray, 1999; Waltham, 2015). First of all, our result from the Joffre Member indicates a clearly shorter (10 - 18 thousand kilometer) distance than suggested by two tidal estimates from the slightly younger Weeli Wolli Formation at ~2.45 Ga (Fig. 4a). However, these values are based on two fundamentally different interpretations of the same record, namely i) bundles of 23 microbands interpreted as annual layers modulated by the lunar nodal tide cycle (Walker and Zahnle, 1986), versus ii) bundles of 28 – 30 microbands interpreted as lunar fortnightly cycles grouped into solar years (Williams, 1989; Williams, 2000). This means that at least one of them must be incorrect and illustrates the large uncertainty involved in using such estimates (Williams, 2000; Sonett et al., 1996; Sonett and Chan, 1998).

The Earth-Moon distance indicated by the Joffre is remarkably consistent with that of the 'ocean model' curves *c* (Webb, 1982) and *e* (Waltham, 2015), while it rules out models that are based on a constant tidal dissipation quality factor corresponding to an initial tidal dissipation rate of about 1/3 of the present-day rate (curves *g*, *f* in Fig. 4). These ocean models, and ocean models in general, are based on an exponential growth of tidal dissipation within the ocean over time due to a gradually lengthening day, which causes a progressively smaller offset between the frequency of the diurnal tide and the longer-period tidal forces. Note that while curve *c* of Webb (1982) indicates a too old (~5.3 Ga) Moon age, it is based on a tidal dissipation curve calculated from an actual model for the tides in the 'average' past ocean, which, coupled to an astronomical model, is then numerically integrated back in time, whereas Waltham (2015) merely provides a simplified mathematical description of the typical shape of ocean models (range of possible trajectories) as a function of the empirical variable tau, the timescale of significant change in Earth's rotation rate, taking the Moon's present-day and interpreted 4.5 Ga position as fixed end points. Note also that curve *d* (Fig. 4) is adapted from the Waltham (2015) model and represents the trajectory for a tau value of 600 Ma, which closely matches our result from Joffre as well as curve *c*, apart from the oldest part (> 4.0 Ga) due to the assumed ~4.5 Ga Moon origin.

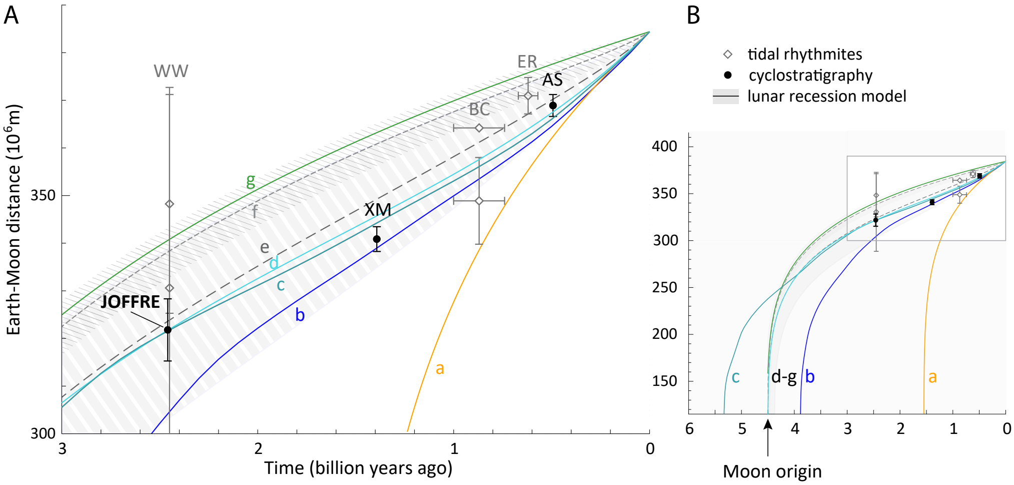

Figure 4. (Pre)cambrian estimates of lunar recession history (continues next page)

(**A**) Geological data: uncertainties in Earth-Moon distance are ± 2 sigma (where available). Age uncertainties represent maximum and minimum values; where absent the uncertainties fall within the size of the symbols. Reconstructions based on cyclostratigraphy are from the Joffre BIF at 2459 ± 1.3 Ma (this study), the ~1.4 Ga Xiamaling Formation (XM; Meyers and Malinverno, 2018) and ~493 Ma Alum Shale (AS; Sørenson et al., 2020). Reconstructions based on tidal laminae are from Elatina-Reynella (ER; Williams 1989; 2000) and two alternative estimates from the Big Cottonwood (BC; Sonett et al., 1996 vs. Sonett and Chan, 1998) and the ~2450 Ga Weeli Wolli (WW) BIF. Note that the Weeli Wolli estimates are based on conflicting interpretations of the same record (Walker and Zahnle, 1986 vs. Williams, 2000) and lack independent radio-isotopic control. See Table S5 for plotting data and age references. Models: curves a and g are adapted from Bills and Ray (1999) and are based on a constant tidal dissipation quality factor that corresponds to the present-day value and 35% of the present-day value, respectively. Curves b and c represent 'Curve d' (= ocean + solid Earth model) and 'Curve c' (= ocean model) from Webb (1982), respectively. Curves d-f derive from Waltham (2015) where e and f represent the average trajectories of the 'secular/smooth-change' versus 'stochastic/fluctuating drag' models, respectively. Note the large uncertainty in the secular model (grey shaded area) which is defined by an upper and lower estimated value for the variable τ between 100 –1000 Ma; see eq. 5-6 in Waltham (2015); curve d was adapted from Waltham (2015) and represents the trajectory for τ = 600 Ma. (**B**) Modelled trajectories for evolution of the Earth-Moon system over its full history. Note that models a-c violate the Moon formation age of ~4.5 Ga.

Adding the two younger cyclostratigraphic estimates from the Xiamaling Formation at ~1.4 Ga (Meyers and Malinverno, 2018) and Alum Shale at 493 Ma (Sørensen et al., 2020), which are likely to be more accurate than estimates based on tidal laminae, yields a long-term trend that also appears compatible with an ocean model type of evolution. The Xiamaling data point however, falls below the trajectory of curves *c* – *e*, overlapping with the unrealistic curve *b* of Webb (1982), which crosses the x-axis too early at ~3.9 Ga. While the Xiamaling could point to a considerable reduction in tidal dissipation between 2.46 and 1.4 Ga, we have some doubt about the cyclostratigraphic interpretation of the Xiamaling data by Meyers and Malinverno (2018). The climatic precession signal, as reconstructed from the Cu/Al record (Figure 1c in Meyers and Malinverno, 2018), shows an unusual amplitude modulation pattern with successively 7, 11, 9 and again 11 precession-related cycles per interpreted short eccentricity-related bundle. Such an alternating pattern is difficult to reconcile with the typical differences in durations seen between successive short eccentricity cycles in eccentricity time series of astronomical solutions. Similarly, the occurrence of short eccentricity-related bundles longer than 150 kyr (as suggested by the 11:1 cycle ratio with precession) is unlikely, firstly because this duration far exceeds the ~131 kyr period of the longest short eccentricity component $g_3 - g_2$. Secondly, while 'shoulder formation', the merging of two successive weak short eccentricity cycles, could be the case, this only develops occasionally during 405 kyr minima of very long eccentricity ($g_4 - g_3$) nodes and thus cannot occur two times within half a 405 kyr-related cycle, as suggested by the single bundle of 9 in between. In fact, the anomalously long eccentricity-related bundles interpreted by Meyers and Malinverno

(2018) may explain why their reconstructed average precession period (~14 kyr), and thus Earth-Moon distance, is too short.

A preliminary conclusion from our data might be that, over the history of the Earth, the effect of Earth's decreasing spin velocity on tidal dissipation within the ocean was a determining factor for the long-term evolution of lunar retreat. However, we take this position with great caution, given that the consistency between the cyclostratigraphic data and ocean models may as well be pure coincidence considering the scarce number of data points thus far and the methodological limitations involved. In fact, this is very likely to be the case for the almost exact match between the Joffre and curve *c* of the numerical model of Webb (1982), taking into account the uncertainty in the Joffre mean value and the simplified assumptions in Webb (1982). For example, a 4.4 km deep, hemispherical ocean with a linear bottom friction term was assumed, while most energy is thought to be dissipated on continental shelves and may differ by a factor of 10^3 depending on the specific paleo-continental and -bathymetric configuration (Green et al., 2017; Blackledge et al., 2020). Fluctuations in tidal drag resulting from changes in tectonic setting, sea level and dynamical ellipticity were thus superimposed on the mean rotation rate-dominated trend (Waltham, 2015). Furthermore, the fact that curve *c* of Webb (1982) crosses the x-axis at ~5.3 Ga obviously indicates that a continued reduction in tidal drag within the Earth-Moon system with age is not valid for the earliest stages of geologic history.

Hence, more reliable and precise data from the Precambrian are needed to constrain the main trajectory of lunar retreat and potential superimposed variations, to improve our understanding of the main drivers and other processes at play. Considering the regular precession-scale (Lantink et al., 2019; de Oliveira Carvalho Rodriguez et al., 2019) Calamina cyclothem reported for certain intervals of the Dales Gorge Member (Trendall and Blockley, 1970), this unit seems a logical target for testing and extending our result from the Joffre Member. In fact, a precession period of 8 - 12 kyr was already tentatively suggested by de Oliveira Carvalho Rodriguez et al. (2019), although their interpretation of the thickness for long eccentricity (8 m; Table 5a in de Oliveira Carvalho Rodriguez et al., 2019) is not compatible with the expected 4-6 m thickness based on the results for the Kuruman IF of Lantink et al. (2019) and time series analysis by Cowan and Cooper, 2003. More well-constrained cyclostratigraphic data points would be particularly welcome from the younger part of the Proterozoic to further test the ocean model hypothesis, and vice versa, to create more realistic models. At the same time, this will serve as a test for the more speculative models for the Proterozoic that propose a ~1 – 2 Gyr episode of constant Earth-Moon distance and daylength of 21h due to 'resonance-stabilization' by the atmospheric thermal tide (Zahnle and Walker, 1987; Bartlett and Stevenson, 2016; Klatt et al., 2021), and/or extreme changes in dynamically ellipticity associated with Snowball Earth events (Mitchell et al., 2021a). Considering the age span over which BIF are largely found (3.8 – 1.9 Ga; Klein, 2005), these deposits are potential candidates for reconstructing the Earth-Moon distance during even more distant time intervals, which would have interesting implications for the history of the continental and oceanic crust.

Materials and Methods

Cyclostratigraphic analyses

From the outcrops of the Joffre Member within the Karijini National Park, a ~47 m interval at Joffre Falls was selected for logging of the regular BIF-shale alternations and the development of a ranked relief record of the associated changes in weathering profile. From a lower, middle and upper part, three short intervals were selected for logging of the small-scale alternations where these were particularly clear, complemented by non-destructive color and XRF analysis for which we targeted the freshest rock exposures close to the water fall. MTM power spectral analysis (using a time-bandwidth product of 3), bandpass filtering (using a rectangular window) and Hilbert transform analysis was carried out on linearly detrended and interpolated records using the functions in Astrochron (Meyers, 2014). See SI Appendix for a full description of the methodology including cycle counting procedures.

TIMS U-Pb geochronology

From shale S39, a thin band sample with high Zr content (measured by handheld XRF) was collected for extraction of zircon crystals, which were chemically abraded to remove the effect of decay-damage-related Pb loss and dated using CA-ID-TIMS techniques outlined in (Lantink et al., 2019) and briefly described in the SI Appendix. The here reported ^{207}Pb/^{206}Pb age (Fig. 2; Fig. S12) represents the weighted mean of one concordant and one close to concordant analysis.

Determining the Earth-Moon distance

The result of options 2a and 2b (see main text and Table 2) was averaged to arrive at a mean value for the precession frequency p using the following approximation: frequency (freq.) p = freq. mean climatic precession - (amplitude fraction g_5 * freq. g_5 + amplitude fraction g_2 * freq. g_2 + amplitude fraction g_4 * freq. g_4 + amplitude fraction g_3 * freq. g_3). Earth-Moon distance and daylength were subsequently determined using the same method as Meyers and Malinverno (2018). A complete explanation of the approach, and determination and propagation of errors, is given in the SI Appendix.

Acknowledgements

We thank the Geological Survey of Western Australia and D. Martin for logistical support during two field campaigns (‘18-’19). We thank G.H Jack and P. Mason for with help with the XRF and colorimetric scanning; R. Ray for sharing D. Webb’s curves c-d and D. Waltham for his model calculations. This study was funded by the Dutch National Science Foundation (grant NWO ALWOP.192) and the Swiss National Science Foundation (grant 200021_169086). M.L.L. and F.J.H. acknowledge support from the Foundation Stichting Dr. Schürmann Foundation (grants no. 2018-136 and 2019-145).

Supplementary Information

Stratigraphic background

The Brockman IF (~620 m thick) of the Neoarchean – early Paleoproterozoic Hamersley Group, Mount Bruce Supergroup, extends over ~500 km in WNW-ESE direction on the Pilbara craton (Fig. S1a). The Joffre Member (~350 m average thickness) is the second and younger BIF unit of the Brockman IF, overlying the Dales Gorge Member BIF (~140 m) and Whaleback Shale Member (~50 m) (Fig. S1b), and is named after its remarkable cliff exposures in Joffre Gorge within the Karijini National Park (Fig. S1c-d).

Previous cyclostratigraphic observations at Joffre Falls

In the Joffre Member stratigraphy two main types (scales) of regular bedding have been initially recognized and described by (Trendall, 1969) and (Trendall and Blockley, 1970) from the outcrops at and downstream of Joffre Falls (Fig. S1d, S2). In Trendall and Blockley (1970), a "*main type of lithological discontinuity within the predominant and rather uniform iron formation of the Joffre Member is stilpnomelane-rich shale bands between about an inch and about one foot thick*" was defined. These shale beds proved to be laterally continuous within the gorges, and served as useful marker horizons for Trendall's stratigraphic height measurements (log) of the Joffre Member from its interpreted base downstream at Wittenoom Gorge all the way up to Joffre Falls (Fig. S1d), indicating a 217.8 m height for the base of the Falls (Fig. S2). At this locality, a conspicuously regular occurrence of the shale beds was noted, about which Trendall (1969) reported the following: "*In the well exposed Joffre Member in the cliffs at and below Joffre Falls, stilpnomelane tuff bands 2 to 4 inches thick are distributed within the iron formation at remarkably regular intervals. The average separation is about 2 $^1/_2$ feet, with a range of about 2 to 5 feet. The stilpnomelane bands weather back to emphasize the regularity of their distribution.(…)..This regularity is here superimposed on the Knox cyclothem, several of which are included between successive stilpnomelane bands.*" This smaller-scale so-called Knox cyclothem was defined in Trendall and Blockley (1970) as "*a common cyclic sequence of mesoband types in the Joffre Member, in which one or more white chert mesobands alternate repeatedly at regular intervals with one or more red chert mesobands, with all the cherts separated by chert-matrix*" at a thickness "*just over 3 inches*", and its specific expression at Joffre Falls was described as "*a white striping; each stripe consists of a double white chert*".

Regular large-scale ("shale-BIF") alternations

Constructing the composite log of Joffre Falls

For our cyclostratigraphic examination of the large-scale changes in lithology and weathering profile observed in the stratigraphy of Joffre Falls, three intervals (subsections) where the alternations were well expressed and easily accessible were selected and formed our trajectory for logging (Fig. S1d). Using tape measure, the individual stratigraphic thicknesses of the more indurated 'BIF' and more weathered 'shaley' intervals were measured at centimeter resolution. The logged sub-intervals were called 'Bottom', 'Middle' and 'Top' (Fig. 3) and were combined into a composite log, covering a total thickness of 46.7 m (Fig. S4).

To create a numerical log suitable for time series analysis that also includes the more subtle, larger-scale variations in weathering profile, observable in the bundling of shales (see next section), we subsequently ranked the logged intervals in terms of their relief or 'shale-BIF index' following the same approach as in Lantink et al. (2019). Negative values were assigned to the more weathered, low-relief shaley intervals on a scale from 0 for the very faint shaley levels to -5 for the most prominent shales, characterized by the darkest shadows cast by the BIF units above. Positive values were assigned to the non-shaley BIF intervals on a scale from 1 to 3. Because we observed little variability in the relief between successive BIF units, these were given a standard value of 3, and only clearly lower relief intervals were given values of 2 or 1. We performed the ranking visually from multiple viewpoints, including locations with a direct view and those with an oblique view on the alternations. In this way the average expression over several hundreds of meters in lateral direction could be determined. Ranking in this manner was completed independently by all co-authors assigning whole to half points. Individual gradings turned out to be in close agreement, with a maximum difference of 1, and were subsequently averaged into a final ranking. Slight modifications were made based on inspections of photos.

Large-scale cycle pattern

Besides the alternations in weathering profile at a scale of ~85 cm, the Joffre Falls composite log (Fig. 2) highlights the presence of longer-period variations manifested by the intensity and thickness of the shale horizons ("shaleyness"). For example, there are a number of intervals where one or two distinct shales are followed by two or three weaker shales, such as from S16 to S18 - 19; from S35 - 36 to S39 - 40 to S43; and from S52 - S53 to S57. This suggests the presence of an alternation at a scale of about 3 to 4 BIF-shale repetitions (corresponding to ~3 m). In addition, there is an even larger-scale modulation visible in a number of more prominent shales versus more blocky, BIF-dominated intervals with thin, poorly developed shales. This seems to recur each ten to twelve BIF-shale repetitions, for example from S20 - 22 to S30 - 34 to S41 - 42 (~8 - 9 m). However, there are fourteen to fifteen alternations to the next blocky unit S55 - 56 (~11 - 12 m). Larger-scale modulations are less apparent in the bottom exposures of Joffre Falls closer to the water level (Fig. S3a), though an alternation seems to be present of a supposedly double BIF versus a single shale, e.g. from S10 to S12 to S14 (corresponding to ~1.5 m). Compared to the shales there is only limited modulation visible in the relief of the BIF units, but note the lower relief of for example the BIFs above S44 and S49.
Regular small-scale ("Knox cyclothem") alternations

Basic structure of the Knox cyclothem and variants

Within the stratigraphy of Joffre Falls, we encountered various expressions (different types) of the smaller-scale Knox cyclothem (see Figs. S5, S7) which we have categorized as follows (see also Fig. 3a):

- Basic alternation. This consists of (i) a double white chert of circa 1-2 cm thick (nicknamed the "tramrails") surrounded by metallic- to dark blueish grey-colored magnetite-rich lithology, alternating with (ii) a red chert centered within a brown-greenish-grey, more weathering-prone interval ("mixed" lithology). The red cherts are finely microlaminated and have a somewhat wavy appearance or can form oval-shaped "podding" structures (Fig. S5b,e). In between the tramrails, a few millimeters thick greenish-colored layer may be visible (Fig. S5e) which, similar to the mixed intervals, is more weathering-prone.

- Red chert absent. In some of the alternations no red chert is developed and only a softer "mixed" lithology is present. This mixed lithology consists of a mixture of magnetite-rich and more shaley lithology, indicated by its elevated K % (see section *Color and XRF analysis*), and possibly some carbonate. There are several degrees of this magnetite-shale(-carbonate) mixture possible characterized by subtle differences in color (from blueish-grey to brownish-green) and relief. In the upper section that was logged in detail (see section *Constructing the lithological logs* below), the red "cherts" in many of the alternations typically have a much lower relief, representing a transitional lithology between red chert and mixed.

- Addition of a blue chert. Prominent blue-colored cherts (indicating the presence of the mineral riebeckite) may develop at the center of a red chert, and substantially contribute to the thickness of the alternation as they can be up to 10 cm thick. The cherts can be finely microlaminated or have a more wavy or podded texture related to overgrowing red chert pods (Fig. S5g). In the lower and middle logged sections, blue cherts mainly occur within (in case of a weak shale) and symmetrically around the shaley intervals, while in the upper interval they mostly occur in the alternations preceding the shales, yet following the zebra units (see *"Zebra Intervals"* below).

- Shaley intervals. In green layers that are particularly soft, cracks may develop which appear as weak shaley horizons in the larger-scale BIF-shale cyclicity of Joffre Gorge (see e.g. S30 – S32 in Fig. S6b; top of Fig. S5d). In these intervals the white chert bands become thinner, especially the upper one, or only a single chert is present. In the more distinct shales (e.g. S53, 54 and 57) the alternations become very thin (~5cm) due to the complete absence of white (and blue) cherts. In these intervals (Fig. S7j) the regularity is defined by a single, prominent green or black shale (i.e. a very thick green layer) alternating with a slightly more prominent magnetite-rich unit intercalated by a thin brownish interval ("faint red chert"). These faint red cherts are much softer i.e. less cherty than normal red cherts and only have a faint reddish taint. Shales S10 and S12 have a different structure as they contain “tough, black, blocky and macroscopically homogenous” shales of about ~8 cm thick (Figs. S7a-d) which have previously been named “black porcelanites” (Trendall, 1969; Trendall and Blockley, 1970). These porcelanites are interpreted as stilpnomelane-rich shales and/or tuffs given their very high K (%), and seem to occur at the same position within the basic cyclicity as the green layers (see also *Uncertainties in the counting*).

- Zebra intervals. Thick (≥ 25 cm), prominent ledges are present in some of the BIF units (above S52, S53 and S56) which are composed of multiple, discontinuous white chert bands within a blueish-grey magnetite-bearing matrix (Figs. S7e-h). In these so-called “zebra intervals” there is no clear alternation visible between white chert versus softer lithology (mixed or shale) or red chert, which is why they stand out from the rest of the stratigraphy and which makes it difficult to identify individual small-scale cycles (see also *Uncertainties in the counting* below). However, in some parts reddish-white chert pods (“podded chert”) occur, which likely represent a very weakly developed red-blue chert interval (see e.g. cycles 11b in Figs. S7f,g)

A note on lateral continuity: the small-scale alternations can be visually traced within the fresh exposures at Joffre Falls, and have also been recognized in deeper parts of the gorge as well as in drill-core intersections (Trendall and Blockley, 1970). However, individual white chert bands are sometimes not perfectly continuous, especially in the zebra intervals. The cherts can vary significantly in thickness and may even disappear for a short horizontal interval, or conversely, split up into multiple chert bands or form pods. Lateral thickness variations occur to a lesser degree with the blue and red cherts.

Constructing the lithological logs

To generate a detailed record of the small-scale cyclicity and the hierarchical relationship with the larger-scale cyclicity in weathering profile, we selected three shorter intervals from a lower, middle and upper part of the Joffre Falls section (Fig. 2) covering two, three and over four consecutive BIF-shale alternations, respectively. The two main criteria for selecting the intervals, i.e. S10 to S12, S30 to S33, and Z52 to S57, were 1) a clear and continuous expression of the Knox cyclothem, and 2) the inclusion of shales of various distinctiveness / thicknesses. Some trade-off had to be made between these two criteria as the stratigraphic intervals characterized by thick, distinct shales are typically preceded or followed by BIF intervals containing zebra facies (i.e. a relatively poor expression the Knox cyclothem) – this may be a reflection of the larger difference in precession amplitude between a short eccentricity maximum and minimum during long eccentricity maxima.

The intervals were logged at a different location than the trajectory followed for logging the BIF-shale alternations in the main section, that is, closer to the waterfall, where the rocks are more freshly exposed and easier to access. Thickness measurements of the different lithological layers were measured with a tape measure and rounded to the nearest 0.5 centimeters because of the wavy character of the layers (see *Basic alternation* above), however, thin (0.1 – 0.2 cm) but distinct laminae were also recorded. In addition, individual lithological units were given a value for their relief on a similar scale as used for the large-scale BIF-shale alternations. For the BIF intervals we generally gave values of 0 or 1 for the green and mixed lithologies, values between 2 - 3 for the more magnetite-rich layers and 3.5 and 4 for the blue and white cherts, respectively. Red cherts were given a wide range of values between 0 and 3.25 as their degree of weathering was quite variable between the intervals. In the distinct shale bands the standard relief values were lowered by 2 points (so white cherts were given a 2, magnetite-rich units a 1 etc.). The shales themselves were given negative values matching those of the BIF-shale record. For the prominent zebra ledges in the upper interval we increased all values by 1 point (so white cherts were given a value of 5), as to represent their particularly high relief. Slight modifications were made afterwards to the relief based on photographs. For the final figures (Fig. S6) the blocky relief record was smoothed using Adobe Illustrator to create a more realistic weathering profile.

Color and XRF analysis

The Joffre Falls section is situated in the Karijini National Park and therefore (extensive) sampling is not permitted. In an attempt to produce a quantitative record through the sections, we conducted non-destructive color reflectance and X-ray fluorescence (XRF) analyses, using a portable spectrophotometer (Konica Minolta CM-700d) and handheld XRF gun (Thermo Scientific Niton XL3t), respectively. Measurements were placed in the middle of each discernible layer that was previously logged as a separate lithological layer, and an additional measurement point was placed halfway in between each of the lithological midpoint analyses. For thick lithological layers such as the blue cherts (e.g. Fig. S5g) and zebra intervals (Fig. S7e-h) we increased the number of analyses. Successive analyses were often overlapping since the individual layers were often thinner than both the instruments' aperture size of 1 cm. To capture the 'true' (i.e. unweathered) color and chemical composition of the layers we only targeted the relatively fresh (river-polished) surface exposures, which sometimes required lateral shifting between successive analyses of a few meters. Due to the variations in the relief, it was not always possible to measure on a flat surface and was particularly challenging for deeply incised, thin shale intervals, and this likely created an un-quantifiable bias in both the color and XRF records.

Color spectra were converted to the CIElab color space (L* a* b*) using the software SpectraMagic NX (Konica Minolta). Differences in the absolute L* values between the white chert bands should be interpreted with caution, since these noticeably varied depending on how 'clean' the cherts were. As a quality control for the XRF data we measured 2 to 3 reference powders (NIST 2790, USGS SAR-M and Till 4) after every 15 to 20 analyses to check the accuracy, precision and stability over time. Over a period of two weeks there is a small drift visible in the Si content, but a linear regression correction makes no difference for the final Si/Fe pattern and was therefore not incorporated. Because the rock measurements (both XRF and color) could not be carried out on a perfectly flat surface, uncertainties on the absolute values are likely to be high and so the data should be interpreted in a qualitative way.

Determining the small- to large-scale cycle ratio

Problem of using spectral analysis for establishing the Knox cyclothem period

Multiple peaks in the thickness range of the Knox cyclothem are visible in the MTM power spectra of the geochemical (Si/Fe and K %) records (Fig. S10), with the wavelengths around 2 – 6 cm often exceeding the 99% confidence level, and wavelengths around 9 - 12 cm (and a peak around 17 cm) often, but not always exceeding 90 - 95% confidence. Bandpass filtering (Fig. S11) indicates that, apart from recording the thinner shaley alternations, the dominant 2 - 6 cm components seem mostly related to the characteristic double to triple Si/Fe and K% maxima per single Knox cyclothem alternation: the Si/Fe (as well as lightness) records typically show two stronger maxima at the position of the double white chert ("tramrails"), and one weaker third peak corresponding to the red (or blue) chert layer; the K (%) data (but also Al, Zr, Ti and Rb %) typically show one peak below and above the red (or blue) cherts associated with the "mixed" layers, and a third weaker one in between the tramrails, corresponding to the thin green layers. The weaker 9 – 12 cm spectral peaks, on the other hand, appear to be a better reflection of the true wavelength of the small-scale cyclicity, however, they are skewed towards a too large thickness, as implied by their correspondingly filtered curves, which do not follow the thinner shaley alternations (Fig. S11).

The alternative approach of counting cycles

To avoid these complications in determining the Knox cyclothem wavelength and hierarchical relationship to the larger-scale cyclicity with times series analysis, we switched to the visual approach of cycle counting. For each of the three logged short intervals, we counted the number of small-scale alternations per larger-scale bundle based on a visual inspection of the systematic layering pattern as described in detail above (section *Basic structure of the Knox cyclothem and variants*) and as schematically illustrated in Figure 3a. Clear alternations were numbered with 1, 2, 3 etc. and uncertainties (see *Uncertainteis in the counting* below) were denoted by adding 'a' and 'b' (Fig. S6-S7). Since the shales represent an endmember lithology that only develops in a specific range of the larger-scale modulating cycle (during interpreted eccentricity-scale maxima – see p. 133), counting was done from shale midpoint to shale midpoint, that is, starting from the alternation that overlaps with the center of the shaley interval. For the lower interval (S10 – S12) we determined the number of small-scale alternations for the two bundles together because of the uncertainty in the position of separating shale S11 (see Figs. S5a, 6a). For the upper interval we counted both from (i) the midpoints of S53 to S57 and from (ii) zebra ledge 52 to zebra ledge 56, since these units also occur only in a specific part of the modulating cycle (i.e. opposite to the shales).

Uncertainties in the counting

Lower interval. In the lower interval there is some uncertainty in the number of cycles in shales S10 and S12. They have a different appearance and structure compared to the other shaley intervals that we observed at Joffre Falls, and can be subdivided into three parts (Fig. S7a-d):

Part 1 is a thick (7 - 8 cm) homogenous black shale (black porcelanite). In S12 it occurs above a white chert and thus seems equivalent to the green or black shales that typically develop in between the tramrails. However, in S10 it occurs on top of a red-blue chert interval without a visible white chert in between (i.e. seemingly in the other part of the alternation).

Part 2 consists of several magnetite-rich bands intercalated by brownish-colored softer lithology. This part looks similar to the metallic units intercalated by faint red chert characteristic for the more intense shales (Fig. S7j). There are more than two magnetite-rich layers and more than one brownish softer interval present in this part, which might suggest the presence of multiple alternations. However, the thickness of the alternations then seems too thin (< 1 cm) considering the minimum thickness observed in the other shale intervals (4 cm).

Part 3 consists of a slightly more prominent, blueish- (in S10) or ochre-colored layer (in S12) surrounded by green-black shale. The two thin orange layers at the edge of the more prominent layer in S10 look similar to the thin red chert layers below and above the blue chert in the overlying BIF unit. In this case the softer layers in part 2 should be equivalent to the shales within the tramrails part of the cycle, instead of the red chert-part. However, the more prominent layer in part 3 could alternatively represent a poorly developed, first (lower) white chert band of a tramrails, since the overlying BIF interval starts with a single white chert followed by a red-blue-red chert.

For estimating the total number of small-scale cycles in this lower interval we made the following assumptions. Because of the very specific characteristics of the two black porcelanites (part 1) in S10 and S12 we assumed that they occur (i) at the same relative position within the small-scale alternation and (ii) within the same part of the modulating (short eccentricity) cycle, and thus that we can count from the base of S10 to the base of S12. Because the position of the black porcelanite within the alternation in S12 is clear (i.e. equivalent to the green-black shales within the tramrails) we assumed that the porcelanite in S10 also occurs at this position, and thus that a white chert below is not developed here. In addition, we assumed that (iii) the thickness of the alternations cannot be much lower than in the other shales (4 cm), and so parts 2 and 3 cannot represent more than one full alternation. Then there are either 16 or 17 alternations present from S10 to S12, if we consider:

- the whole of S10 to be 0.5 alternation (green-black shale in between tramrails). We consider this interpretation less likely because of the similarities between part 2 in S12 with the magnetite-red chert units in S53 and S54 (and the seemingly similar build-up of S10 and S12), however, it is still included as an option;

- parts 1 and 3 to be two separate shales and part 2 a magnetite-red chert unit (1.5 cycle); or

- parts 1 and 2 to be a green-black shale, the blue-orange unit in part 3 to be equivalent to a red-blue-red chert and the top of part 3 again a green shale (1.5 cycle).

This corresponds to 8.25 ± 0.25 small-scale alternations per short eccentricity cycle for the Lower interval. We did not make a distinction between the number of alternations from S10 to S11 and from S11 to S12 because the definition (and position) of S11 is a bit arbitrary (Fig. S5a, 6a).

Middle interval. For the middle interval the number of alternations from S32 to S33 lies between 9 and 10 (so 9.5 ±0.5) because we do not know the exact position of the modulating (short eccentricity-related) cycle extreme within S33. S30 – S32 are thin shaley intervals occurring only within one alternation, and so we can count from one shale to the next shale. However, S33 consists of two shales of more or less equal thickness occurring in two subsequent alternations, and so the question is whether to count to the base, midpoint or top of S33.

Upper interval. In the upper interval the uncertainty in the number of alternations is mainly controlled by the high-relief zebra ledges in BIFs 53, 54 and 56. In these intervals the expression of the small-scale cyclicity is weak due to the occurrence of multiple white cherts showing irregular layering or podding textures, and the absence of clearly visible softer (mixed) intervals or red cherts.

Zebra interval in BIF 53 (Fig. S7e):
We assume that this interval consists of at least two small-scale alternations because of its thickness (33 cm versus ~15 cm for alternations containing a thick blue chert), and because of the presence of a slightly softer magnetite-mixed interval (2 cm thick) at about 21 cm height. There are no lithologic indications for another cycle visible in the lower 21 cm of this zebra interval, but considering its thickness compared to the thickest cycle in BIF53 (16 cm for cycle 3) we include this as an option (1a and 1b).

Zebra interval in BIF 54 (Fig. S7f,g):
We interpret this unit to contain at least two small-scale cycles, considering its thickness (~30 cm) and the occurrence of a softer magnetite-mixed interval at about 9 cm height followed by and interval of white-reddish oval-shaped chert pods. This is overlain again by

a more solid band of white chert that looks like a tramrails interval, i.e. implying the start of a second alternation. The red crack that occurs in between two white chert intervals at ~5 cm height might indicate the presence of a third alternation (11a and 11b). However, it is not visible everywhere (in lateral sense) and so the two white chert intervals could alternatively represent one tramrails facies.

Zebra interval in BIF56 (Fig. S7h):
This zebra interval does not show any obvious subdivision but considering its thickness (25 cm) it likely represents a double cycle (35a and 35b).

S54 and BIF54 (Fig. S7i,j):
Apart from the zebra intervals, there is some uncertainty in the number of alternations in S54 and BIF 54, with possibly an extra cycle 9a and 19b.

Link to the Milankovitch cycles

U-Pb and cyclostratigraphic evidence from drill-core

In a parallel study, we have established an average depositional rate of ~5 - 15 m/Myr for the Joffre Member based on high-precision CA-ID-TIMS zircon dating of core DD98SGP001 (DD98) of Silvergrass (Fig. S1), for which we have targeted four high-Zr shale intervals between 371 to 186 m depth (Lantink et al. manuscript in review). In this core interval, we encountered a similar regular expression of the Knox cyclothem throughout the majority of stratigraphy, likely corresponding to the rhythmical "chert-BIF" and "chert-mudrock" couplets mentioned in Pickard (2002). The Knox cyclothem alternations in the studied core interval are of the same thickness scale as at Joffre Falls (i.e. ranging from 3-4 cm to up to 20-25 cm), and exhibit a wide variety of lithological types that are very similar but not identical to their more weathered expression at Joffre Falls, with a most notable difference the absence of (conspicuous) double white chert layers in the lower part of the core. In addition, a larger-scale variation was observed in certain intervals, manifested by the occurrence of thick stilpnomelane shales and changing ferric oxide mineral content, which appears equivalent to, but is less obvious than, the regular ~85 cm alternations at Joffre Falls, given a ~8:1 – 9:1 cycle period ratio with the Knox cyclothem determined with spectral analysis.

TIMS U-Pb dating of S39

Due to the absence of unique, unambiguous marker beds in the stratigraphy of the Joffre Member, previous attempts at a lithostratigraphic correlation between core DD98 and Joffre Gorge and/or the Joffre Member type column (Trendall and Blockley, 1970) have proven far from trivial (see next section). Therefore, in an attempt to independently correlate our section to the core, a thin band within shale S39 with high Zr content (measured by handheld XRF) from Joffre Falls was collected for CA-ID-TIMS U-Pb zircon dating. The sample was subsequently crushed to <250 μm and passed over a

Wilfley table before zircon grains extracted under a binocular microscope. The most prismatic, clear and euhedral zircon grains were then annealed at 950°C for 48h and then chemically abraded in concentrated HF at 210°C for 4x3h (Widmann et al., 2019). After chemical abrasion, the zircons were cleaned then spiked with ~5 mg of the EARTHTIME ^{202}Pb + ^{205}Pb + ^{233}U + ^{235}U tracer solution (Condon et al., 2015; McLean et al., 2015) and dissolved in 70 µl of concentrated HF at the high precision U-Pb geochronology lab at the University of Geneva following the techniques outlined in Lantink et al. (2019) and briefly described here. After digestion, the U and Pb fractions were separated using anion exchange columns. The aliquots of U and Pb were then loaded onto outgassed zone-refined Re filaments and placed into a Thermo Scientific TRITON. Pb was measured in dynamic peak jumping mode using a secondary electron multiplier, whereas UO_2 was measured in static mode using Faraday cups attached 1012 Ω resistors or when the UO_2 signal was small the electron multiplier was used in dynamic peak jumping mode. All common Pb was attributed to laboratory blank and was assigned the long-term isotopic composition of the Geneva procedural blank (Schaltegger et al., 2021). All U-Pb data processing was conducted using the Tripoli and Redux software packages, following the algorithms of (McLean et al., 2011). Ages reported here are given without the additional uncertainty associated with the tracer calibration and uranium decay constants. All ages were corrected for initial ^{230}Th and ^{231}Pa disequilibrium in the melt using a U/Th ratio of the magma of 3.5 and an initial ^{231}Pa/^{235}U ratio of 1.1.

Inconsistency between the exact U-Pb age of S39 and existing stratigraphic correlations

The ^{207}Pb/^{206}Pb age of 2459.2 ±1.3 Ma obtained for S39, falling well within the 2469 – 2454 Ma range, suggests that the Joffre Falls section correlates to the dated 371 – 186m core interval of DD98, i.e. correlating to the lower 185-meter-interval of the Joffre Member, assuming that its base in that core occurs at 372m depth (Pickard, 2002). This result deviates from the estimated 250m stratigraphic height of S39 above the base of the Joffre Member identified downstream of Joffre Falls in the gorges of Karijini National Park by Trendall (1969) (Figs. S1-2), and is in conflict with the lithostratigraphic and natural gamma log interpretation of core DD98 by Pickard (2002). According to Pickard (2002), the high gamma response shales at 186 m core depth (which is the youngest dated 2454 Ma shale) and at 127m core depth correspond to Trendall's 1st and 5th porcelanites (P1 and P5), respectively, which he identified in the gorges downstream of Joffre Falls i.e. at a lower stratigraphic position within the Joffre Member (see Plate 26 in Trendall, 1969). Unfortunately, a substantial part of the lithology between P1 and the higher P5 in core DD98 is brecciated / disrupted, possibly due to a nearby dolerite intrusion in the Silvergrass area (Pickard, 2002), as a consequence of which the presence of the interstitial porcelanites P2-P4 could not be verified, thus leaving the correlation open to doubt (Trendall et al., 2004).

Nevertheless, given a reasonable plausibility that these earlier correlations are correct, this could mean that our age derived from S39 is several millions of years too old, for example, because the two zircons that were dated are inherited and therefore do not accurately reflect the deposition age of the unit. In that case, the S39 age can be used as a maximum depositional age, which is close to, but slightly older than the expected age, and thus only provides a loose indication for the correlation between Joffre Falls and core DD98 / the stratigraphy at Silvergrass. Regardless of this uncertainty which, unless/ until more U-Pb ages are generated from the Joffre Falls stratigraphy remains unresolved. However, we have good reason to assume that the same depositional rate established for core DD98 is extended to the Joffre Falls interval, given the observed similar thickness of the Knox cyclothem and cycle hierarchy (see *Chapter 3*).

Short- and long-eccentricity origin

The thickness and 1:4 ratio of the main 78 – 93 cm and ~3.3 m cycles is fully consistent with a short (~100 kyr-) and long (405 kyr-)eccentricity origin, if we take a sedimentation rate of ~10 m/Myr based on the U-Pb results of the Joffre Member, as well as underlying Kuruman IF-Dales Gorge Member BIFs (Lantink et al., 2019). More specifically, the partitioning into separate 78 and 93 peaks as seen in the MTM spectrum of the Joffre Falls composite record (Fig. 4; Fig. S8a-b), which when linking 3.3 m to 405 kyr (Table S2) convert to periodicities around 95 and 113 kyr, respectively, could reflect the partial decomposition of the short eccentricity signal into its two main pairs or the two corresponding strongest individual terms, i.e. the 95 kyr ($g_4 - g_5$) and 124 kyr ($g_4 - g_2$) cycles (see e.g. the power spectra for the Capo Rosello section in Fig. 5 of Hilgen et al. (2014)). This interpretation is supported by the relationship between the lithology, the phase relation of the separately filtered 78 cm and 93 cm cycles (at 65 – 85 cm and 85 – 105 cm, respectively), and the amplitude of their combined filter (65 – 105 cm) in Figure S9, which shows an alternating constructive - destructive interference pattern equal to that of the 95 kyr and 124 kyr cycles as determined by the 405 kyr ($g_2 - g_5$) cycle (Laurin et al., 2016). The decoupling in amplitude of the separately filtered cycles to the top of the Joffre Falls record (cycles no. 51 – 57 in Fig. S9) and absence of a second > 90 cm peak in the MTM spectrum when this upper interval is excluded (Fig. S13), however, suggest that the majority of spectral power around 93 cm in the MTM spectrum of the complete Joffre Falls composite record (Fig. 4; Fig. S13) is due to an overall increase in thickness of the alternations (compacted depositional rate) at the top.

The longer-period amplitude modulation cycles seen in the MTM spectrum of Joffre Falls around 5 m, 8m and 11m (Fig. 4; Fig. S8) convert to time periodicities around 650 kyr, 980 kyr and 1.35 Myr, the shortest two of which closely approximate those of the weaker 680 kyr and 980 kyr eccentricity cycles related to $g_2 - g_1$ and $g_1 - g_5$ respectively (Table S2). The third, longest cycle may be linked to the unstable, now 2.4 Myr-period eccentricity cycle related to $g_4 - g_3$. In this case, its interpreted much reduced period implies a significant change (transition) in mode of the secular resonance between the precessional motion of the perihelia and nodes of the orbits of Earth and Mars compared to the present day (for a detailed explanation see e.g. Ma et al., 2019; Olsen et al., 2019; Laskar, 2020).

Climatic precession origin

Considering the evidence for a dominant imprint of short- and long-eccentricity-related cyclicity within the Joffre Falls stratigraphy, as well as the potential presence of eccentricity's longer-period weaker cycles, the most logical explanation for the small-scale Knox cyclothem alternations is that they represent climatic precession. This interpretation is further supported by the potential amplitude modulation relationship (see Fig. S6d), and the observed ~1 : 9 ratio between the small-scale cycles and larger-scale shale-BIF alternations. This ratio exceeds the 1:7 ratio established for 1.4 Ga derived from cyclostratigraphic analysis of the Xiamaling record (Zhang et al., 2015; Meyers and Malinverno, 2018), and is consistent with the modelled climatic precession period of 11-12 kyr at 2.5 Ga by Berger and Loutre (1994) and Waltham (2015).

Based on high-resolution XRF core scan analysis of core DD98, combined with geochemical modelling (see *Chapter 3*), a first-order paleoenvironmental interpretation was formulated for the Knox cyclothems, linking them to precession-forced changes in marine primary productivity, deposition of organic matter and iron (oxyhydr)oxides precipitation, which induced considerable changes in early diagenetic redox conditions. These diagenetic changes may also be an underlying cause for the intricate layering structure of the Knox cycles at Joffre Falls, i.e., the occurrence of the double white chert bands and up to three shaley/clay beds per single alternation. While paleogeographic reconstructions place the Hamersley-Transvaal Basin at low latitude (de Kock et al., 2009; Gumsley et al., 2017), the alternative option of a semi-precession origin is not logical because of the unique sequence rather than symmetrical repetition of lithologies (Fig. 3a). Moreover, in that case you would expect to have a stronger, second clay layer developed in the shales, the inferred eccentricity maxima (see p.133), while instead a repetition of lithologies is lacking in these intervals. The absence of an obvious obliquity signal is consistent with the observed eccentricity dominance and inferred low-latitude position of the Joffre Falls site, although interference of obliquity with precession might be responsible for sub-eccentricity-scale variability seen in the expression of the Knox cyclothems in some of the BIF intervals. Note for instance the return of a more shaly cycle from cycle no. 1 to 4 in the S30-31 interval (Fig. S6b, S5c), which is consistent with the 4:3 period ratio between obliquity and precession.

Determining the Earth-Moon distance and daylength

Three methods for calculating the average climatic precession period

Using our established ratio between the small-scale cycles and larger-scale bundles (Table 1), a mean duration of the average climatic precession signal was determined according options 1, 2a and 2b which are explained in the main text. For option 1, average thicknesses of the precession-related cycles per logged interval were calculated from their corresponding stratigraphic interval (thickness) in the Joffre Falls composite record. We decided to use these thicknesses instead of the measurements from the detailed logs, because the mean wavelength of the 405 kyr cycle (i.e. ~3.3 m), used to convert the thickness of the small-scale cycles to time, was determined with MTM analysis of the large-scale log (Fig. S13); since the small-scale alternations were logged at different lateral position than the trajectory followed for the large-scale log, using the thickness of the detailed logs would introduce unnecessary extra bias from lateral changes in sediment compaction and differences in the measurements themselves (e.g. for the detailed logs, measurements were rounded up to the nearest 0.5 cm – see *Constructing the lithological logs* above). This is also the reason why the total number of precession-related cycles in the three intervals in Table S1 deviates slightly from the number in Table 1 in the main text, because the upper and lower boundaries were defined by measured stratigraphic horizons in the large-scale log and not by inferred short eccentricity cycle extremes (i.e. shale midpoints or zebra ledges). For the upper interval, we applied a thickness correction for the wavelength of the 405 kyr-related cycle (using 3.8 m instead of 3.3 m), which is based on the thickness of the main spectral wavelength of the short-eccentricity-related alternations (Fig. S11), suggesting a 14% increase in compacted sedimentation rate in that interval.

For options 2a and 2b we used the 'peak' function in Astrochron (Meyers, 2014) to identify successive short eccentricity maxima from the La2004 eccentricity solution from 0 to 50 Ma (1 kyr time steps) and ZB18a 50 – 80 kyr (1 kyr time steps), respectively. Afterwards we visually checked all extracted peaks and made slight modifications to the list if some peaks were very weak or were not picked up by the peak function, or if closely spaced double peaks were identified at plateaus (see Fig. S15). We subsequently made a list of successive durations from which anomalously short i.e. < 80 kyr and long i.e. > 115 kyr cycles were removed. From this filtered list we created three new lists with sums of 2, 3 and 4 successive cycles. Using a Monte Carlo simulation, we subsequently made 60,000 and 80,000 random selections from each of these three list acquired from the La2004 0 – 50 Ma and ZB18a 50 – 80 Ma intervals, respectively. The corresponding average duration of 2 successive cycles was used to calculate the duration of precession based on the lower interval, the average of 3 successive cycles for the middle interval and the average of 4 cycles for the upper interval. For determining the overall mean period and 2SD error for the three intervals combined, we took the sum of the randomly selected of 2, 3 and 4 successive cycle durations for each of the simulations.

Note that our choice of selecting short eccentricity maxima instead of minima builds on the premise that the shale intervals correspond to eccentricity maxima. While we cannot be sure about this assumption, we have several reasons to belief that this is in fact the case. For example, a very large K % amplitude for the precession-related cycles is observed in the shales (Fig. S6d), compared to a very weak cyclothem precession in the opposing zebra intervals; also, the limited variability in relief seen between successive BIF intervals (see *Constructing the composite log* above) may be a consequence of a reduced precession amplitude. However, regardless of the true phase relation between the lithology and eccentricity, our approach of selecting the duration between eccentricity maxima as opposed to minima makes no difference for the calculation of the mean short eccentricity period.

Uncertainty:
For option 1 we assumed a 2% uncertainty in the thickness measurements, based on the difference in stratigraphic thickness measurements between S10 and S27 in this study and in Trendall 1969 (see Fig. S2 caption); and 10% uncertainty in the 3.3 m periodicity, based on the MTM peak broadness (see Fig. S14). For the total error on the average precession periods obtained via options 2a and 2b, we used (i) full uncertainties in the number of small-scale cycles per chosen interval and (ii) 2 sigma uncertainties of the average eccentricity durations derived from the 60,000 / 80,000 random samples of 2, 3 and 4 successive short eccentricity durations from the La2004 / ZB18a solutions.

Extracting Earth's axial precession frequency p

The 'average' climatic precession signal reflects the sum of individual $p + g_k$ components, whereby the strongest (largest amplitude) cycles have the largest effect on the total. As such, we have formulated the following approximation (only considering the four strongest terms):

(1) Average climatic precession = amplitude fraction g_5 * $(p + g_5)$ + amplitude fraction g_2 * $(p + g_2)$ + amplitude fraction g_4 * $(p + g_4)$ + amplitude fraction g_3 * $(p + g_3)$, or:

$$average\ climatic\ precession = \sum_{k=2}^{5} \frac{b_k}{b_{2,3,4,5}} (p + \ g_k) \qquad \text{Eq. 1}$$

where g_k indicates the fundamental terms in the frequency decomposition of the eccentricity signal in arcseconds year^{-1} ("/yr) of planets k (as indicated in Table 4.3 in Laskar, 2020), b_k represents the corresponding amplitudes and $b_{2,3,4,5}$ indicates the sum of the amplitude values of the four leading g_k terms that are considered.

We have tested the validity of this approximation by comparing i) the reconstructed mean climatic precession period from three different time intervals of the La2004 climatic precession solution (0-10 Ma, 25-35 Ma and 40-50 Ma), with ii) the mean climatic precession period calculated via eq. 1 given known values of p at 5 Ma, 30 Ma and 45 Ma, respectively. The mean climatic precession periods from the La2004 solution intervals were determined using the 'peak' function in Astrochron (Meyers, 2014) whereby anomalously short (< 10 kyr) and long (>30 kyr) cycles were excluded. The corresponding p values were derived from eq. 40 in Laskar et al. (2004), which is a polynomial approximation for the secular evolution of the p frequency with time due to tidal dissipation as implemented in the La2004 precession solution. For g_k and b_k we used the values from the La2004 [-15 + 5 Ma] interval as listed in Table 4 of Laskar et al. (2004). This resulted in very similar values for each of the three time intervals (Table S4).

Rewriting eq. 2 gives:

p = average precession frequency - (amplitude fraction g_5 * g_5 + amplitude fraction g_2 * g_2 + amplitude fraction g_4 * g_4 + amplitude fraction g_3 * g_3), or:

$$p = average\ climatic\ precession - \sum_{k=2}^{5} \frac{b_k}{b_{2,3,4,5}}\, g_k \qquad \text{Eq. 2}$$

Thus, using equation 2, we can subsequently estimate p from our reconstructed mean climatic precession period (Table 2), assuming known values for g_k and b_k. Because the drift in the g frequencies is negligible compared to the uncertainty in MTM peaks, as well as the uncertainty in the Knox cyclothem counts and mean short eccentricity durations, we similarly used the g_k values (b_k values) for g_5, g_2 and g_4 and g_3 from the La2004 [-15 + 5 Ma] time interval as listed in Table 4 of Laskar et al. (2004), which are 4.257 "/yr (0.0189), 7.457"/yr (0.0163), 17.91"/yr (0.013) and 17.367 "/yr (0.0088), respectively.

Uncertainty:

Our uncertainty on the calculated p frequency (10.9 ± 0.8 kyr) includes the propagated 2SD errors of our final estimated value for the mean climatic precession period, obtained by combining the outcomes of options 2a and 2b (Table 2). In this way, our result also includes some, though an unknown proportion, of the uncertainty in the g_k frequencies (and corresponding b_k values) for the part of the Solar System history that cannot be accurately predicted from the present conditions.

Converting *p* to Earth-Moon distance and daylength

To estimate the E-M distance from our reconstructed axial precession frequency p we followed the same approach as Meyers and Malinverno (2018) by employing cubic spline interpolation of a grid of modelled values for Earth's axial precession frequency versus Earth-Moon distance (Fig. S18) derived from eq. 13 -15 in Waltham (2015); the dataset with the calculations was personally provided by D. Waltham. Equations 13-15 in Waltham (2015) are simplified from those of Berger and Loutre (1992) by assuming co-planar circular orbits, and provide a finite difference solution that quantifies Earth-Moon distance as a function of obliquity. As such, this enables the precession frequency p to be estimated from the Earth-Moon distance. Note that the calculations for the obliquity of the Earth as a function of Earth-Moon distance from Waltham (2015) are indistinguishable from the full solution of Goldreich (1986) (see Figure 5 in Waltham, 2015). From our established Earth-Moon distance, we then calculated the length of day (LOD) from eq. 10 in Berger and Loutre (1992), which links the Earth's rotational angular velocity to E-M distance and accounts for changes in dynamical ellipticity associated with changes in rotation rate (Lambeck, 1980).

Uncertainty: propagation of the 2SD uncertainties for the reconstructed axial precession frequency to Earth-Moon distance was done by fitting the grid of modelled *p* (x) vs Earth-Moon distance (y) with a power law function, which gave: y = 169.04x^0.2577; $R^2 = 0.998$ (Fig. S18). The 2SD uncertainties could subsequently be translated following the standard rule for a function of the form y = x^n: δy = |n|*δx/|x|*|y|. The same error propagation method was used for the conversion of Earth-Moon distance to LOD, given the exponential eq. 10 in Berger and Loutre (1992).

Supplementary Figures

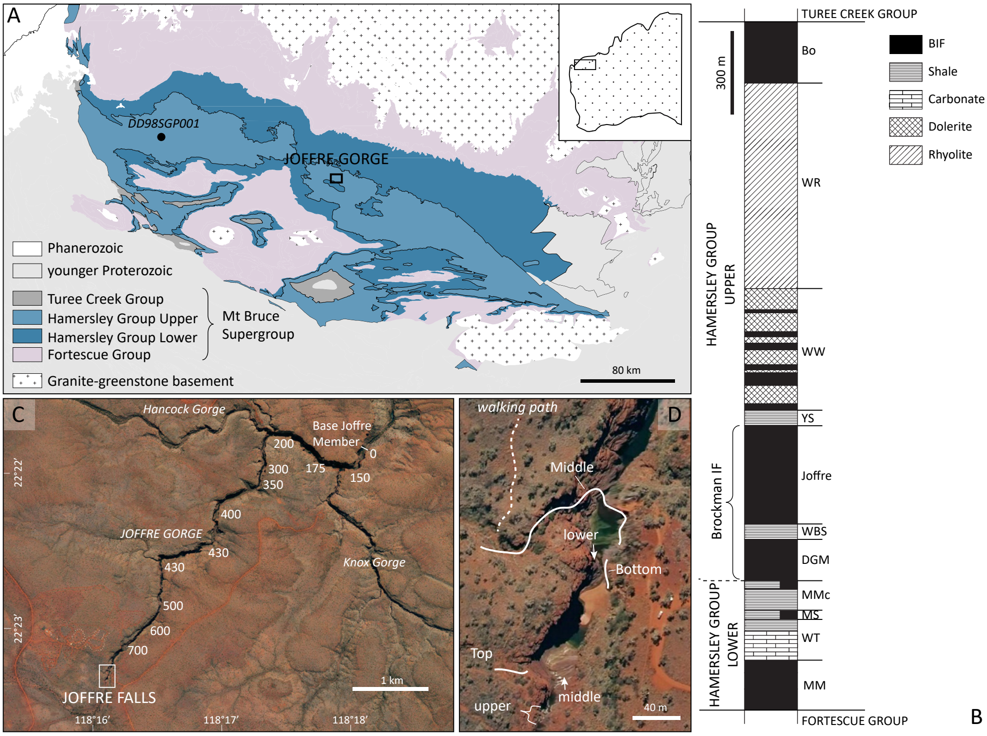
A
DD98SGP001
JOFFRE GORGE
Phanerozoic
younger Proterozoic
Turee Creek Group
Hamersley Group Upper
Hamersley Group Lower
Fortescue Group
Mt Bruce Supergroup
Granite-greenstone basement
80 km
C
Hancock Gorge
Base Joffre Member
0
200
175
150
300
350
400
JOFFRE GORGE
430
430
Knox Gorge
500
600
700
JOFFRE FALLS
1 km
22°22'
22°23'
118°16'
118°17'
118°18'
walking path
D
Middle
lower
Bottom
Top
upper
middle
40 m
TUREE CREEK GROUP
300 m
Bo
WR
WW
YS
Joffre
WBS
DGM
MMc
MS
WT
MM
HAMERSLEY GROUP UPPER
Brockman IF
HAMERSLEY GROUP LOWER
FORTESCUE GROUP
BIF
Shale
Carbonate
Dolerite
Rhyolite
B

Figure S1. ((**A**) Geological map of the Hamersley Basin on the Pilbara Craton in NW Australia with the location of Joffre Gorge and core DD98SGP001 (22°03’29.9”S 116°50’06.0”E). Image extracted and modified from the GSWA 2020, GeoVIEW.WA. (**B**) Generalized stratigraphy of the Hamersley Group. Modified from Harmsworth et al. (1990). (**C**) Aerial view of Joffre Gorge and connected gorges within the Karijini National Park. Numbers in white represent the stratigraphic height of the Joffre Member in feet above adjacent gorge floor according to measurements by Trendall (1969; adapted from Plate 25). Image from GeoVIEW.WA. (**D**) Zoom-in on section Joffre Falls (22°23'24"S 118°16'08"E). White lines labelled with ‘Bottom’, ‘Middle’ and ‘Top’ indicate the approximate logging trajectory for the large-scale alternations. The position of the detailed logs is indicated with ‘lower’, ‘middle’ and ‘upper’.

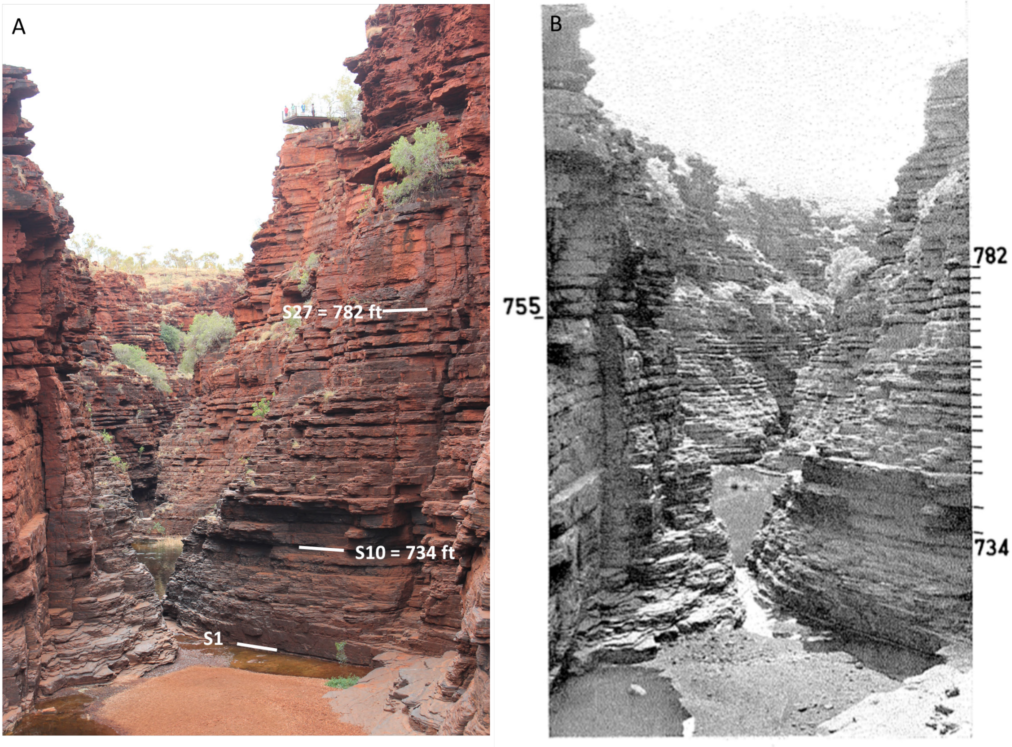

Figure S2. Comparison of (**A**) the shale numbers in our log of Joffre Falls to (**B**) stratigraphic measurements (in feet) by A.F. Trendall from the base of the Joffre Member downstream (photo: Plate 28D in Trendall, 1969). Black horizontal lines indicate the regularly occurring stilpnomelane-rich shale bands. The shales at 734 and 782 feet in **B** correspond to shales S10 and S27 from our log, respectively. According to our measurements, there is 14.3 m in between the midpoints of S10 and S27, which agrees quite well with Trendall's measurements: (782 ft – 734 ft) x (0.3048m/ft) = 14.6 m. There is 5.96 m of stratigraphy between the midpoints of S1 and S10, so following Trendall (1969), the base of our log would be at 734 ft x (0.3048 m/ft) – 5.96 m = 217.8 m above the base of the Joffre Member and 46 m above the JP5 (fifth porcelanite marker bed). Shale S39 would correspond to a height of 248.6 m above the Joffre Member base.

Figure S3. Photographs of the logged shale-BIF alternations at Joffre Falls. (**A** - **B**) Bottom section (S1 – S14). The alternations at the base of the gorge have a more blocky appearance, which we suspect is mainly related to a difference in weathering compared to higher up in the sequence. The rocks at the base of the gorge are more frequently polished by river water resulting in a fresher surface exposure. (**C**-**E**) Middle section (S14 – S49). Note the distinct shales S16, S18-S19 and S23 – S29 surrounded by intervals with weaker shales. (**F** - **G**) Top section (S49 – S57). This section is relatively far away from the waterfall and so the rocks have been more affected by chemical weathering, producing larger and more gradual relief changes from 'BIF' to 'shale'. This is incorporated in the logs as transitional 'platy' intervals between the shale and BIF units occurring in BIF 51 to 56 (Fig. S4).

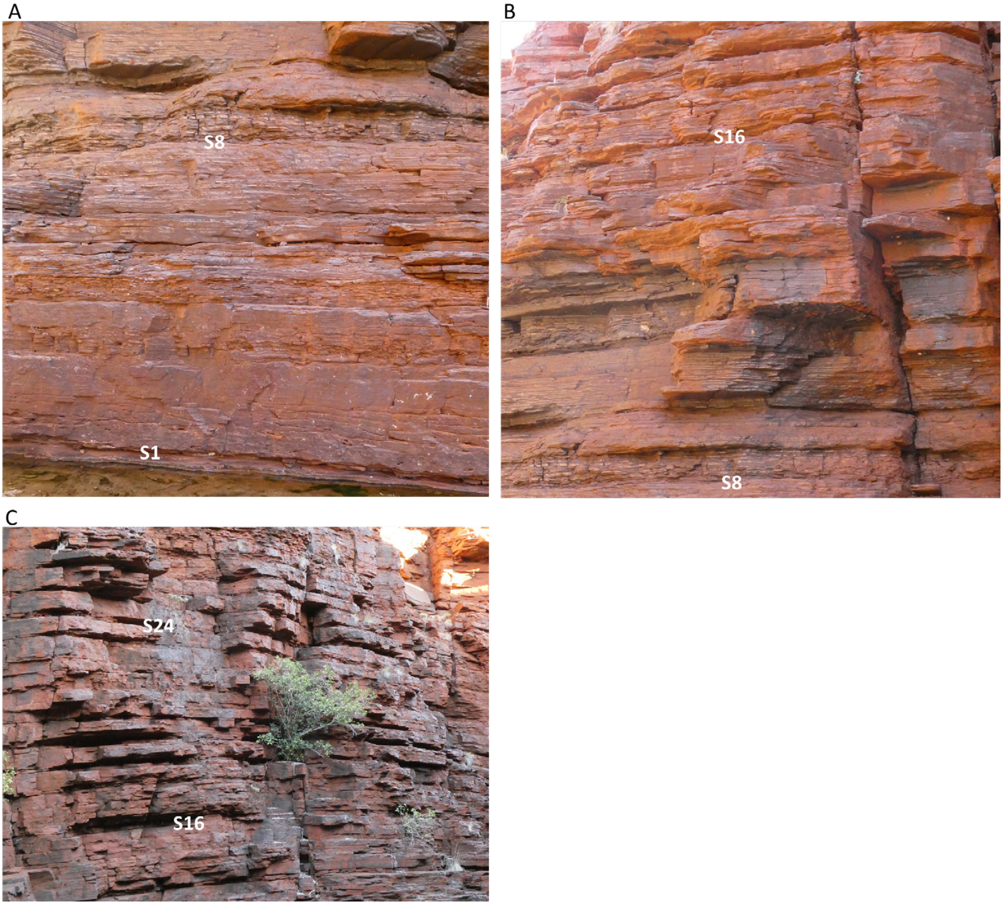

D

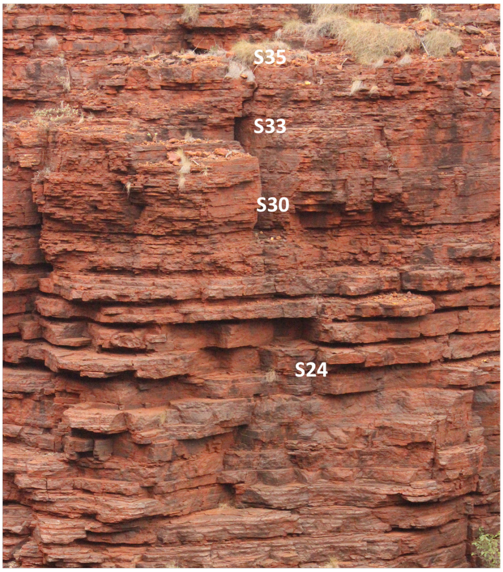
S35
S33
S30
S24

E

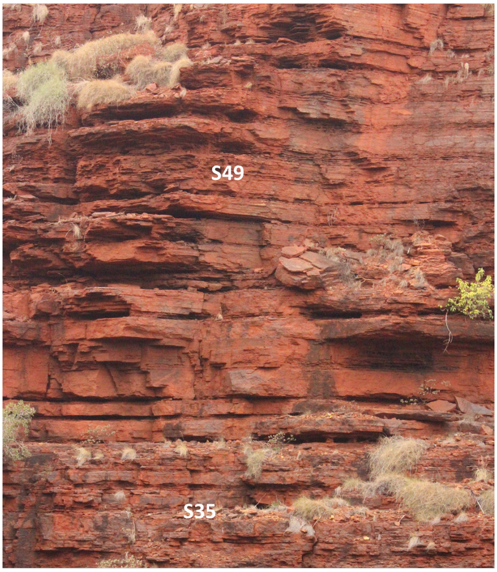

F

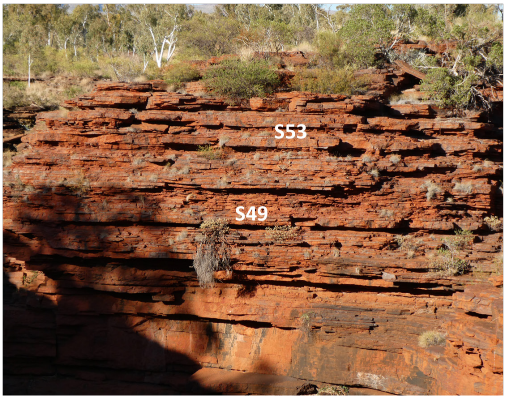

G

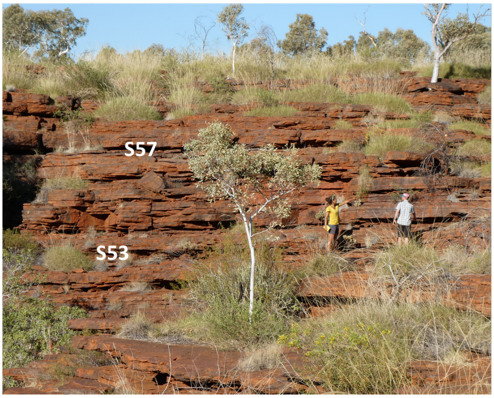

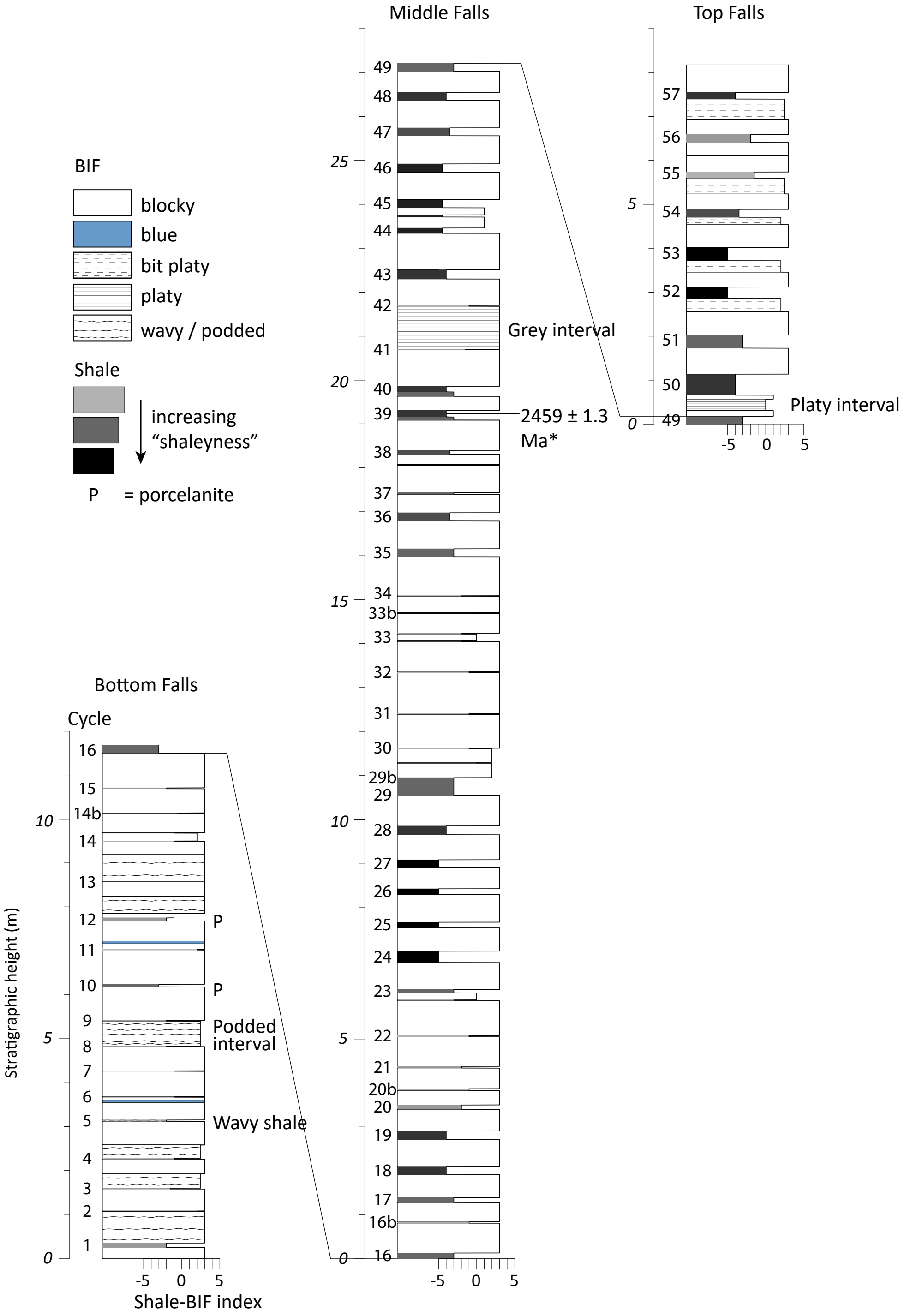

Middle Falls
Top Falls
BIF
blocky
blue
bit platy
platy
wavy / podded
Shale
increasing "shaleyness"
P = porcelanite
Grey interval
2459 ± 1.3 Ma*
Platy interval
Bottom Falls
Cycle
Stratigraphic height (m)
Shale-BIF index
-5 0 5
P
P
Podded interval
Wavy shale

Figure S4 (previous page). Composite log and weathering profile of section Joffre Falls. “Podded interval”, “wavy shale”, “grey interval”, “platy interval” indicate characteristic horizons that were useful for field correlation in addition to the characteristic shale-BIF pattern. “Blue” indicates distinct blue riebeckite chert layers. Note that BIFs 3, 4, 11 and 12 at the base are subdivided into a lower podded and upper rectangular-shaped interval, and that transitional platy intervals occur on top of more prominent zebra ledges in the upper part of the Falls. *CA-ID-TIMS zircon age from this study.

Figure S5 (continues next page). Photographs of the logged intervals for the small-scale alternations. (**A**) Overview of the lower interval S10 - S12. Note that S11 is very weak. (**B**) Detail of clear alternations between a double white chert (tramrails) and a red chert in cycles 4 – 7. A blue chert appears in between the red chert in cycle 8. S11 was defined as the thin orange layer at the top of this cycle, above which cycle 9 forms a small overhang. Yellow crosses mark the positions of the color and XRF analyses. (**C**) Overview of the middle interval S30 – S33. (**D**) Detail of the S31- S32 interval showing cycles 11 - 20. Note that only a single white chert band is present in cycle 12. (**E**) Zoom-in on cycles 16 and 16 showing the appearance of thin green layers in between the tramrails. (**F**) Overview of the upper interval BIF52 – S57. Note the thin and very regular alternations in visible in S53 and the prominent zebra ledges Z52, Z53 and Z56. (**G**) Detail of cycles 17 – 28. The hammer indicates the approximate vertical extent of S55. In the bottom alternations (cycles 17 – 21) multiple, irregular white chert bands occur instead of a two white bands, and red cherts are absent.

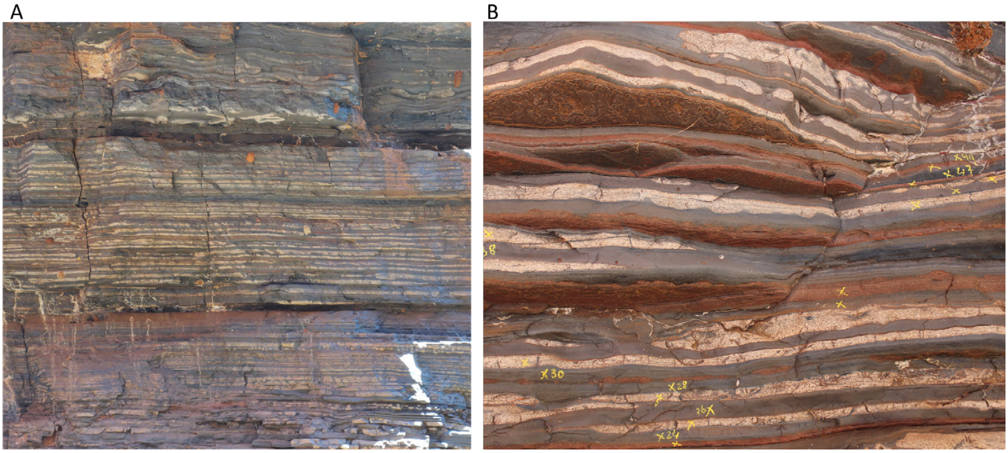

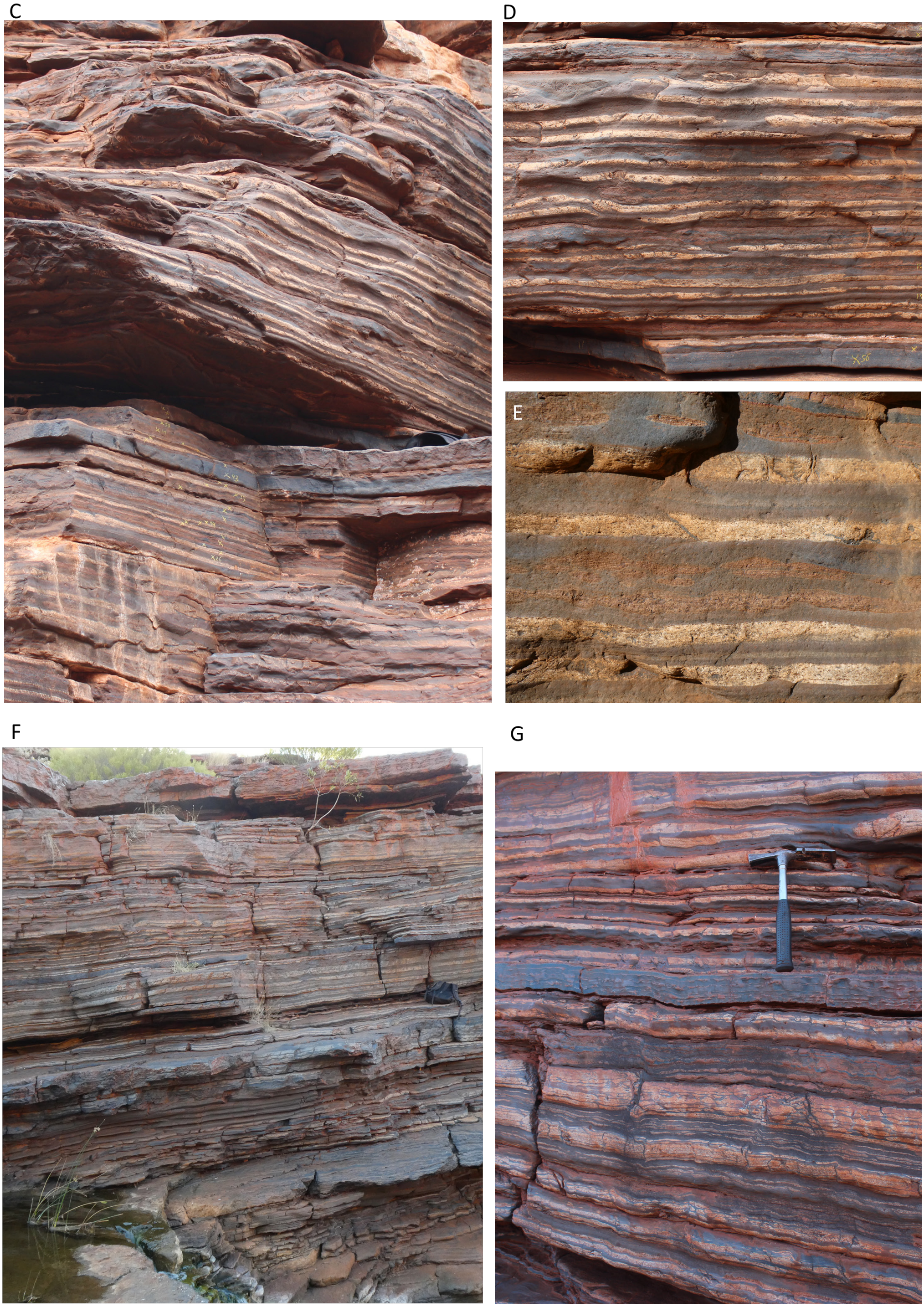
C
D
E
F
G

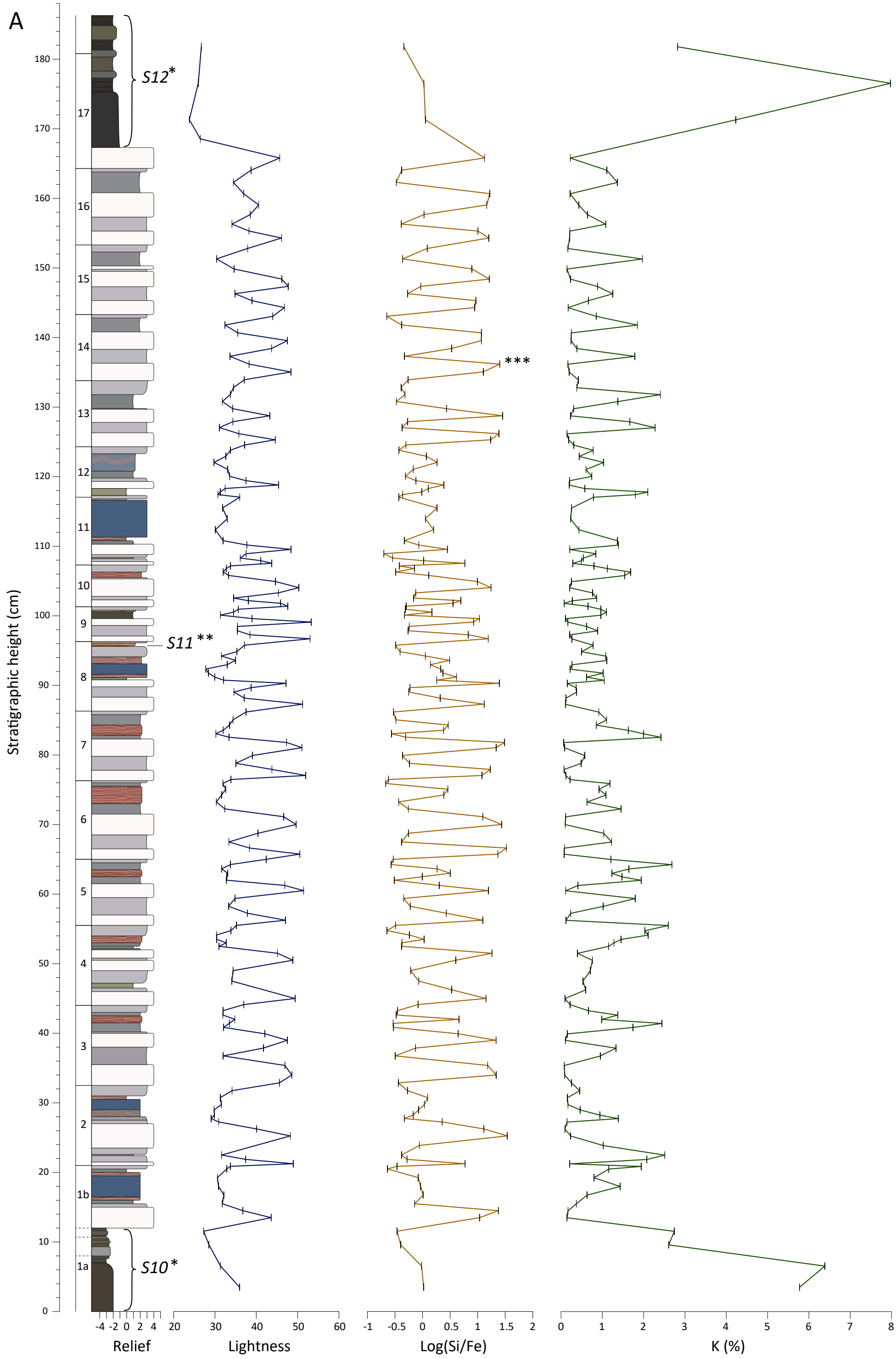
A
Stratigraphic height (cm)
0
10
20
30
40
50
60
70
80
90
100
110
120
130
140
150
160
170
180
1a
1b
2
3
4
5
6
7
8
9
10
11
12
13
14
15
16
17
S12*
S11**
S10*
***
-4 -2 0 2 4
Relief
20 30 40 50 60
Lightness
-1 -0.5 0 0.5 1 1.5 2
Log(Si/Fe)
0 1 2 3 4 5 6 7 8
K (%)

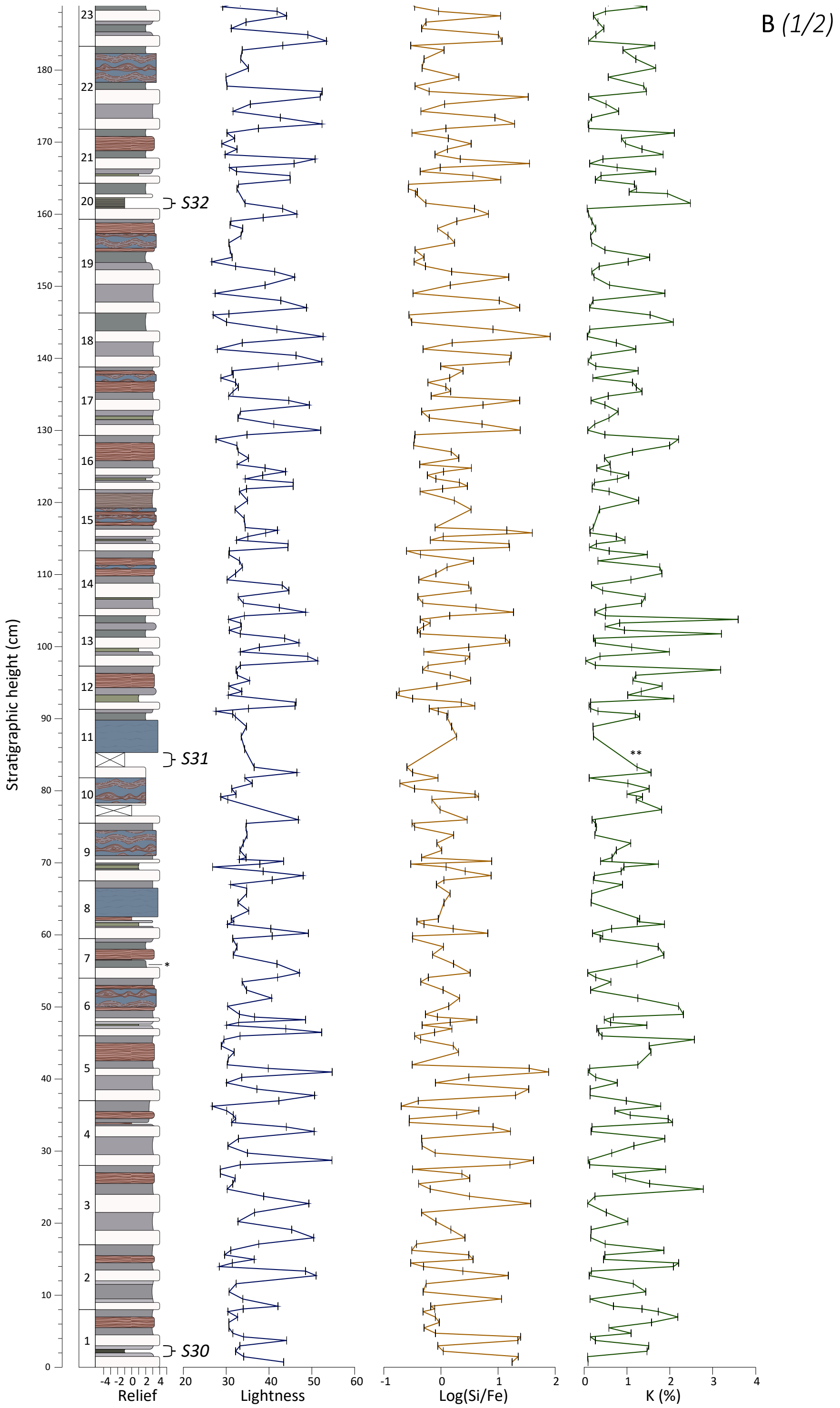
B (1/2)
Stratigraphic height (cm)
0
10
20
30
40
50
60
70
80
90
100
110
120
130
140
150
160
170
180
1
2
3
4
5
6
7
8
9
10
11
12
13
14
15
16
17
18
19
20
21
22
23
S30
S31
S32
*
**
-4 -2 0 2 4
Relief
20 30 40 50 60
Lightness
-1 0 1 2
Log(Si/Fe)
0 1 2 3 4
K (%)

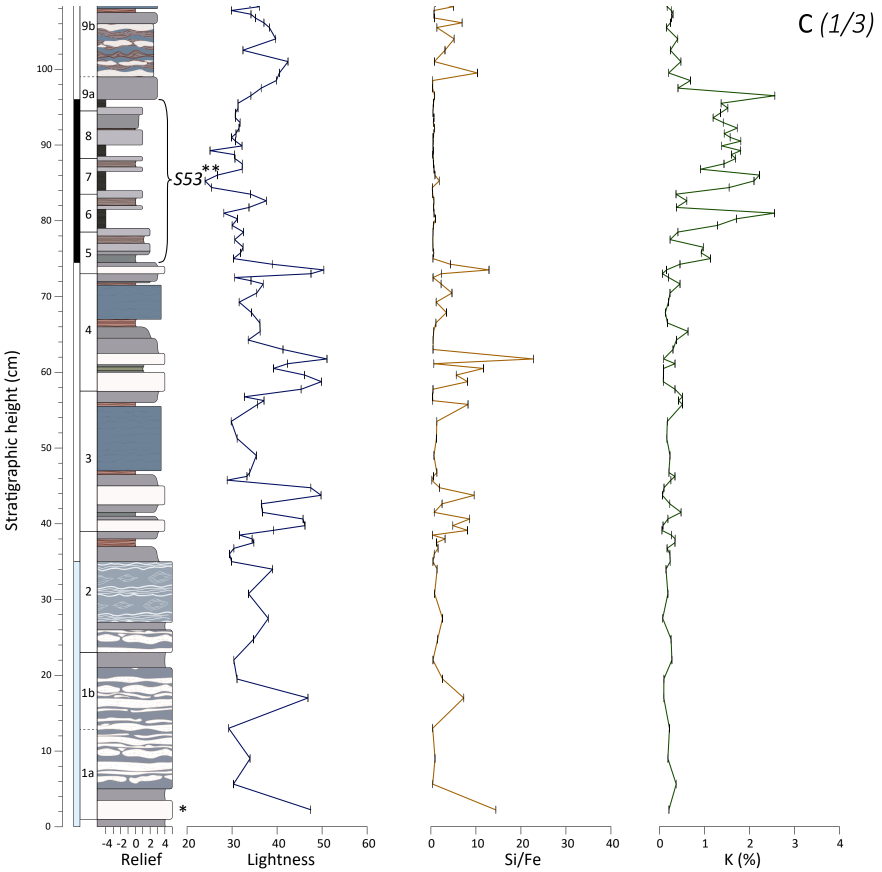
C (1/3)
Stratigraphic height (cm)
0
10
20
30
40
50
60
70
80
90
100
1a
1b
2
3
4
5
6
7
8
9a
9b
S53
**
*
-4 -2 0 2 4
Relief
20 30 40 50 60
Lightness
0 10 20 30 40
Si/Fe
0 1 2 3 4
K (%)

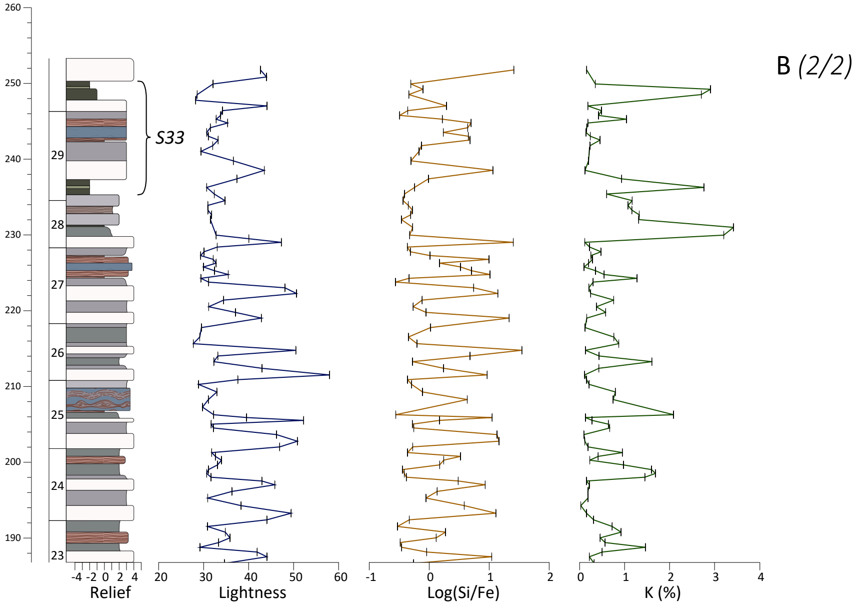
B (2/2)
190
200
210
220
230
240
250
260
23
24
25
26
27
28
29
S33
-4 -2 0 2 4
Relief
20 30 40 50 60
Lightness
-1 0 1 2
Log(Si/Fe)
0 1 2 3 4
K (%)

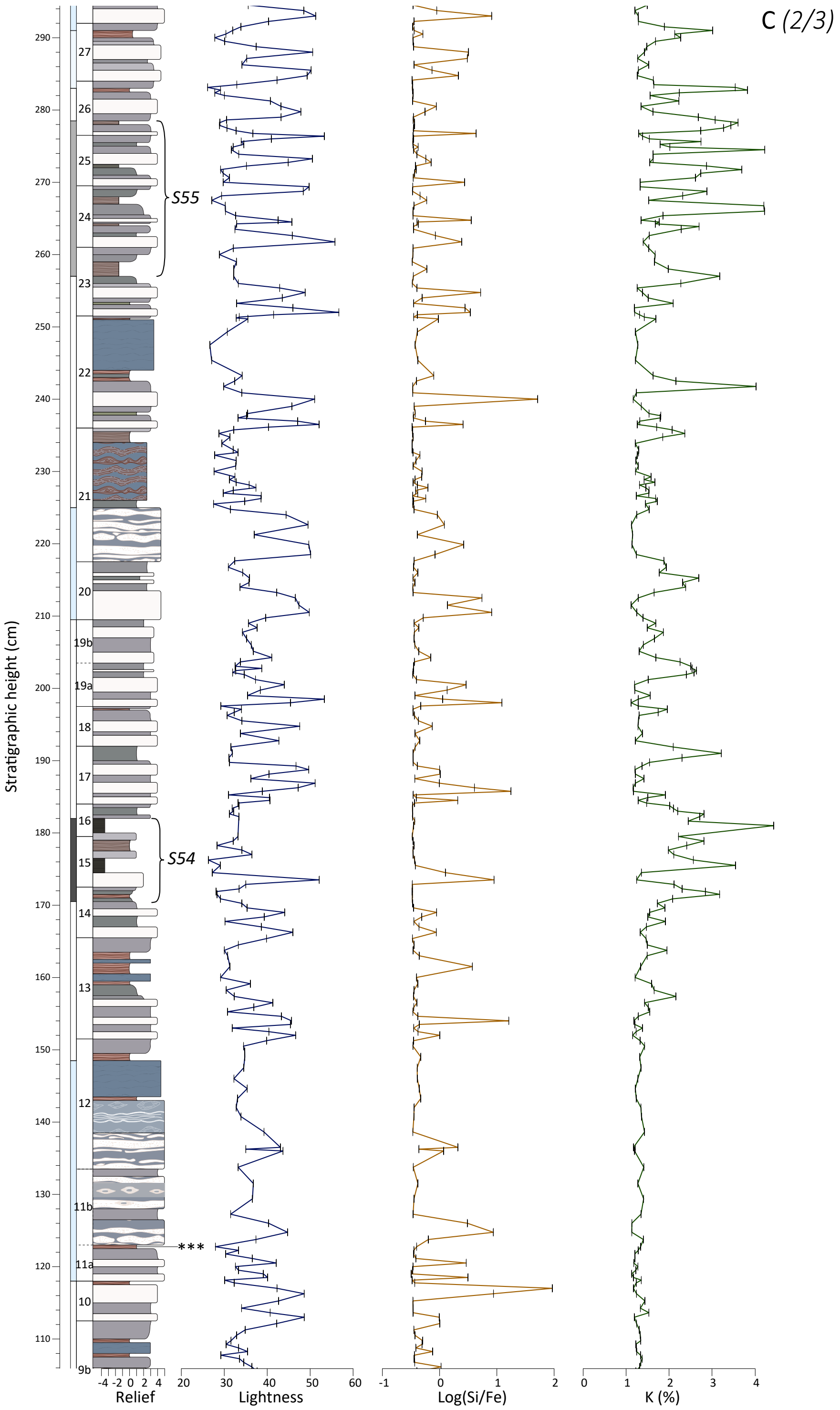
C (2/3)
Stratigraphic height (cm)
290
280
270
260
250
240
230
220
210
200
190
180
170
160
150
140
130
120
110
27
26
25
24
23
22
21
20
19b
19a
18
17
16
15
14
13
12
11b
11a
10
9b
S55
S54
***
-4 -2 0 2 4
Relief
20 30 40 50 60
Lightness
-1 0 1 2
Log(Si/Fe)
0 1 2 3 4
K (%)

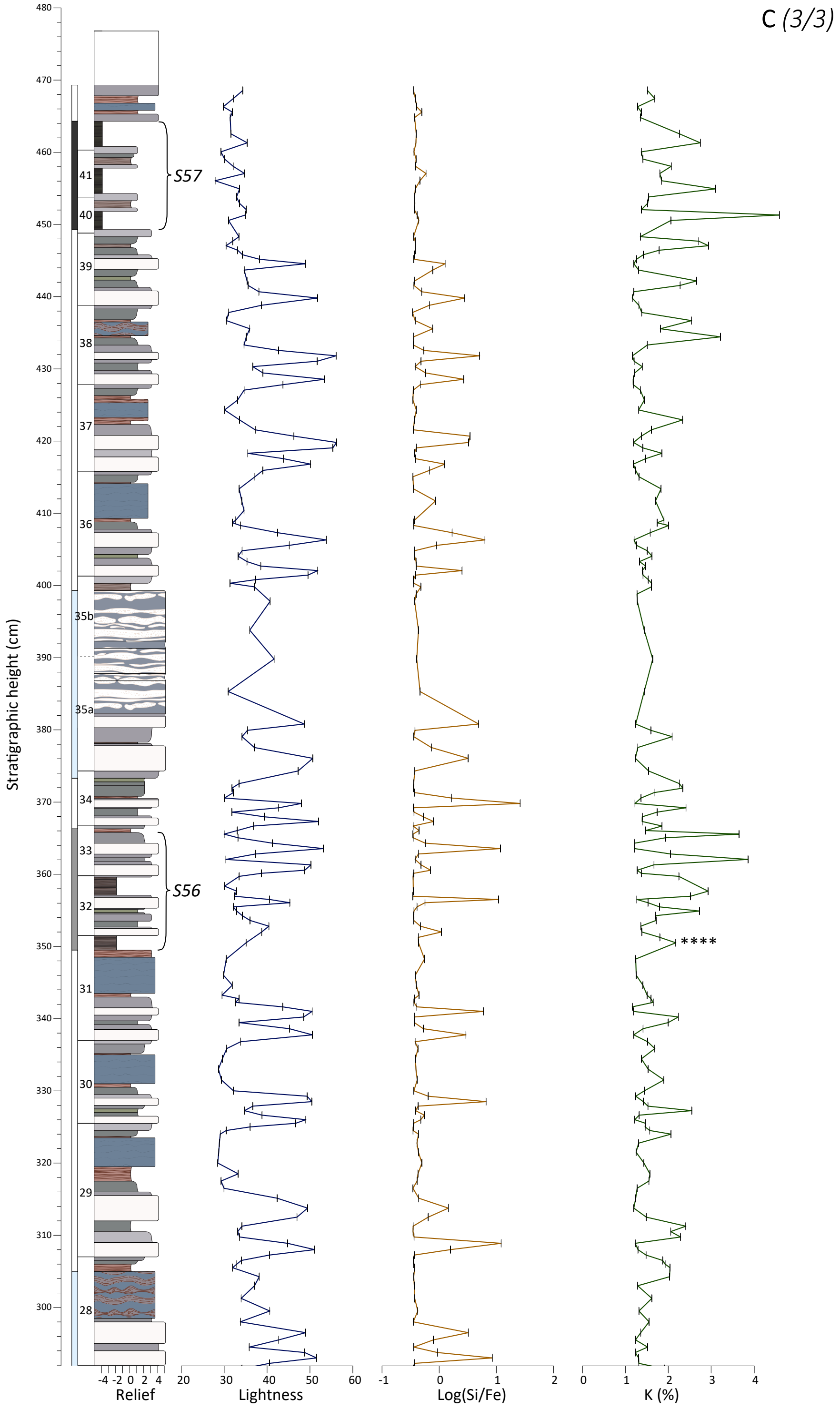
C (3/3)
Stratigraphic height (cm)
480
470
460
450
440
430
420
410
400
390
380
370
360
350
340
330
320
310
300
41
40
39
38
37
36
35b
35a
34
33
32
31
30
29
28
S57
S56
****
-4 -2 0 2 4
Relief
20 30 40 50 60
Lightness
-1 0 1 2
Log(Si/Fe)
0 1 2 3 4
K (%)

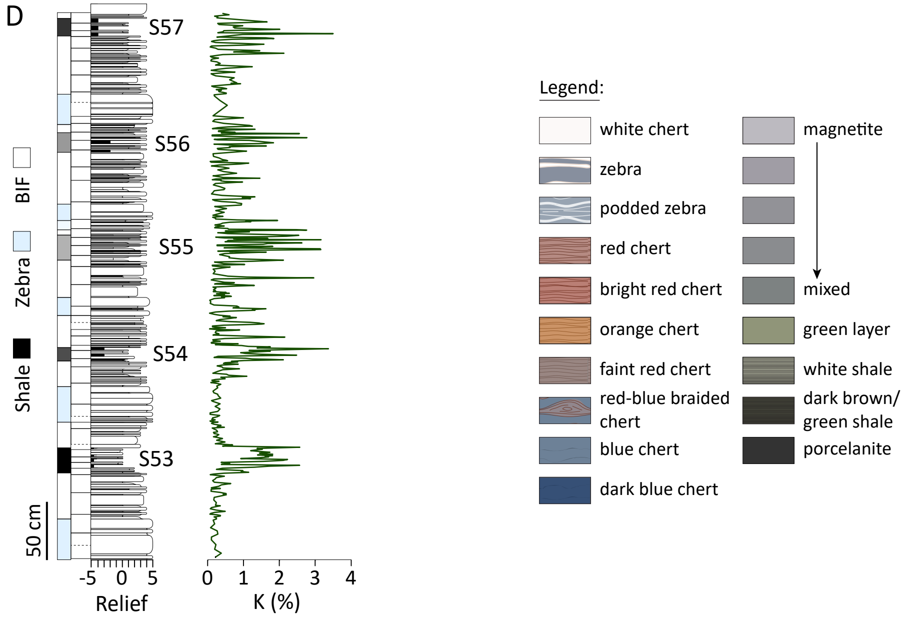

Figure S6. Detailed logs of the small-scale alternations. Cycle numbers are indicated in the left columns; dotted lines with 'b' labels indicate uncertainties in the counting. Vertical lines in the L*, Si/Fe and K records represent the position of the spectrophotometer and XRF handgun measurements (1 cm aperture diameter). (**A**) Lower interval. (*) Thin laminations drawn in S10 and S12 are not in the legend but represent true colors of individual laminations visible in these two intervals (see Fig. S7a-d for photos). (**) The shaley layers in the interval of S11 have a low K (%) yield because they are very thin and were therefore difficult to analyze with the XRF handgun. The position of S11 is defined as the thin orange line at the top of cycle 8, but this definition is a bit arbitrary and could alternatively have been placed in the dark green shaley layer in cycle 9. (***) There is a small phase lag between the L* and Si/Fe (and K%) records in the top part due to a slight offset in the position of the measurements between the color measuring tool and XRF handgun. (**B**) Middle interval. (*) The second white chert band is missing here, though we observed a very thin, higher-relief magnetite layer just above the white chert typically indicating the position of a 'failed' white chert (similar to in cycle 8 and 12). (**) We have no K (%) data of the shales in cycle 11 and also 12 because they were too deeply weathered away and could therefore not be reached for analyses. This is why the cycles above have higher K (%) maxima than S31. (**C**) Upper interval. The grey and light blue bars on the left indicate the vertical extent of the shale and zebra intervals, respectively, and correlate to the simplified log presented in **D**. The red "cherts" in many of the alternations typically have a much lower relief, representing a less cherty and more mixed lithology. (*) White cherts are typically more irregularly banded in the upper interval. (**) S53 actually has a relief of -5 but a relief of -4 is plotted here because the shales would otherwise not be visible in this figure. (***) This red layer is not laterally continuous, leaving two possible cycle interpretations (see SI text and Fig. S7f-g). (****) Lower K (%) yield than the other shales above because this shale was difficult to reach with the XRF handgun. (**D**) Simplified log of the upper interval. Note that large amplitude variations in the K (%) representing the shaley intervals.

Figure S7 (continues next page). Uncertainties in the number of small-scale alternations. (**A**) Cycle interpretation of the lower part of BIF10 and subdivision of S10 into parts 1 – 3. For detailed discussion see section *Uncertainties in the counting* above. (**B**) Zoom-in on the thin laminations within S10. Part 1: black porcelanite, part 2: thin green-black shale with magnetite laminae, and part 3: thin green-black shale with blue-orange band in between. (**C**) Cycle interpretation of the upper part of BIF11 and subdivision of S12. (**D**) Zoom-in on the laminations within S12. Part 1: black porcelanite, part 2: magnetite-faint red chert unit looking similar to those in S53 (Fig. S7j), part 3: ochre-colored band within green-black shale. (**E**) Cycle interpretation of the zebra interval Z53. Note that the photograph is taken from an angle and so 1a and 1b do not seem that thick but are in fact 23 cm. (**F-G**) Two possible cycle interpretations of the zebra interval Z54. The red crack just below the dotted line is present in (**F**) but absent in other lateral parts (**G**). (**H**) Cycle interpretation of the zebra interval Z56, which is anomalously thick (25 cm) but lacks lithological indications for the presence of a double cycle. (**I**) Cycle interpretation of the lower part of BIF54. The thin white chert bands at the base of cycle 19b suggest it is an extra alternation but it is rather thin compared to the alternations below and above. (**J**) Cycle interpretation of S53. Cycles 6 – 8 are typical shale – magnetite alternations (with faint red chert in between) as represented by the shaley facies in Figure 3a. Note that above cycle 8, a fourth soft interval occurs just underneath the more prominent band of magnetite and white chert representing the base of BIF53.

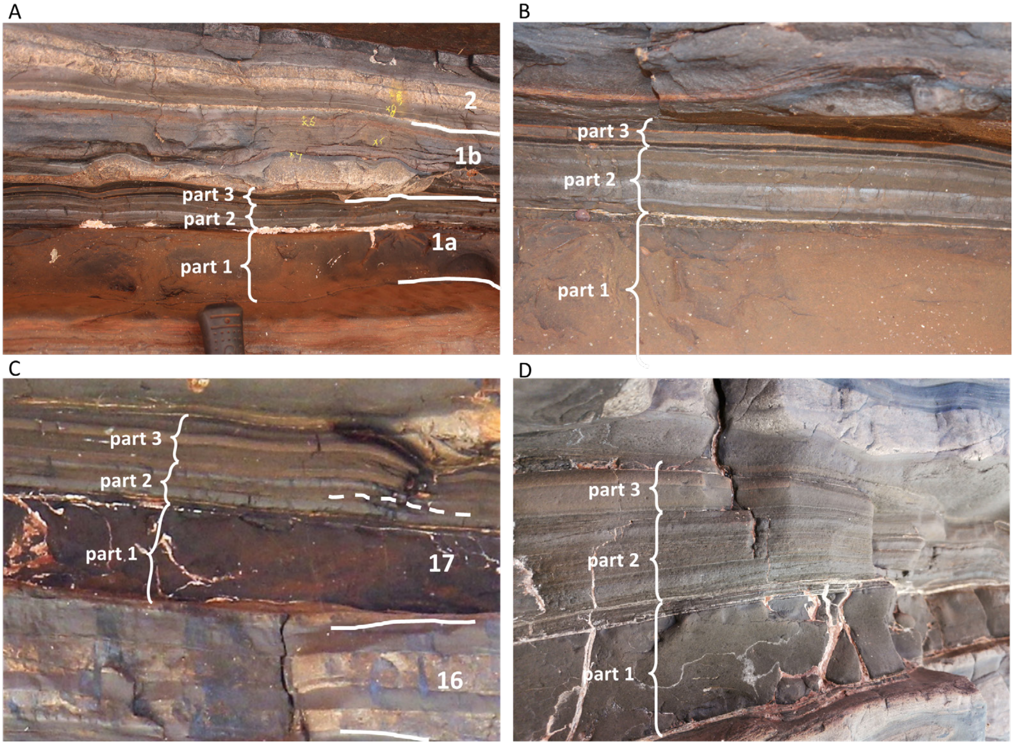

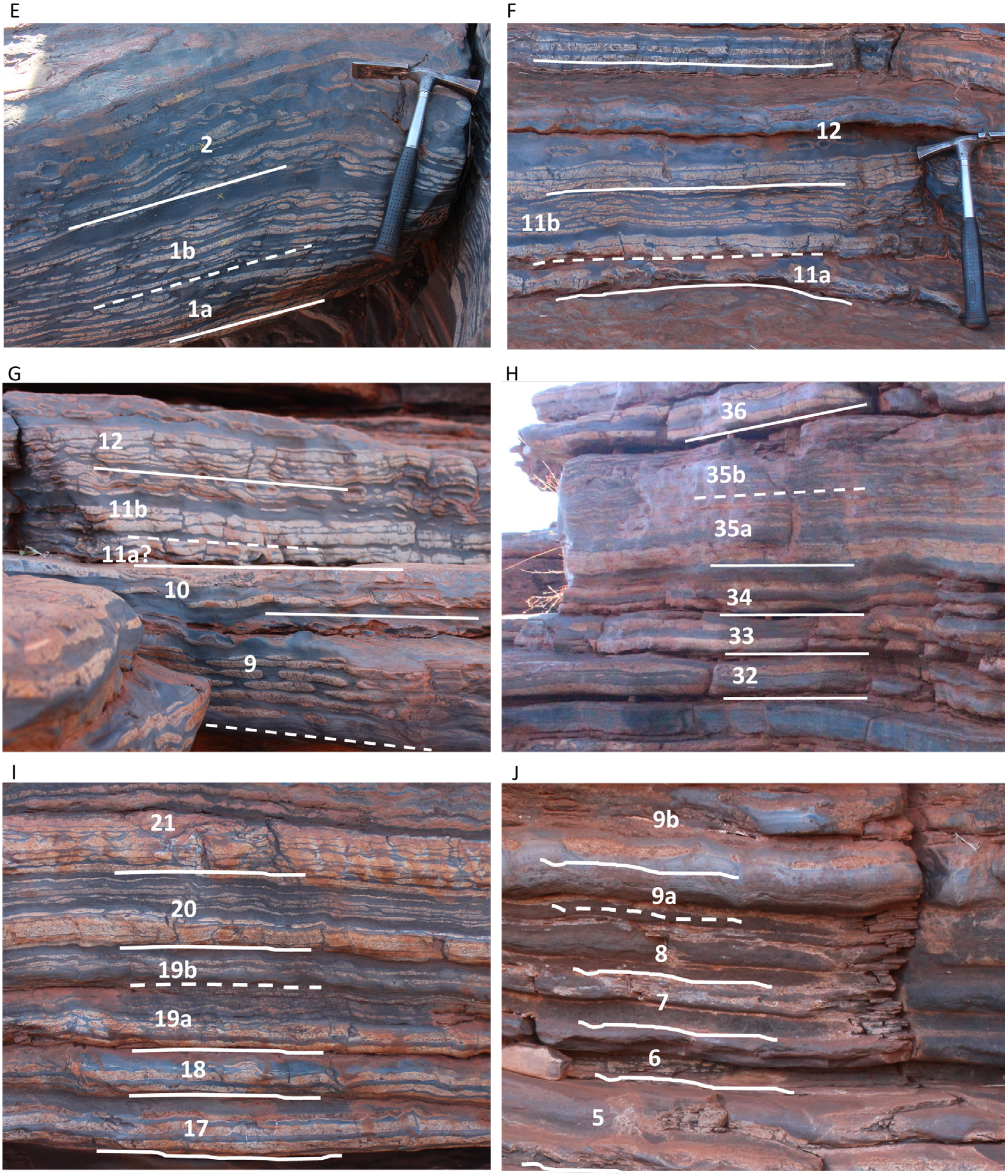
E
2
1b
1a
F
12
11b
11a
G
12
11b
11a?
10
9
H
36
35b
35a
34
33
32
I
21
20
19b
19a
18
17
J
9b
9a
8
7
6
5

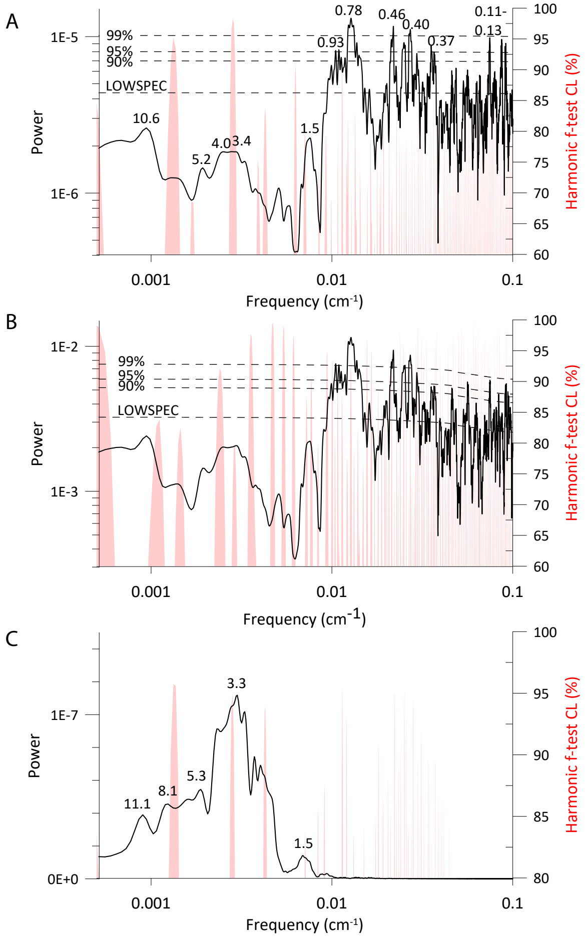

Figure S8. Spectral analysis results of the Joffre Falls shale-BIF record. (**A**-**B**) MTM power spectra with LOWSPEC confidence and f-test significance levels of the shale-BIF record interpolated at 0.15 cm (**A**) and 5 cm (**B**). Peak labels are in meters. Note that for the 5 cm interpolated record, the 78 and 93 cm spectral peaks both exceed the 99% confidence level. Also note that the high-power components around 37 – 46 m are artefactual harmonics of the 78 – 93 cm cycles resulting from the fact that spectral (sine wave) analysis is carried out on a rectangular-shaped log (see Fig. S9). (**C**) MTM power spectrum and f-test significance for the Hilbert transform of the 65 – 105 cm filtered cycle of Figure 2.

Figure S9 (see next page). Comparison between the shale-BIF record of Joffre Falls and bandpass filters of the 93, 78 and 37 - 46 cm spectral peaks. Dashed (dotted) lines indicate intervals of maximum (minimum) amplitude in the 65 – 105 cm filtered signal - corresponding to alternations with a relatively thicker (thinner) shale - that coincide with an in-phase (anti-phase) relationship between the 85 – 105 cm and 65 – 85 cm filters, occurring each four alternations. This pattern is reminiscent of how the phasing of

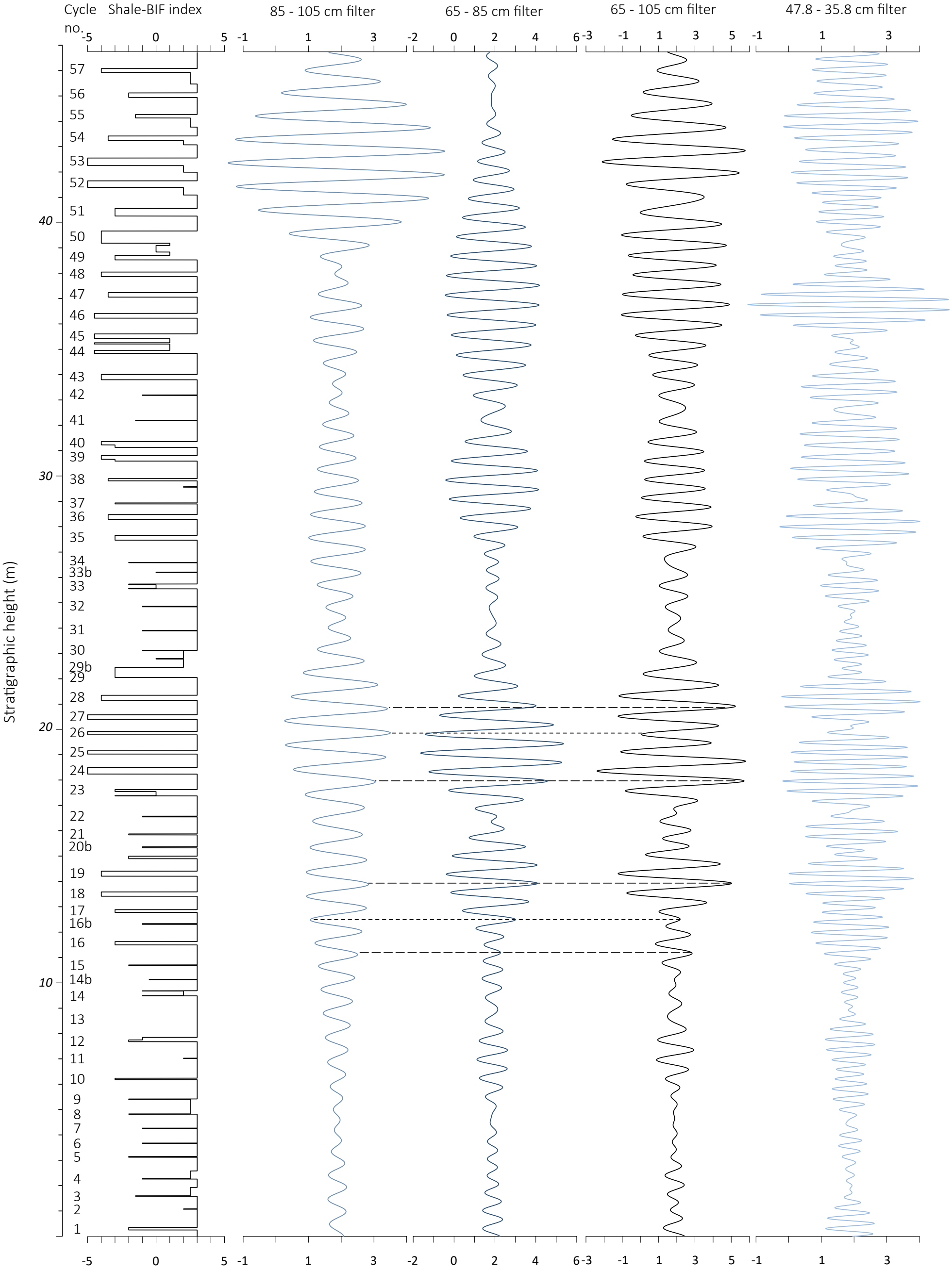

the two main short eccentricity cycles (95 and 124 kyr) relates to the phasing of the 405 kyr eccentricity cycle (Laurin et al., 2016). Note further that the amplitude of the 48 – 36 cm filtered cycle almost exactly follows that of the 65 – 105 cm filter, with maxima coinciding with the edges of the rectangular BIF units, implying an artefactual origin.

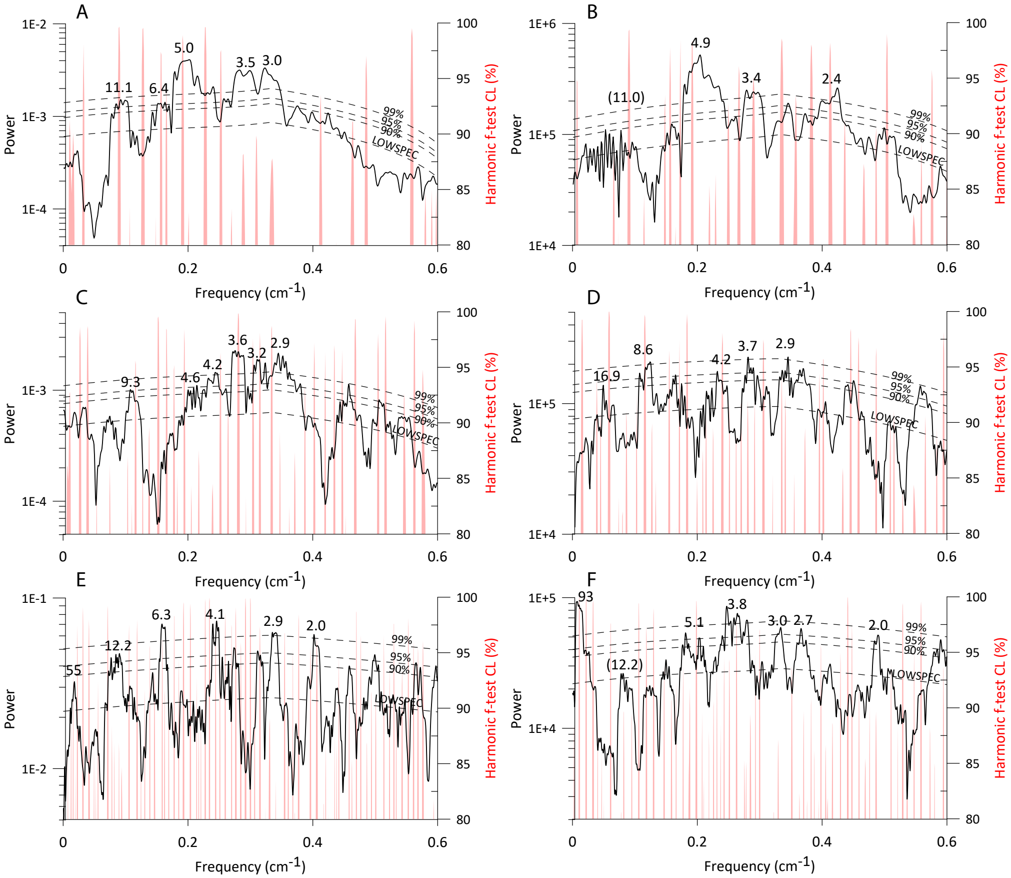

Figure S10. Spectral analysis results of the detailed logs. MTM power spectra with LOWSPEC confidence and f-test significance levels; peak labels are in centimeters. All records were interpolated at 0.75 cm. (**A**) Lower interval log(Si/Fe). (**B**) Lower interval K (%). (**C**) Middle interval log(Si/Fe). (**D**) Middle interval K (%). (**E**) Upper interval Si/Fe. (**F**) Upper interval K (%).

Figure S11 (see next page). Origin of the different peaks in the MTM spectra of the detailed logs. (**A**). Bandpass filtered cycles for the XRF records of the lower interval. The bandpass filtered 9.4 – 13.2 cm cycle of the Si/Fe record follows the individual small-scale alternations, apart from the thinner cycle 9 (see red arrow), whereas the filtered shorter period cycles show two or three maxima per alternation at the position of the white and red cherts (Si/Fe maxima). In the K % record, the 4.1 – 5.6 cm filtered cycle follows the double maxima per alternation while showing one (weak) maximum at the position of the thinner cycles 9 and 10. (**B**) Bandpass filtered cycles for the upper interval. Again, the 10.5 – 13.8 cm filtered cycle follows the small-scale alternations, apart from the relatively thinner cycle 25 and thicker cycle 29 (see red arrow). The filtered shorter period cycles follow the characteristic double or triple maxima in Si/Fe and K (%) per single small-scale alternation. The 63 – 167 cm filtered signal indicates the larger shale-BIF cyclicity, particularly well expressed in the K (%) record of this upper interval (Fig. S6d).

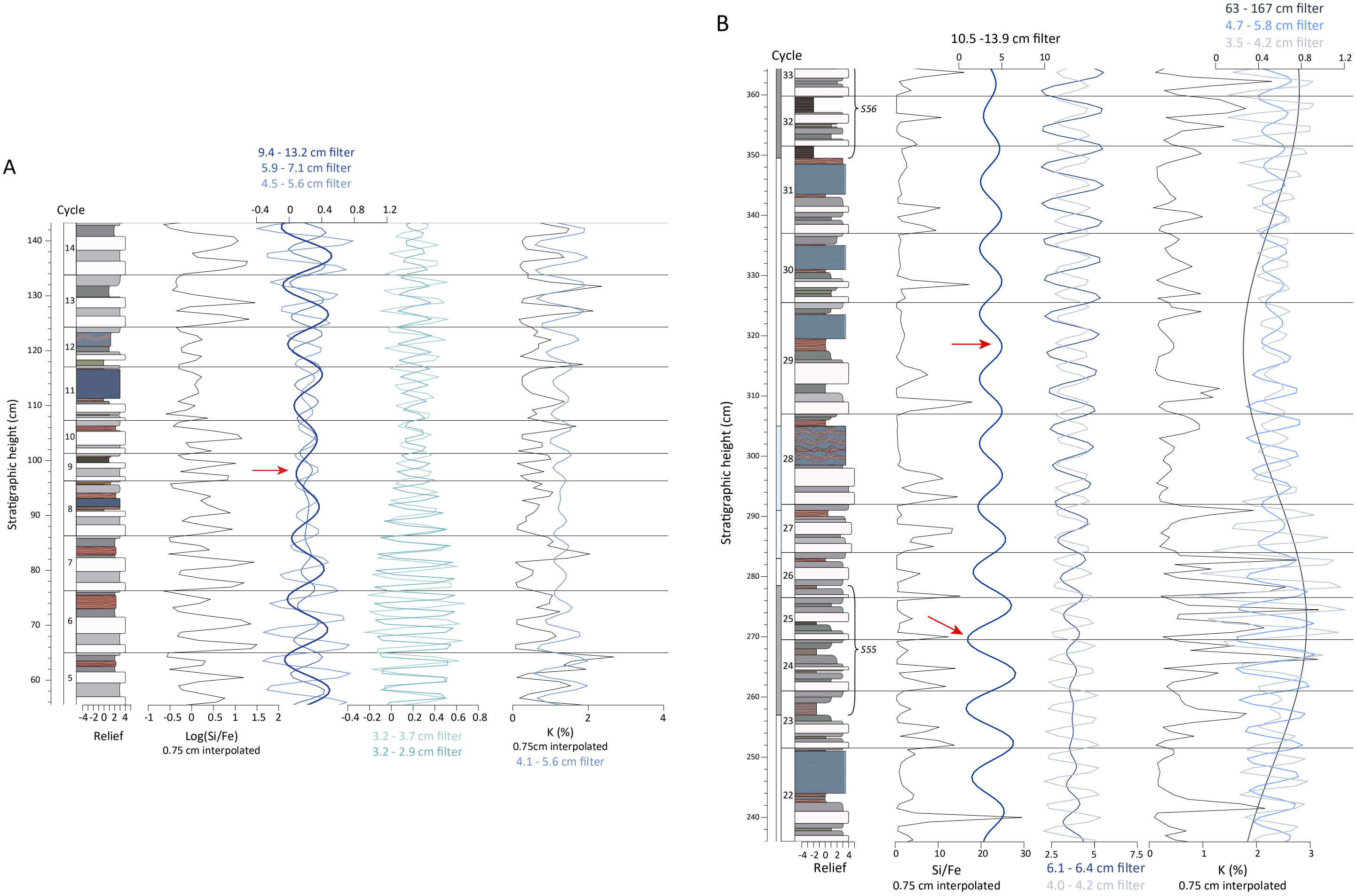
A
9.4 - 13.2 cm filter
5.9 - 7.1 cm filter
4.5 - 5.6 cm filter
Cycle
-0.4
0
0.4
0.8
1.2
Stratigraphic height (cm)
140
130
120
110
100
90
80
70
60
14
13
12
11
10
9
8
7
6
5
-4 -2 0 2 4
Relief
-1 -0.5 0 0.5 1 1.5 2
Log(Si/Fe)
0.75 cm interpolated
-0.4 -0.2 0 0.2 0.4 0.6 0.8
3.2 - 3.7 cm filter
3.2 - 2.9 cm filter
0 2 4
K (%)
0.75cm interpolated
4.1 - 5.6 cm filter
B
63 - 167 cm filter
4.7 - 5.8 cm filter
3.5 - 4.2 cm filter
10.5 -13.9 cm filter
Cycle
0 5 10
0 0.4 0.8 1.2
Stratigraphic height (cm)
360
350
340
330
320
310
300
290
280
270
260
250
240
33
32
31
30
29
28
27
26
25
24
23
22
S56
S55
-4 -2 0 2 4
Relief
0 10 20 30
Si/Fe
0.75 cm interpolated
2.5 5 7.5
6.1 - 6.4 cm filter
4.0 - 4.2 cm filter
0 1 2 3
K (%)
0.75 cm interpolated

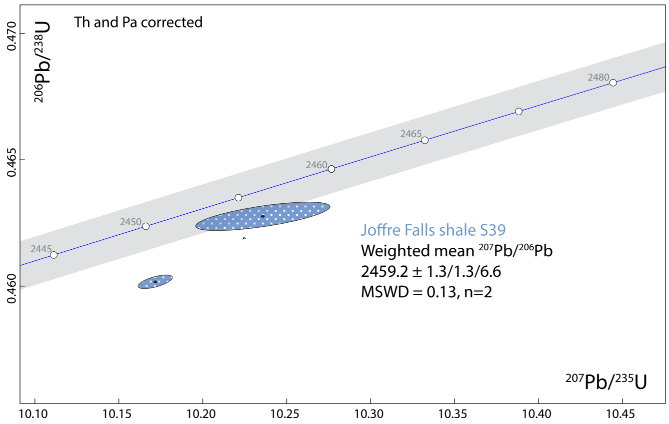

Figure S12. Concordia diagram showing the U–Pb TIMS results for shale S39. The grey band represents the uncertainty on the Concordia curve due to the decay constant uncertainties. The ellipses represent the U–Pb isotopic data and 2σ uncertainty for individual chemically abraded zircon fragments. The ^{207}Pb/^{206}Pb age represents a weighted mean of the two analyses (one concordant and one close to concordant). MSWD, mean square of the weighted deviates

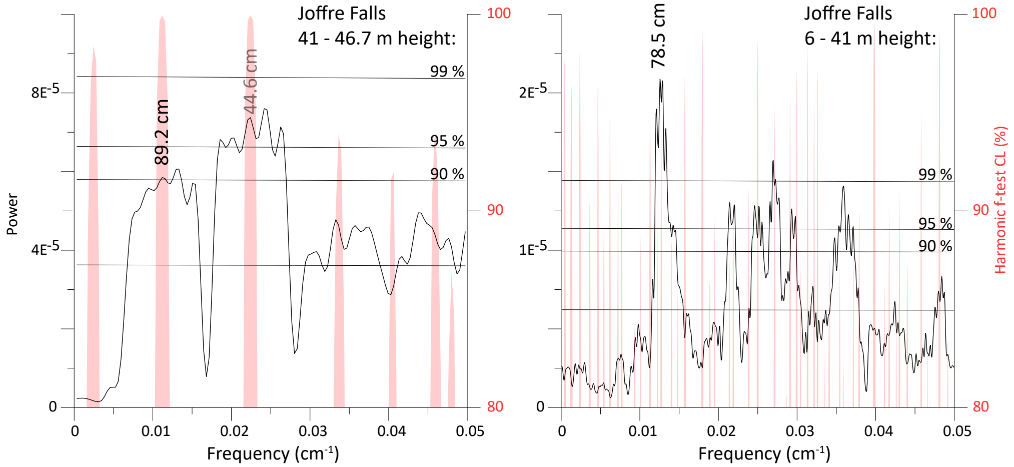

Figure S13. MTM power spectra with LOWSPEC confidence and f-test significance levels for the upper part of Joffre Falls at 41 – 46.7 m height (left) versus 6 – 41 m height (right). Comparison of the ~89 cm peak in the left spectrum with the dominant ~79 cm peak in the right spectrum suggests that the shale-BIF alternations in the upper part of Joffre Falls are 14 % thicker on average. Note that the ~45 cm peak in the left spectrum is the first harmonic of the ~89 cm cycle but also arises from the subdivision of the BIF units into a zebra (high relief) and platy BIF (intermediate relief) interval in this upper part of the log.

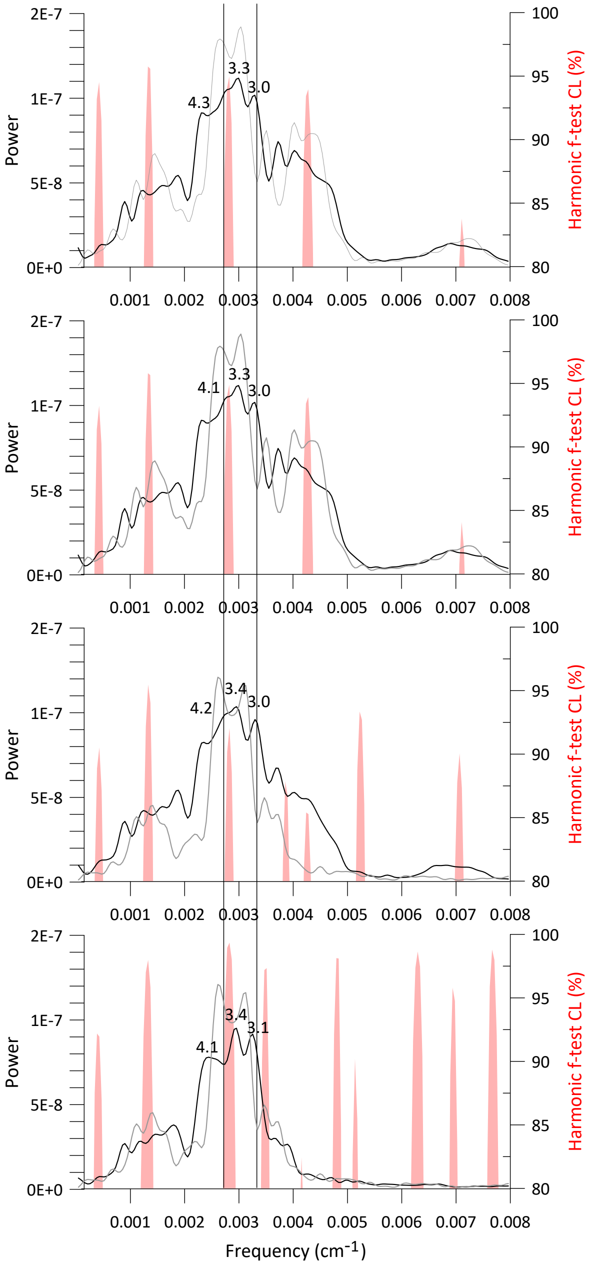

Figure S14. Estimation of the uncertainty in the wavelength of the 3.3 m cycle. MTM power spectra with LOWSPEC confidence and f-test significance for the Hilbert transforms of the bandpass filtered shale-BIF cyclicity from Joffre Falls for different interpolation steps and filter windows. From top to bottom: 1) 0.15 cm interpolated and 65 – 105 cm filtered; 2) 5 cm interpolated and 65 – 105 cm filtered; 3) 0.15 cm interpolated and 67 – 105 cm filtered; 4) 0.15 cm interpolated and 70 – 100 cm filtered. Black lines indicate power spectra applying a time-bandwidth product of 3 and grey lines applying a time-bandwidth product of 2. Note that the frequency range of enhanced spectral power around 3.3 m is very broad (i.e. not well defined) and is split into three peaks, but that the position of the highest middle peak (3.3 m) does not vary much for the different applied settings. For the purpose of estimating the uncertainty of the 405 kyr-related cycle thickness we excluded the ~4 m component because of its significantly larger wavelength. We included the harmonic f-test peak (around 3.5 m) and the weaker shorter period (around 3.0 m) peak within the uncertainty range (vertical black lines) for the 405 kyr-related cycle thickness that we consider plausible based on these spectra. This selected range (0.00333 – 0.00272 cm-1) corresponds to an uncertainty of ~10% in the 3.3 m cycle thickness.

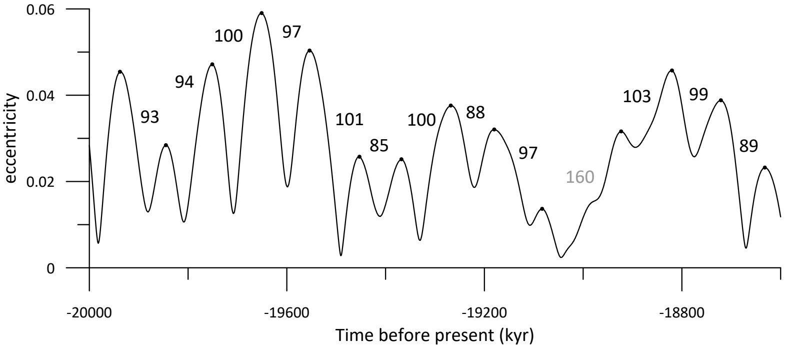

Figure S15. Variability in the duration of successive short eccentricity maxima. Example interval from the La2004 solution with eccentricity maxima indicated by the black dots and interstitial time labelled in kyr. The shoulder at ~18 Myr is not included as an eccentricity maximum; the resulting 160 kyr interval is considered as anomalously long and therefore excluded from the list for determining the mean period of short eccentricity.

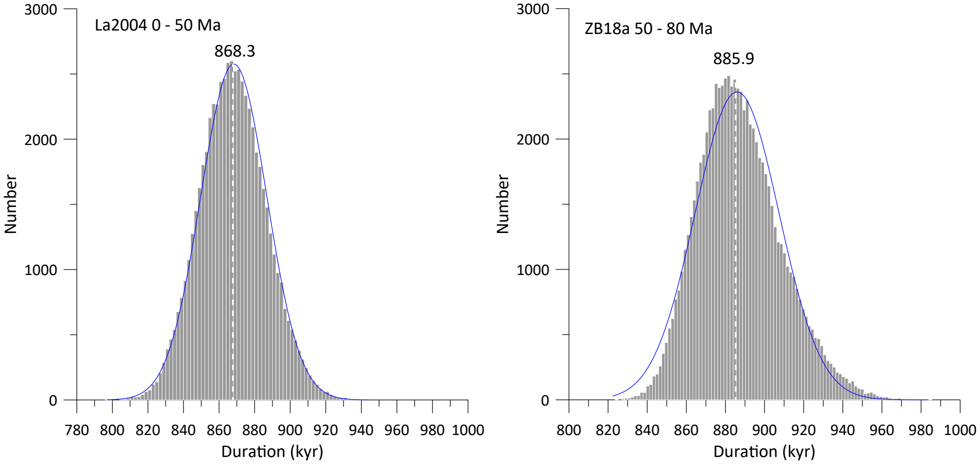

Figure S16. Histograms for the sum of the Monte Carlo simulations of two, three and four successive short eccentricity cycle durations from the La2004 0 – 50 Ma (left) and ZB18a 50 – 80 Ma solutions (right). Blue line represents a Gaussian normal distribution fit.

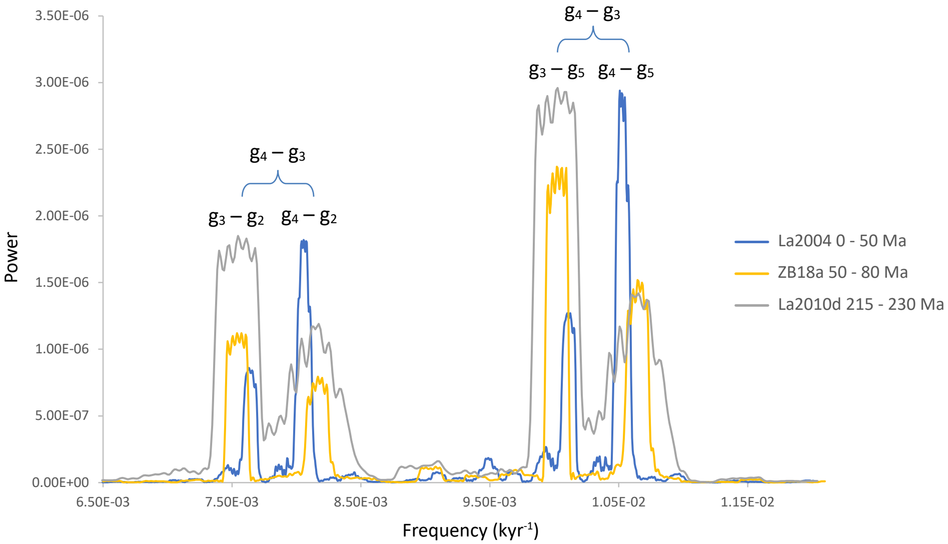

Figure S17. Comparison of the MTM power spectra of three eccentricity solutions with different periods for the $g_4 - g_3$ cycle. In the La2004 0 – 50 Ma interval, the $g_4 - g_3$ term has a period of ~2.4 Myr (Laskar et al., 2004); in the La2010d 215 – 230 Ma interval it has a period of ~1.8 Myr (Laskar et al., 2011; Olsen et al., 2019); and in the ZB18a 50 – 80 Ma interval it has a period of ~1.6 Myr (Zeebe and Lourens 2019). The corresponding MTM spectra show that with increasing frequency of $g_4 - g_3$ (from 0.55 “/yr to 0.82 “/yr) the distance between the peaks related to $g_3 - g_2$ and $g_4 - g_2$, which is determined by $g_4 - g_3$, increases more or less symmetrically around their combined average; the same is the case for the distance between $g_3 - g_5$ and $g_4 - g_5$. This may explain why the reduction in the period of $g_4 - g_3$ does not fundamentally affect the mean short eccentricity duration. However, the ZB18a and La2010d spectra also consistently show an increase in power (amplitude) of the $g_3 - g_2$ and $g_3 - g_5$ terms relative to that of $g_4 - g_2$ and $g_4 - g_5$, respectively. This relative amplitude shift may be responsible for the small i.e. ~2 kyr increase in the average short eccentricity period determined for the ZB18a 50 – 80 Ma interval compared to the result of the La2004 0 - 50 Ma interval (Table S3).

Figure S18. Grid of *p* vs Earth-Moon distance values derived from equations 13-15 in Waltham (2105). Dotted lines denote the relationship between the reconstructed astronomical precession period *p* from Joffre Falls (11.9 kyr) to Earth-Moon distance (321.8 thousand km) determined by cubic spline interpolation. Dashed line indicates the fitted power law equation used for propagation of the 2SD errors.

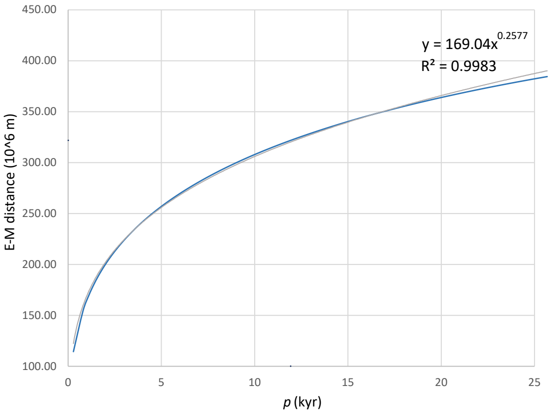

Supplementary Tables

Table S1. Average thickness and calculated period of the small-scale cycles (Knox cyclothems) according to Option 1. The mean cycle thicknesses are converted to time based on the assumption 3.34 m = 405 kyr.

	No. of cycles	±	Interval thickness (cm)[b]	Mean small-scale cycle thickness (cm)	± cm[c]	Mean period (kyr)	± cm[d]
S10 --> S12	18.5	0.5	167	9.0	0.3	10.9	1.6
S30 --> S33[a]	27	0	244	9.0	0.2	11.0	1.3
Z52 --> S57	44	2.5	443	10.1	0.6	12.2	2.2
Z52 --> S57*	44	2.5	390	8.9	0.5	10.7	1.9
Total	89.5	3	854	9.5	0.4	11.6	1.8
Total*	89.5	3	801	8.9	0.3	**10.9**	**1.7**

*The calculations for the (Z52 -> S57) interval are corrected for the inferred 14% sedimentation rate increase in the upper part of Joffre Falls (see SI text and Fig. S13)

a: up to S33 but not including S33

b: thicknesses from the large-scale log i.e. not from the detailed logs

c: assuming a 2% measurement uncertainty

d: assuming 10% uncertainty in the 3.3 m periodicity (see SI text and Fig. S14).

Table S2. Periods of the larger (meter)-scale variations in the stratigraphy of section Joffre Falls and possible origin in terms of Earth's orbital eccentricity components.

MTM peak (m)	Period* (kyr)	Possible origin	La2004 [-15 + 5] Myr period (kyr)
3.34	**405**	$g_2 - g_5$	405
5.3	643	$g_2 - g_1$	688
8.1	982	$g_1 - g_5$	978
11.1	1346	$g_4 - g_3$	2373
1.5	182	$-2g_2 + g_4 + g_5$ or $2g_2 – 2g_5$	~180 or ~200
0.78 & 0.93	95 & 113	$g_4 - g_5$, $g_3 - g_5$ & $g_4 - g_2$, $g_3 - g_2$ (?)	95, 99 & 124, 131

*Periodicities in meter are converted to time assuming 3.34 m = 405 kyr.

Table S3. Mean short eccentricity durations and corresponding 2 sigma uncertainties from the La2004 0 - 50 Ma and ZB18a 50 – 80 Ma solutions derived from Monte Carlo simulations (Option 2a and 2b, respectively).

	2 cycles		3 cycles		4 cycles		2, 3 and 4 cycles		per 1 cycle*	
	mean (kyr)	± 2σ	mean (kyr)	± 2σ	mean (kyr)	± 2σ	mean (kyr)	± 2σ	mean (kyr)	± 2σ
La2004 0 - 50 Ma	193.7	22.1	289.5	22.7	385.0	19.5	868.3	37.2	96.5	4.1
ZB18a 50 - 80 Ma	197.3	21.7	295.3	24.7	393.3	27.5	885.9	42.9	98.4	4.8

*the sum of 2, 3 and 4 successive cycles divided by 9

Table S4. Validity test for linking the average climatic precession signal to astronomical precession *p*.

Time[1] (Ma)	axial precession freq.[1] ("/yr)	calculated[2] mean climatic precession freq. ("/yr)	calculated[2] mean climatic precession period (kyr)	La2004 time interval (Ma)	reconstructed[3] mean climatic precession period (kyr)
5	50.61	60.92	21.27	0 - 10	21.16
30	51.29	61.60	21.04	25 - 35	21.01
45	51.71	62.02	20.90	40 - 50	20.67

1: obtained from eq. 40 in Laskar et al. (2004)

2: according to equation 1 (see SI text)

3: based on the time differences between successive climatic precession maxima.

Table S5. Data and references for Figure 4.

Unit	Age (Ma)	± (Ma)	Reference	E-M distance (x10^3 km)	Reference	± 2σ (km)	Reference
Joffre BIF	2459.2	1.3	This study	321.8	This study	6.5	This study
Weeli Wolli	2450	3.0	Barley et al. (1997)	330.6	Walker and Zahnle (1986)	42.1	Walker and Zahnle (1986)
Weeli Wolli	2450	3.0	Barley et al. (1997)	348.2	Williams (2000)	23.0	Williams (2000)
Xiamaling	1392.2	1.0	Zhang et al. (2015)	340.9	Meyers and Malinverno (2018)	2.6	Meyers and Malinverno (2018)
Cottonwood	870	130	Hintze (1988); Dehler et al. (2017)	364.2	Sonett et al. (1996)		
Cottonwood	870	130	Hintze (1988); Dehler et al. (2017)	348.9	Sonett and Chan (1998)	9.1	Sonett and Chan (1998)
Elatina-Reynella	620	50	Williams (2008)	371.0	Williams (1989; 2000)	3.8	Williams (1989; 2000)
Alum Shale	493	10	Sørensen et al. (2020)	368.9	Sørensen et al. (2020)	2.3	Sørensen et al. (2020)

Chapter 5

Towards an astrochronological framework for the early Paleoproterozoic and origin of very long-period astronomical-induced cyclicity

Towards an astrochronological framework for the early Paleoproterozoic and origin of very long-period astronomical-induced cyclicity

Margriet L. Lantink, Joshua H.F.L. Davies, Rick Hennekam, David McB. Martin, Paul R.D. Mason, Gert-Jan Reichart and Frederik J. Hilgen

Abstract

Recent evidence for astronomical-induced cycles in banded iron formations (BIFs) hints at the intriguing possibility of developing astrochronological, i.e., precise time-stratigraphic, frameworks for the earliest Proterozoic as also reconstructed for parts of the Mesozoic and Paleozoic. The ~2.47 Gyr old Kuruman Iron Formation (Griqualand West basin, South Africa) and Dales Gorge Member of the Brockman Iron Formation (Hamersley basin, Western Australia) are of special interest in this regard, given their inferred temporal overlap and similar long-period eccentricity imprint. This suggests that these two BIFs can be correlated on the basis of their large-scale cycle patterns and using additional radio-isotopic age constraints.

To examine the possibility of such a framework, we generated and used several high-resolution proxy records from both drill-core and natural outcrop, combined with high-precision CA-ID-TIMS U-Pb zircon dating. Timeseries analysis of these records yields a wide variety of spectral peaks, of which a prominent ~5 and ~16m cycle correspond to the basic alternations and bundling observed in the lithology. New and improved U-Pb ages of the Dales Gorge Member and Kuruman Iron Formation, respectively, indicate an essentially identical average sedimentation rate of 10 - 12 m/Myr for both BIF units. Based on this rate, the ~5m cycle can be convincingly attributed to the long 405-kyr eccentricity cycle. More tentatively, we interpret the ~16m cycle to reflect the very long 2.4-Myr eccentricity cycle, but with a reduced period of ~1.3 Myr as a consequence of the chaotic behaviour of the Solar System. Other identified cycles (~580 kyr, ~700 kyr and ~1.9 Myr) might be explained in terms of weaker eccentricity components and/or as harmonics and combination tones of these cycles.

An initial attempt to establish cyclostratigraphic correlations between the Kuruman Iron Formation and Dales Gorge Member solely based on the characteristic hierarchical cycle patterns proved unsuccessful, which may be due to a difference in recording of the cycles between their different depositional environments. Next, we used the U-Pb ages to first constrain correlations at the ~16m cycle scale, as a necessary step to correlate the basic ~5m cycles. The resultant framework remains problematical and debatable at the individual 405 kyr cycle level, and should rather be considered as a starting point for further studies. However, the outcome of our study should by no means be regarded as an argument to disregard the impact of astronomical (Milankovitch) climate forcing on regular banding seen in these BIFs. It rather reflects our limited understanding of how this forcing is exactly registered under different paleo-environmental conditions at times that Earth System operated fundamentally different than today.

1. Introduction

Astronomical age models based on the calibration of sedimentary cycles to astronomical target curves of precession, obliquity, eccentricity and/or insolation have now been constructed for the entire Cenozoic (Gradstein et al., 2020; Hinnov, 2018; Hinnov and Hilgen, 2012). Due to their high resolution, these age models or astrochronologies have been key to solving fundamental research questions concerning the astronomical origin and pacing ("Milankovitch forcing") of e.g. ice ages and hyperthermals, and associated non-linear feedbacks within Earth's climate system (Hays et al., 1976; Hilgen, 1991; Imbrie et al., 1984; Sexton et al., 2011; Westerhold et al., 2020; Zachos et al., 2010). In addition, the development of very long, tuned paleoclimate records has enabled to differentiate the contribution of especially the Milankovitch "Grand cycles" - having periodicities in the order of millions of years - from other forcing mechanisms such as tectonics and volcanism that operate on the same time scale (Boulila, 2019; Boulila et al., 2012; Martinez and Dera, 2015). Similar astrochronologies have also been developed for parts of the Mesozoic (e.g. Batenburg et al., 2012; Sprovieri et al., 2013; Ikeda and Tada, 2014; Huang, 2018; Olsen et al., 2019) and Paleozoic (e.g. Wu et al., 2013; Fang et al., 2015; Sinnesael et al., 2021), yet these are essentially relative i.e. providing astronomical duration but not age, due in part to the absence of a reliable astronomical solution prior to 50 Ma. Instead, these 'floating' or radioisotopically-anchored age models are based on identification of the long 405-kyr eccentricity cycle, the only cycle whose period is regarded stable in deep time (Laskar et al., 2004, 2011) while of sufficiently large amplitude to be typically expressed in sedimentary sequences.

Recently, the expression of the 405 kyr cycle was detected in ancient marine deposits at ~2.47 Ga (Lantink et al., 2019; de Oliveira Carvalho Rodrigues et al., 2019), in so-called banded iron formations (BIFs), deposited in the prelude to the Great Oxidation Event (GOE; Bekker et al., 2004; Holland, 2002). This raises the question whether a similar integrated stratigraphic framework and astrochronology may be developed for these BIFs, namely the Kuruman Iron Formation (IF) in South Africa and the Dales Gorge Member of the Brockman IF in NW Australia. It is generally assumed that these lithostratigraphic units were deposited more or less synchronously, and possibly even in the same basin, based on similarities in the succession of lithofacies and SHRIMP U-Pb zircon ages (Button, 1976; Cheney, 1996; Nelson et al., 1999; Pickard, 2003; Trendall, 1968; Trendall et al., 2004). Establishing a cyclostratigraphic framework would, for the first time, allow their relative timing to be determined much more precisely, and as such, be of important value for reconstructions of both paleogeography/basin evolution (Beukes and Gutzmer, 2008; Knoll and Beukes, 2009) as well as environmental redox changes during this critical period (e.g. Anbar et al., 2007; Kendall et al., 2010; Gumsley et al., 2017).

Here we combine cyclostratigraphic analysis and chemical abrasion (CA-) ID-TIMS U-Pb zircon dating of the Kuruman and Dales Gorge Member BIFs to examine their potential for establishing high-resolution correlations using the inferred eccentricity-related cycle patterns, and a 405 kyr cycle-based framework for the earliest Paleoproterozoic in South Africa and Western Australia. Secondly, this correlation exercise will be used to determine the occurrence and period of very long (multi-million year) orbital cycles. Very promisingly, a ~1.2-1.6 Myr cycle has already been described from the Kuruman IF, which supposedly represents the present-day very long 2.4-Myr eccentricity cycle with a much-reduced period, due to the chaotic Earth-Mars orbital resonance (Lantink et al. 2019). Determining their periods as exactly as possible will not only offer insight into the chaotic planetary behaviour in the ancient Solar System, more than halfway back along its 4.56 Gyr history, but may also be used to examine the presence of even longer cycles with a period of 9-10 million years that have recently been found in the Phanerozoic.

2. Geological setting and stratigraphy

The largest BIF successions of the Precambrian rock archive are found along the transition from the Archean to Proterozoic between approximately ~2.6 – 2.4 Ga. These iron- and silica-rich, largely chemical sedimentary deposits are exceptionally well-preserved in the Griqualand West basin in South Africa and the Hamersley basin in NW Australia, each of which extend over several hundred kilometres on the Kaapvaal and Pilbara cratons, respectively (Fig. 1). In both areas, the BIF-hosting Ghaap (SA) and Hamersley (WA) Groups show a remarkably similar and roughly in age corresponding succession of lithofacies, from relatively shallow-marine (platform) carbonates, (black) shale to deeper-marine iron formation of the Kuruman and Brockman IFs, respectively (Fig. S1); in the Griqualand West basin, such a shelf-to-basin facies transition is also preserved in lateral sense, from the central Ghaap plateau area to Prieska in the south (Fig. 2; Beukes and Gutzmer, 2008; Beukes, 1980, 1983; Knoll and Beukes, 2009)). The strong lithostratigraphic correlation between the Ghaap and Hamersley sequences, combined with paleomagnetic support for a Pilbara-Kaapvaal supercraton ('Vaalbara') around that time (de Kock et al., 2009; Gumsley et al., 2017), suggests that deposition may have occurred in a single large marine depository and/or (partly) connected basins (Beukes and Gutzmer, 2008; Cheney, 1996; Martin et al. 1998).

The stratigraphy of the Kuruman IF as visible in outcrop (Fig. 3a) is characterised by a pattern of regular alternations in the weathering profile at a basic thickness scale of ~5 m, and a larger-scale bundling of around ~16 – 22 m, which was laterally correlated over 250 km, from Kuruman Kop to Prieska (Fig. 1) by Lantink et al. (2019). The alternations partly correspond to the 'stilpnomelane lutite - BIF macrocycles' of Beukes (1978, 1980) described from drill-core (Fig. S1), who originally proposed a volcanic-biogenic origin. Based on evidence from high-precision U-Pb dating, Lantink et al. (2019) attributed the alternations to the long (405 kyr) and very long-period (now ~2.4 Myr) eccentricity cycle of the Earth's orbit ("Hypothesis 2") and suggested a low-latitude climatic, potentially monsoonal control on changes in runoff and productivity. A similar cycle hierarchy and same Milankovitch origin was proposed for the metre-scale "BIF – S macrobanding"

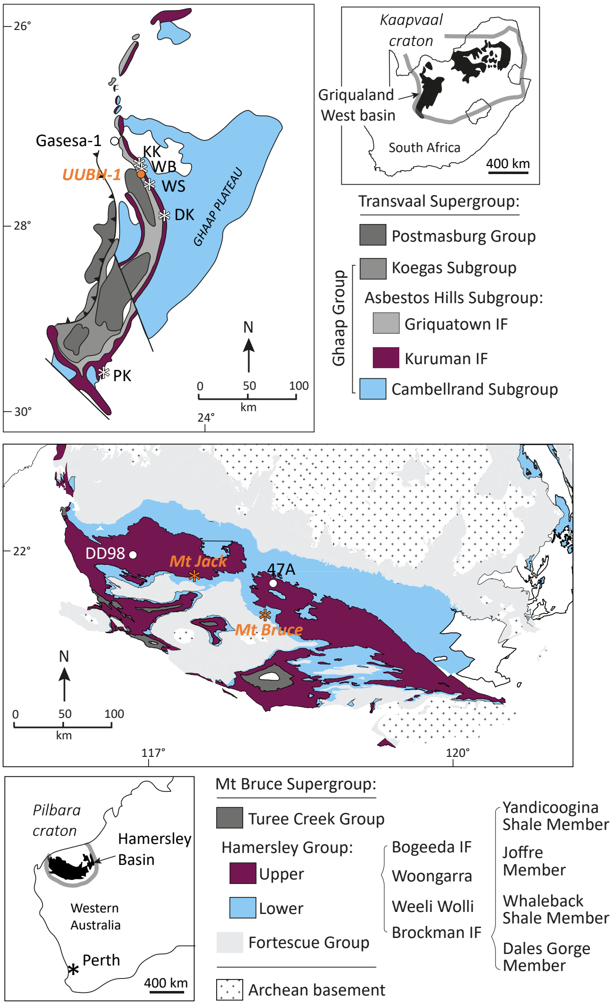
26°
28°
30°
24°
Gasesa-1
UUBH-1
KK
WB
WS
DK
PK
GHAAP PLATEAU
N
0
50
100
km
Kaapvaal
craton
Griqualand
West basin
South Africa
400 km
Transvaal Supergroup:
Postmasburg Group
Koegas Subgroup
Ghaap Group
Asbestos Hills Subgroup:
Griquatown IF
Kuruman IF
Cambellrand Subgroup
22°
DD98
Mt Jack
47A
Mt Bruce
N
0
50
100
km
117°
120°
Pilbara
craton
Hamersley
Basin
Western
Australia
Perth
400 km
Mt Bruce Supergroup:
Turee Creek Group
Hamersley Group:
Upper
Lower
Fortescue Group
Archean basement
Bogeeda IF
Woongarra
Weeli Wolli
Brockman IF
Yandicoogina
Shale Member
Joffre
Member
Whaleback
Shale Member
Dales Gorge
Member

Figure 1. Geological map of the Griqualand West basin (South Africa) and Hamersley basin (NW Australia) and the locations of the studied sections and drill-cores of the Kuruman and Brockman iron formations, respectively.

Figure 2 (next page). Schematic cross-section of the Ghaap and Hamersley Groups on the Kaapvaal and Pilbara cratons, respectively, showing their broadly correlative succession of lithofacies; a similar facies transition is also preserved laterally in South Africa (figure adapted from Beukes and Gutzmer, 2008). Purple bands mark the stratigraphic intervals of the Kuruman and Dales Gorge Member BIFs that are the focus of this study. Note that the connecting band for the Kuruman IF between the central Kuruman and southern Prieska area is based on the cyclostratigraphic correlations of Lantink et al. 2019, and are contrary to Beukes' (1980; 1983) correlations of macro- and megacycles which imply a much higher depositional rate in the south.

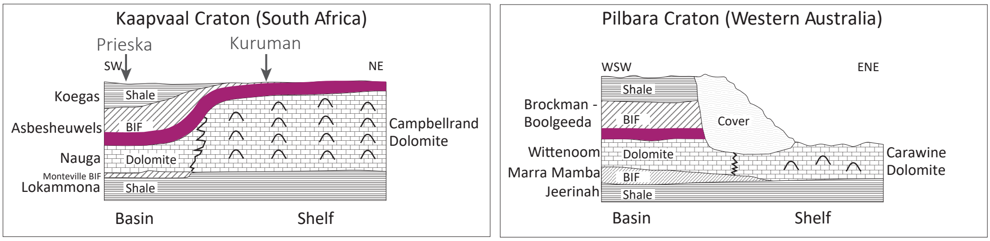
Kaapvaal Craton (South Africa)
Prieska
Kuruman
SW
NE
Koegas
Asbesheuwels
Nauga
Monteville BIF
Lokammona
Shale
BIF
Dolomite
Shale
Campbellrand Dolomite
Basin
Shelf
Pilbara Craton (Western Australia)
WSW
ENE
Brockman - Boolgeeda
Wittenoom
Marra Mamba
Jeerinah
Shale
BIF
Dolomite
BIF
Shale
Cover
Carawine Dolomite
Basin
Shelf

as manifested in the weathering profile of the Dales Gorge Member (Fig. 2b; Lantink et al., 2019). Of these, 17 macroband alternations have been formally defined and are known to correlate within the entire Hamersley region (see Fig. S1; Harmsworth et al., 1990; Trendall and Blockley, 1970). Based on sequence stratigraphic analysis, Krapež et al. (2003) and Pickard et al. (2004) have interpreted the S (as well as BIF) macrobands as distal density currents linked eustatic sea level variations. However, in line with a dominant eccentricity and thus low-latitude climate control (Lantink et al., 2019), such turbidites could be alternatively or additionally explained by enhanced delta- or shelf-slope instability during periods of increased runoff (Postma et al., 1993; Weltje and De Boer, 1993).

3. Materials and methods

3.1 Studied sections / cores

For our cyclostratigraphic study of the Kuruman IF and Dales Gorge Member, new proxy records needed to be generated and/or were used from a number of selected drill-cores and sections in the field. For the analysis of the Kuruman IF, high-resolution lithological, geochemical and well-log data were acquired from the new UUBH-1 core drilled near section Whitebank (Figs. 1, 3). The rationale behind the UUBH-1 drilling project was to provide a stratigraphically accurate, detailed record of the Kuruman IF cyclostratigraphy to complement the more basic logs of the alternations in the weathering profile and lithology in Lantink et al. (2019). For the investigation of the Dales Gorge Member, drone-based 'verticality' profiles were generated from its outcrops within the Hamersley Range at two different locations, namely at the Mount Bruce type locality, and at a section ~5 km west of Mount Jack (Fig. 1). These field sections were selected for their representative pattern of the distinct metre-scale alternations in relief and relative distance from each other (~80 m). In addition, we used existing high-resolution mineral abundance data from drill-cores DG47A (47A) and DD98SGP001 (DD98), obtained from hyperspectral scanning and made available by the Geological Survey of Western Australia. Core 47A forms the basis of the Dales Gorge Member 'type section' published photograph composite of Trendall and Blockley (1968), and was also analysed in the cyclostratigraphic study of (de Oliveira Carvalho Rodrigues et al., 2019) from a grayscale image. The DD98 core was drilled at the Silvergrass area ~150 km to the west of hole 47A, and intersects only the upper part of the Dales Gorge Member.

3.2 Kuruman proxy records from the new UUBH-1 core

3.2.1. Drlling and on-site logging

The UUBH-1 core was drilled ~15 km west of the Kuruman town at Fairholt farm (S27 28 44.4 E23 19 13.0), using NQ diamond casing and orientation drilling (~10° off vertical to the NE, perpendicular to an overall stratigraphic dip of 7° SW) from September to November 2017. Retrieved core material was carefully checked on a daily basis to ensure the correct stratigraphic order was maintained during the entire duration of the project. In addition, a schematic lithological log was made (Fig. S3) according to the same lithological facies ranking as explained in (Lantink et al., 2019) (0 = stilpnomelane lutite, 1 = siderite, 2 = siderite-magnetite, 3 = magnetite-siderite, 4 = magnetite-chert "zebra facies", 5 = magnetite). A complete succession of the Kuruman IF, from the lower Griquatown IF into the upper Gamohaan Formation, was intersected between 51.31 to 327.15 m depth with only a minor (~1.3 m) interval of core loss. Downhole geophysical logging (yielding magnetic susceptibility, natural gamma and density) was carried out after completion of the drilling. The core was subsequently sawed into halves at the University of Johannesburg. One archive half was kept in South Africa, and the other half was shipped to The Netherlands.

3.2.2 XRF core scanning and calibration

To obtain a high-resolution chemical record of the Kuruman and upper Gamohaan Formations, X-ray fluorescence (XRF) core scanning was carried out with the Avaatech core scanner at the Royal Netherlands institute of Sea Research on Texel. Prior to the analyses, the stratigraphic order of the core was again carefully checked using the original drill-site photos. In case of shattered lithology, true stratigraphic thicknesses were also estimated from the photos and/or drill-core metre marks. Individual core segments were placed into split plastic tubes (max. 1 m long sections) and supported from underneath with foam to create a stable and even surface. The XRF analyses were carried out with a 12 x 10 mm slit at 1 cm intervals on cleaned surfaces covered with a 4-μm SPEXCerti Ultralene foil to prevent any cross contamination. Calcite veins were circumvented by changing the Y direction of the detector (more towards the sides). Tube energy settings (10, 30 and 50 kV at a maximum of 2 mA), primary beam filters and measurement time were optimised for minor/trace elements while maintaining a dead time between 20 to 40 % (see Table S1 for applied settings), and spectral data were interpreted using bAxil spectrum analysis software developed by Brightspec. Eight external reference standards (GSR-4, GSR-6, GSD-10, JSd-1, JSd-3, MESS 3, SARM 2, and SARM 3; see (Hennekam et al., 2019)) were scanned every two weeks, indicating a constant performance of the XRF core scanner during the entire duration of the experiment (~2 months).

To convert the raw core scanner data to element concentrations, a large subset of discrete samples was selected and prepared for bulk-rock quantitative XRF analysis. About 100 samples of ~10 cm thickness spaced at 1 metre intervals were powdered and homogenized using a Retsch tungsten carbide jaw crusher and Herzog mill. Approximately 0.6 g of dry rock powder was fused into glass beads at 1,200 °C and analysed with an ARL Perform'X sequential XRF spectrometer at Utrecht University. For the calibration we used the multivariate log-ratio approach of (G. J. Weltje et al., 2015) as implemented within the AvaaXelerate software package of (Bloemsma, 2015). This resulted in a much cleaner i.e. less noisy pattern for many of the elements of interest - in particular Fe, Mn and Al - and high R^2 values in the corresponding cross-plots with the bulk-rock XRF reference values (Fig. S2).

3.2.3 XRF depth scale

Individually scanned core segments were combined into a single 'XRF composite record' by precisely determining the overlap between successive intervals, for which we used the high-resolution photos that were taken from every interval when placed inside the scanner (Fig. S4). To enable comparison to the well log data this composite depth record was subsequently recalibrated by matching the positions of the distinct shale layers within the XRF records (peaks in Zr, Al, K etc.) to the depths of their corresponding peaks in the downhole natural gamma signal. This yielded a stratigraphically accurate "NGL-corrected depth scale", which is presented in the main figures and was used for time series analysis. No further stratigraphic dip corrections were made because of the very minor overall ~3° offset from drilling perpendicular to the bedding, yielding a thickness change of only 0.15%.

3.3 Dales Gorge Member field logs and core proxy records

3.3.1 3-D outcrop models and verticality profiles

Since the Dales Gorge Member outcrops turned out to be too steep for manual logging of its basic lithology and weathering profile, 3-D photogrammetry models were constructed for the Mt Bruce and Mt Jack locations using an unmanned aerial vehicle (UAV). To limit the model size (i.e. number of included photos) but at the same time maintain enough stratigraphic detail, we concentrated for the Mt Bruce section on two narrower subsections located on its north-eastern face, namely "Mt Bruce West" and "Mt Bruce East", that were representative for the upper and lower part of the Dales Gorge Member stratigraphy, respectively. The same was done for section Mt Jack, which was studied at a "Mt Jack East" and "Mt Jack West" subsection. Photographs were taken manually by a 20-megapixel camera mounted on a multirotor UAV (DJI Mavic 2 Pro), which was flown parallel to the outcrop surface and provided approximately 70% horizontal overlap between successive photos. Each outcrop area was photographed from different heights and camera angles (at 0, 45 and 90 degrees) to provide complete coverage and to aid alignment during processing.

To ensure correct stratigraphic thicknesses were maintained in the photogrammetric model, 1 to 3 ground control points (GCPs) were placed at the base and top of each subsection (apart from Mt Jack West) and surveyed using an Emlid Reach RS+ GNSS receiver ("rover"). Raw GNSS measurements of the rover and a second Emlid receiver ("base station") were processed using the post-processing package RTKLIB and provided centimetre accuracy of the GCP locations relative to the base station. GCP positions were then used to optimise camera positions during the digital 3-D model building as done in Agisoft Metashape, yielding less than 0.1% error in the z direction (Fig. S5).

High-resolution dense point clouds were subsequently imported into the visualisation and interpretation software Cloudcompare. After applying a stratigraphic dip correction (using 'matrix transformation'), a simple log was made from the individual thicknesses of alternating high- versus low-relief intervals (using 'point picking'). In addition, a quantitative record of the outcrop's verticality (using 'compute geometrical features') was extracted along representative sections/slices, by compressing and averaging the computed verticality point cloud in the y/x relative to z direction. Individual verticality records and corresponding logs were subsequently combined into a single Mt Bruce and Mt Jack composite (Fig. S6).

3.3.2 Hylogger records cores 47A and DD98

To complement our analysis of the Dales Gorge Member outcrop data, we used already collected mineral reflectance data from cores 47A and DD98 at the courtesy of the Geological Survey of Western Australia (GSWA), measured with the Hylogger spectral scanner at the Perth Core library (Hancock and Huntington, 2010). From this dataset, the pattern of total ferric oxide mineral abundance (i.e. hematite and goethite), as well as total carbonate abundance, turned out to particularly well reflect the characteristic macroband pattern of the Dales Gorge upon initial inspection in 'The Spectral Geologist' (TSG) visualization programme during our visit to the core library. With thanks to the GSWA, these proxy records were subsequently extracted at a 1 cm depth resolution using the TSG software - from the visible near-infrared and short-wave plus thermal infrared range, respectively - for our cyclostratigraphic purposes. Note that the ferric oxide and carbonate abundances constitute relative weight percentage (wt%) and should be regarded in a purely qualitative way, since only a subset of minerals i.e. those present in the TSG software library are included in the determination of the total wt%, while minerals not visible in the targeted spectral range, as well as aspectral minerals such as magnetite, are excluded. Importantly, we further applied several corrections/adjustments to the 47A depth record, as careful inspection of the original Trendall and Blockley (1968) photographs revealed that several pieces of core had been turned upside down or were in the wrong position during acquisition of the Hylogger data.

3.4 Time series analysis

Time series analyses on all datasets, including record preparation, Fourier analyses and bandpass filtering, were performed with the Matlab program Acycle (Li et al., 2019) and the Astrochron R package (Meyers, 2014).

3.5 CA-ID-TIMS zircon dating

To obtain accurate and precise U-Pb zircon ages for the Dales Gorge Member, several of its shale macrobands as exposed in the gorges of the Karijini National Park and in the 47A drill-core were sampled for zircon extraction. The two shale samples used in this study are DS1 and DS9, which come from the Wittenoom Gorge type outcrop section as illustrated in Figure 4 of Trendall and Blockley (1970) and represent repeats of samples previously collected by A.F. Trendall (e.g. Trendall et al. 2004). The DS1 sample was collected over the entire width of the upper stilpnomelane-rich shale and corresponds to an approximate height of 13.9m in the 47A type section core (this core has a stratigraphic height scale instead of depth scale). The DS9 sample comes from the upper stilpnomelane-rich shale band of this macroband intervals, corresponding to a heigh of 64.9m in core 47A.

In an attempt to generate additional and more precise age constraints from the Kuruman IF, quarter core samples were taken from the stilpnomelane-rich shales at 110.75 m, 130.44 and 212.38 m depth in UUBH-1, corresponding to the lutite 4, 3 and 2 intervals which had previously been dated in Lantink et al. (2019) using material from the other half core left in Johannesburg. All samples were subsequently prepared for zircon extraction, which were chemically abraded to remove the effect of decay-damage-related Pb loss and dated using ID-TIMS techniques outlined in Lantink et al. (2019).

Depositional rate modelling was conducted using the R package Bchron (Haslett and Parnell, 2008) with concordant weighted mean $^{207}Pb/^{206}Pb$ ages or single grain $^{207}Pb/^{206}Pb$ ages depending on how many concordant analysis were found in the sample. For the lower Brockman IF, a third recently derived CA-ID-TIMS age from a shale close to the base of the Joffre Member at 371.2 m depth in core DD98 (Lantink et al., in review) was included in the calculation of the depositional rate, together with the new ages from DS1 and DS9. For this purpose, a single depth scale for these three samples had to be created which we did by correlating the Hylogger patterns of the DD98 and 47A cores. This yielded a corresponding virtual depth of 495.2 m for DS9 and 546.2 m for DS1 below the 371.2 m shale in DD98. A slightly updated depositional rate model was established for the Kuruman IF based on additional concordant zircon analyses obtained for the shales at 110m and 212m depth in core UUBH-1.

4. Results

4.1 Cyclostratigraphic analysis of the Kuruman Iron Formation

For our cyclostratigraphic study of the Kuruman IF we focus on two key proxies - that is, the iron-manganese ratio (Fe/Mn) and magnetic susceptibility (MS) signal - which were

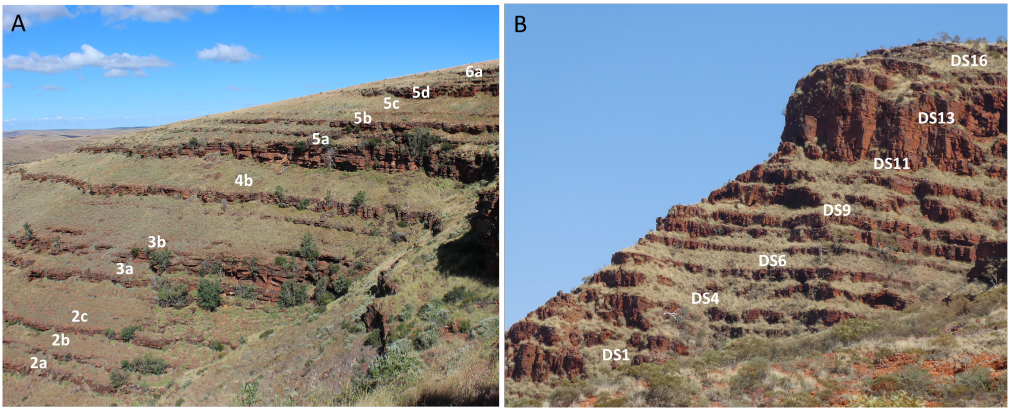

Figure 3. Regular metre-scale alternations and bundling in the weathering profile of the Kuruman IF at section Whitebank (**A**) and in the Dales Gorge Member near section Mount Jack (**B**). White labels in (**A**) denote the characteristic prominent BIF intervals as defined in Lantink et al. (2019). For the Dales Gorge Member the thicker S macrobands of the BIF-S macroband pattern of Trendall and Blockley (1970) are indicated.

selected from the XRF core scanning and geophysical logging data set, respectively, as obtained from the UUBH-1 core. We chose these two proxies because overall, they proved to most accurately reflect the characteristic cycle pattern of the Kuruman IF as described from outcrop (Lantink et al., 2019). Note, however, that the ratio of iron over aluminium (Fe/Al) shows an almost identical pattern to the Fe/Mn record (Fig. S7), and that this pattern is also reflected in our lithofacies rank series (Fig. S3). Below, we will first describe how this characteristic cycle pattern was recognised in the UUBH-1 core and compares to the original field logs of Lantink et al. (2019), before proceeding to a more detailed examination of the cyclostratigraphy using time series analysis.

4.1.1 Visual identification

The Fe/Mn and MS records of core UUBH-1 show distinct regular alternations throughout the stratigraphy of the Kuruman IF (100 - 302m depth) and upper Gamohaan Formation (302 - 327m depth) that, upon initial inspection, seem to occur on two principle thickness scales. First, large amplitude swings can be distinguished at a thickness scale of about 5m, which are particularly evident in the log(Fe/Mn) record, and below a depth of ~170 m (Fig. 4). The maxima of this basic ~5m-scale alternation correspond to intervals which are relatively rich in iron oxides, hereafter referred to as 'BIF', while the minima represent intervals relatively rich in iron carbonate and shale. These alternations, in turn, are grouped into larger-scale bundles composed one to three more pronounced ~5m-scale maxima, occurring at an approximate 15 to 20 m spacing.

The more pronounced ~5m-scale BIF intervals and bundles expressed in the normal Fe/Mn record can be readily identified as the characteristic cycle pattern observed in the

Kuruman IF weathering profile by Lantink et al. (2019), when compared to the original field logs of Whitebank and Woodstock (Fig. 4). The strongest and thickest Fe/Mn peaks – i.e., the three maxima at 260 - 275m depth; followed by two maxima at 240-250 m; followed by a single pronounced interval at 215m; and then four alternations from 180 – 200m with an anomalously thick and prominent zone at 200 m – bear a remarkable resemblance to the characteristic sequence of indurated BIF intervals labelled as cycles 2abc, 3ab, 4b and 5abcd. Recognising this link, the identification of the other previously defined BIF intervals – i.e. 1abc at the base of the Kuruman IF; 2d and 4a; and 6abc, 7a, 7bc and 8a in the upper part - becomes relatively straightforward. One notable exception is BIF 6a, which is rather poorly developed in the Fe/Mn record around 170m depth, but nevertheless manifested in the MS, and to a moderate degree in the Fe/Al, records.

When we correlate this characteristic pattern of pronounced BIFs between the core and field logs (see thick correlation lines in Fig. 4), additional more subtle Fe/Mn maxima at a regular 4-5m spacing can be distinguished in the relatively iron oxide-poor intervals separating bundles 1 to 6. These weaker ~5m-scale 'BIF' intervals - which we indicate with 1a.1, 1d, 2e, 3c-3e, 4c-4d, 5a.2, 5e and 6a.2 - are only partially expressed in the (logs of the) weathering profile at Woodstock and Whitebank. Given their clear manifestation in the core data, however, we can now add them to the original Lantink et al. (2019) cycle numbering and our correlations between the field logs and core UUBH-1 (see thinner horizontal lines in Fig. 4).

Taking a second, closer look at our established field-to-core framework reveals that, due to a different expression of several of the 'weaker' BIF intervals, the core proxy records exhibit a somewhat deviating bundling pattern than the general pattern observed in outcrop. For example, in both the Fe/Mn and MS records, 'BIF' 1d is substantially more pronounced than in the weathering profile logs, which results in a much less clear definition of bundles 1 and 2; note, incidentally, the distinct semi-5m-scale variability present in this lower part of the Kuruman IF. In addition, 'BIFs' 3d-e are slightly more pronounced in the log(Fe/Mn) record than in the field and much more pronounced in the MS signal, pointing to the presence of an additional 'BIF' bundle in between 3 and 4. Note also, however, that the MS record shows a notoriously different bundling pattern than that of the log(Fe/Mn) record around this stratigraphic interval, with 3a and 3b seemingly forming part of two separate bundles.

4.1.2 Spectral analysis and bandpass filtering

To examine this apparently more complex bundling pattern in more detail, we switch to time series analysis. In Fig. 5, the results of Lomb-Scargle (L-S; Lomb, 1976; Scargle, 1982) and multitaper method (MTM; Thomson, 1982) spectral analysis are presented for the log(Fe/Mn) and MS records, showing high concentration of power around three low-frequency bands, namely at ~4.5 – 6.5 m, ~14 – 25 m and ~30-50 m. More specifically, the log(Fe/Mn) MTM spectrum shows a dominant peak at 15.8 m and strong peaks at 5.6 m, 22.8 m and 46m, exceeding both the 99% LOWSPEC significance level (Meyers, 2012)

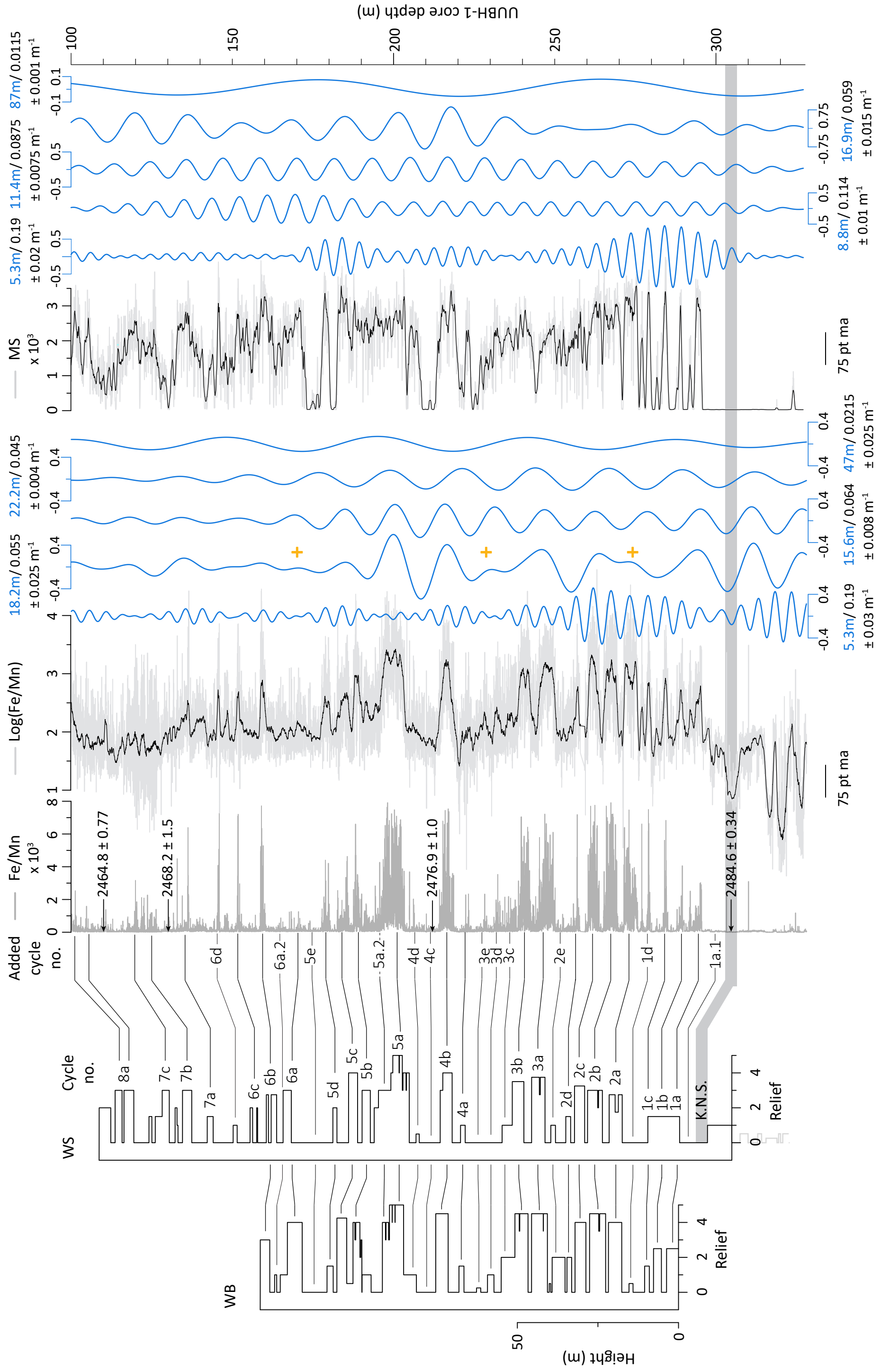
UUBH-1 core depth (m)
100
150
200
250
300
87m/ 0.0115 ± 0.001 m^{-1}
0.1
-0.1
11.4m/ 0.0875 ± 0.0075 m^{-1}
0.5
-0.5
16.9m/ 0.059 ± 0.015 m^{-1}
-0.75
0.75
8.8m/ 0.114 ± 0.01 m^{-1}
-0.5
0.5
5.3m/ 0.19 ± 0.02 m^{-1}
0.5
-0.5
MS x 10^3
0
1
2
3
75 pt ma
22.2m/ 0.045 ± 0.004 m^{-1}
0.4
-0.4
47m/ 0.0215 ± 0.025 m^{-1}
18.2m/ 0.055 ± 0.025 m^{-1}
15.6m/ 0.064 ± 0.008 m^{-1}
5.3m/ 0.19 ± 0.03 m^{-1}
Log(Fe/Mn)
1
2
3
4
75 pt ma
Fe/Mn x 10^3
0
2
4
6
8
2464.8 ± 0.77
2468.2 ± 1.5
2476.9 ± 1.0
2484.6 ± 0.34
Added cycle no.
6d
6a.2
5e
5a.2
4d
4c
3e
3d
3c
2e
1d
1a.1
Cycle no.
8a
7c
7b
7a
6c
6b
6a
5d
5c
5b
5a
4b
4a
3b
3a
2d
2c
2b
2a
1c
1b
1a
K.N.S.
WS
Relief
0
2
4
WB
Relief
0
2
4
Height (m)
50
0

Figure 4. Stratigraphic panel and TIMS U-Pb ages for the Kuruman (and upper Gamohaan) Formation showing the correlation of its characteristic cycle pattern as schematically logged in field sections Whitebank (WB) and Woodstock (WS) in Lantink et al. (2019) to the higher-resolution Fe/Mn and magnetic susceptibility records of core UUBH-1 from this study. Black lines for the MS and log(Fe/Mn) records indicate in a 75-point moving average of the original records (in grey) and blue curves on the right represent the output of Gaussian bandpass filtering. Horizontal black lines and corresponding cycle numbers on the left of the panel mark the 'BIF' intervals of individual ~5m-scale alternations, represented by maxima in the relief and/or core proxies; thicker black lines indicate the correlation of the more pronounced BIF intervals included in the original cycle numbering of Lantink et al. (2019). Orange '+' symbols mark the intervals where an additional ~16m-scale bundle is recognised relative to Lantink et al. (2019), as reflected by an additional maximum in the 0.055 m^{-1} ± 0.025 filtered log(Fe/Mn) signal. Note that there is a ~1.3m interval of core loss above 2c. 'K.N.S.' = Kleine Naute shale.

and 90% harmonic F-test confidence level (Fig. 5). For the MS record we find essentially the same results, except that a strong 22.8 m and 46m peak are absent in its corresponding MTM spectrum. Instead, additional significant peaks (i.e. satisfying both the required LOWSPEC and harmonic confidence levels of Meyers, 2014), are observed at 8.8 m and 11.4m, as well as around 87m.

Next, we use bandpass filtering to extract these main low-frequency cycles from the log(Fe/Mn) and MS records. For extracting the ~4.5 – 6.5 m components, we applied a wide (Gaussian) filter bandwidth centred around 5.3m which, as expected, picks up each of the previously identified abc-alternations (Fig. 4). Furthermore, an additional filtered ~5m cycle is recognised in the relatively thick interval between 5a.2 and 5b ("5a.3") in the filtered log(Fe/Mn) record, but this cycle is not picked up in the filtered MS record. For extracting the ~14 – 25m components we applied a narrow filtering around 15.6m and 22.2m to the log(Fe/Mn) record, as well as a broad filtering around 18.2 m (Fig. 4). As shown in Fig. 4, each of the previously identified bundles, including the weak 3d-e in between bundles no. 3 and 4, are followed by the filtered ~16m cycle, which furthermore places additional cycles in between bundles no. 1 and 2 (i.e. around 1d) and around bundles no. 5 and 6 (i.e. around 5a, 5c, 6a and 6c). These "~16m-scale" bundles are also picked up by the broad ~18m filter, which recognises 1d-2a, 3d-e and 6a as relatively weak additional ~16m cycles. In contrast, the filtered ~22m cycle only follows the more pronounced BIF bundles 1 to 5a, coinciding with distinct ~18m filter maxima, and shows minima around 1d, 3d-e, and 6a, coinciding with weak ~18m filter maxima. Thus, two simultaneously occurring cycles with periodicities of ~16m and ~23m appear to determine (largely) the characteristic bundling of ~5m-scale BIF intervals in this main part of the Kuruman IF stratigraphy (i.e. below 170 m core depth).

These results differ from Lantink et al. (2019), where similar MTM power spectra where generated for weathering profile logs, with dominant periodicities around ~4.3 – 6.3m and ~16m - 22m. However, in that study, the ~16m and ~22m components were attributed to a single cycle resulting from an upward change (i.e. decrease) in depositional rate, as a much stronger amplitude was observed for the ~22m cycle in the lower part of the Kuruman IF versus a much stronger ~16m cycle amplitude in the upper part from 4ab upwards. This interpretation was supported by a similar parallel shift in the dominant wavelength associated with the basic abc-alternations from ~6m to ~4.5m. However, no such a distinct trend is observed here in the amplitude or thickness of the filtered ~5m cycle in the log(Fe/Mn) and MS records, nor do we see any changes in the amplitude of the filtered ~16m or ~22m cycles, between 170m to 320m core depth.

Extraction of the ~47m cycle from the log(Fe/Mn) record reveals a link with the phasing of the ~16m and ~23m cycles (Fig. 4). When the filtered ~16 and ~23m cycles are in phase, corresponding to a maximum in the amplitude of the broadly filtered ~18m cycle, this coincides (roughly) with a maximum in the filtered ~47m cycle. Conversely, minima in the filtered ~47m cycle correspond to an out-of-phase relationship between the filtered ~16m and ~23m cycles, i.e. during ~23m cycle maxima that coincide with a minimum in the ~16m cycle (and minimum amplitude of the broadly filtered ~18m cycle).

Lastly, we apply bandpass filtering to the MS record for extracting the moderately strong ~9m, ~11.5m and ~87m cycles present in its corresponding MTM spectrum. As visible in Fig. 4, the filtered ~9m curve exhibits largest amplitude around bundle 6, placing successive maxima around 6a, 6b, 6c and 6d, which are also partially followed by the ~11.5 m filter. Lower in the stratigraphy, the filtered 11.5m cycle also picks up BIFs 5a-5a.2, the relatively thick 4b, and the slightly more pronounced 2a and 2c relative to 2b. Both the filtered ~9m and ~11.5m cycles exhibit a minimum around the pronounced MS minimum in between 3a and 3b. This minimum is further recognised as a minimum in the filtered ~16m MS cycle; note that in the filtered ~16m log(Fe/Mn) signal this minimum is placed above 3b. The filtered ~87m MS signal shows successive maxima at bundle 2 and in between bundles 5-6, thus seemingly arising from the relatively thick carbonaceous/shaley intervals surrounding BIF bundle 4.

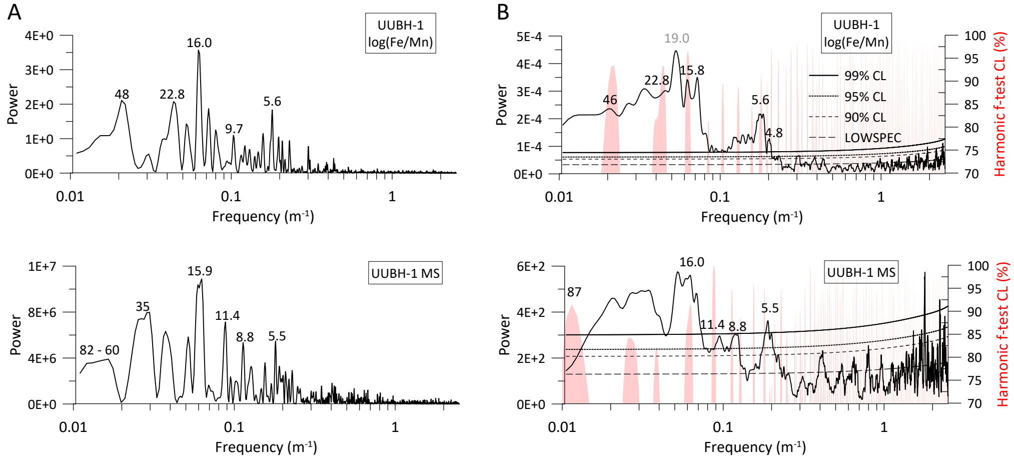

Figure 5. Spectral analysis results for the Dales Gorge Member. (**A**) Lomb-Scargle power spectra of LOWESS detrended log(Fe/Mn) and MS depth records. Peak labels of prominent spectral peaks are indicated in metres. (**B**) MTM (3 2π) power spectra of the records in (**A**) after applying a 0.1 m interpolation, with LOWSPEC background estimation and in red the harmonic F-test. Peak labels in black represent significant spectral peaks according to the requirements of Meyers (2012) i.e. satisfying both the 90% LOWSPEC confidence level and 90% harmonic F-test confidence level; for the peak label in light grey the latter is not the case.

4.2 Cyclostratigraphic analysis of the Dales Gorge Member

4.2.1 Visual identification

The cyclostratigraphy of the Dales Gorge Member as reflected in the logs and verticality profiles of the Mt Bruce and Mt Jack sections (Fig. 6) shows clear similarities but also differences with the Kuruman IF. In the first place, regular metre-scale alternations are visible between well-exposed ridges or cliffs and more weathered, low-relief intervals, which occur at a basic thickness scale of about ~5 - 7m in the lower ~2/3 part of the stratigraphy. The alternations are associated with the formal 'BIF-S macrobanding' of Harmsworth et al. (1990); Trendall and Blockley (1968) and have been labelled accordingly (Fig. 6). However, they are not completely the same as our "S intervals" are relatively thicker given that they are based on relief and not lithology. Still, the relative thickness proportion of 'BIF' versus 'S' in the Dales Gorge Member is generally larger than in the Kuruman IF, which creates a more staircase-like weathering profile with steeper slopes.

In the second place, a regular ~15-20m-scale variability is visible, most clearly in the interval from DB1- DB12, which is manifested by the occurrence of relatively thicker S macroband intervals, i.e. DS4, 6, 9, 11. However, the number of BIF-S alternations in each bundle is less than the characteristic three to four BIF intervals per large-scale bundle observed for the Kuruman IF, with instead groups of alternatingly three and two BIF macrobands (namely DB1-3, DB4-5, DB6-8, DB9-10). In the bundles constituting just two BIF-S macroband alternations, one of the two BIFs is ~1.5 times thicker than its neighbour and occurs adjacent to a thicker (~3-5m) S interval.

A seemingly different bundling pattern is observed in the lowermost (DB0) and upper 1/3 part (DB12-16) of the Dales Gorge Member (Fig. 6). These intervals are characterised by a larger absolute as well as relative proportion of BIF versus S intervals in terms of stratigraphic thickness, with BIF macrobands that are at least 1.5 to more than 2 times thicker than in the 'normal' BIF-S alternations in central part of the Dales Gorge Member. The very thick (~12-13m) DB0 at the base seems to represent a single BIF bundle on its own, while also showing some affinity with the overlying DB1 due to its more pronounced upper part and the relatively thin DS1 (compared to DS4, DS6 etc.). Similarly, the four ~5m-scale 'cherty BIF'-S alternations of the Colonial Chert Member below DB0 do not show any obvious grouping, apart from that the upper two beds are slightly more

Figure 6 (next page). Composite relief logs and verticality profiles for the Mt Bruce and Mt Jack sections with corresponding bandpass filters in blue. Indicated on the left of the schematic columns are the S macrobands of the characteristic 'BIF-S' macroband alternations of the Dales Gorge Member, the underlying Colonial Chert Member and overlying Whaleback Shale Member, according to the nomenclature of Morris (1983); Harmsworth et al. (1990).

pronounced and demonstrate some affinity with DB0 due to the relatively thin interstitial S interval CS6. Above DB12, the separation of DB13-15 from DB16-16a by the thicker S interval DS16 looks as a continuation of the 2-3-2 BIF grouping, but it occurs at a much larger thickness scale of ~25 - 30m. In addition, DB12 and DB13 show a slight affinity towards each other due to the relatively thin DS13 and more pronounced lower part of DB13.

Further insight into the internal structure of the thicker BIF macrobands can be gained if we look more closely at the verticality profiles and their correlative Hylogger mineral records from cores 47A and DD98 (Fig. 7). In particular in the ferric oxide record, a clear subdivision is noticeable in several of the thicker BIF intervals, indicating that they consist of a merged (partially) double ~5m-scale BIF-S alternation. This is particularly evident in DB12, whose ferric oxide signal reveals two distinct ~5m-scale maxima and a pronounced minimum halfway in between, indicating a poorly developed S layer at that position. In this way, DB12 looks somewhat analogous to the double BIFs DB16-16A, which are also separated by a very weak shale S16A, although their individual BIF-S alternations are significantly thicker (~7m in 47A and DD98; 8-9m at Mt Bruce) than those in DB12. Double alternations are further noticeable in DB13, DB15, DB9 and to some extent in DB4. For DB13 and 15, the subdivision as seen in the verticality and ferric oxide profiles is more asymmetric, with a second upper 'BIF' maximum that is relatively thinner (3-4m).

At comparable thickness scale, thin slightly more prominent beds/ferric oxide maxima can be distinguished in the thicker S macrobands, suggesting the presence of an additional BIF-S alternation in these intervals. This is particularly obvious for the faint maximum in the Mt Bruce verticality profile around DS6, which occurs at the same ~5m scale as DB6-8 above. However, the thinner (1.5 -2 m) spacing of the two conspicuous 'BIF' beds in DS11 seems to indicate variability at the sub-macroband level, as also seen in between CB4 and CB6 of the Mt Jack log. In general, this sub- or semi-5m-scale variability is more strongly developed in the carbonate record of core 47A (Fig. 7) such as around DS1-DB1 and DB4. Note further that the position of the carbonate minima associated with the ~5m-scale BIF-S variability are offset from those in the ferric oxide record, as can for instance be seen from the more symmetric subdivision of DB15 and DB16A (Fig. 7).

4.2.2 Spectral analysis and bandpass filtering

Spectral analysis was carried out on all four Dales Gorge Member proxies to independently test for cyclicity associated with the observed metre-scale BIF-S alternations and bundling. The resultant MTM spectrum of the Mt Jack verticality record

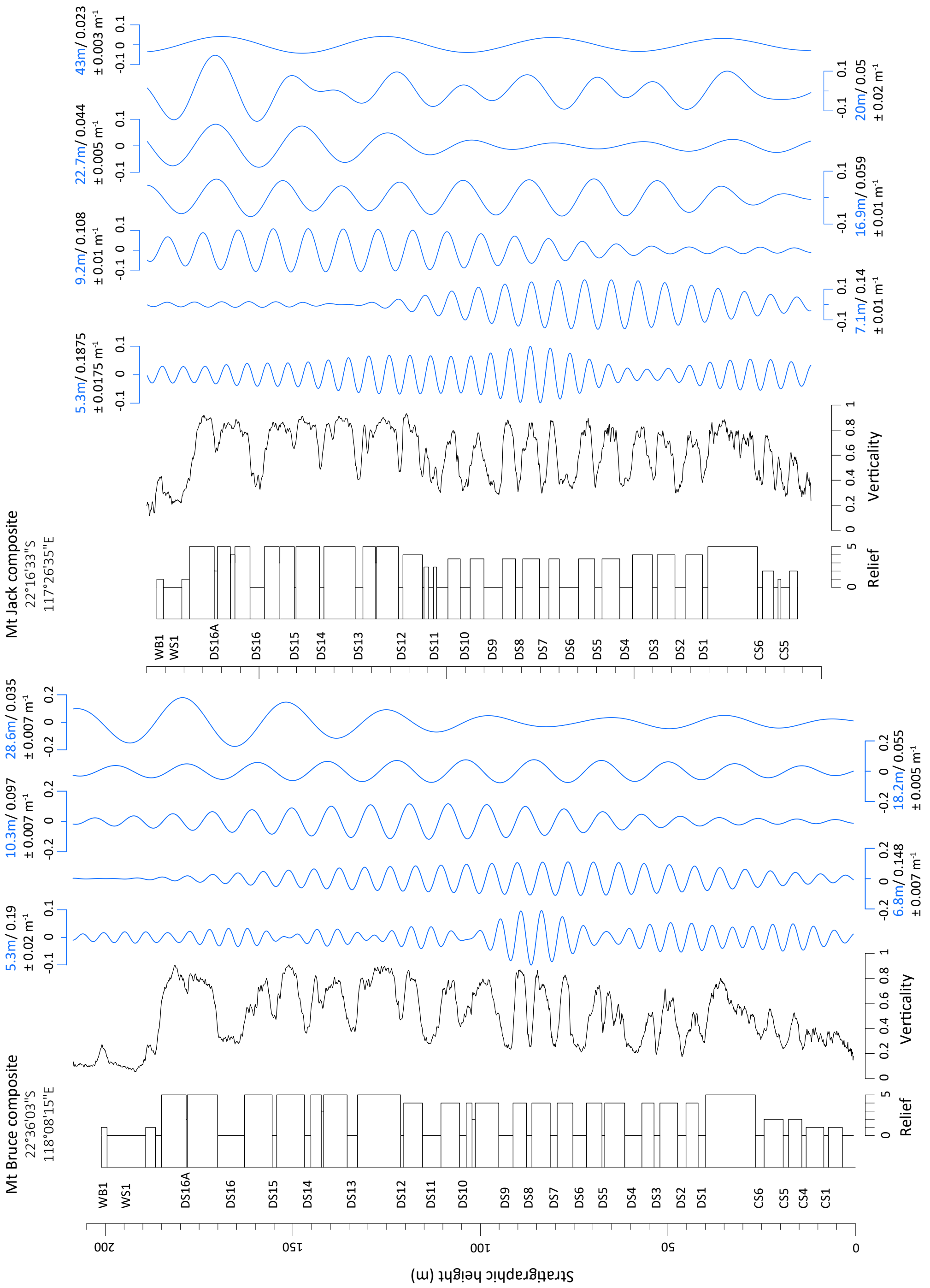
Mt Bruce composite
22°36'03"S
118°08'15"E
Mt Jack composite
22°16'33"S
117°26'35"E
Stratigraphic height (m)
0
50
100
150
200
WB1
WS1
DS16A
DS16
DS15
DS14
DS13
DS12
DS11
DS10
DS9
DS8
DS7
DS6
DS5
DS4
DS3
DS2
DS1
CS6
CS5
CS4
CS1
Relief
0
5
Verticality
0
0.2
0.4
0.6
0.8
1
5.3m/ 0.19
± 0.02 m-1
6.8m/ 0.148
± 0.007 m-1
10.3m/ 0.097
± 0.007 m-1
18.2m/ 0.055
± 0.005 m-1
28.6m/ 0.035
± 0.007 m-1
-0.2
0
0.2
-0.1
0.1
5.3m/ 0.1875
± 0.0175 m-1
7.1m/ 0.14
± 0.01 m-1
9.2m/ 0.108
± 0.01 m-1
16.9m/ 0.059
± 0.01 m-1
22.7m/ 0.044
± 0.005 m-1
20m/ 0.05
± 0.02 m-1
43m/ 0.023
± 0.003 m-1

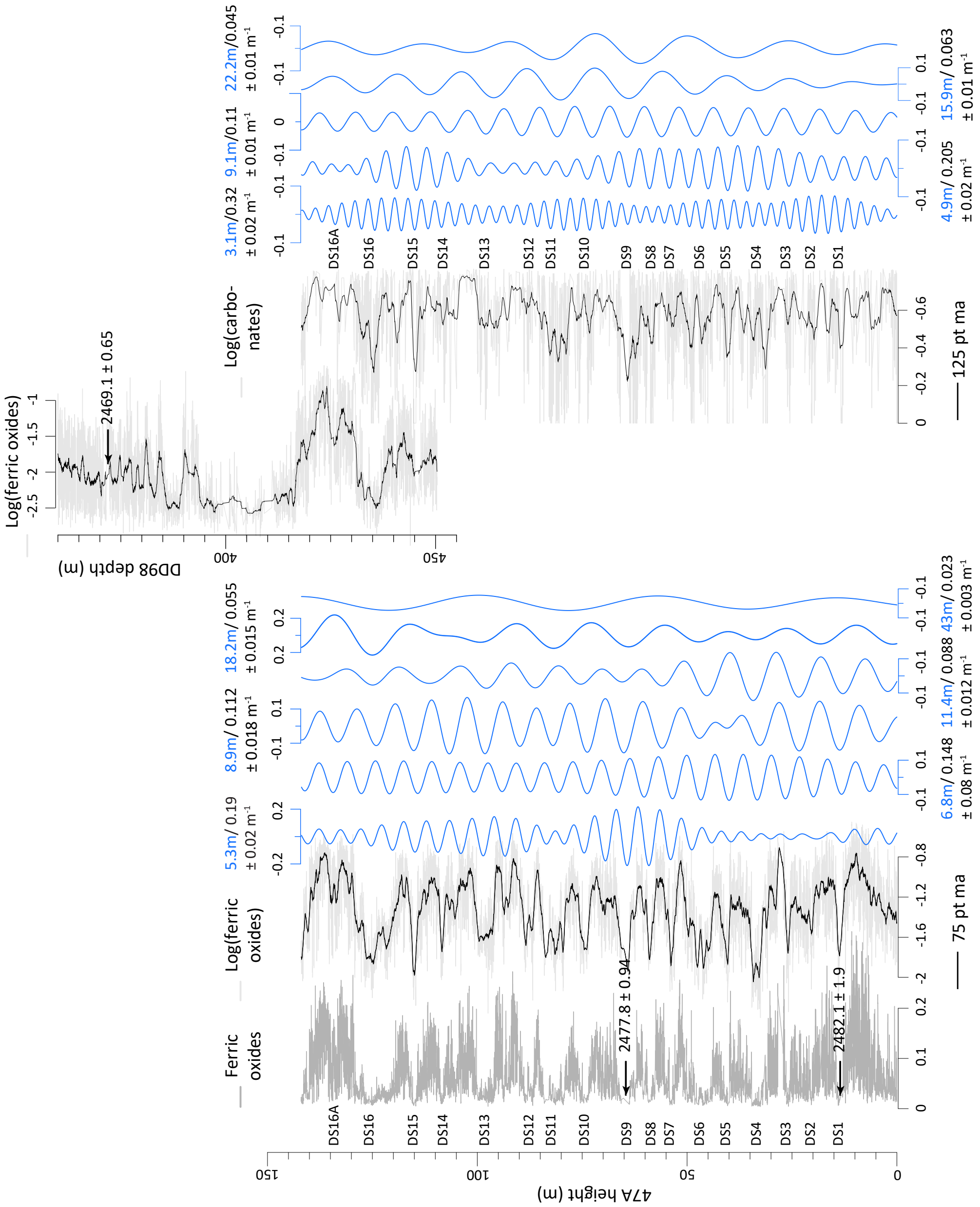

Figure 7. Hylogger ferric oxide and carbonate abundance records from cores 47A and DD98 and TIMS U-Pb ages. Results of bandpass filtering (in blue) and a 75-point and 125-point moving average (in black) are given for the log(ferric oxide) and log(carbonate) records, respectively. The position of the S macroband numbers is again indicated on the left.

shows dominant power concentration around 7m, in addition to strong peaks at 3.5m, 5.4m and 9m, each exceeding the 99% LOWSPEC and 90% harmonic confidence level. The L-S and MTM spectra of the Mt Bruce record look essentially the same as for the Mt Jack record, apart from that all periodicities (except the 7m cycle) are ~10% thicker, and an additional ~18m and 29m peak are recognised as significant peaks (reaching 90-95% LOWSPEC confidence). A very similar L-S spectrum is also found for the 47A ferric oxide record, but in this case the main periodicities are ~10% thinner compared to those in the Mt Jack spectrum (i.e. the 5.4m peak has become 4.9m). In addition, significant peaks are identified around 20-25m, ~42m, and at 10.4, 11.3 and 12.9m in the equivalent MTM spectrum, but note that not all of these peaks correspond to a harmonic F-test peak (Fig. 8) and that the spectrum is relatively noisy. In contrast, the MTM spectrum of the 47A carbonate record shows a much 'cleaner' pattern of well isolated peaks at 3.1m, 5m, 8.3m and 15.4m which does not show any significant cycles in the 10-13m range or around 7m.

For all four Dales Gorge Member proxies, bandpass filtering was again used for isolating the most prominent cyclical components, and whose filter outputs are subsequently compared to the original records (Fig. 6-7). First of all, extraction of the very strong ~7m cycle from the verticality and ferric oxide records shows that it follows the individual BIF-S macroband alternations 1-11. In particular, the filtered ~7m cycle show a good match with the relatively (~1.5 times) thicker BIFs DB1-3, 4 and 9. The filtered ~5m cycle, on the other hand, tracks only the thinner BIF-S alternations 5, 6-8, 10 and 11, as well as the four cherty BIF-S alternations of the Colonial Chert Member. Thus, the combination of a ~7m and ~5m cycle seems responsible for the basic BIF-S alternations characteristic of the lower 2/3 part of the Dales Gorge Member. In addition, the ~5m filtering places an additional cycle in each of the thicker S intervals (i.e. DS6, 11) or at the transition from thick S to thicker (~7m) BIF intervals (i.e. DS4-DB4 and DS9-DB9). The maxima of these filtered extra ~5m cycles coincide with a minimum in the filtered ~7m cycle, indicating the development of, indeed, an additional ~5m-scale BIF in the thick S macrobands, but which is suppressed by the strong ~7m cycle.

Besides the ~5m and ~7m cycles, bandpass filtering around ~9m reveals a correspondence to the even (~2 times) thicker BIF-S alternations, as characteristic of the upper 1/3 of the Dales Gorge Member stratigraphy. In particular, the filtered ~9m cycle shows a clear match with the double DB12, placing a maximum in the middle which counteracts the minimum in the filtered ~5m cycle at that position. In addition, the filtered ~9m cycle follows the thicker and more pronounced lower part of DB13 and 15, which both represent double ~5m cycles according to the filtering. In the ferric oxide record, DB13-15 are also picked up by the filtered ~7m cycle; note that the very low filter amplitude in the Mt Bruce and Mt Jack records is because of the significantly larger thickness of their upper BIF-S macrobands. Moreover, the thick and double BIFs DB16-16A are recognised as a double (filtered) ~7m cycle, as well as ~9m cycle, while being recognised as three (filtered) ~5m cycles.

Similar to for the Kuruman IF, filtering of the strong ~16m cycle shows that is follows the characteristic bundling of two or three BIF-S alternations of the Dales Gorge Member.

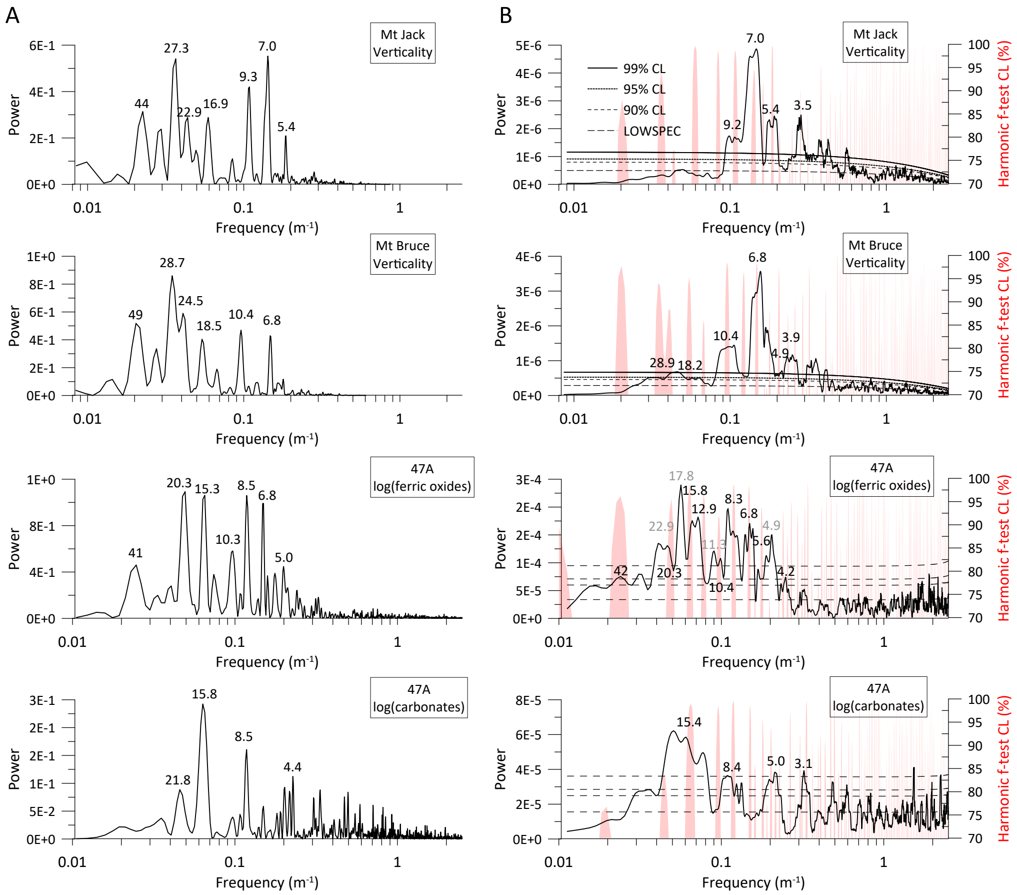

Figure 8.. Spectral analysis results for the Dales Gorge Member. (**A**) Lomb-Scargle power spectra of LOWESS detrended verticality profiles (Mt Bruce and Mt Jack) and core 47A Hylogger depth records. Peak labels of prominent spectral peaks are indicated in metres. (**B**) MTM (3 2π) power spectra of the records in (**A**) after applying a 0.1 m interpolation, with LOWSPEC background estimation and in red the harmonic F-test. The spectrum of the log(ferric oxide) record was made with a time-bandwidth product of 2 instead of 3. Peak labels in black represent significant spectral peaks according to the requirements of Meyers (2012) i.e. satisfying both the 90% LOWSPEC confidence level and 90% harmonic F-test confidence level; for peak labels in light grey the latter is not the case.

In Figs. 6-7, both the filtered ~16 – 18m cycles (using a narrow filter bandwidth) and the filtered ~18 - 20m cycles (using a broad filter bandwidth) track each of the thicker S macrobands defining the bundles, including DS13. Note that these thicker S intervals seem to be reinforced also by minima in the filtered ~9 (and often the ~7m) cycle. In the basal part of the Dales Gorge Member, however, the ~16m filtering does not follow the characteristic group of three BIFs DB1-3: the filtered ~16m cycle minimum is situated higher (around DS2 instead of DS1), while a filtered ~16m maximum is accordingly recognised around the top part of DB0. This appears to explain the apparent merging / affinity of DB1 with DB0. Secondly, the very thick bundle DB13-15 higher up in the stratigraphy is recognised as a double rather than single ~16m cycle.

This thicker bundle in the upper part of the Dales Gorge Member appears to be related instead to the lower-power cycles in the ~20 – 29 m range (Fig. 8). As visible in Figs. 6-7, their correspondingly filtered curves recognise bundle DB13-15 as a single cycle and generally exhibit largest amplitude in this upper interval. More specifically, the ~27-29m cycle present in the Mt Bruce and Mt Jack spectra seems the consequence of the relatively thicker upper macrobands in these two sections compared to in core 47A (Fig. 6). An exception is the 47A carbonate record (Fig. 7), where the filtered ~22m cycle shows a relatively constant amplitude throughout the stratigraphy, recognising DS1, DB4 and DB8 as successive (filtered) ~22m cycle minima. As in the Kuruman IF, filtering of the ~42-43m cycle indicates a link with the ~16m and ~22m cycle: maxima in the filtered ~43m cycle (shown for the Mt Jack record; Fig. 6) coincide roughly with maxima in the amplitude of the broadly filtered ~18-20m cycle, which in turn correspond with a combined maximum in the narrowly filtered ~16 and 22m cycles reinforcing each other.

To extract the ~10 - 13m spectral components in the 47A ferric oxide record (Fig. 8), a broad filtering was applied around 11.5m. The resultantly filtered ~11.5m cycle shows a particular correspondence with the alternatingly strong-weak-strong BIF pattern of DB1-3 and DB13-15, as well as with DB0 (Fig. 7).

Lastly, we applied a bandpass filter to the Mt Jack verticality and 47A carbonate records for extracting the strong ~3 - 3.5m components (Fig. 7; Fig. S8) present in their corresponding power spectra (Fig. 8). Comparison of the filtered ~3.5m cycle in the Mt Jack record shows a consistent 2:1 hierarchy with the filtered ~7m cycle, with maxima in the filtered ~3.5m cycle occurring systematically at the transition from S to BIF interval. This suggests that the ~3.5m cycle in this record represents largely, but not exclusively (Fig. S8), a harmonic resulting from the somewhat ‘rectangular’ shape of the BIF-S alternations (i.e. larger thickness proportion of the BIF relative to S intervals). In contrast, the filtering results for the carbonate record (Fig. 7) indicate the presence of a real ~3.1m cycle that is manifested as splitting of the thicker (~7m-scale) BIF-S alternations.

4.3 U-Pb ages and sedimentation rate

Concordant high-precision U-Pb TIMS results were obtained from the targeted stilpnomelane-rich shale intervals of the Dales Gorge Member (DS1 and DS9 upper), as well as from the Kuruman IF, which allow for a much more robust assessment of their relative timing than was hitherto possible based on available U-Pb SHRIMP ages of the Dales Gorge Member (Nelson et al., 1999; Trendall et al., 2004). The calculated $^{207}Pb/^{206}Pb$ ages derived from shale DS1 and DS9 upper are 2482.1 ± 1.9 Ma (2σ) and 2477.8 ± 0.9 Ma, respectively (Fig. S9) corresponding to 13.9m and 64.9m height in the 47A core. These ages constrain the depositional time frame of the Dales Gorge Member to the lower

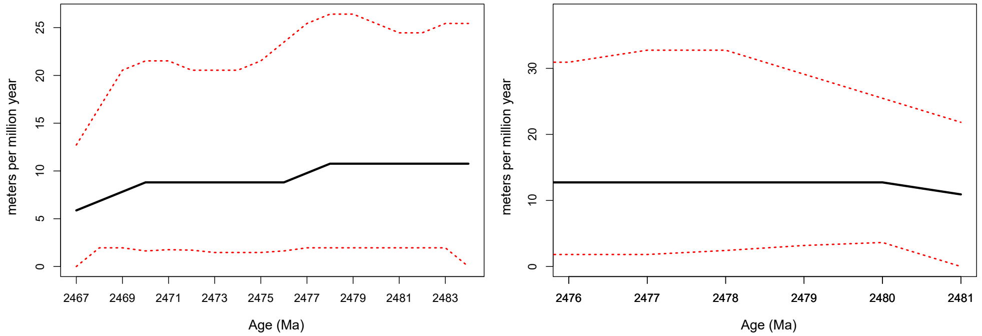

Figure 9..Bchron depositional rate model for the lower Brockman IF (left) based on the high-precision U-Pb ages from DS1, DS9 of the Dales Gorge Member and shale 371 from core DD98 of Lantink et al. (in review), and updated depositional rate model for the Kuruman IF (right) based on the improved ages of the shales at 212m and 110m depth in core UUBH-1. The red dotted lines indicate 97.5% confidence intervals. See Figure S8 for the Concordia diagrams.

circa ¾ of the Kuruman IF, whose onset is estimated at 2484.6 ± 0.34 Ma, reflecting the previously acquired TIMS U-Pb age for the basal Kleine Naute Shale of Lantink et al. (2019). In addition, revised $^{207}Pb/^{206}Pb$ ages were calculated for the shales at 212m and 110m depth in core UUBH-1 (lutites 2 and 4 of Lantink et al. 2019) from the adding of one concordant zircon analysis obtained from each sample. This yielded slightly older and significantly more precise ages of 2476.9 ± 0.9 Ma and 2464.8 ± 0.77 Ma, respectively (Fig. S9), compared to the initial results of Lantink et al. (2019).

Importantly, the U-Pb ages indicate an essentially identical accumulation rate for the Dales Gorge Member and Kuruman IF. An average accumulation rate of 12 (+20 -10) m/Myr is estimated for the Dales Gorge and overlying Whaleback Shale Member (Fig. 8), which includes a third, recently established TIMS U-Pb age from a shale at 371 m depth in core DD98 of 2469.1 ± 0.65 Ma (Lantink et al., in review). Likewise, our updated depositional rate model for the Kuruman IF suggests an average accumulation rate of 10 – 12 ± 10 m/Myr for the time interval corresponding to the Dales Gorge Member, which decreases slightly with increasing stratigraphic height. Thus the U-Pb geochronology appears to be consistent with a common/shared origin for the in thickness-matching cycles of Kuruman IF and Dales Gorge Member described in Sections 4.1 and 4.2. Whether and how these cycles can be interpreted in terms of an astronomical forcing control will be discussed in the following section.

5. Time calibration of the observed cycles and possible origin

The goal of this study was to examine the possibility of a correlation between the Kuruman IF and Dales Gorge Member based on their inferred long-period eccentricity related cycle pattern. As such, we must first turn to the question of whether such a Milankovitch control is indeed a (most) plausible explanation.

5.1 Astronomical interpretation

As previously discussed in Lantink et al. (2019), we cannot think of any phenomenon other than astronomical forcing that can explain the periodic nature, hierarchical stacking (i.e. bundling) and vast lateral continuity of the observed metre-scale alternations in the Kuruman IF and Dales Gorge Member. The lateral continuity of the alternations in the Kuruman IF spans at least 250 km (Lantink et al., 2019). Similarly for the Dales Gorge Member, a lateral continuity of ~150 km of the characteristic BIF-S macroband pattern is indicated by the four localities targeted in the current study (Fig. 1). However, this continuity may in fact be extended to almost 500 km knowing that the classical BIF-S macroband pattern of the Dales Gorge Member can be laterally traced over the full W-E stretch of the Hamersley Basin (Harmsworth et al., 1990; Trendall and Blockley, 1970).

For the Kuruman IF, independent support from U-Pb dating was already provided in Lantink et al. 2019 for the hypothesis that the main ~5m-scale iron oxide ('BIF') vs. carbonate/shale cyclicity represents the stratigraphic expression of the long 405 kyr eccentricity cycle (see also Section 2). Our updated, slightly higher sedimentation rate established for the lower half of the UUBH-1 core however, seems in even better agreement with this interpretation (Fig. 9). This is especially true if we take the somewhat weaker, but significant peak at 4.8 m, instead of the dominant 5.6 m peak, from the log(Fe/Mn) MTM spectrum (Fig. 8); this cycle lasts 400 kyr if we use the sedimentation rate of 12 m/Myr.

For the equivalent BIF vs. S cyclicity in the Dales Gorge Member, the sedimentation rate of 12 m/Myr for core 47A (Fig. 9) yields a period of 408 kyr in case the average 4.9 m wavelength (peak) in the ferric iron record is selected (MTM spectrum; Fig. 8). Again, the calculated period is remarkably close to that of the 405-kyr eccentricity cycle. Thus, as for the Kuruman IF, the cyclostratigraphic and U-Pb dating results are in mutual support of a long eccentricity origin for the ~5m-scale cyclicity in the Dales Gorge Member. This interpretation is different from that of de Oliveira Carvalho Rodrigues et al. (2019), who also suggested a link between the BIF-S macrobanding and the 405 kyr eccentricity cycle in their "Timescale 1", but reported a main '8 m' cycle as opposed to our ~5m.

It was further argued by Lantink et al. (2019) according to their "Hypothesis 2" that the very long ~2.4 Myr eccentricity cycle is most logical candidate for explaining the apparent "~16 – 22m" cycle responsible for the bundling of the ~5m cycles. Also denoted as the Mars-Earth $g_4 - g_3$ cycle, with g terms referring to the fundamental frequency of the rotation of the orbits of Mars (4) and Earth (3) on their respective orbital planes, this cycle is the strongest eccentricity component after the 405 kyr and short (~100 kyr) eccentricity cycles (e.g. Laskar et al., 2004). Hence, it was argued that, given the dominant expression of the 405 kyr cycle, a similarly strong imprint of the $g_4 - g_3$ eccentricity cycle could be expected, in case of a strong non-linear response and associated power transfer from climatic precession (the inferred primary insolation driver) to its longer-period amplitude modulating cycles of eccentricity. The ~1:3 – 1:4 ratio between the inferred 405 kyr- and (g_4 – g_3)-related cycles was attributed to a reduction in the period of g_4 – g_3 (to ~1.2 – 1.6 Myr), due to chaotic diffusion (Lantink et al., 2019), as also observed in the Mesozoic (e.g. Olsen and Kent, 1999; Ma et al., 2017; see also Section 7.3).

Unlike the g_4 – g_3 cycle, the period of the 405 kyr (g_2 – g_5) cycle – arising from the secular orbital motions of Venus and Jupiter – is considered relatively stable over the history of the Solar System (e.g. Hoang et al., 2021; Laskar et al., 2004, 2011; Laskar, 1993). Accordingly, this cycle can be used for time calibration of other (longer-period) cycles. Lantink et al. (2019) related the 4.5 - 6.1m cycle as seen in the evolutive harmonic spectrum of the Whitebank section to the stable 405 kyr eccentricity cycle to obtain a period between ~1.4 and 1.6 Myr for the single larger-scale cycle associated with the bundling. However, based on our more detailed cyclostratigraphic account of the Kuruman IF and Dales Gorge Member (Sections 4.1.2 and 4.2.2), now at least two cycles appear to be involved in this bundling, of which the dominant cycle has a period of ~16m. Therefore, it currently seems more logical to attribute this ~16m cycle to g_4 – g_3. Using the established mean cycle thickness of the 405 kyr-related cyclicity, this converts to a mean period of ~1.3 Myr (Table 1), i.e. shorter than initially estimated by Lantink et al. (2019).

However, in that case, what could be the origin of the weaker ~22-23m cycle additionally involved in the bundling particularly in the Kuruman IF weathering profile, and of the ~7m, ~9m and ~11.5m (10 – 13m) cycles responsible for the characteristic 'merging' of BIF intervals mainly in the Dales Gorge Member? From an eccentricity perspective, straightforward candidates for the ~9m and 11.5m cycles in terms of their time-calibrated periods (i.e. ~700 kyr and ~1 Myr; Table 1) are the present-day 690 kyr (g_2 – g_1) and 980 kyr (g_1 – g_5) eccentricity terms, respectively. Curiously, however, the amplitude of the ~9m cycle in the studied Dales Gorge Member records is much larger than expected given the relatively low amplitude of the g_2 – g_1 cycle, also compared to the weaker g_1 – g_5 cycle (Table 1; Laskar et al., 2004).

Of comparable amplitude to g_2 – g_1 is the eccentricity term (g_2 – g_5) – (g_4 – g_3), which occurs as the upper side band of the 405 kyr cycle in eccentricity power spectra (see for example Fig. 4 in (Laskar, 2020)). In the La2004 solution (Laskar et al., 2004), this cycle has a period of 490 kyr, but this period becomes ~590 kyr when adjusted for the supposed ~1.3 Myr period of g_4 – g_3, approximating the period estimated for the strong ~7m cycle (i.e. ~560 kyr) as identified in the Dales Gorge Member verticality and ferric oxide records. Despite its relative weakness, it has previously been suggested that this cycle is detectable in stratigraphic records (e.g. Olsen et al., 2019). Nonetheless the question remains why such a weak eccentricity term, resulting from the combination of four g-frequencies, would be so strongly present as a cycle in the Dales Gorge Member (i.e., being responsible for the ~1.5 times thicker BIF macrobands).

Even more puzzling is the origin of the ~22m cycle. Looking at the 0 - 33 Ma eccentricity spectrum of La2004 (Fig. 4 of Laskar, 2020) there is no obvious candidate which matches the estimated ~1.7 - 1.9 Myr period of this cycle apart from a minor peak around ~1.6 Myr, and given the fact that we already attributed $g_4 - g_3$ to the stronger ~16m cycle. This weak ~1.6 Myr cycle is attributed to $g_4 - \nu_6$ (Boulila, 2019; Laskar, 1990; Laskar et al., 2004, 2011) where ν_6 stands for the secular resonance term $g - g_6$ associated with asteroids in the main asteroid belt and Saturn, respectively (Froeschle and Morbidelli, 1994). However, the amplitude of $g_4 - \nu_6$ is five times lower than that of the $g_4 - g_3$ cycle and its period of ~1.6 Myr will have been different given a different g_4 value at that time. An alternative scenario that we need to consider is that the ~22m cycle represents $g_4 - g_3$, and that the ~16m cycle instead reflects the ~1.2 Myr obliquity amplitude modulation term $s_3 - s_4$ (s terms referring to the precession of the orbit's ascending nodes). This obliquity cycle is dynamically linked to the $g_4 - g_3$ cycle in the secular resonance theta (θ) currently manifested as $\theta = (s_3 - s_4) - 2(g_4 - g_3)$ (Laskar, 1990; see also Section 7.3). However, a stronger expression of $s_3 - s_4$ than $g_4 - g_3$ seems less likely given the evidence for a strong long eccentricity imprint, implying a dominant precession control, and the low paleolatitude position indicated by paleomagnetic data (Gumsley et al., 2017). Moreover, the fact that the ~16m cycle is relatively stronger in the Dales Gorge Member than in the Kuruman IF is in opposite direction to what would be expected if it represents $s_3 - s_4$, given that the Dales Gorge Member shows an overall clearer imprint of supposedly precession-related variability (the ~15 cm-thick Calamina cyclothem; de Oliveira Carvalho Rodrigues et al., 2019; Lantink et al., 2019; Trendall and Blockley, 1970), although de Oliveira Carvalho Rodrigues et al. (2019) also suggest the presence of an obliquity-related (~33cm) signal according to their Timescale 1.

5.2 Indirect terms resulting from non-linear response?

The question is whether we can explain the ~22m cycle in a different way, given the absence of an obvious astronomical candidate for this cycle. It is well-established from the younger part of the geological record that harmonics and combination tones of the primary astronomical signal can develop as a result of a non-linear response by the climate (e.g. Crowley et al., 1992; Imbrie et al., 1993; Le Treut and Ghil, 1983; Ruddiman et al., 1989; Short et al., 1991) and/or depositional system (e.g. Herbert, 1994; von Dobeneck and Schmieder, 1999; Weedon, 2003; Westphal et al., 2004). In fact, such a non-linear response is rather the rule than the exception. While the responsible nonlinear dynamics are often poorly understood, harmonic cycles may result from distortion of a single orbital cycle, while combination tones ('intermodulation frequencies') arise from nonlinear coupling of two or more primary cycles (von Dobeneck and Schmieder, 1999). An obvious example is the occurrence of an ~80 kyr double obliquity cycle in Pleistocene climate-sensitive proxy records (Marino et al., 2009; Raymo and Nisancioglu, 2003; Ruddiman et al., 1989).

Such nonlinear effects were likely playing a role as well during deposition of the Kuruman and Brockman IFs, as indicated by i) the ~2 – 2.5m variability in the lower part of the Kuruman IF, the Colonial Chert Member and the Dales Gorge Member (Section 4.1.1 and 4.2.1), which appears to reflect a semi-405 kyr cycle and/or double ~100 kyr cycle; ii) the 3 – 3.5m cycle in the Dales Gorge Member, which may represent a semi-

Table 1. Time calibrated period, relative strength and proposed astronomical origin (or otherwise) of the different cycles identified in the stratigraphy of the Kuruman IF and Dales Gorge Member.

Dales Gorge Member			Kuruman Formation					
L-S /MTM peak (m)	Period (kyr) assuming 4.9m = 405 kyr	strength	L-S/ MTM peak (m)	Period (kyr) assuming 4.8m = 405 kyr	strength	possible origin	Laskar et al. 2004 [-15 +5] Myr mean period (kyr)	Laskar et al. 2004 amplitude b'k x 10^4
3.1	262	+			-	$(g_2 - g_5) + (g_1 - g_5)$ (?) and/or ~560 kyr harmonic?	285	
4.9	405	+	4.8	405	+	$g_2 - g_5$	405	107
			5.6	473	++	thicker 405 kyr cycle?		
6.8	562	++			-	$(g_2 - g_5) - (g_4 - g_3)$ (?)	486 / 593*	20
8.3	686	++	8.8	743	+/-	$g_2 - g_1$ (?) and/or ~1.3 Myr harmonic?	688	18
10.4	860	+/-	9.7	818	-	thinner ~1 Myr cycle??		
11.3	934	-	11.4	962	+/-	$g_1 - g_5$ (?)	967	28
12.9	1066	-				thicker ~1 Myr cycle or thinner/shorter ~1.3 Myr cycle??		
15.8	1306	++	15.9	1342	++	$g_4 - g_3$ (?); or $s_3 - s_4$??	2369	30
20.3 / 21.8	1678 / 1802	+/-	22.8	1924	+	beat of ~690 kyr and ~1 Myr cycle and/or double ~11m cycle??		
42	3471	+/-	47	3966	+	beat of ~1.3 and ~1.9 Myr cycle and/or double ~22m cycle (?)		
			87	7341	-	~9 Myr cycle (?)		

*when assuming $g_4 - g_3$ has a period of 1.3 Myr.

7m cycle (Fig. S8); and iii) a ~46 m cycle, which may correspond to a difference tone of the ~16m and ~22 - 23m cycle. As such, we consider it not unlikely if the 22-23m cycle similarly represents a harmonic and/or combination term induced by nonlinear response. Based on its period, we may speculate that the ~22m cycle represents a double ~11.5m (possible $g_1 - g_5$-related) cycle or a difference term arising from the ~7m (or ~9m) cycle with the ~11.5m cycle. Such a more indirect astronomical origin of the ~22-23m cycle could also explain why its estimated mean period from MTM analysis differs between the Dales Gorge Member (i.e. 1.7 – 1.8 Myr) and the Kuruman IF (i.e. > 1.9 Myr; Table 1).

Likewise, we can formulate an alternative explanation for the origin of the strong ~7m cycle as a non-orbital difference term of the ~5m (g_2 – g_5-related) and ~16m (possible g_4 – g_3-related) cycle, arising from the non-linear response within the climate and/or depositional system, as well as for the ~9m cycle as a climatic/depositional harmonic of the ~16m ($g_4 - g_3$) cycle and/or a difference term of the ~5m ($g_2 - g_5$) and ~11.5m ($g_1 - g_5$) cycles (Table 1).

However, at the same time, we know that the astronomical cycles represent harmonic/combination cycles themselves, as they originate from the Earth's precession frequency (p) and/or the fundamental planetary frequencies (g and s). More specifically, the main eccentricity cycles can be written as combinations of two g_i frequencies of the inner planets plus Jupiter (with i = 1 to 5) or in fact, of their corresponding climatic precession terms $p + g_i$. These can in turn be combined to form higher-order eccentricity terms which become progressively weaker. Thus by definition, the relatively weak ($g_2 - g_5$) – ($g_4 - g_3$) eccentricity term is a difference tone of the $g_2 - g_5$ and $g_4 - g_3$ cycle. In addition, the $g_2 - g_1$ cycle represents a difference cycle of the fundamental g_2 and g_2 frequencies, but can also be written as the combination of $g_2 - g_5$ and $g_1 - g_5$. Thus, instead of representing harmonics and/or combination tones arising from the nonlinear response of the climate and/or depositional system, the ~7 and ~9m cycles could alternatively, or additionally, result from amplitude distortion of the primary eccentricity terms ($g_2 - g_5$) – ($g_4 - g_3$) and $g_2 - g_1$. This same explanation may even be invoked for the ~2 - 2.5m variability, being possibly associated with amplitude distortion of the very weak ~200 kyr eccentricity cycle $-2g_2 - 2g_5$ (Hilgen et al., 2020), as well as for the 3 – 3.5m cycle, being possibly related to the very weak ~280 kyr eccentricity term arising from ($g_2 - g_5$) + ($g_1 - g_5$ (Table 1).

In summary, much uncertainty remains concerning the specific astronomical origin – either linear or nonlinear - of several cyclic components involved in the characteristic cycle patterns of the Kuruman IF and Dales Gorge Member, in particular the ~7, ~9 and ~22m cycles. Nonetheless, we consider the cyclostratigraphic and U-Pb evidence presented in Section 4 sufficiently convincing in support of the Milankovitch interpretation of Lantink et al. (2019) for their main hierarchy of two cycles, namely i) a ~5m cycle defining (largely) the basic 'BIF' versus 'S' alternations related to the 405 kyr eccentricity cycle; and ii) a ~16m cycle dominantly responsible for the bundling of several BIF intervals (associated with the ~5m cycle), which may reflect the expression of the g_4 – g_3 cycle with a periodicity of ~1.3 Myr. Therefore, we consider it justified to proceed with our attempt to establish a detailed cyclostratigraphic correlation between the Kuruman IF and Dales Gorge Member, focusing in particular on the expression and scale of the ~5 and ~16m cycles.

6. Establishing of a 405 kyr-scale cycle framework

6.1 Correlation option I: based on the characteristic weathering profile pattern

Cyclostratigraphic correlations between outcrops of the Kuruman IF in the Griqualand West basin have previously been established over a distance of 250 km on the basis of the characteristic pattern in the succession of prominent BIF bundles as seen in weathering profile (i.e., 2abc, 3ab, 4(a)b, and the double (~16m-scale) bundle 5abcd, see Lantink et al., 2019). Likewise the correlation between the weathering profile logs and the new UUBH-1 core proxy records based on identification of this characteristic pattern proved relatively straightforward in the present study (Section 4.1). Similarly the distinctive cycle pattern seen in outcrops and cores of the Dales Gorge Member has been used for detailed correlations across the Hamersley basin over many hundreds of kilometres. Thus, adopting the same visual approach seems a promising (starting) strategy for establishing the intended high-resolution correlations between the Kuruman IF and the Dales Gorge Member. To establish these correlations, we will use the log(Fe/Mn) (rather than MS) record of the Kuruman IF, which is generally more representative for its weathering profile. For the Dales Gorge Member, we will use the log(ferric oxide) record of core 47A as representative proxy, also because the cycle thicknesses in that record are more similar to those in the Kuruman IF than the verticality profiles of Mt Jack and Mt Bruce.

As a starting point for our correlation we choose 2abc, the characteristic group of three prominent BIFs seen in the Kuruman IF weathering profile (Lantink et al., 2019). Looking at the outcrop pictures of the Dales Gorge Member (Fig. 3; Fig. S5), and the verticality and log(ferric oxide) records (Fig. 6-7), the three well-defined alternations of roughly equal thickness DB6-8 bear most resemblance to 2abc, and were correlated accordingly (Fig. S10). Subsequently, the most logical correlation, when focusing on the more pronounced and/or thicker BIF intervals, is to correlate 3ab to DB9-10, 4ab to DB11-12 (where 4b corresponds to the lower part of DB12), and the very prominent bundle 5abcd to DB13-15, interpreting DB13 and DB15 as a double ~5m cycle. Also, the conspicuous resemblance of the distinct double DB13, as expressed in the 47A carbonate record, and 5a is in line with this correlation (Fig. 7). To complete our scheme, we must correlate the lower bundle 1abc in the Kuruman IF to DB4-5, and 6ab to the very prominent DB16-16A at the top of the Dales Gorge Member.

However, starting from this initial correlation option Ia, we encounter two critical inconsistencies with regard to our cyclostratigraphic and U-Pb results. Firstly, there are no correlative ~5m-scale BIF-S alternations in the Dales Gorge Member for the three weaker BIFs 3c-e in the extra ~16m-scale bundle in between 3 and 4 of the Kuruman IF. As a consequence, 3c-e need to be correlated to DS11, implying a condensed interval. To avoid this condensed interval (or alternatively hiatus), the correlations of the cycles above 3b can be shifted upwards by two ~5m cycles in the Dales Gorge Member (option Ib). However, this revision results in a loss of the fit between the cycle patterns in the two units (Fig. S10).

Secondly, correlation option I (both Ia and Ib) is incompatible with the U-Pb geochronology, especially with regards to the ages of DS9 (Dales Gorge Member) and the shale at 212m in core UUBH-1 (Kuruman IF). The 2σ age uncertainties associated with these ages allow for a maximum difference of 2.8 Myr between the two dated stratigraphic levels. This is in direct conflict with the at least eight ~5m or 405 kyr eccentricity-related cycles recognised in this interval, implying a duration of 3.2 Myr (Fig. 10). This implies that the Dales Gorge Member needs to be shifted upwards relative to the Kuruman IF by at least one (filtered) ~16m cycle to make the cyclostratigraphic correlations consistent with the U-Pb results.

6.2 Correlation option IIa: most consistent with the U-Pb geochronology and characteristic pattern

We therefore explore a second, alternative correlation between the Kuruman IF and Dales Gorge Member that is both consistent with the U-Pb dates and the characteristic cycle patterns (succession of prominent BIF bundles) by shifting the Dales Gorge Member two (filtered) ~16m cycles upwards. In this way, the 212m shale and DS9 are placed within two or three ~5m cycles from each other, which is consistent with their mean U-Pb age difference of 1.2 Myr. From a cyclostratigraphic point of view, this two-bundle shift is required to correlate 2abc to the other group of three pronounced, roughly equal BIFs in the Dales Gorge Member, namely DB1-3. For the remainder of the stratigraphy, we proceed by first correlating at the 16 m bundle level, followed by linking the more prominent ~5m-scale BIFs of each bundle. Accordingly, 3ab correspond to DB4-5, 4b to DB9 and 5a to DB12. For the upper part, we shift the Dales Gorge Member upwards by only one filtered ~16m in order for the correlation to make most sense in terms of pattern resemblance by linking the characteristic group of three prominent BIFs 5bcd to DB13-15 and 6a to DB16 (Fig. 10).

Although this second correlation (option IIa) initially did not seem most logical in terms of resemblance in characteristic pattern, similarities in the expression and/or number of prominent BIFs per correlated bundle are still largely maintained and are in some cases even improved. In particular, the correlation of 2abc to DB1-3 instead of to DB6-8 (as was the case for option I) makes sense from the perspective of the UUBH-1 proxy records (as opposed to weathering profile expression), in which 2a forms part of bundle 2abc as well as showing affinity with the distinct 1d below. This pattern looks similar to the characteristic merging of DB1 with the top of DB0; both features are related to the somewhat higher stratigraphic position of a ~16m-scale cycle maximum (i.e., around 1d and the top of DB0, respectively; see narrow ~16m filter output in Fig. 4). In addition, 2a and 2c are slightly more pronounced than 2b, as are DB1 and DB3, which in both cases is related to a strong expression of the ~11.5 m cycle. Moreover, higher up in the stratigraphy, the resemblance of 4d followed by the very prominent, double 5a with DB11-12 (according to option II) is improved and appears more logical than with DS12-DB13 (according to option Ia).

However, at the individual ~5m- and ~16m-cycle level, we encounter several misfits as well if we stick to our strategy of linking the most prominent BIF intervals. In the middle section, the result of correlating 3ab to DB4-5 is that an additional ~5m cycle is required in DS4, on top of an already-inferred extra cycle, as well as one additional ~5m cycle in

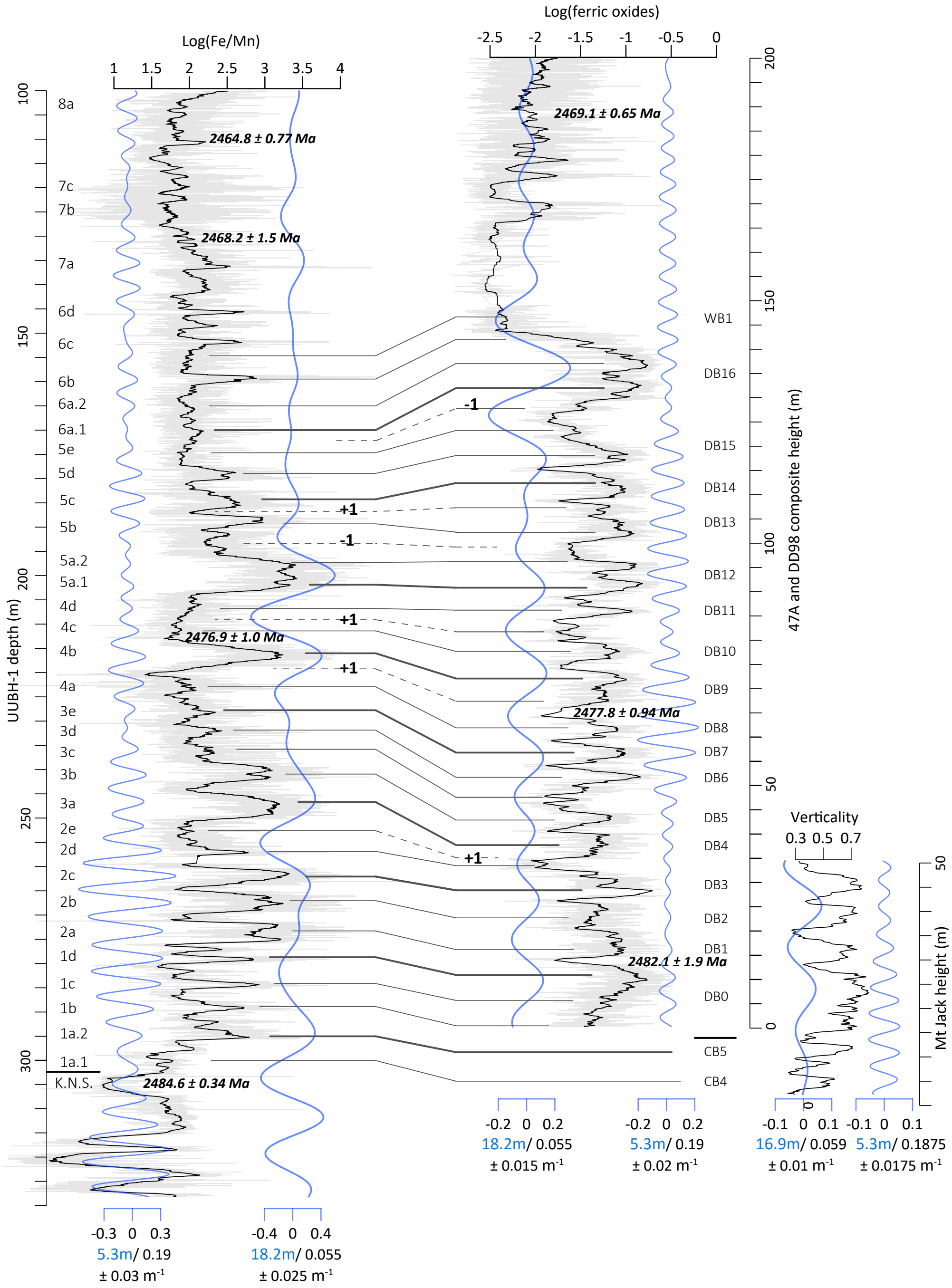

Log(Fe/Mn)
1 1.5 2 2.5 3 3.5 4
Log(ferric oxides)
-2.5 -2 -1.5 -1 -0.5 0
UUBH-1 depth (m)
100
150
200
250
300
8a
7c
7b
7a
6d
6c
6b
6a.2
6a.1
5e
5d
5c
5b
5a.2
5a.1
4d
4c
4b
4a
3e
3d
3c
3b
3a
2e
2d
2c
2b
2a
1d
1c
1b
1a.2
1a.1
K.N.S.
2464.8 ± 0.77 Ma
2468.2 ± 1.5 Ma
2476.9 ± 1.0 Ma
2484.6 ± 0.34 Ma
2469.1 ± 0.65 Ma
2477.8 ± 0.94 Ma
2482.1 ± 1.9 Ma
-1
+1
-1
+1
+1
+1
47A and DD98 composite height (m)
200
150
100
50
0
WB1
DB16
DB15
DB14
DB13
DB12
DB11
DB10
DB9
DB8
DB7
DB6
DB5
DB4
DB3
DB2
DB1
DB0
CB5
CB4
Verticality
0.3 0.5 0.7
Mt Jack height (m)
50
0
-0.3 0 0.3
5.3m/ 0.19
± 0.03 m^{-1}
-0.4 0 0.4
18.2m/ 0.055
± 0.025 m^{-1}
-0.2 0 0.2
18.2m/ 0.055
± 0.015 m^{-1}
-0.2 0 0.2
5.3m/ 0.19
± 0.02 m^{-1}
-0.1 0 0.1
16.9m/ 0.059
± 0.01 m^{-1}
-0.1 0 0.1
5.3m/ 0.1875
± 0.0175 m^{-1}

Figure 10. Correlation option IIa for the Kuruman IF and Dales Gorge Member, based on the highest resemblance in their characteristic pattern and consistency with the U-Pb ages. Horizontal lines indicate the correlation of observed ~5m-scale BIF intervals and/or interpreted 405 kyr cycles (dotted lines where this is uncertain). Thick lines mark the more prominent BIFs of each interpreted ~16m bundle (broad ~18m filter outputs shown). Note that this correlation implies the presence of two condensed 405 kyr-related cycles in DS4, one in between 4a and 4b and one in between 4b and 4c. It also implies that the top of DB15-DS16 represent a single 405 kyr.

between 4c and 4d. In addition, this correlation implies that the top of DB9 correlates to the interval in between 4a and 4b in the Kuruman IF. Higher up in the stratigraphy, the consequence of linking 5b to the lower, more pronounced part of DB13 is that it requires the absence of an additional ~5m cycle above 5a.2 (“5a.3”), but again the addition of a ~5m cycle in between 5b and 5c, if we assume that DB13 represents a double ~5m cycle. In addition, correlation IIa implies the absence of a second ~5m cycle for the upper part of DB15.

Furthermore, with correlation IIa we have thus far treated bundle DB13-15 as a single ~16m bundle, in contradiction with what is suggested by the double (filtered) ~16m maximum around this interval. The problem is that it is unclear whether the depositional rate of the Dales Gorge Member has increased in the upper part, in which case DB13-15 could be regarded a single ~16m bundle equivalent to DB1-3; or whether the depositional rate has stayed relatively constant, in which case the overall thicker (>7m) BIFs are due to a weaker expression of the ~5m cycle. A further complicating factor is the uncertainty in the period of the 16m-scale cycle interpreted as $g_4 - g_3$, which is inherently unstable.

6.3 Correlation option IIb: most consistent with the ~5m and ~16m filtering

The discrepancies of correlation IIa with respect to the postulated number of ~5m and (filtered) ~16m cycles in the Dales Gorge Member can largely be resolved when considering a third, modified correlation II (option IIb) if we attach more importance to the ~5m and ~16m filtering of the Kuruman IF and Dales Gorge Member than to the resemblance in cycle pattern. This results in modified correlation option IIb in which the cycles in the 2e - 4c interval of the Kuruman IF are shifted upwards by one (filtered) ~5m cycle with respect to the Dales Gorge Member. In that case, no extra ~5m cycles need to be assumed in DS4 and 4c-d. However, this means that the very prominent BIFs 3b and 4b in the Kuruman IF are now correlated to shale DS6 and to the less prominent BIF DB10, respectively, in the Dales Gorge Member.

Similarly, shifting the correlations above double 5a – DB12 from the Kuruman IF to the Dales Gorge Member by two (filtered) ~5m cycles upwards resolves the need for an additional ~5m cycle between 5b and 5c, and is compatible with a second ~5m cycle in the top of DB15. However, as a consequence, 5c is now correlated to the less prominent upper part of DB13, the weak 5e to the prominent lower part of DB15, and the less prominent 6c to the very prominent DB16A. In this way, we have arrived at a correlation that is based on

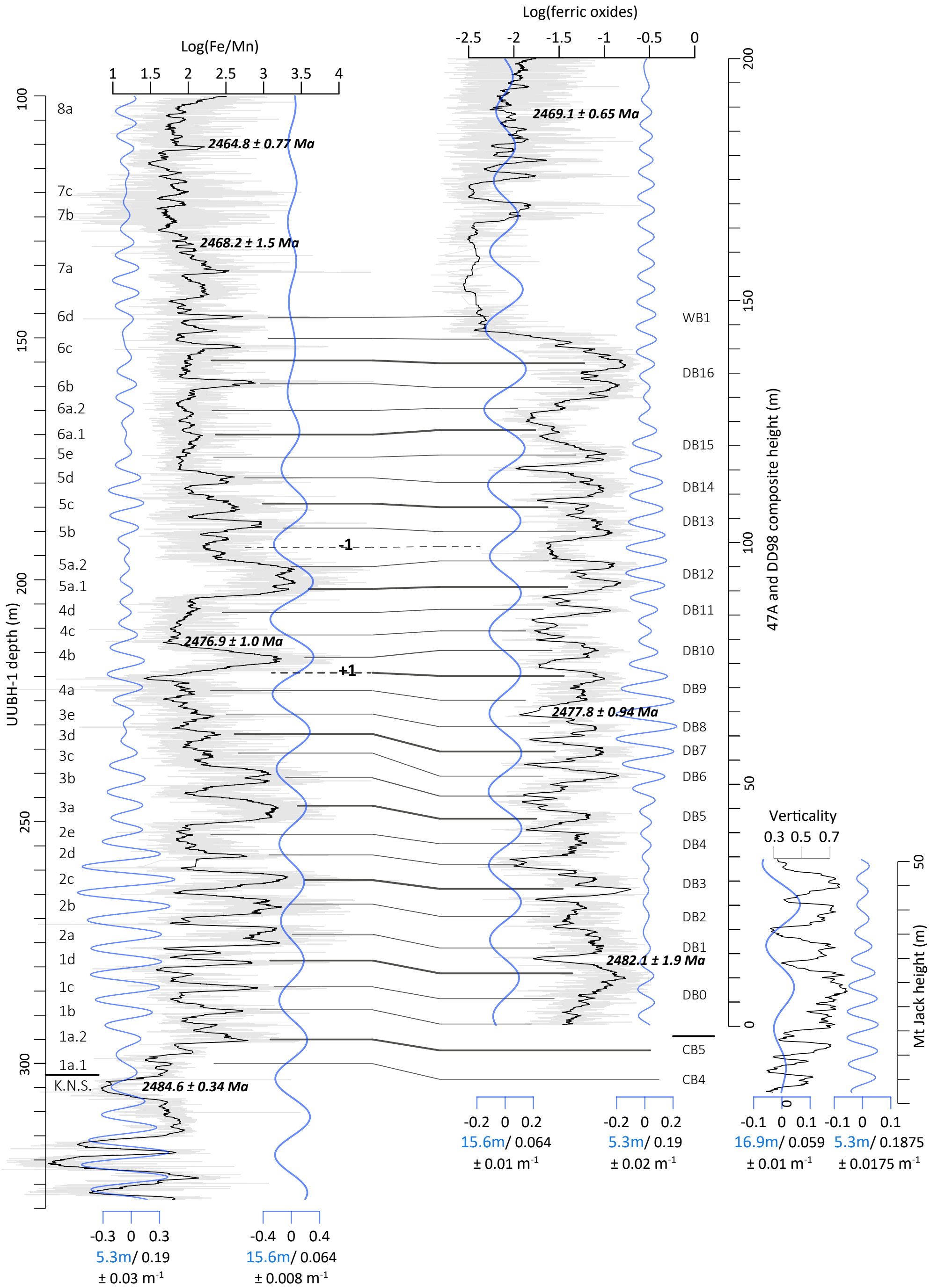

Log(Fe/Mn)
1
1.5
2
2.5
3
3.5
4
Log(ferric oxides)
-2.5
-2
-1.5
-1
-0.5
0
UUBH-1 depth (m)
100
150
200
250
300
8a
7c
7b
7a
6d
6c
6b
6a.2
6a.1
5e
5d
5c
5b
5a.2
5a.1
4d
4c
4b
4a
3e
3d
3c
3b
3a
2e
2d
2c
2b
2a
1d
1c
1b
1a.2
1a.1
K.N.S.
2464.8 ± 0.77 Ma
2468.2 ± 1.5 Ma
2476.9 ± 1.0 Ma
2484.6 ± 0.34 Ma
2469.1 ± 0.65 Ma
2477.8 ± 0.94 Ma
2482.1 ± 1.9 Ma
-1
+1
WB1
DB16
DB15
DB14
DB13
DB12
DB11
DB10
DB9
DB8
DB7
DB6
DB5
DB4
DB3
DB2
DB1
DB0
CB5
CB4
47A and DD98 composite height (m)
200
150
100
50
0
Verticality
0.3 0.5 0.7
Mt Jack height (m)
50
0
-0.3 0 0.3
5.3m/ 0.19
± 0.03 m-1
-0.4 0 0.4
15.6m/ 0.064
± 0.008 m-1
-0.2 0 0.2
15.6m/ 0.064
± 0.01 m-1
-0.2 0 0.2
5.3m/ 0.19
± 0.02 m-1
-0.1 0 0.1
16.9m/ 0.059
± 0.01 m-1
-0.1 0 0.1
5.3m/ 0.1875
± 0.0175 m-1

Figure 11. Correlation option IIb for the Kuruman IF and Dales Gorge Member, most consistent with the ~5 and ~16m filtering. Horizontal lines indicate the correlation of observed ~5m-scale BIF intervals and/or interpreted 405 kyr cycles (dotted lines where this is uncertain). Thick horizontal lines indicate the correlations of ~5m-scale BIF intervals that occur near or closest to maxima in the (filtered) ~16m cycle in the Kuruman IF and/or DGM (narrow ~16m bandpass filter outputs shown). Compared to option IIa this correlation is shifted by one (filtered) ~5m cycle in the interval 2e-4c and 5b, and by one (filtered) ~16m cycle (two ~5m cycles) in the interval DB13-16.

a maximum alignment of the filtered ~5 and ~16m cycles between the Kuruman IF and Dales Gorge Member (Fig. 11) by abandoning our previous strategy of trying to achieve the best possible pattern fit.

The resultant mismatch in stratigraphic expression (i.e. amplitude) of some correlated ~5m-scale "BIF" and "S" intervals seems difficult to reconcile at first. However, this pattern misfit can be potentially explained by taking the marked differences in the cyclostratigraphy of the Kuruman IF and Dales Gorge Member into account, which seem to underlie the problems that we encounter in establishing the correlations. These differences, which are detailed in the Appendix (SI Text 1), pertain to the much stronger expression of the ~7, ~9 and 11 m cycles in the Dales Gorge Member as compared to Kuruman IF (see also Section 7.1).

Finally, we note that correlation IIb seems less consistent with the U-Pb results and the number of filtered ~16m cycles in the uncorrelated upper part of the Kuruman IF and Whaleback Shale-Joffre Members above the Dales Gorge Member. Specifically, there is only one filtered ~16m cycle recognised between 6c and the shale in between 7a and 7b, having a calculated mean age of 2468.2 ± 1.5 Ma, in contrast to three (filtered) ~16m cycles between DB16A and the shale at the Whaleback Shale-Joffre Member boundary, having an older mean age of 2469.1 ± 0.65 Ma (Fig. 11). However, the many in-situ brecciation textures encountered above 7a (see Figs. S3-4 of Lantink et al., 2019), as well as the large time difference between the U-Pb ages of the shales at 110 and 130m depth (~4 Myr), point to the likely occurrence of hiatuses in this upper part of the Kuruman IF; this may be related to the transition towards a more shallow-marine setting as represented by the granular IF facies of the overlying Griquatown IF. As such, it could be that number of ~1.2-1.3 Myr cycles above 6c was in reality larger. Indeed, the addition of two additional 1.2 Myr cycles would still be within error consistent with the 2488.2 ± 1.5 Ma age given its large uncertainty range, and would imply that its calculated mean age is older than the actual depositional age.

7. Discussion

7.1 Difficulties in establishing the correlations

Our various correlation strategies and attempts as detailed in the preceding section illustrate that establishing a cyclostratigraphic correlation between the Kuruman IF and

Dales Gorge Member is far from straightforward. This is contrary to what one would expect given the likely (predominantly) astronomical origin of the cycles. In fact, we anticipated that finding the correct correlation based on pattern matching would not be a problem, given the relatively straightforward correlations of the cycles within the Kuruman IF and Dales Gorge Member. However, this does not appear to be the case, as our initial preferred correlation based on pattern resemblance (option I) turns out to be incompatible with the results of high-precision U-Pb dating. Given that these same U-Pb ages are in almost perfect agreement with our Milankovitch hypothesis and thus cyclostratigraphic interpretation of the Kuruman IF and Dales Gorge Member, our trust in these ages is high, meaning that, in principle, correlation option I must be rejected.

But also our second "preferred" correlation, combining pattern resemblance with U-Pb age constraints (option IIa), results in inconsistencies regarding the exact number of identified ~5m cycles in the Kuruman IF and Dales Gorge Member. On the other hand, we can establish a modified correlation option II (option IIb) that largely eliminates these inconsistencies, by focusing mainly on the number of (filtered) ~5m and ~16m cycles. However, this correlation seems to make much less sense in terms of the expected overall similarity in the cycle pattern. Besides, we cannot exclude additional options that differ by one or two 405 kyr-related cycles from correlation option IIb, given the remaining uncertainty in the exact number of 5m cycles.

This raises the important question why establishing a correct cyclostratigraphic correlation between the Kuruman IF and Dales Gorge Member is so much more difficult than expected, if we accept that the regular alternations in these units are Milankovitch controlled. Below we discuss three possible reasons.

7.1.1 Possible reasons for the difficulty in identifying the correlations

- (1) Difference in depositional environment.

Whereas the Kuruman IF and Dales Gorge Member cycle patterns can individually be traced over hundreds of kilometres within their respective sedimentary basins (see Section 5), significant problems are encountered when we try to cyclostratigraphically correlate the two units. In essence, this tells us that local climate and/or depositional response to the astronomical forcing was apparently very different between these two basins, to the extent that it caused significant differences in stratigraphic expression.

It is well-known from previous studies (e.g. Beukes and Gutzmer, 2008; Beukes, 1980, 1987) that a large carbonate platform existed in the central part of the Griqualand West Basin prior to and possibly during deposition of the Kuruman IF (Fig. 2). By contrast, indications for the presence of distal low-density turbidites in the siliciclastic/mudrock facies of the Hamersley Group BIFs, including in the S bands of the Dales Gorge Member (Krapež et al., 2003; Pickard et al., 2004), point to a relatively greater proximity to a delta and/or submarine fan system during deposition of the Dales Gorge Member. Recent observations from the slightly younger Joffre Member of the Brockman Iron Formation (see *Chapter 3*) indicate that the main influence of the climatic precession cycle occurred via, possibly monsoonal-induced, changes in continental runoff and nutrient input, resulting in variations in marine productivity and associated changes in organic carbon export and iron (oxyhydr)oxide precipitation. Accordingly, this would mean that the Dales Gorge Member was under a more 'direct' control of the astronomical forcing - in the sense of being more strongly affected by variations in terrigenous input and bioproductivity - compared to the Kuruman IF. Indeed, a greater proximity of the Dales Gorge Member with respect to the fluvial terrigenous input associated with the astronomical forcing seems reflected in the nature of its long eccentricity-related cycles, consisting of distinct alternations of iron oxide-facies BIF and thick organic-rich shale facies. By contrast, the more mixed iron oxide-carbonate composition of the equivalent alternations in the Kuruman IF (as indicated by the more gradual changes in relief and gentler slopes; Fig. 3) and thinner shale beds (Beukes, 1980; Trendall and Blockley, 1970) are indicative of a less extreme response of the lithological endmembers in line with a more remote influence/distal position with respect to the terrestrial input.

The question remains whether this difference in depositional environments can be related to the observed differences in cycle pattern between the Kuruman IF and Dales Gorge Member. We could speculate that the strong ~7 and ~9m cycles in the Dales Gorge Member (which are much weaker in the Kuruman IF; Table 1) result from a stronger non-linear response to the astronomical forcing (see Section 5.2) that is more characteristic for the delta/submarine fan-influenced, high-productivity BIF sedimentary environment of the Dales Gorge Member. We can imagine that, for example, thresholds and stochastic processes were involved with the transport and deposition of suspended river load and/or shelf sediment, such as arising from delta/shelf slope (in)stability (Postma et al., 1993). In addition, post-depositional alterations, such as internal redistribution (i.e., dissolution-reprecipitation) of carbonate, iron and silica as a result of organic matter degradation, may have played an important distortive role. In fact, the rectangular shape of the Dales Gorge Member's BIF-S alternations, the occurrence of iron sawtooth patterns (de Oliveira Carvalho Rodrigues et al., 2019), and the development of silica hardgrounds (Bekker et al., 2010; Krapež et al., 2003; Rasmussen et al., 2015), are already an indication that non-linear responses and thresholds were involved for the transition from BIF to S deposition. However, we are well aware that we do not yet understand enough about the origin of the different cycles or the functioning of the early Paleoproterozoic climate/BIF system in relation to astronomical forcing to provide a meaningful answer to this question at this stage.

- (2) Difference in proxy expression.

Related to the difference in (nonlinear response of) the depositional environment, is that the expression of the Kuruman IF and Dales Gorge Member cycle patterns also depends on the type of proxy. For both the Kuruman IF and Dales Gorge Member, we sometimes noted marked differences in expression and/or the manifestation of specific cycles between the different proxies used (see Section 4; Figs. 4, 6-7). One problem is that these proxies have been selected based mostly on empirical grounds (i.e., visual inspection of regular stratigraphic changes), rather than on an intrinsic understanding of their relation to the astronomical forcing. As such, it is not always clear which of these proxy records provide a better representation of the astronomical-forcing signal and is thus most suitable for establishing the correlation. Also, we realise that there is already an inherent mismatch or asymmetry between the proxies that reflect the long eccentricity-related cycles (e.g., the Fe/Mn ratio for alternations between 'BIF' and carbonate/shale), and those reflecting the alternations at the precession scale (e.g., Si, Fe and K reflecting for regular successions of chert, iron oxide and mudrock (*Chapter 3*). Moreover, a general problem with using lithological proxies is that these may depend more on local depositional conditions than on regional or global climate signals and are more susceptible to distortion resulting from dilution and diagenetic effects (Herbert, 1994; von Dobeneck and Schmieder, 1999; Weedon, 2003; Westphal et al., 2004).

An additional factor potentially contributing to the Kuruman IF-Dales Gorge Member correlation problem is that not the same proxy was used. In particular, we compared the log(Fe/Mn) signal of the Kuruman IF with the log(ferric oxide) record of the Dales Gorge Member, each combined with the general expression of the cycles in their own weathering profile (Figs. 10-11; Fig. S10). However, the log(Fe/Mn) vs. log(ferric oxide) comparison is somewhat flawed because total Fe content is not the same as total ferric (Fe^{3+}) oxide abundance (i.e., hematite and goethite; Section 3.3.2). The proportion of Fe^{3+}/Fe^{2+} minerals in BIF is generally thought to reflect a balance between input of iron (oxyhydr)oxide and organic carbon to the seabed via dissimilatory iron reduction (DIR; Baur, 1985; Heimann et al., 2010; Konhauser et al., 2017; Perry et al., 1973). As such, this proxy seems more closely related to the inferred astronomically-induced changes, in light of the previously mentioned climate model presented in Chapter 3. In this respect, the MS signal of the Kuruman IF may be more suitable for comparison with the Dales Gorge Member, as this proxy tracks mainly the abundance of magnetite, a mixed valence iron mineral resulting from partial iron (oxyhdr)oxide reduction according to the DIR model (Baur, 1985; Heimann et al., 2010; Johnson et al., 2008; Konhauser et al., 2017; Perry et al., 1973). Indeed, the bundling pattern around 2d-3e in the MS record, which deviates from that seen in the weathering profile and Fe/Mn signal (Section 4.1; Fig. 4), appears to be in better agreement with correlation IIb (Section 6.3). Thus the MS record might be considered as a kind of "in between" proxy for the patterns observed in Kuruman IF and Dales Gorge Member weathering profiles. However, the overall cycle expression in this proxy is generally less clear and therefore far from ideal either. Future attempts to improve the cyclostratigraphic framework of the Kuruman IF and Dales Gorge Member may therefore benefit from the development and use of more suitable (i.e., more directly climate sensitive) proxy records for both stratigraphic units.

- (3) Our relative ignorance of the cycle patterns.

A third but in fact more general, overarching explanation for the problems with identifying the correlation between the Kuruman IF and Dales Gorge Member, is our relative lack of knowledge of the cycles. More specifically, there is still much uncertainty about the precise origin and composition of the patterns both from an astronomical perspective (i.e., which Milankovitch cycles were playing a role, and what was their period and amplitude) and geological perspective (i.e., how are these cycles recorded).

An important aspect that has not been addressed so far is the so-called "phase relation" between the long-period eccentricity cycles and the lithological changes. Based on the precession climate model established for the Joffre Member, it seems most likely that the “S” intervals represent eccentricity maxima (*Chapter 3*). Given the larger precession amplitude and hence larger amplitude of the climate oscillations during eccentricity maxima, we would expect to find a stronger lithological imprint of the astronomical signal, i.e. one that is more characteristic, in the more shaley/carbonaceous intervals. However, during our search for the most plausible correlation based on pattern resemblance (Section 6.1 and 6.2), we have mainly focused on the characteristic pattern exhibited by the "BIF" intervals. This strategy has partly a historical reason, as a characteristic cycle pattern was initially identified on the basis of the prominence of the BIF intervals as visible in the weathering profile of the Kuruman IF (Lantink et al., 2019).

Similarly, a lack of experience in how to examine these ancient cyclostratigraphic patterns plays an important role in the interpretation of the characteristic bundling and their precise cycle build-up. In several parts of the stratigraphy, particularly in the upper part of the Dales Gorge Member as well as the thicker S macrobands, the exact number of ~5m cycles remains uncertain. This proved an important additional handicap for the establishing of the cyclostratigraphic framework, which should start from this key cycle that is supposed to be related to the stable long 405-kyr eccentricity cycle (Figs. 10-11). In conjunction with a degree of uncertainty in depositional rate, this is due to the fact that the period of the ~16m cycle interpreted as $g_4 - g_3$ is fundamentally uncertain, and as a result, also the expected number of ~5m cycles per bundle.

As illustrated in Figure 12, we can create a pattern fairly similar to the characteristic 2-3-2 BIF bundling of e.g. DB5-6, 6-8, 9-10 by taking the sum of two sine waves with a ratio of their periods larger than 1:3 and smaller than 1:4, and amplitude ratio of 1.5:1 (i.e., to represent the 5m / 405 kyr and 16 m / ~1.3 Myr cycles). By adding a third, somewhat weaker sine wave having a 1:2.5 period ratio with respect to the shorter cycle (i.e., to simulate the ~1 Myr eccentricity cycle), we create interference patterns of alternatingly 2, 4 and 2 pronounced short-period cycle minima which bear resemblance to the characteristic sequence of prominent BIFs 5a-5a.2, 5bcd and 6a-6a.2 in the Kuruman IF, and of DB12, DB13-15 and DB16-16A in the Dales Gorge Member. However, we are unable to simulate the occurrence of a 2-3-2 followed by 2-4-2 bundling in one sequence (as observed in the Dales Gorge Member), indicating that obviously, the patterns cannot be explained by a simple addition of these three sine waves. Moreover, it remains hitherto unclear whether the strong-weak-strong pattern of DB13, 14 and 15 is solely due to the strong expression of a ~1 Myr eccentricity cycle, or whether it also represents a double ~16m cycle maximum

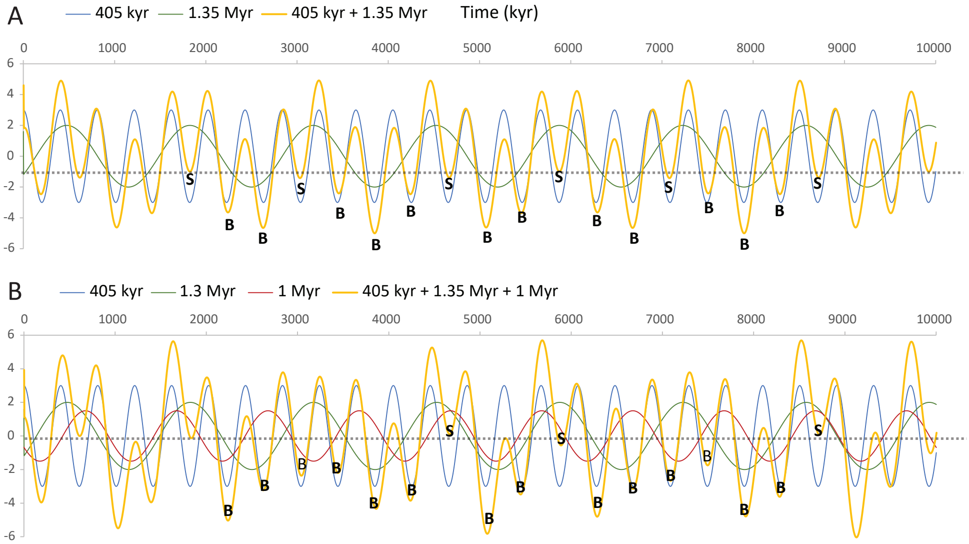

Figure 12. An attempt to simulate the characteristic BIF-S bundling patterns of the Kuruman IF and Dales Gorge Member by simple addition of sine waves. (**A**) The addition of two cosines with periods of 405 kyr and 1.35 Myr and amplitudes 3 and 2, respectively, produces an interference pattern (in yellow) of two or three more pronounced 405 kyr minima (indicated with the letter "B") alternating with one less well-developed 405 kyr minimum (indicated with "S"), somewhat resembling the characteristic BIF bundling sequence of DB5-6, DB6-8 and DB9-10 in the Dales Gorge Member. How often the pattern exhibits a jump from two to three pronounced short-period cycle minima depends on the exact length of the longer-period cycle. (**B**) By adding a third cosine with a period of 1 Myr and amplitude of 1.5, we can create a pattern of four successive, relatively prominent 405 kyr minima, surrounded by groups of two extra prominent 405 kyr minima, looking somewhat comparable to BIFs 5a-5a.2, 5bcd and 6a-6a.2 in the KIF, and of DB12, DB13-15 and DB16-16A in the Dales Gorge Member.

(Sections 6.2); the latter would imply that the $g_4 - g_3$ period supposedly associated with this cycle shifted from ~1.3 Myr to 1.2 Myr in the upper part of the Dales Gorge Member (see the 1:3 ratio with the ~5m filtering in Fig. 11).

Thus, to gain a better understanding of these cycle patterns, we need more realistic examples, preferably from eccentricity solutions which show a chaotic reduction of the $g_4 - g_3$ cycle period to ~1.3 Myr, and in which all amplitude-, frequency- and phase modulations resulting from the interference of the different orbital cycles are properly included. For example, an alternating ~2 – 2.8 Myr frequency modulation pattern can be observed in eccentricity solutions for the last 50 Myrs when the $g_4 - g_3$ cycle had a mean period of ~2.4 Myr, an interference pattern which arises from the ~9 Myr cycle (Boulila, 2019; Laskar et al., 2004; Pälike, 2001). Furthermore, we may want to include modelling of the distortion caused by non-linear response (e.g. Herbert, 1994; Ripepe and Fischer, 1991), to see if specific features, such as the ~1.5 - 2 times thicker BIFs, can be reproduced. However, this is far beyond the scope of the present paper.

Finally, we have so far largely ignored the potential contribution of obliquity, and hence the possible manifestation of its longer-period amplitude modulators as well. As mentioned in Section 5.1, the main reason for this is the combined cyclostratigraphic and U-Pb evidence for a strong 405 kyr eccentricity imprint, which is the amplitude modulator of precession and not obliquity. However, this does not mean that obliquity could not have had a significant influence, given that an additional obliquity signal is often present in sediment sequences deposited around mid-low latitudes during icehouse/coldhouse periods (e.g. De Vleeschouwer et al., 2017; Lourens et al., 1996; van der Laan et al., 2012), and it may even directly affect low-latitude climate systems as the monsoon (Bosmans et al., 2015; Tuenter et al., 2003). The former would be consistent with the density current structures reported for the Dales Gorge Member that are ascribed to (glacio)eustatic sea level variations (Krapež et al, 2003; Pickard et al. 2004), but alternatively these could also arise from the direct low-latitude forcing (Postma et al., 1993; Weltje and De Boer, 1993). Another explanation may be that we are simply not yet used to recognising the stratigraphic imprint of obliquity, given that its period ratio with precession becomes progressively smaller than the current ~2:1 ratio the further back one goes in the history of the Earth-Moon system (Berger and Loutre, 1994; Laskar et al., 2004; Waltham, 2015). Given a precession period of 11 kyr at 2.46 Ga (*see Chapter 4*), obliquity would have had a period of ~15 kyr (Waltham, 2015), corresponding to a ~3:4 ratio. Accordingly, ~45 kyr cycle patterns may result from the interference of precession and obliquity. Potentially, the complex ~45 cm mesoband bundle patterns observed in certain parts of the Dales Gorge Member by de Oliveira Carvalho Rodrigues et al. (2019) have to be explained in this way.

7.1.2 Potential solutions

Our expectations for establishing a 405 kyr-cycle based cyclostratigraphic framework and associated high-resolution astrochronology for the lower Paleoproterozoic in the Hamersley and Griqualand West basins have been somewhat tempered, given the serious difficulties encountered during our current attempt (Section 6). However, this does not necessarily imply that this goal cannot be reached, and significant progress can be made through a better understanding of the various sources of uncertainty discussed in Section 7.1.1. For example, we suspect that a systematic analysis of variability at the short eccentricity-, precession- and/or obliquity-scale will help reducing the uncertainties in the origin of the cycle patterns and precise number of 405 kyr-related cycles. As mentioned earlier, this could be done in conjunction with the development of other proxy records and more realistic eccentricity solutions to use as example.

Another possible albeit challenging strategy is to generate more, and more precise U-Pb TIMS ages. We note that some of the existing U-Pb ages have a very small full uncertainty, in particular, the 2σ uncertainty of the Kleine Naute shale, which is only ± 0.34 Myrs, while others have much larger uncertainties (> 1.5 Myrs). If possible, reducing this uncertainty in the U-Pb ages from the analysis of additional zircons will help to more precisely constrain specific correlation options, or a small subset of correlations.

Thus far, the small size of the grains and large amount of chemical abrasion needed to remove the radiation-damaged parts unfortunately resulted in only tiny amounts of Pb left for analysis. Importantly this strategy could also provide more insight into the origin of the sampled zircons: whether they originate from discrete tuff horizons, or represent sedimentary re-working of recently deposited ashes into the BIF source region (Krapež et al., 2003; Pickard, 2003; Trendall et al., 2004; Zi et al., 2021). In the latter case, this is expected to have an effect on the accuracy of the age of the dated shale horizons as they may suffer from a certain degree of memory effect.

In addition, we can look for additional, independent time-stratigraphic markers to constrain our cyclostratigraphic correlations. In the absence of a well-established magnetostratigraphy, correlation of meteorite impact layers might present a suitable alternative given their relatively frequent occurrence in successions of Neoarchean - early Paleoproterozoic age in both Western Australia and South Africa (Glikson, 2014). In particular, a discrete impact spherule layer present in the DS4 macroband of the Dales Gorge Member (Glikson and Allen, 2004; Hassler and Simonson, 2001) has previously been linked to a 1-cm-thick spherule layer around ~50m height above the base of the Kuruman Iron Formation (Glass and Simonson, 2012; Simonson et al., 2009). This stratigraphic height corresponds roughly to cycle 2d-e, which is in line with our preferred correlation options IIa/b based on the additional constraints from U-Pb dating.

7.2 Implications of the early Paleoproterozoic astrochronological framework and basin development

Despite the ongoing uncertainties in the exact correlation (i.e., at the individual 405 kyr-cycle level), we can state that our joint cyclostratigraphic and U-Pb dating efforts in the end resulting in correlation options IIa/b are consistent with a "near"-synchronous onset of the Kuruman IF and Dales Gorge Member, in confirmation of the long-standing presumption (e.g. Beukes and Gutzmer, 2008; Button, 1976; Cheney, 1996; Nelson et al., 1999; Pickard, 2003; Trendall, 1968; Trendall et al., 2004).

At a more precise level, correlation options IIa/b suggest a slightly earlier onset of BIF deposition in South Africa by at least one 405 kyr cycle, given the fact that BIF 1a.2 of the Kuruman IF is correlated to CB5 of the top of the Colonial Chert Member (Figs. 10-11); note that 1a.1 of the Kuruman IF forms part of the Kliphuis Member chert, see Fig. S3). While this one ~5m cycle offset may not be correct, lithological observations from the southern Prieska area in the Griqualand West basin reveal that the onset of BIF formation locally starts at 1b, while 1a is still composed of ferruginous carbonate (see SI Fig. S4 in Lantink et al. (2019). This indicates that BIF deposition in the Prieska area also started one 405-kyr cycle later than in the central Ghaap plateau area, but at the same time as the Dales Gorge Member, if correlation options IIa/b are correct. In addition, prolonged BIF deposition at Prieska, where the Kuruman IF is much thicker, has been demonstrated by the cyclostratigraphic correlations of Lantink et al. (2019) (see also Fig. 2). Likewise, BIF deposition obviously continued for much longer in the Hamersley basin with respect to in the central Ghaap plateau area, as represented by the ~350m thick Joffre Member, the base of which loosely corresponds to 7a according to correlation options IIa/b (Figs. 10-11). Thus options IIa/b seem to be supportive of the hypothesis that the Kuruman IF facies in the south of the Griqualand West basin were deposited more proximal (Cheney, 1996) and/or in a similarly deeper-marine (i.e., basinal) setting as the Dales Gorge Member (Beukes and Gutzmer, 2008).

This further implies that the very large-scale trends in occurrence of BIF (vs. non-BIF) units in the Hamersley and Griqualand West basins primarily reflect basin evolution related to tectonic-scale changes in relative sea level, rather than to global-scale changes in, for example, oceanic redox state. It has further been speculated that the whiff of oxygen interpreted from the organic-rich "S1" shale of the McRae Shale Member (Anbar et al., 2007) is equivalent to the Naute Shale interpreted oxygen oasis of the Gamohaan Formation (Kendall et al., 2010). A proper evaluation/testing of this hypothesis based on cyclostratigraphy may be a feasible exercise in the future, given that these mixed shale-carbonate successions below the Kuruman IF and Dales Gorge Member are expected to reveal a strong and more direct influence of the astronomical forcing, following the conceptual depositional model of Lantink et al. (in review) for precession-scale cycles in the Joffre Member.

7.3 Presence of very long-period orbital cycles

7.3.1 Multi-million-year modulations

At the same time, we have to take into account that very long-period orbital forcing or pacing may have played a role in inducing synchronous variations in the deposition of relatively more BIF- versus carbonate/shale-dominated facies, on a thickness scale ranging from multiple tens of metres to almost one hundred metres.

For example, evidence from different paleoclimate records of the Phanerozoic has revealed the imprint of a ~9 Myr year cycle, which may represent an amplitude modulating term of the $g_4 - g_3$ cycle (Boulila, 2019; Boulila et al., 2012; Ikeda et al., 2020; Martinez and Dera, 2015; Sprovieri et al., 2013). A possibly similar manifestation of this ~9 Myr orbital "Grand cycle" in the Kuruman IF and Dales Gorge Member is suggested by the sequence of very prominent BIFs DB0-3 and DB12-16 in the Dales Gorge Member, which are separated by an interval of less prominent, more shaley alternations (e.g. Figs. 3; 6-7), and a significant ~87 m cycle identified in the KIF log(Fe/Mn) record (Fig. 5). The bandpass filtered ~87m signal in the log(Fe/Mn) record shows successive maxima around the prominent BIFs 2b and 5d-e, suggesting a period of ~8 Myrs (Fig. 4). This position is in approximate agreement with the midpoints of the prominent sequences of BIF intervals DB0-3 and DB12-16, respectively, in line with correlation options IIa/b. The expression of a possible older ~9 Myr cycle is found ~100 m stratigraphically below the Dales Gorge Member and Kuruman IF, corresponding to "Bruno's Band" and "Bruno's BIF", respectively; these two units have previously been suggested to correlate (Beukes and

Gutzmer, 2008; Knoll and Beukes, 2009). Note that in this case the existing Re/Os age of 2501 ± 8 Ma Ma for S1 (Anbar et al., 2007; Fig. S1) would be too old, as Bruno's Band has an implied age of around ~2492 Ma.

In addition, our cyclostratigraphic observations have indicated the presence of a ~46 m cycle in both the stratigraphy of the Kuruman IF and Dales Gorge Member (Table 1). As indicated by bandpass filtering, this cycle is manifested as a longer-period modulation in the prominence of successive BIF bundles and/or broad S intervals, and seems to arise as an amplitude modulation cycle, i.e., a difference term, of the ~16 and ~23m cycles (Figs. 4, 6-7). Comparison of the bandpass filtered maxima of this ~46 m cycle between the Kuruman IF and Dales Gorge Member (Mt Jack profile) indicates a roughly identical positioning for each, in accordance with correlation options IIa/b, i.e., around 1c-d vs. top DB0-DS1, 3b-3c vs. DS6-DB6 and 5a.2-5b vs. DB12-DS13. Given its estimated period of ~3.8-3.9 Myr, there are several possible astronomical cycles to explain its origin, such as $g_4 - v_7$ (now: ~5 Myr) or $-g_3 + v_7$ (now: ~4.5 Myr) (pers. comm. J. Laskar; Boulila, 2019), given that we do not know the exact values of g_4 and g_3 at that time. Intriguingly, the possible origin of the ~46m cycle as amplitude modulation term of the ~16 and ~23m cycles hints at the alternative scenario that this cycle results from the secular resonance θ. This resonance term has a current period of ~4.6 Myr associated with the 2:1 ratio between the periods of $g_4 - g_3$ (~2.4 Myr) and $s_3 - s_4$ (~1.2 Myr) (Laskar, 1990; Laskar et al., 2004, 2011) and has been previously recognised in Phanerozoic records (Boulila, 2019; Da Silva et al., 2016; Sproson, 2020). However, in case the ~16m cycle represents $s_3 - s_4$, and the ~23m cycle $g_4 - g_3$, this would be consistent with a 3:2 resonance state θ with a corresponding period of 3.9 Myr. A similar explanation was proposed for a ~3.5 Myr cycle identified in the Newark-Hartford records where the $g_4 - g_3$ cycle has a period of ~1.7 Myr and is interpreted to be in a 2:1 resonance (Olsen, 2001; Olsen et al., 2019). Alternatively, the ~46m cycle could just represent a beat cycle of the 23m and 16 m cycles and/or a double 23m cycle arising from non-linear response.

7.3.2 Implications for the chaotic Mars-Earth cycle

Given our reservations about the cyclostratigraphic interpretation of the ~16m cycle as discussed in Section 5.1 and in the previous paragraph, i.e., that it represents the Mars-Earth $g_4 - g_3$ eccentricity cycle (Table 1), we cannot say anything conclusively about the significance of this cycle for the chaotic behaviour of the Earth-Mars resonance θ at ~2.47 Ga.

But if the ~16m cycle is indeed related to $g_4 - g_3$, the fact that its estimated period of ~1.3 Myr remains this low for an interval of more than 10 Myrs would be unprecedented from the viewpoint of previous geological observations. A period of ~1.2 Myr of the $g_4 - g_3$ cycle has been reconstructed from a Cretaceous paleoclimate record by Ma et al. (2017), and is implied for the Paleocene-Eocene transition by Zeebe and Lourens (2019). However, both intervals represent chaotic resonance transitions that occur over the duration of only two 1.2 Myr cycles, i.e., from libration to circulation, rapidly returning to libration (Laskar et al., 2004; Pälike et al., 2004). To date, the most striking evidence for a sustained (> 20 Myr) shortening of the $g_4 - g_3$ period is a ~1.7 Myr cycle identified in upper Triassic to lower Jurassic lake-level records from the Newark-Hartford Basin (Olsen and Kent, 1999; Olsen et al., 2019), as well as in contemporaneous deep-sea sequences from Inuyama (Ikeda and Tada, 2013, 2020). To our knowledge, no shorter period than ~1.5 Myr has yet been identified for $g_4 - g_3$ in other Meso-/Paleozoic Milankovitch archives (Fang et al., 2015; Grippo et al., 2004; Chunju Huang et al., 2011; Ma et al., 2019; Wu et al., 2013; Table 3 in Hinnov, 2013).

Also, from available (numerical) astronomical calculations, the ZB18a eccentricity solution of Zeebe (2017) and Zeebe and Lourens (2019) draws particular interest, as a persistent 1.5-1.6 Myr period for $g_4 - g_3$ is developed between 50 to 80 Ma, attributed to a chaotic resonance transition. The fact that the period of $g_4 - g_3$ remains stable around this value over an interval of ~30 Myr raises similar doubt about the (physical) likelihood of the manifestation of prolonged time intervals during the history of the Solar System in which the period of the $g_4 - g_3$ cycle was much shorter (i.e. ~1.3 Myr).

However, the results of a recent statistical evaluation of the behaviour of the $g_4 - g_3$ cycle, based on 120,000 orbital solutions calculated up to 5 Gyrs back in time (Hoang et al., 2021), indicate a very low, but non-negligible probability of a $g_4 - g_3$ period of 1.3 Myr for time steps of 10 Myrs (see probability density functions (PDFs) in Figure 14 of Hoang et al., 2021). When this very low probability is interpreted in a quantitative way, however, one can still wonder whether it is realistic that the first Precambrian record of sufficient length that has been analysed cyclostratigraphically suggests that the $g_4 - g_3$ cycle had such a short period. This could of course be a coincidence. However, we must also realise that the PDFs of Hoang et al. (2021), although based on astronomical solutions to the past, still reflect the probability of a chaotic resonance transition occurring in the future. This may not be the same as the chance of such an event occurring in the past. So what the PDFs simply tell us is that the occurrence of a ~1.3 Myr period of $g_4 - g_3$ for more than 10 Myr is possible. However, reiterating our uncertainty about the interpretation of the ~16m cycle, other Precambrian records of high quality are essential to gain further insight into this.

8. Conclusions

The primary aim of this study has been to establish a 405 kyr cycle-based framework for the early Paleoproterozoic Kuruman IF of South Africa and Dales Gorge Member of Western Australia. Achieving this goal seemed realistic at first given the evidence from cyclostratigraphic analysis and TIMS U-Pb dating for a 405-kyr eccentricity origin for the prominent ~5 cycle, and a strong ~1.3 Myr cycle possibly related to $g_4 - g_3$, identified in both stratigraphic units. However, we subsequently encountered significant problems when trying to determine a correlation based on matching their characteristic cycle patterns, and the final correlation remains unsolved to date. In part, the difficulty in correlating appears to stem from a difference in expression and amplitude of certain cycles (i.e., a ~7m / 590 kyr, ~9m / 700 kyr and ~23m / 1.9 Myr cycle) whose origin remains enigmatic, but which may be related to a difference in depositional environment. But more generally, it illustrates our current lack of understanding of the (nonlinear and likely complex) response of the early Proterozoic climate and BIF system to the astronomical forcing, as well as the fundamental uncertainty about the astronomical forcing itself i.e. Solar System behaviour at that time.

Nevertheless, our correlation efforts have provided a much more precise estimate of the absolute and relative timing of Kuruman IF and Dales Gorge Member BIF deposition than was previously available. This illustrates the potential strength of the integrated (cyclo)stratigraphic approach in enabling more precise reconstructions of the sedimentary and paleogeographic histories of the Griqualand West and Hamersley basins. In addition, our preliminary framework suggests the manifestation of a ~3.8 Myr and 9 Myr cycle in both the South African and Western Australian early Proterozoic successions. Possible strategies to further constrain the correlations and gain more insight into the origin of the cycle patterns include a systematic analysis of sub-405 kyr-scale variability (i.e. precession-, short eccentricity-, and possible obliquity-related patterns), further improving of the U-Pb geochronology, searching for other (more) climate-sensitive proxies, and the use of suitable astronomical models and climate/geochemical simulations.

Acknowledgements

This research was funded by the Dutch National Science Foundation grant NWO ALWOP.190 (FJH, PRDM, MLL); Swiss National Science Foundation grant 200021_169086 (JHFLD); Dr. Schurmannfonds grants 2017-126, 2018-136 and 2019-145 (FJH, PRDM, MLL). We gratefully acknowledge Nic Beukes for his guidance in the UUBH-1 drilling project; Keith Saunders and Allan Bennet from Wireline Alliance for the downhole geophysical logging; Michael Wawrick and Lena Hancock from the GSWA for the Hylogger data extraction from cores 47A and DD98; Gregory Jack for arranging of the drone flying and fieldwork logistics together with the GSWA; Marcel van Maarssenveen, Jakob Steiner and Timothy Baars for their advice on the GPS measurements, photogrammetric modelling; and Jacques Laskar, Nam Hoang and Federico Mogavero for their expertise and discussions on the behaviour of θ. Our special thanks go to the late Rineke Gieles for her dedicated help with the XRF core scanning and who sadly passed away in 2020.

Supplementary information

Supplementary Text 1

The mismatch in stratigraphic expression (i.e., amplitude) of correlation option IIb can be potentially justified when we recall the marked differences in cycle manifestation and amplitude noted between the Dales Gorge Member and Kuruman IF (Table 1). For instance, a stronger expression and opposite sign of the ~23m cycle in the Kuruman IF relative to specifically the ~7m and ~9m cycles in the Dales Gorge Member might explain why 3b, while it forms a pronounced ~5m-scale BIF interval in the Kuruman IF, may still correlate to the poorly developed ~5m-scale 'BIF' in the thick DS6 macroband in the Dales Gorge Member (according to correlation IIb): in the Dales Gorge Member log(ferric oxide) record, the filtered ~5m maximum in DS6 corresponds to a combined ~7, 9, 11.5 and 16m (filtered) cycle minimum (see Figs. 6-7), while in the Kuruman IF log(Fe/Mn) record, the supposedly equivalent 3b coincides with a (filtered) ~23m cycle maximum. In addition, in the log(Fe/Mn) record, 3b corresponds roughly to a filtered ~16 m cycle maximum, while in the MS record it corresponds to a ~16m minimum, (more) consistent with its manifestation in the Dales Gorge Member. Essentially the same explanation may be invoked for the difference in expression of DB9-10 versus 4ab: in the Dales Gorge Member, the thicker DB9 corresponds to a filtered ~7m, 9m and 11.5m cycle maximum, while the overlying DB10 occurs in between a minimum and maximum of these same (filtered) cycles. Instead, 4b in the Kuruman IF, the supposed equivalent of DB10, corresponds to a combined ~16m and 23m cycle maximum.

For the correlations above double 5a - DB12, we can think of similar explanations for the misfit in characteristic cycle pattern expression. For example, the much stronger expression of the ~9m cycle in the DB13-14 interval, which causes a less pronounced upper part of DB13, may justify why this interval could still correspond to 5bcd in the Kuruman IF, in which 5c is more pronounced than 5d (in the weathering profile). Also, note that the expression of 5c in the log(Fe/Mn) record of core UUBH-1 is actually not that pronounced at all (Fig. 11). However, it remains very strange why the very weak 5e would correlate to DB15, although the link to 6a.1-6a.2 to the upper part of DB15-DS16 may be reconciled given their anomalously weak expression in the UUBH-1 log(Fe/Mn) record compared to in the Kuruman IF weathering profile logs (Fig. 4).

Further discussion points concerning option IIb are the implied absence of an extra 405 kyr-related cycle in between 5a.2 and 5b, and the implied extra 405 kyr-related cycle in between 4a and 4b. Concerning the 5a.2 - 5b interval however, the absence of a "5a.3" may not be unrealistic given that the ~5m filtering of the MS record (as opposed to the log(Fe/Mn) record) does not pick up an additional ~5m maximum. Similarly for the 4a-4b interval, the existence of an additional 'hidden' 405 kyr-related cycle seems not unrealistic given its relatively large thickness. Moreover, the addition of a 405 kyr-related cycle would increase the total number of recognised 405 kyr-related cycles between the well-dated Kleine Naute shale and the shale at 212m depth to 18.5 cycles, yielding a duration of 7.5 Myr; this in almost perfect agreement with their mean U-Pb age difference of 7.7 Myr.

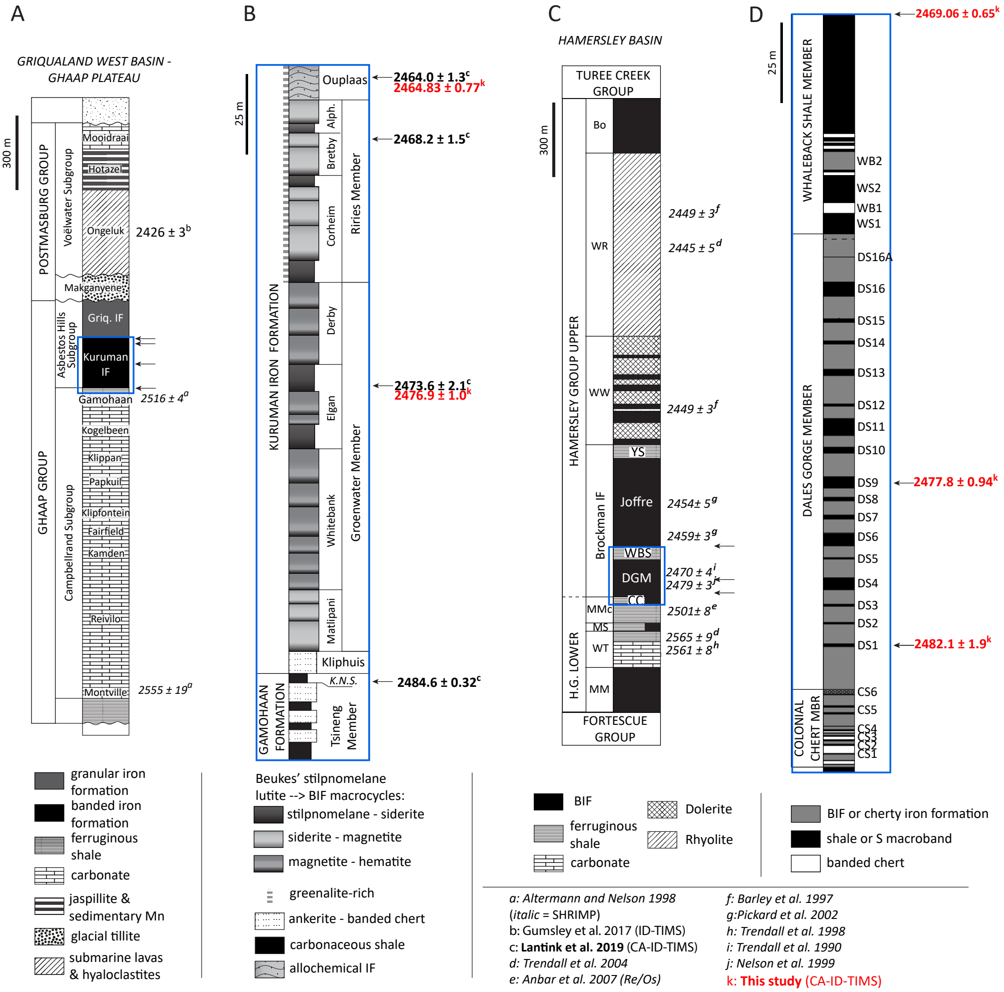
A
GRIQUALAND WEST BASIN - GHAAP PLATEAU
300 m
POSTMASBURG GROUP
Voëlwater Subgroup
Mooidraai
Hotazel
Ongeluk
2426 ± 3^b
Makganyene
Asbestos Hills Subgroup
Griq. IF
Kuruman IF
Gamohaan
2516 ± 4^a
GHAAP GROUP
Campbellrand Subgroup
Kogelbeen
Klippan
Papkuil
Klipfontein
Fairfield
Kamden
Reivilo
Montville
2555 ± 19^a
granular iron formation
banded iron formation
ferruginous shale
carbonate
jaspillite & sedimentary Mn
glacial tillite
submarine lavas & hyaloclastites
B
25 m
KURUMAN IRON FORMATION
Ouplaas
2464.0 ± 1.3^c
2464.83 ± 0.77^k
Alph.
Bretby
2468.2 ± 1.5^c
Corheim
Riries Member
Derby
Elgan
2473.6 ± 2.1^c
2476.9 ± 1.0^k
Whitebank
Groenwater Member
Matlipani
Kliphuis
K.N.S.
2484.6 ± 0.32^c
GAMOHAAN FORMATION
Tsineng Member
Beukes' stilpnomelane lutite --> BIF macrocycles:
stilpnomelane - siderite
siderite - magnetite
magnetite - hematite
greenalite-rich
ankerite - banded chert
carbonaceous shale
allochemical IF
C
HAMERSLEY BASIN
TUREE CREEK GROUP
300 m
HAMERSLEY GROUP UPPER
Bo
WR
2449 ± 3^f
2445 ± 5^d
WW
2449 ± 3^f
YS
Brockman IF
Joffre
2454± 5^g
2459± 3^g
WBS
DGM
2470 ± 4^i
2479 ± 3^j
CC
H.G. LOWER
MMc
2501± 8^e
MS
WT
2565 ± 9^d
2561 ± 8^h
MM
FORTESCUE GROUP
BIF
ferruginous shale
carbonate
Dolerite
Rhyolite
D
25 m
2469.06 ± 0.65^k
WHALEBACK SHALE MEMBER
WB2
WS2
WB1
WS1
DALES GORGE MEMBER
DS16A
DS16
DS15
DS14
DS13
DS12
DS11
DS10
DS9
2477.8 ± 0.94^k
DS8
DS7
DS6
DS5
DS4
DS3
DS2
DS1
2482.1 ± 1.9^k
COLONIAL CHERT MBR
CS6
CS5
CS4
CS3
CS2
CS1
BIF or cherty iron formation
shale or S macroband
banded chert
a: Altermann and Nelson 1998 (italic = SHRIMP)
b: Gumsley et al. 2017 (ID-TIMS)
c: Lantink et al. 2019 (CA-ID-TIMS)
d: Trendall et al. 2004
e: Anbar et al. 2007 (Re/Os)
f: Barley et al. 1997
g: Pickard et al. 2002
h: Trendall et al. 1998
i: Trendall et al. 1990
j: Nelson et al. 1999
k: This study (CA-ID-TIMS)

Figure S1. Stratigraphy and ages of the Transvaal Supergroup in the Griqualand West Basin and Mount Bruce Supergroup in the Hamersley Basin. (**A**) Schematic column for the Ghaap carbonate platform area adapted from Fig. 2 in Beukes (1987) and Fig. 2 in Pickard et al. (2003). Arrows indicate the positions of CA-ID-TIMS zircon ages from lutites 1 – 4 of Lantink et al. (2019) shown in **B**. (**B**) Zoom-in on the Kuruman Iron Formation and upper Gamohaan Formation showing the classical stilpnomelane lutite --> BIF macrocycles and members as identified by Beukes in the old core WB98 from Whitebank. Adapted from Fig. 5 in Beukes (1980) and Fig. 4 in Beukes (1983). (**C**) Schematic column for Mount Bruce Supergroup, modified after Fig. 2 in Pickard et al. 2002. For abbreviations see (**D**) Zoom-in on the stratigraphy of Colonial Chert, Dales Gorge and Whaleback Shale Members representative for the Karijini (Wittenoom) area based on Trendall and Blockley (1970) pages 37, 73 and 87. S macrobands are labelled according to the later established formal nomenclature as e.g. presented in Harmsworth et al. (1990).

Table S1. Instrument settings of the XRF core scanner.

Tube voltage (kV)	Current (μA)	Time analysed (s)	Filter	Elements (atomic number)
10	200	15	none	Mg (12) - (Mn (25)
30	150	15	Pb-thin	Fe (26) - U (92)
50	1,000	45	Cu	Ba (56)

Table S1. Results of multivariate log-ratio calibration using the AvaaXelere software of Bloemsma (2015) using the approach of Weltje et al. (2015). X-Y plots (logarithmic scale) show a comparison of the measured concentration of the reference samples versus their predicted concentration (according to the calibration) in weight % with linear regression coefficient of determination (R²) values.

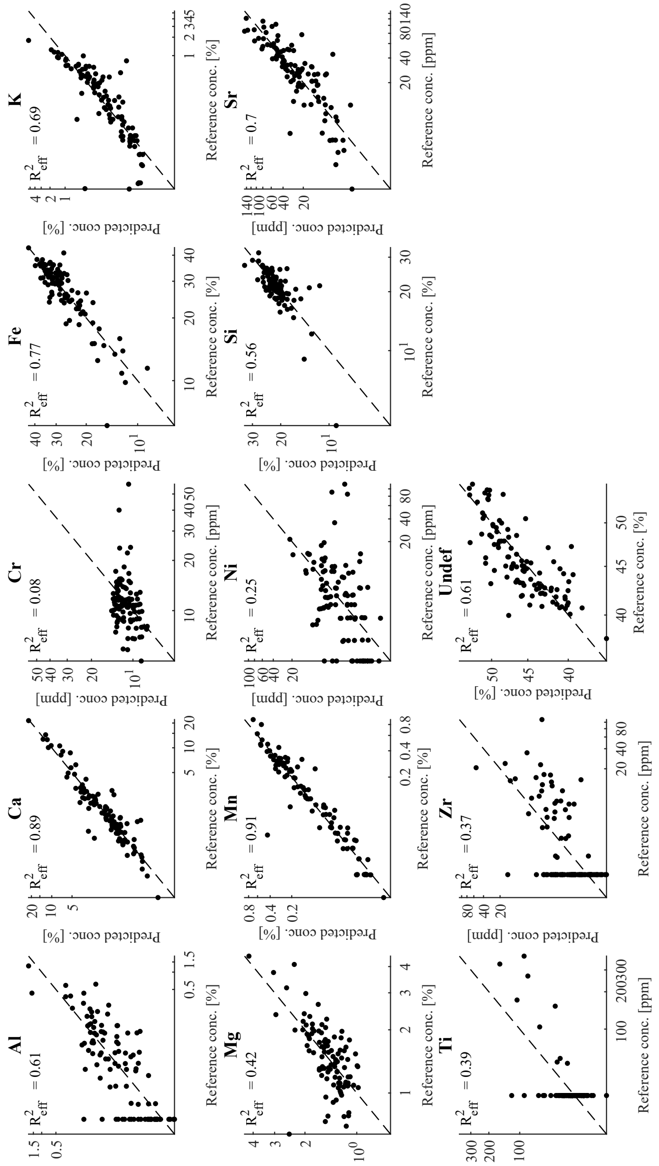

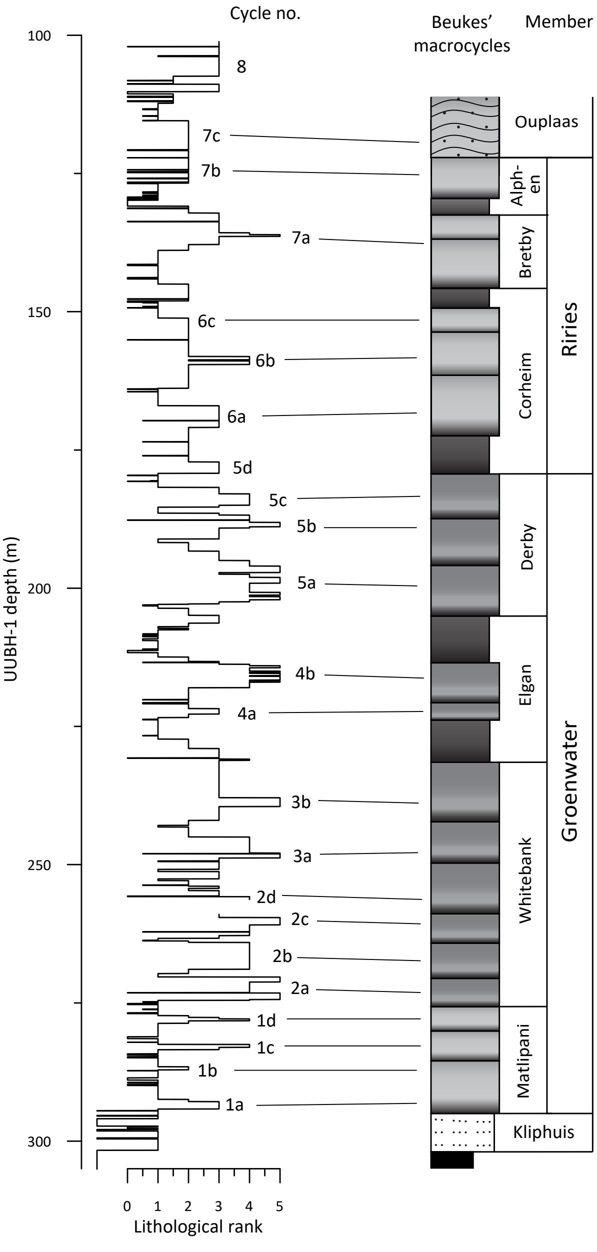

Figure S3. Lithological rank series of UUBH-1 revealing the characteristic cycles of Lantink et al. (2019) (left) and comparison to Beukes' macrocycles and traditional members (right) observed in the old core WB98 from Whitebank (modified after Beukes 1980; 1983).

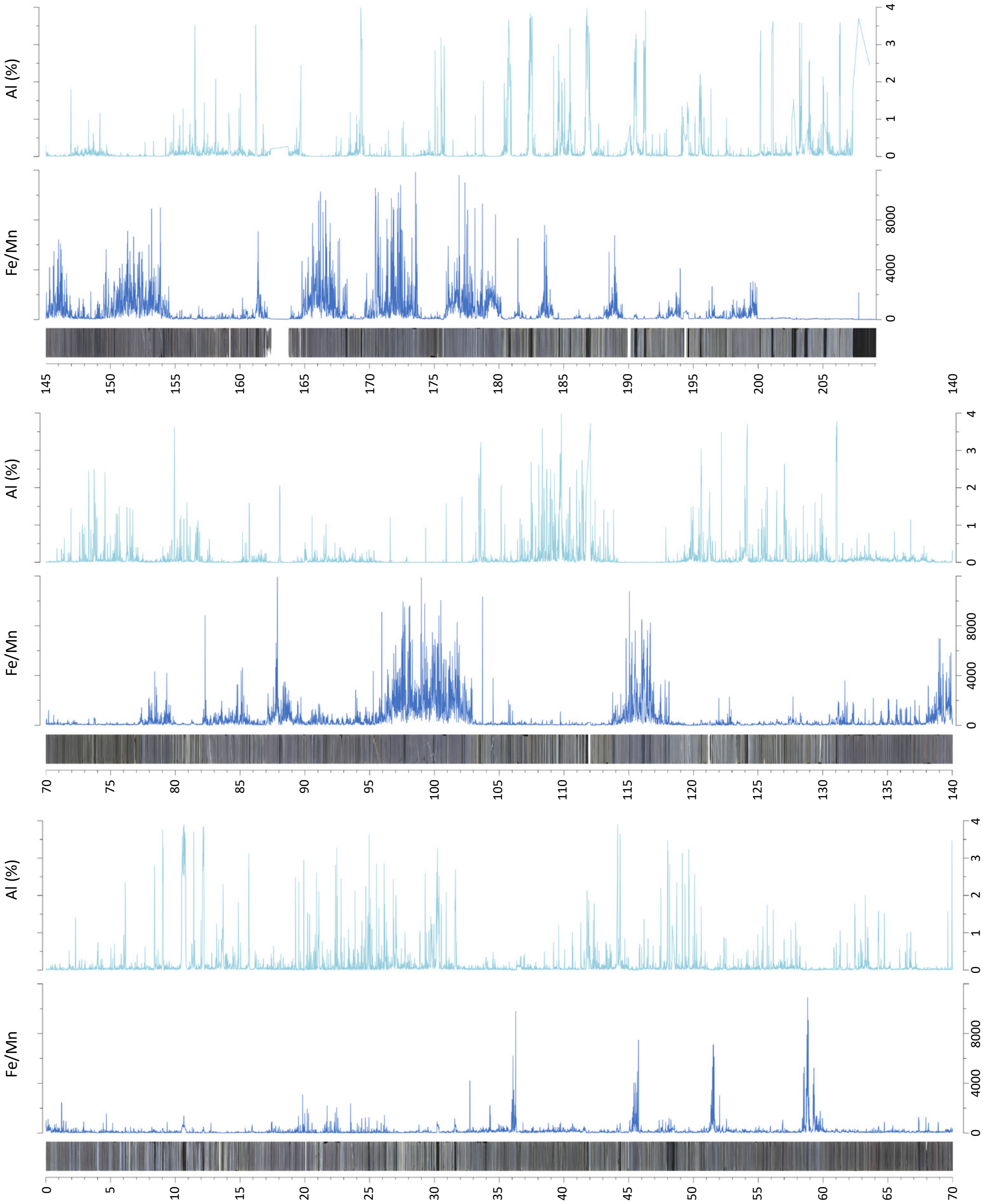

Figure S4. XRF core scanning and photo composite of UUBH-1 for the depth interval that includes the Kuruman Formation (100 – 302m). Calibrated Fe/Mn and Al (wt %) records are shown.

Figure S5. Construction of UAV-derived photogrammetry models for the Dales Gorge Member field sections at Mt Bruce and Mt Jack and extraction of stratigraphic data.

Mt Bruce West

Textured 2.5D mesh with GCP marker positions constructed in Agisoft Metashape:

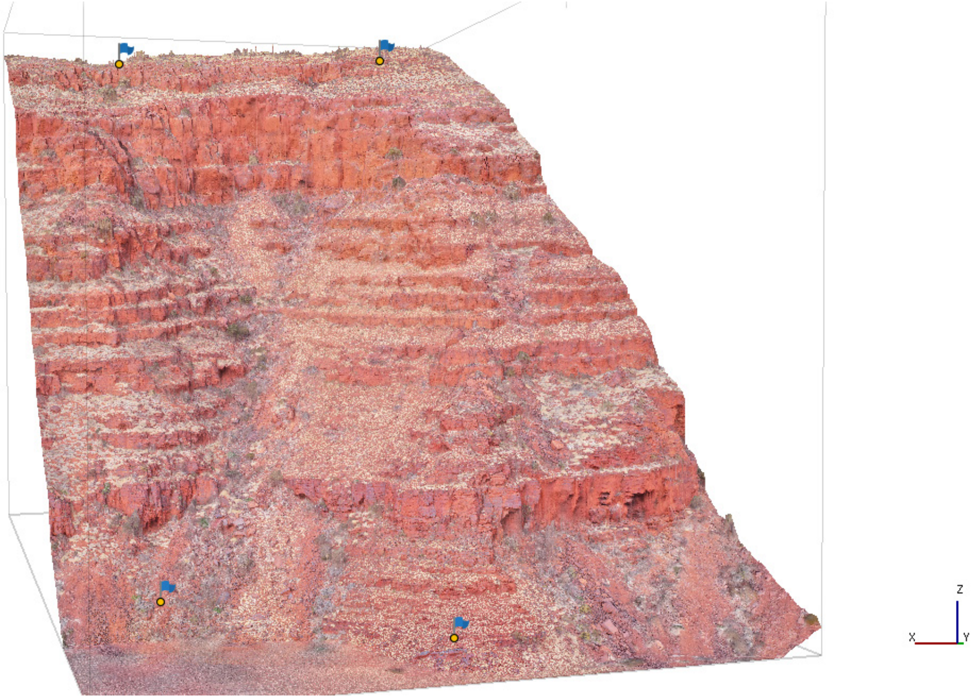

GCP positions and error (in metres):

GCP	X/Longitude	Y/Latitude	Z/Altitude	X_model	Y_model	Z_model	X_error	Y_error	Z_error
1	118.136749	-22.601359	1102.6066	118.13675	-22.601358	1102.472446	0.11	0.08	-0.13
2	118.135667	-22.601266	1105.564	118.135665	-22.601266	1105.607911	-0.14	0.02	0.04
3	118.136721	-22.599511	912.0408	118.136724	-22.599512	912.134382	0.28	-0.18	0.09
4	118.136032	-22.599088	909.7827	118.13603	-22.599087	909.77934	-0.25	0.08	0.00

Next page): dip corrected point cloud in CloudCompare (~8°/25° determined by visual fitting of plane with stratigraphic layers). Yellow boxes indicate selected points used for manual logging (point picking upper and lower boundary of layers: purple dots) and extraction of semi-quantitative 'verticality' scalar values (colour scale):

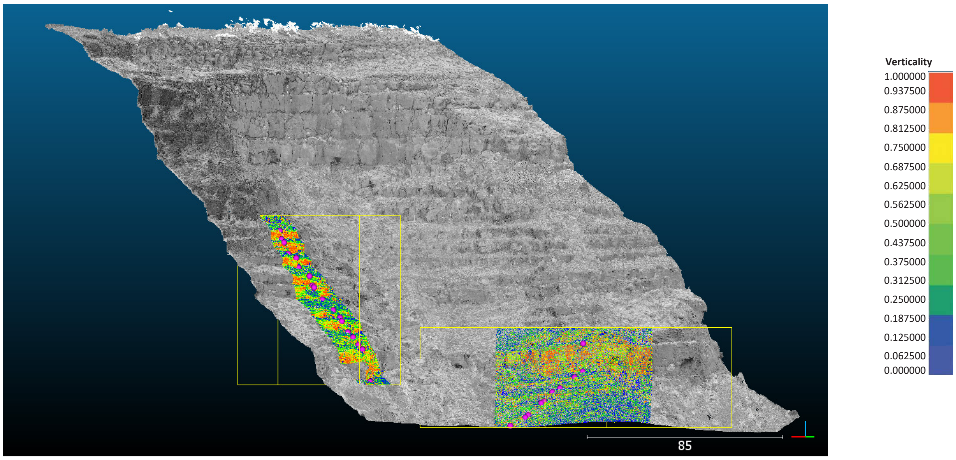
Verticality
1.000000
0.937500
0.875000
0.812500
0.750000
0.687500
0.625000
0.562500
0.500000
0.437500
0.375000
0.312500
0.250000
0.187500
0.125000
0.062500
0.000000
85

Lower section. Counter dip correction of 6°/205:

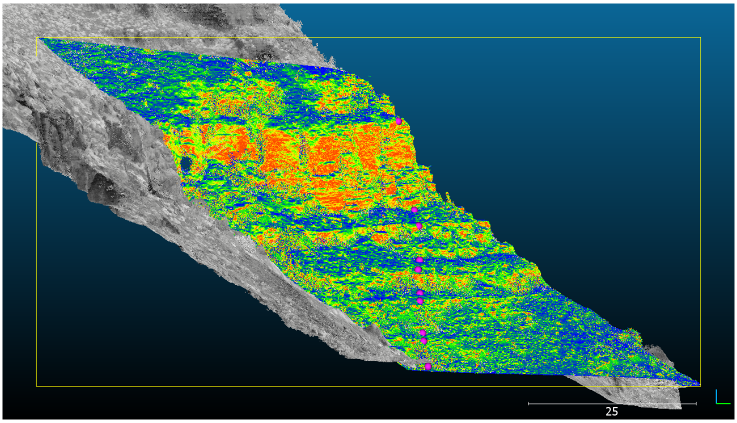

Upper section:

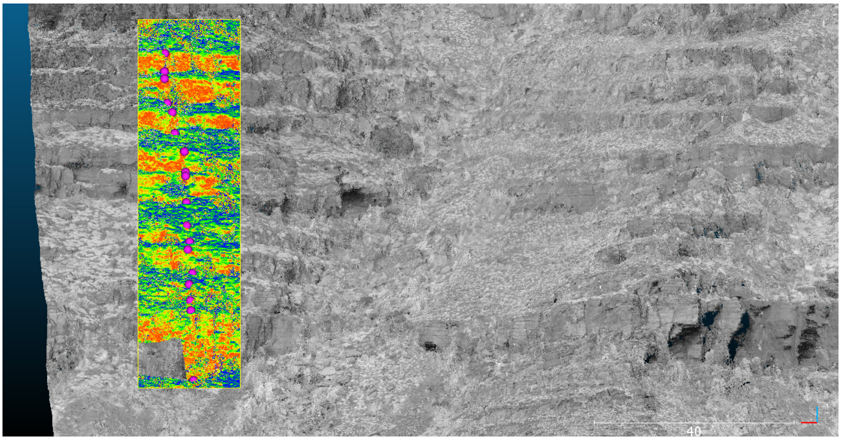

Mt Bruce East

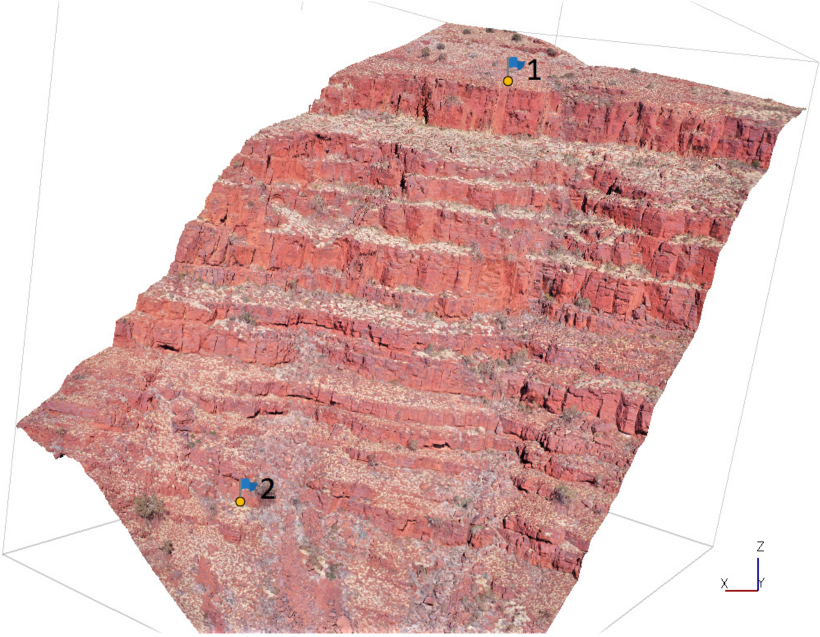

GCP	X/Longitude	Y/Latitude	Z/Altitude	X_model	Y_model	Z_model	X_error	Y_error	Z_error
1	118.1391	-22.602	1094.169	118.1391	-22.602	1094.283	0.22334	-0.02986	0.114268
2	118.14	-22.6012	963.9399	118.14	-22.6012	963.9461	0.032086	0.01303	0.0062

12.5°/330° dip corrected:

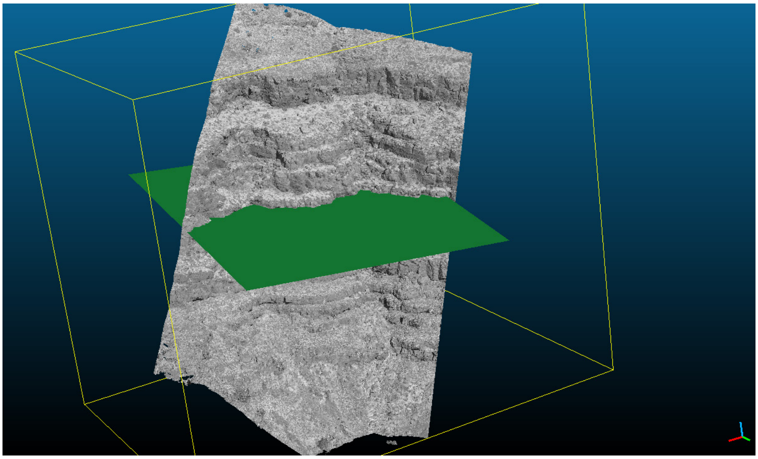

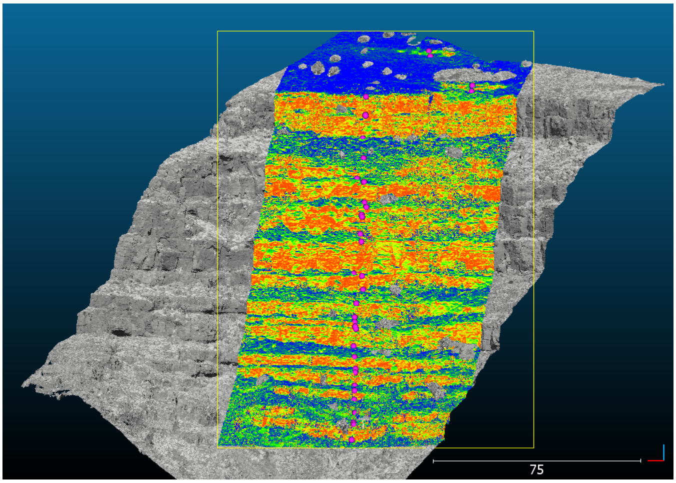

Mt Jack East

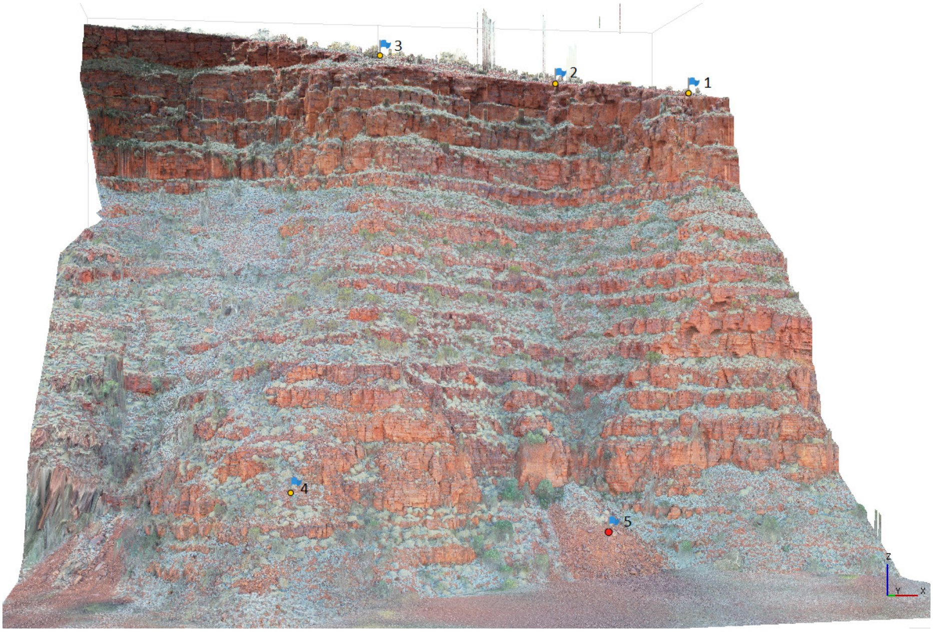

GCP	X/Longitude	Y/Latitude	Z/Altitude	X_model	Y_model	Z_model	X_error	Y_error	Z_error
1	117.4434	-22.2754	935.0897	117.4434	-22.2754	935.0912	0.006	0.009	0.002
2	117.443	-22.2753	941.2268	117.443	-22.2753	941.2386	0.011	0.003	0.012
3	117.4424	-22.2753	953.4025	117.4424	-22.2753	953.3886	-0.004	-0.007	-0.014
4	117.4426	-22.2767	827.867	117.4426	-22.2767	827.8555	0.007	-0.006	-0.012
5	117.4433	-22.2763	814.997	117.4433	-22.2763	815.0091	-0.020	0.001	0.012

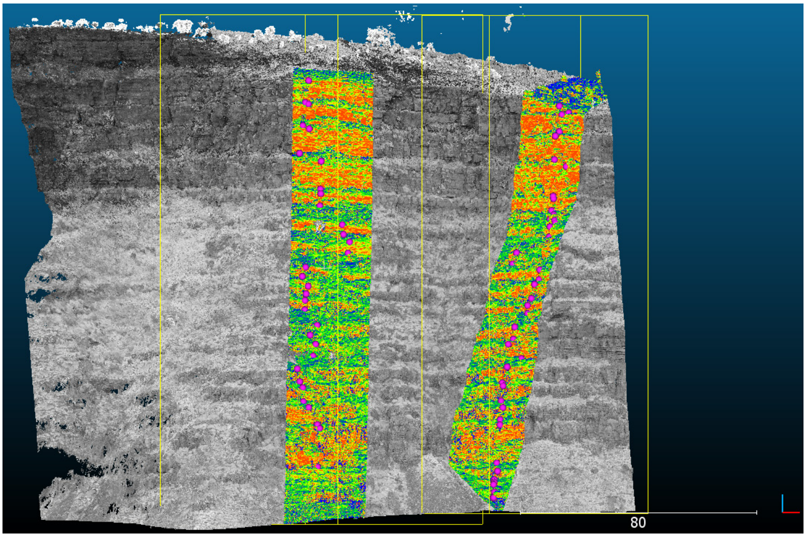

Mt Jack West

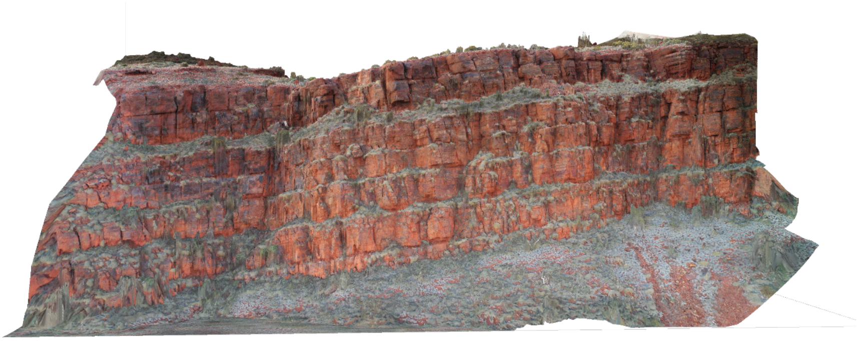

8°/275°dip corrected:

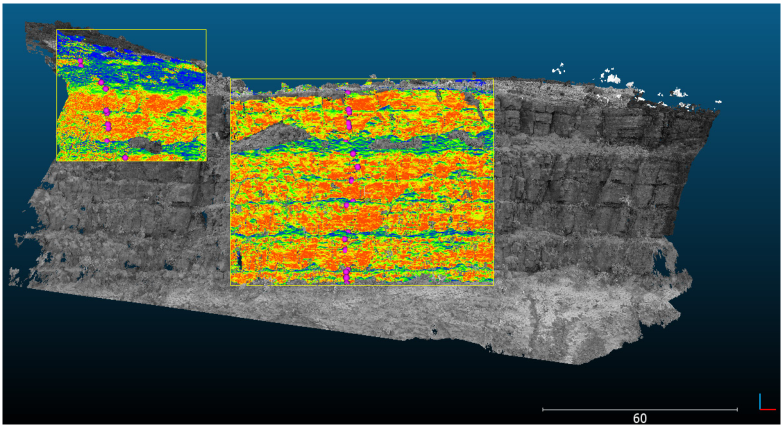

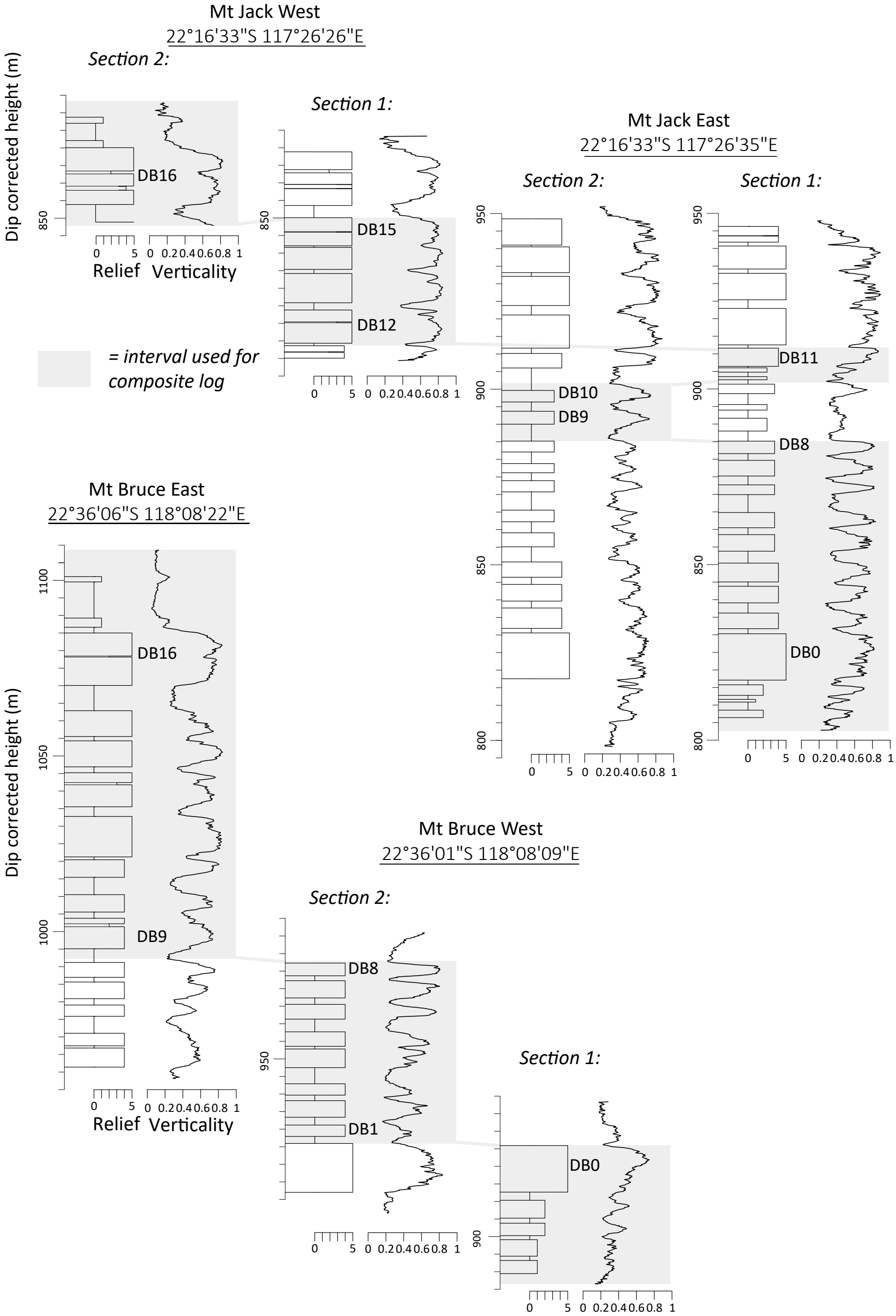

Figure S6. Compilation of the Mt Bruce and Mt Jack composite logs and verticality profiles obtained from their different subsections.

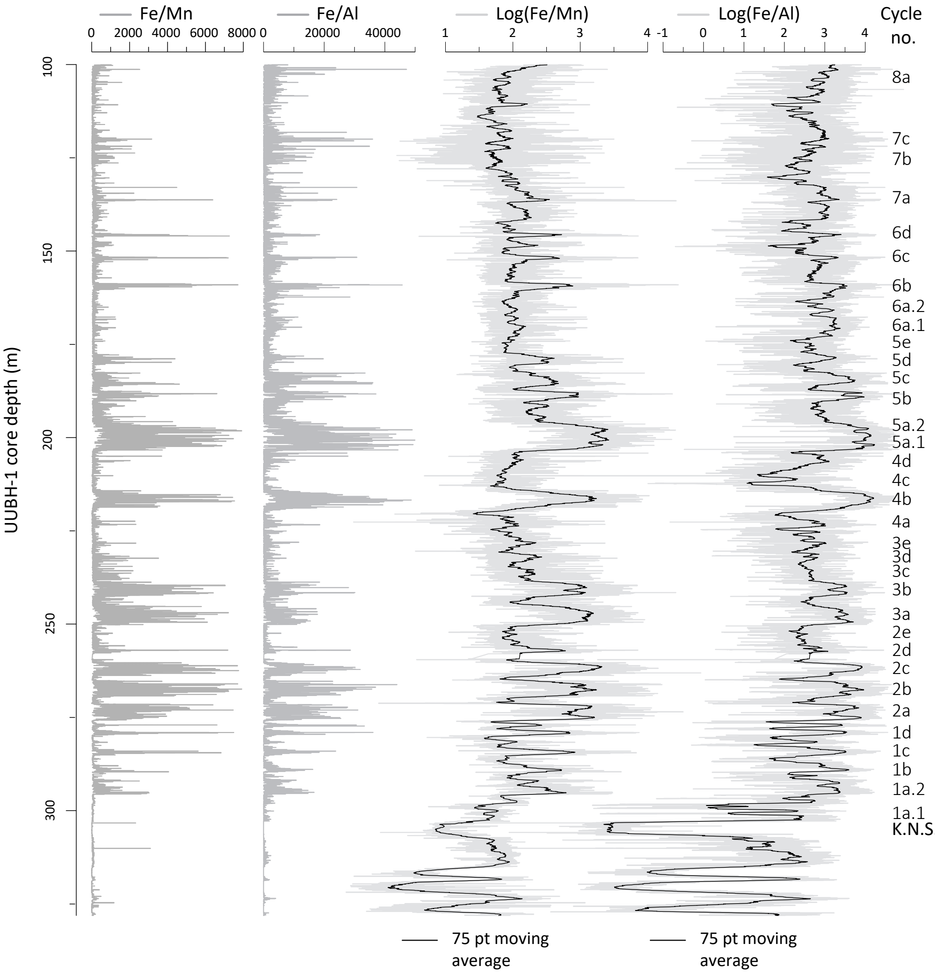

Figure S7. Comparison of the Fe/Mn and Fe/Al records with updated cycle numbers indicated, showing an almost identical pattern of regular metre-scale alternations between relatively iron oxide- and iron carbonate/shale-rich intervals.

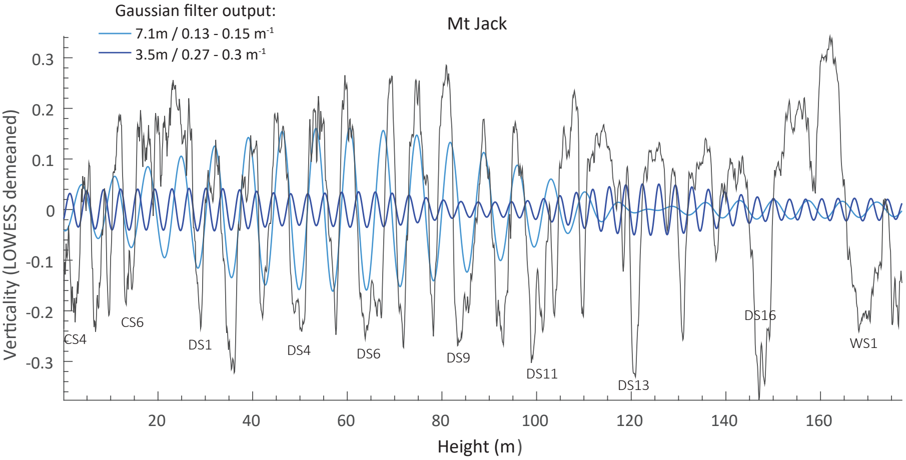

Figure S8. Comparison of the filtered ~3.5m and ~7m cycles in the Mt Jack verticality record. First of all, it is clear from this figure that the ~3.5m cycle is a harmonic of the ~7m cycle, showing exactly two filtered ~3.5m cycles per filtered ~7m cycle. Maxima in the filtered ~3.5m cycle coincide (often) with the edges of the BIF intervals and minima fitting in the thinner S intervals, suggesting that the ~3.5m cycle arises from the somewhat rectangular shape of the BIF-S alternations, i.e., the larger proportional thickness of the BIF relative to S intervals. Note however that the ~3.5m filter also picks up faint splitting features visible in several of the thicker BIF macrobands such as in the upper half of the Dales Gorge Member, as well as the extra maximum in between CB4 and CB5 of the Colonial Chert Member.

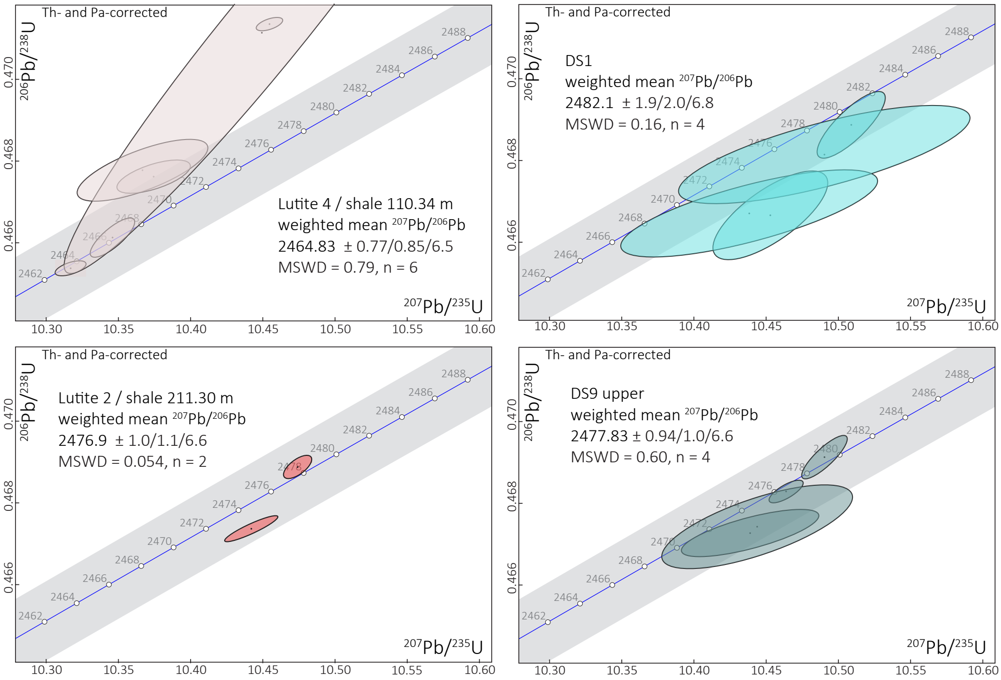

Figure S9. Concordia diagrams showing the concordant high-precision U–Pb TIMS results and the calculated ages for DS1 and DS9 (Dales Gorge Member) and shales 212m and 110m (Kuruman Formation). The grey band represents the uncertainty on the Concordia curve due to the decay constant uncertainties. The ellipses represent the U–Pb isotopic data and 2σ uncertainty for individual chemically abraded zircon fragments. MSWD: mean square of the weighted deviates.

Figure S10 (next page). Correlation option I for the Kuruman IF and Dales Gorge Member. Horizontal lines indicate the correlation of ~5m-scale 'BIF' intervals and/or interpreted 405 kyr cycles (dotted lines where this is uncertain), with thicker lines marking the more prominent BIFs that form the basis of the correlation. Black lines indicate our initial correlation (option Ia) based on a largest resemblance in the characteristic weathering profile pattern. However, note that this correlation implies the presence of three condensed 405 kyr-related cycles in DS11, and is in disagreement with the TIMS U-Pb ages, which require that DS4 is within 3 Myrs, i.e., less than eight 405 kyr-related cycles separated from the shale below 4c in the Kuruman IF. Option Ib (gold lines) circumvents the need for a hiatus in DS11 but results in a poor pattern match and is still incompatible with the U-Pb ages.

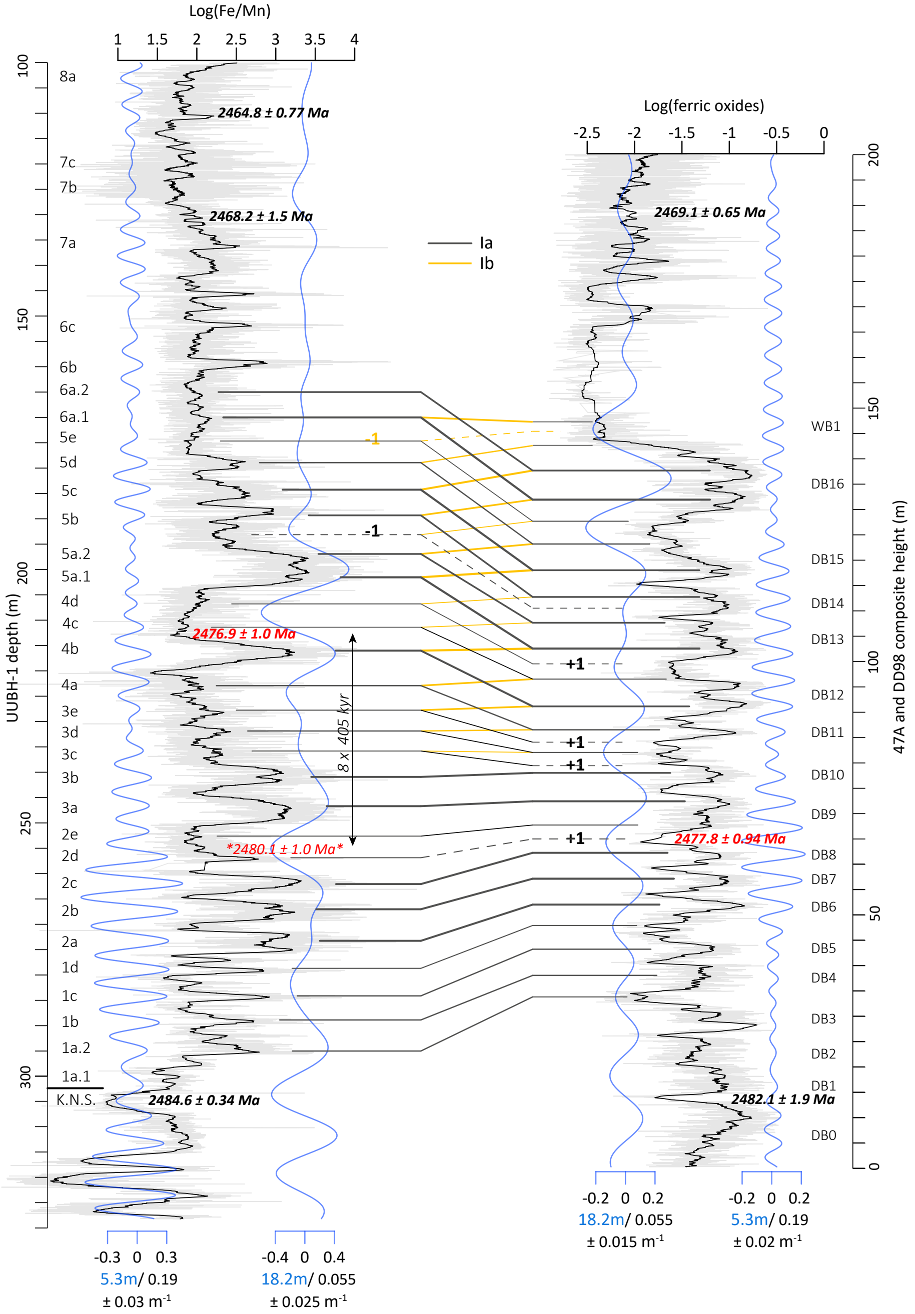
Log(Fe/Mn)
1
1.5
2
2.5
3
3.5
4
Log(ferric oxides)
-2.5
-2
-1.5
-1
-0.5
0
UUBH-1 depth (m)
100
150
200
250
300
47A and DD98 composite height (m)
0
50
100
150
200
8a
7c
7b
7a
6c
6b
6a.2
6a.1
5e
5d
5c
5b
5a.2
5a.1
4d
4c
4b
4a
3e
3d
3c
3b
3a
2e
2d
2c
2b
2a
1d
1c
1b
1a.2
1a.1
K.N.S.
2464.8 ± 0.77 Ma
2468.2 ± 1.5 Ma
2476.9 ± 1.0 Ma
2480.1 ± 1.0 Ma
2484.6 ± 0.34 Ma
2469.1 ± 0.65 Ma
2477.8 ± 0.94 Ma
2482.1 ± 1.9 Ma
Ia
Ib
-1
-1
+1
+1
+1
+1
8 x 405 kyr
WB1
DB16
DB15
DB14
DB13
DB12
DB11
DB10
DB9
DB8
DB7
DB6
DB5
DB4
DB3
DB2
DB1
DB0
-0.3 0 0.3
5.3m/ 0.19
± 0.03 m⁻¹
-0.4 0 0.4
18.2m/ 0.055
± 0.025 m⁻¹
-0.2 0 0.2
18.2m/ 0.055
± 0.015 m⁻¹
-0.2 0 0.2
5.3m/ 0.19
± 0.02 m⁻¹

References

Abels, H. A., Kraus, M. J., & Gingerich, P. D. (2013). Precession-scale cyclicity in the fluvial lower Eocene Willwood Formation of the Bighorn Basin, Wyoming (USA). *Sedimentology*, 60(6), 1467-1483.

Adhémar, J.A. (1842). Revolutions de la mer, privately published.

Ahn, J. H., & Buseck, P. R. (1990). Hematite nanospheres of possible colloidal origin from a Precambrian banded iron formation. *Science*, *250*(4977), 111-113.

Alcott, L. J., Mills, B. J., & Poulton, S. W. (2019). Stepwise Earth oxygenation is an inherent property of global biogeochemical cycling. *Science*, *366*(6471), 1333-1337.

Alibert, C., & McCulloch, M. T. (1993). Rare earth element and neodymium isotopic compositions of the banded iron-formations and associated shales from Hamersley, Western Australia. *Geochimica et Cosmochimica Acta*, *57*(1), 187-204.

Altermann, W., & Nelson, D. R. (1998). Sedimentation rates, basin analysis and regional correlations of three Neoarchaean and Palaeoproterozoic sub-basins of the Kaapvaal craton as inferred from precise U–Pb zircon ages from volcaniclastic sediments. *Sedimentary Geology, 120*(1-4), 225-256.

Anbar, A. D., Duan, Y., Lyons, T. W., Arnold, G. L., Kendall, B., Creaser, R. A., ... & Buick, R. (2007). A whiff of oxygen before the great oxidation event?. *Science*, *317*(5846), 1903-1906.

Ayres, D. E. (1972). Genesis of iron-bearing minerals in banded iron formation mesobands in the Dales Gorge Member, Hamersley Group, Western Australia. *Economic Geology*, *67*(8), 1214-1233.

Bao, X., Zhang, S., Jiang, G., Wu, H., Li, H., Wang, X., ... & Yang, T. (2018). Cyclostratigraphic constraints on the duration of the Datangpo Formation and the onset age of the Nantuo (Marinoan) glaciation in South China. *Earth and Planetary Science Letters*, *483*, 52-63.

Barboni, M., Boehnke, P., Keller, B., Kohl, I. E., Schoene, B., Young, E. D., & McKeegan, K. D. (2017). Early formation of the Moon 4.51 billion years ago. *Science advances*, *3*(1), e1602365.

Barley, M. E., Pickard, A. L., & Sylvester, P. J. (1997). Emplacement of a large igneous province as a possible cause of banded iron formation 2.45 billion years ago. *Nature*, *385*(6611), 55-58.

Barnet, J. S. K., Littler, K., Westerhold, T., Kroon, D., Leng, M. J., Bailey, I., Röhl, U., and Zachos, J. C. (2019). A high-fidelity benthic stable isotope record of late Cretaceous–early Eocene climate change and carbon-cycling. *Paleoceanography and Paleoclimatology*, 34(4), 672-691.

Bartlett, B. C., & Stevenson, D. J. (2016). Analysis of a Precambrian resonance-stabilized day length. *Geophysical Research Letters*, *43*(11), 5716-5724.

Batenburg, S. J., Sprovieri, M., Gale, A. S., Hilgen, F. J., Hüsing, S., Laskar, J., Liebrand, D., Lirer, F., Orue-Etxebarria, X., Pelosi, N., & Smit, J. (2012). Cyclostratigraphy and astronomical tuning of the Late Maastrichtian at Zumaia (Basque country, Northern Spain). *Earth and Planetary Science Letters*, *359–360*, 264–278.

Batenburg, S. J., De Vleeschouwer, D., Sprovieri, M., Hilgen, F. J., Gale, A. S., Singer, B. S., ... & Montanari, A. (2016). Orbital control on the timing of oceanic anoxia in the Late Cretaceous. *Climate of the Past*, *12*(10), 1995-2009.

Baur, M. E., Hayes, J. M., Studley, S. A., & Walter, M. R. (1985). Millimeter-scale variations of stable isotope abundances in carbonates from banded iron-formations in the Hamersley Group of Western Australia. *Economic Geology*, *80*(2), 270-282.

Beckmann, B., Flögel, S., Hofmann, P., Schulz, M., & Wagner, T. (2005). Orbital forcing of Cretaceous river discharge in tropical Africa and ocean response. *Nature*, *437*(7056), 241-244.

Bekker, A., Holland, H. D., Wang, P. L., Rumble, D. I. I. I., Stein, H. J., Hannah, J. L., ... & Beukes, N. J. (2004). Dating the rise of atmospheric oxygen. *Nature*, *427*(6970), 117-120.

Bekker, A., Slack, J. F., Planavsky, N., Krapez, B., Hofmann, A., Konhauser, K. O., & Rouxel, O. J. (2010). Iron formation: the sedimentary product of a complex interplay among mantle, tectonic, oceanic, and biospheric processes. *Economic Geology*, *105*(3), 467-508.

Berger, A. (1978). Long-term variations of daily insolation and Quaternary climatic changes. *Journal of Atmospheric Sciences*, *35*(12), 2362-2367.

Berger, A., & Loutre, M. F. (1994). Astronomical forcing through geological time. In *Orbital forcing and cyclic sequences* (pp. 15–24).

Berger, A., Loutre, M. F., & Laskar, J. (1992). Stability of the astronomical frequencies over the Earth's history for paleoclimate studies. *Science*, *255*(5044), 560-566.

Berner, R. A. (1969). Migration of iron and sulfur within anaerobic sediments during early diagenesis. *American Journal of Science*, *267*(1), 19-42.

Berner, R. A. (1981). A new geochemical classification of sedimentary environments. *Journal of Sedimentary Research*, *51*(2), 359-365.

Beukes, N. J. (1978). *Die Karbonaatgesteentes en Ysterformasies van die Ghaap-groep van die Transvaal-supergroep in Noord-Kaapland*. PhD Thesis.

Beukes, N. J. (1980). Lithofacies and stratigraphy of the Kuruman and Griquatown iron-formations, northern Cape Province, South Africa. *Transactions of the Geological Society of South Africa*, *83*, 69–86.

Beukes, N. J. (1983). Palaeoenvironmental setting of iron-formations in the depositional basin of the Transvaal Supergroup, South Africa. In *Developments in Precambrian Geology* (Vol. 6, pp. 131-198). Elsevier.

Beukes, N. J. (1987). Facies relations, depositional environments and diagenesis in a major Early Proterozoic stromatolitic carbonate platform to basinal sequence, Campbellrand Subgroup, Transvaal Supergroup, Southern Africa. *Sedimentary Geology*, *54*(1–2), 179–546.

Beukes, N. J., & Klein, C. (1990). Geochemistry and sedimentology of a facies transition—from microbanded to granular iron-formation—in the early Proterozoic Transvaal Supergroup, South Africa. *Precambrian Research*, *47*(1-2), 99-139.

Beukes, N. J., Klein, C., Kaufman, A. J., & Hayes, J. M. (1990). Carbonate petrography, kerogen distribution, and carbon and oxygen isotope variations in an early Proterozoic transition from limestone to iron-formation deposition, Transvaal Supergroup, South Africa. *Economic geology and the bulletin of the Society of Economic Geologists*, *85*(4), 663-690.

Beukes, N.J., & Gutzmer, J. (2008). Origin and paleoenvironmental significance of major iron formations at the Archean-Paleoproterozoic boundary. *Society of Economic Geologists Reviews*, *15*(August 2016), 5–47.

Bills, B. G., & Ray, R. D. (1999). Lunar orbital evolution: A synthesis of recent results. *Geophysical Research Letters*, *26*(19), 3045-3048.

Bindeman, I. N., Zakharov, D. O., Palandri, J., Greber, N. D., Dauphas, N., Retallack, G. J., ... & Bekker, A. (2018). Rapid emergence of subaerial landmasses and onset of a modern hydrologic cycle 2.5 billion years ago. *Nature*, *557*(7706), 545-548.

Bjerrum, C. J., & Canfield, D. E. (2002). Ocean productivity before about 1.9 Gyr ago limited by phosphorus adsorption onto iron oxides. *Nature*, *417*(6885), 159-162.

Blackledge, B. W., Green, J. A. M., Barnes, R., & Way, M. J. (2020). Tides on Other Earths: Implications for Exoplanet and Palaeo-Tidal Simulations. *Geophysical Research Letters*, *47*(12), e2019GL085746.

Bloemsma, M. R. (2015). *Development of a Modelling Framework for Core Data Integration Using XRF Scanning*. PhD Thesis.

Bosmans, J. H. C., Drijfhout, S. S., Tuenter, E., Hilgen, F. J., & Lourens, L. J. (2015). Response of the North African summer monsoon to precession and obliquity forcings in the EC - Earth GCM. *Climate Dynamics*, *44*, 279–297.

Boudreau, B. P. (1996a). The diffusive tortuosity of fine-grained unlithified sediments. *Geochimica et cosmochimica acta*, *60*(16), 3139-3142.

Boudreau, B. P. (1996b). A method-of-lines code for carbon and nutrient diagenesis in aquatic sediments. *Computers & Geosciences*, *22*(5), 479-496.

Boudreau, B. P. (1997). *Diagenetic models and their implementation* (Vol. 410). Springer, Berlin.

Boulila, S. (2019). Coupling between Grand cycles and Events in Earth's climate during the past 115 million years. *Scientific Reports*, *9*(1), 1–7.

Boulila, S., Galbrun, B., Laskar, J., & Pälike, H. (2012). A ~9 myr cycle in Cenozoic δ13C record and long-term orbital eccentricity modulation: Is there a link?. *Earth and Planetary Science Letters*, *317*, 273-281.

Buick, R. (2008). When did oxygenic photosynthesis evolve?. *Philosophical Transactions of the Royal Society B: Biological Sciences*, *363*(1504), 2731-2743.

Burdige, D. J. (2006). *Geochemistry of marine sediments*. Princeton University Press.

Busigny, V., Lebeau, O., Ader, M., Krapež, B., & Bekker, A. (2013). Nitrogen cycle in the Late Archean ferruginous ocean. *Chemical Geology*, *362*, 115-130.

Button, A. (1976). *Transvaal and Hamersley Basins: Review of basin development and mineral deposits*.

Cheney, E. S. (1996). Sequence stratigraphy and plate tectonic significance of the Transvaal succession of southern Africa and its equivalent in Western Australia. *Precambrian Research*, *79*(1-2), 3-24.

Cloud, P. (1973). Paleoecological significance of the banded iron-formation. *Economic Geology*, *68*(7), 1135-1143.

Coleman, M. L. (1993). Microbial processes: controls on the shape and composition of carbonate concretions. *Marine geology*, *113*(1-2), 127-140.

Condon, D. J., Schoene, B., McLean, N. M., Bowring, S. A., & Parrish, R. R. (2015). Metrology and traceability of U–Pb isotope dilution geochronology (EARTHTIME Tracer Calibration Part I). *Geochimica et Cosmochimica Acta*, *164*, 464-480.

Cowan, D., & Cooper, G. (2003). Wavelet analysis of detailed drillhole magnetic susceptibility data, Brockman Iron Formation, Hamersley Basin, Western Australia. *Exploration Geophysics*, *34*(2), 63-68.

Crampton, J.S., Meyers, S.R. Cooper, R.A., Sadler, P.M., Foote, M., and Harte, D. (2018). Pacing of Paleozoic macro-evolutionary rates by Milankovitch grand cycles. *Proceedings of the National Academy of Sciences of the United States of America*, *115*(22), 5686-5691.

Croll, J. (1864). XIII. On the physical cause of the change of climate during geological epochs. *The*

London, Edinburgh, and Dublin Philosophical Magazine and Journal of Science, *28*(187), 121-137.

Crowe, S. A., Paris, G., Katsev, S., Jones, C., Kim, S. T., Zerkle, A. L., ... & Canfield, D. E. (2014). Sulfate was a trace constituent of Archean seawater. *Science*, *346*(6210), 735-739.

Crowley, T. J., & Baum, S. K. (1992). Modeling late Paleozoic glaciation. *Geology*, *20*(6), 507-510.

Da Silva, A. C., Hladil, J., Chadimova, L., Slavik, L., Hilgen, F. J., Bábek, O., & Dekkers, M. J. (2016). Refining the Early Devonian time scale using Milankovitch cyclicity in Lochkovian–Pragian sediments (Prague Synform, Czech Republic). *Earth and Planetary Science Letters*, *55*, 125–139.

Daher, H., Arbic, B. K., Williams, J. G., Ansong, J. K., Boggs, D. H., Müller, M., ... & Huber, M. (2021). Long-term Earth-Moon evolution with high-level orbit and ocean tide models. *Journal of Geophysical Research: Planets*, *126*(12), e2021JE006875.

Darwin, G. H. (1879). XIII. On the precession of a viscous spheroid, and on the remote history of the Earth. *Philosophical Transactions of the Royal Society of London*, (170), 447-538.

Darwin, G. H. (1880). XX. On the secular changes in the elements of the orbit of a satellite revolving about a tidally distorted planet. *Philosophical Transactions of the Royal Society of London*, (171), 713-891.

Davydov, V.I., Crowley, J.L., Schmitz, M.D., and Poletaev, V.I. (2010). High-precision U-Pb zircon age calibration of the global Carboniferous time scale and Milankovitch band cyclicity in the Donets basin, eastern Ukraine. *Geochemistry, Geophysics, Geosystems*, 11(2).

de Kock, M. O., Evans, D. A. D., & Beukes, N. J. (2009). Validating the existence of Vaalbara in the Neoarchean. *Precambrian Research*, *174*(1–2), 145–154.

de Lange, G. J., Jarvis, I., & Kuijpers, A. (1987). Geochemical characteristics and provenance of late Quaternary sediments from the Madeira Abyssal Plain, N Atlantic. *Geological Society, London, Special Publications*, *31*(1), 147-165.

de Oliveira Carvalho Rodrigues, P., Hinnov, L. A., & Franco, D. R. (2019). A new appraisal of depositional cyclicity in the Neoarchean- Paleoproterozoic Dales Gorge Member (Brockman Iron Formation, Australia). *Precambrian Research*, *328*, 27–47.

de Vleeschouwer, D., Da Silva, A. C., Sinnesael, M., Chen, D., Day, J. E., Whalen, M. T., Guo, Z., & Claeys, P. (2017). Timing and pacing of the Late Devonian mass extinction event regulated by eccentricity and obliquity. *Nature Communications*, *8*(1), 1–11.

Dehler, C., Gehrels, G., Porter, S., Heizler, M., Karlstrom, K., Cox, G., ... & Timmons, M. *(2017).* Synthesis of the 780–740 Ma Chuar, Uinta Mountain, and Pahrump (ChUMP) groups, western USA: Implications for Laurentia-wide cratonic marine basins. *Geological Society of America Bulletin,* **129**, 607–624.

Derry, L. A., & Jacobsen, S. B. (1990). The chemical evolution of Precambrian seawater: evidence from REEs in banded iron formations. *Geochimica et Cosmochimica Acta*, *54*(11), 2965-2977.

Dickey, J. O., Bender, P. L., Faller, J. E., Newhall, X. X., Ricklefs, R. L., Ries, J. G., ... & Yoder, C. F. (1994). Lunar laser ranging: a continuing legacy of the Apollo program. *Science*, *265*(5171), 482-490.

Ding, Z. L., Derbyshire, E., Yang, S. L., Yu, Z. W., Xiong, S. F., and Liu, T. S. (2002). Stacked 2.6-Ma grain size record from the Chinese loess based on five sections and correlation with the deep-sea δ18O record. *Paleoceanography*, 17(3), 5-1 - 5-21.

Dodd, M.S., Papineau, D., Grenne, T., Slack, J.F., Rittner, M., Pirajno, F., O'Neil, J., and Little, C.T.S. (2017). Evidence for early life in earth's oldest hydrothermal vent precipitates. *Nature*, 543(7643), 60-64

Egger, M., Jilbert, T., Behrends, T., Rivard, C., & Slomp, C. P. (2015). Vivianite is a major sink for phosphorus in methanogenic coastal surface sediments. *Geochimica et Cosmochimica Acta*, *169*, 217-235.

Egger, M., Lenstra, W., Jong, D., Meysman, F. J., Sapart, C. J., Van der Veen, C., ... & Slomp, C. P. (2016). Rapid sediment accumulation results in high methane effluxes from coastal sediments. *PloS one*, *11*(8), e0161609.

Emiliani, C. (1955). Pleistocene temperatures. *The Journal of geology*, *63*(6), 538-578.

Ericson, D. B., & Wollin, G. (1968). Pleistocene Climates and Chronology in Deep-Sea Sediments: Magnetic reversals give a time scale of 2 million years for a complete Pleistocene with four glaciations. *Science*, *162*(3859), 1227-1234.

Ewers, W. E., & Morris, R. C. (1981). Studies of the Dales Gorge member of the Brockman iron formation, Western Australia. *Economic Geology*, *76*(7), 1929-1953.

Fang, Q., Wu, H., Hinnov, L. A., Jing, X., Wang, X., & Jiang, Q. (2015). Geologic evidence for chaotic behavior of the planets and its constraints on the third-order eustatic sequences at the end of the Late Paleozoic Ice Age. *Palaeogeography, Palaeoclimatology, Palaeoecology*, *440*, 848–859.

Fischer, W. W., & Knoll, A. H. (2009). An iron shuttle for deepwater silica in Late Archean and early Paleoproterozoic iron formation. *Geological Society of America Bulletin*, *121*(1-2), 222-235.

Frei, R., Gaucher, C., Poulton, S. W., & Canfield, D. E. (2009). Fluctuations in Precambrian atmospheric oxygenation recorded by chromium isotopes. *Nature*, *461*(7261), 250-253.

Froelich, P., Klinkhammer, G. P., Bender, M. L., Luedtke, N. A., Heath, G. R., Cullen, D., ... & Maynard, V. (1979). Early oxidation of organic matter in pelagic sediments of the eastern equatorial Atlantic: suboxic diagenesis. *Geochimica et cosmochimica acta*, *43*(7), 1075-1090.

Froeschle, C., & Morbidelli, A. (1994). The Secular Resonances in the Solar System. In *Asteroids, Comets, Meteors 1993. International Astronomical Union / Union Astronomique Internationale* (Vol. 160, pp. 189–204).

Williams, V. A. Gostin, D. M. McKirdy, W. V. Preiss, The Elatina glaciation, late Cryogenian (Marinoan Epoch), South Australia: Sedimentary facies and palaeoenvironments. *Precambrian Res.* **163**, 307–331 (2008).

Gerstenkorn, H. (1967). On the controversy over the effect of tidal friction upon the history of the Earth-Moon system. *Icarus*, *7*(1-3), 160-167.

Gerstenkorn, The earliest past of the Earth–Moon system. *Icarus* **11**, 189–207 (1969).

Glass, B. P., & Simonson, B. M. (2012). Distal impact ejecta layers: Spherules and more. *Elements*, *8*(1), 43–48.

Glikson, A. J. (2014). Post-3.2 Ga Basins and Asteroid Impact Units. In *The Archaean: Geological and Geochemical Windows into the Early Earth* (pp. 131–157).

Glikson, A., & Allen, C. (2004). Iridium anomalies and fractionated siderophile element patterns in impact ejecta, Brockman Iron Formation, Hamersley Basin, Western Australia: Evidence for a major asteroid impact in simatic crustal regions of the early Proterozoic earth. *Earth and Planetary Science Letters*, *220*(3–4), 247–264.

Goldreich, P. (1966). History of the lunar orbit. *Reviews of Geophysics*, *4*(4), 411-439.

Gong, Z., Kodama, K. P., & Li, Y. X. (2017). Rock magnetic cyclostratigraphy of the Doushantuo

Formation, South China and its implications for the duration of the Shuram carbon isotope excursion. *Precambrian Research*, *289*, 62-74.

Gradstein, F. M., Ogg, J. G., Schmitz, M. D., & Ogg, G. M. (2020). *The Geologic Time Scale 2020*.

Green, J. A. M., Huber, M., Waltham, D., Buzan, J., & Wells, M. (2017). Explicitly modelled deep-time tidal dissipation and its implication for lunar history. *Earth and Planetary Science Letters*, 461, 46-53.

Grippo, A., Fscher, A. G., Hinnov, L. A., Herbert, T. D., & Silva, I. P. (2004). Cyclostratigraphy and Chronology of the Albian Stage (Piobbico Core, Italy). In *Cyclostratigraphy: Approaches and Case Histories. SEPM Special Publication*, *81*, 57–81.

Grotzinger, J. P. (1986). Cyclicity and paleoenvironmental dynamics, Rocknest platform, northwest Canada. *Geological Society of America Bulletin*, *97*(10), 1208-1231.

Gumsley, A. P., Chamberlain, K. R., Bleeker, W., Söderlund, U., de Kock, M. O., Larsson, E. R., & Bekker, A. (2017). Timing and tempo of the Great Oxidation Event. *Proceedings of the National Academy of Sciences*, *114*(8), 1811–1816.

Habicht, K. S., Gade, M., Thamdrup, B., Berg, P., & Canfield, D. E. (2002). Calibration of sulfate levels in the Archean ocean. *Science*, *298*(5602), 2372-2374.

Hancock, E. A., & Huntington, J. F. (2010). The GSWA NVCL HyLogger: rapid mineralogical analysis for characterizing mineral and petroleum core. In *Geological Survey of Western Australia*.

Hansen, K. S. (1982). Secular effects of oceanic tidal dissipation on the Moon's orbit and the Earth's rotation. *Reviews of Geophysics*, *20*(3), 457-480.

Harmsworth, R. A., Kneeshaw, M., Morris, R. C., Robinson, C. J., & Shrivastava, P. K. (1990). BIF-Derived Iron Ores of the Hamersley Province. *Geology of the Mineral Deposits of Australia and New Guinea*, *642*, 617–642.

Haslett, J., & Parnell, A. (2008). A simple monotone process with application to radiocarbon-dated depth chronologies. *Journal of the Royal Statistical Society: Series C (Applied Statistics)*, *57*(4), 399-418.

Hassler, S. W., & Simonson, B. M. (2001). The sedimentary record of extraterrestrial impacts in deep-shelf environments: Evidence from the early Precambrian. *Journal of Geology*, *109*(1), 1–19.

Haugaard, R., Pecoits, E., Lalonde, S., Rouxel, O., & Konhauser, K. (2016). The Joffre banded iron formation, Hamersley Group, Western Australia: Assessing the palaeoenvironment through detailed petrology and chemostratigraphy. *Precambrian Research*, *273*, 12-37.

Hays, J.D., Imbrie, J., and Shackleton, N.J. (1976). Variations in the Earth's orbit: Pacemaker of the ice ages. *Science*, 194, 1121–1132.

Heckel, P.H. (1986). Sea-level curve for Pennsylvanian eustatic marine transgressive-regressive depositional cycles along midcontinent outcrop belt, North America, *Geology*, 14(4), 330–334.

Heimann, A., Johnson, C. M., Beard, B. L., Valley, J. W., Roden, E. E., Spicuzza, M. J., & Beukes, N. J. (2010). Fe, C, and O isotope compositions of banded iron formation carbonates demonstrate a major role for dissimilatory iron reduction in ~2.5Ga marine environments. *Earth and Planetary Science Letters*, *294*(1–2), 8–18.

Hennekam, R., Jilbert, T., Schnetger, B., & De Lange, G. J. (2014). Solar forcing of Nile discharge and sapropel S1 formation in the early to middle Holocene eastern Mediterranean. *Paleoceanography*, *29*(5), 343-356.

Hennekam, R., Jilbert, T., Mason, P. R., de Lange, G. J., & Reichart, G. J. (2015). High-resolution line-scan analysis of resin-embedded sediments using laser ablation-inductively coupled plasma-mass spectrometry (LA-ICP-MS). *Chemical Geology*, *403*, 42-51.

Hennekam, R., Sweere, T., Tjallingii, R., de Lange, G. J., & Reichart, G. J. (2019). Trace metal analysis of sediment cores using a novel X-ray fluorescence core scanning method. *Quaternary International*, *514*, 55–67.

Herbert, T. D. (1994). Reading orbital signals distorted by sedimentation: models and examples. In *Orbital forcing and cyclic sequences* (pp. 483–507).

Herbert, T.D., and Fischer, A.G. (1986). Milankovitch climatic origin of mid-Cretaceous black shale rhythms in Central Italy. *Nature*, 321(6072), 739-743.

Hiess, J., Condon, D. J., McLean, N., & Noble, S. R. (2012). 238U/235U systematics in terrestrial uranium-bearing minerals. *Science, 335*(6076), 1610-1614.

Hilgen, F. J. (1991). Extension of the astronomically calibrated (polarity) time scale to the Miocene/Pliocene boundary. *Earth and planetary science letters*, *107*(2), 349-368.

Hilgen, F. J., & Langereis, C. G. (1989). Periodicities of CaCO3 cycles in the Pliocene of Sicily: discrepancies with the quasi-periods of the Earth's orbital cycles?. *Terra Nova*, *1*(5), 409-415.

Hilgen, F. J., Hinnov, L. A., Aziz, H. A., Abels, H. A., Batenburg, S., Bosmans, J. H., ... & Zeeden, C. (2015). Stratigraphic continuity and fragmentary sedimentation: the success of cyclostratigraphy as part of integrated stratigraphy. *Geological Society, London, Special Publications*, *404*(1), 157-197.

Hilgen, F. J., Zeeden, C., & Laskar, J. (2020). Paleoclimate records reveal elusive ~200-kyr eccentricity cycle for the first time. *Global and Planetary Change*, *194*, 103296.

Hinnov, L. A. (2013). Cyclostratigraphy and its revolutionizing applications in the earth and planetary sciences. *Bulletin*, *125*(11-12), 1703-1734.

Hinnov, L. A. (2018). Cyclostratigraphy and astrochronology in 2018. In *Stratigraphy & Timescales* (Vol. 3, pp. 1–80).

Hinnov, L.A., and Hilgen, F.J. (2012). Cyclostratigraphy and astrochronology. In *A Geologic Time Scale 2012*, p. 63–83.

Hintze, L.F. (1988). Geologic history of Utah. Brigham Young University, Provo, Utah.

Hoang, N. H., Mogavero, F., & Laskar, J. (2021). Chaotic diffusion of the fundamental frequencies in the Solar System. *Astronomy and Astrophysics*, *654*, A156.

Hoffman, P.F., Kaufman, A.J., Halverson, G.P., and Schrag, D.P. (1998). A Neoproterozoic snowball Earth. *Science*, 281, 1342- 1346.

Hofmann, A., Dirks, P. H., & Jelsma, H. A. (2004). Shallowing-upward carbonate cycles in the Belingwe Greenstone Belt, Zimbabwe: a record of Archean sea-level oscillations. *Journal of Sedimentary Research*, *74*(1), 64-81.

Holland, H.D. (1973). The oceans: a possible source of iron in iron-formations. *Economic Geology*, 68, 1169–1172.

Holland, H. D. (1984). *The chemical evolution of the atmosphere and oceans*. Princeton University Press.

Holland, H. D. (2002). Volcanic gases, black smokers, and the Great Oxidation Event. *Geochimica et Cosmochimica Acta*, *66*(21), 3811-3826.

Huang C. (2018). Astronomical time scale for the Mesozoic. In *Stratigraphy & Timescales* (pp. 81–150).

Huang, C., Hinnov, L., Fischer, A. G., Grippo, A., & Herbert, T. (2010). Astronomical tuning of the Aptian Stage from Italian reference sections. *Geology*, *38*(10), 899-902.

Huang, Chunju, Tong, J., Hinnov, L., & Chen, Z. Q. (2011). Did the great dying of life take 700 k.y.?

Evidence from global astronomical correlation of the Permian-Triassic boundary interval. *Geology*, *39*(8), 779–782.

Ikeda, M., & Tada, R. (2013). Long period astronomical cycles from the triassic to jurassic bedded chert sequence (Inuyama, Japan); Geologic evidences for the chaotic behavior of solar planets. *Earth, Planets and Space*, *65*(4), 351–360.

Ikeda, M., & Tada, R. (2014). A 70 million year astronomical time scale for the deep-sea bedded chert sequence (Inuyama, Japan): Implications for Triassic-Jurassic geochronology. *Earth and Planetary Science Letters*, *399*, 30–43.

Ikeda, M., & Tada, R. (2020). Reconstruction of the chaotic behavior of the Solar System from geologic records. *Earth and Planetary Science Letters*, *537*, 116168.

Ikeda, M., Ozaki, K., & Legrand, J. (2020). Impact of 10-Myr scale monsoon dynamics on Mesozoic climate and ecosystems. *Scientific Reports*, *10*(1), 1–10.

Imbrie, J., Hays, J. D., Martinson, D. G., Mclntyre, A., Mix, A. C., Morley, J. J., Pisias, N. G., Prell and, W. L., & Shackleton, N. J. (1984). The orbital theory of pleistocene climate: support from a revised chronology of the marine O180 record. In *Milankovitch and Climate* (pp. 269–305).

Imbrie, J., Berger, A., Boyle, E. A., Clemens, S. C., Duffy, A., Howard, W. R., Kukla, G., Kutzbach, J., Martinson, D. G., Mcintyre, A., Mix, A. C., Morley, J. J., Peterson, L. C., Pisias, N. G., Prell, W. L., Raymo, M. E., Shackleton, N. J., & Lemaitre, G. (1993). On the structure and origin of major glaciation cycles 2. The 100,000-year cycle. *Paleoceanography and Paleoclimatology*, *8*(6), 699–735.

Isley, A. E. (1995). Hydrothermal plumes and the delivery of iron to banded iron formation. *The Journal of Geology*, *103*(2), 169-185.

James, H.L. (1954). Sedimentary facies of iron-formation. *Economic Geology*, 49, 235–293.

Jin, S., Deng, H., Zhu, X., Liu, Y., Liu, S., & Fu, M. (2020). Orbital control on cyclical organic matter accumulation in Early Silurian Longmaxi Formation shales. *Geoscience Frontiers*, *11*(2), 533-545

Johnson, C. M., Beard, B. L., & Roden, E. E. (2008). The Iron Isotope Fingerprints of Redox and Biogeochemical Cycling in Modern and Ancient Earth. *Annual Review of Earth and Planetary Sciences*, *36*(1), 457–493. h

Jones, C., Nomosatryo, S., Crowe, S. A., Bjerrum, C. J., & Canfield, D. E. (2015). Iron oxides, divalent cations, silica, and te early earth phosphorus crisis. *Geology*, *43*(2), 135-138.

Kasten, S., Zabel, M., Heuer, V., & Hensen, C. (2003). Processes and signals of nonsteady-state diagenesis in deep-sea sediments and their pore waters. In: *The South Atlantic in the Late Quaternary* (pp. 431-459). Springer, Berlin, Heidelberg.

Kendall, B., Creaser, R. A., Reinhard, C. T., Lyons, T. W., & Anbar, A. D. (2015). Transient episodes of mild environmental oxygenation and oxidative continental weathering during the late Archean. *Science advances*, *1*(10), e1500777.

Kendall, B., Reinhard, C. T., Lyons, T. W., Kaufman, A. J., Poulton, S. W., & Anbar, A. D. (2010). Pervasive oxygenation along late Archaean ocean margins. *Nature Geoscience*, *3*(9), 647–652.

Kepert, D. A. (2018). *The mapped stratigraphy and structure of the Mining Area C region, Hamersley Province*. Geological Survey of Western Australia, Report 185, 282 p.

Klatt, J. M., Chennu, A., Arbic, B. K., Biddanda, B. A., & Dick, G. J. (2021). Possible link between Earth's rotation rate and oxygenation. *Nature Geoscience*, *14*(8), 564-570.

Klein, C. (2005). Some Precambrian banded iron-formations (BIFs) from around the world:

Their age, geologic setting, mineralogy, metamorphism, geochemistry, and origins. *American Mineralogist*, *90*(10), 1473-1499.

Klein, C., & Beukes, N. J. (1989). Geochemistry and sedimentology of a facies transition from limestone to iron-formation deposition in the early Proterozoic Transvaal Supergroup, South Africa. *Economic Geology*, *84*(7), 1733-1774.

Kleine, T., Palme, H., Mezger, K., & Halliday, A. N. (2005). Hf-W chronometry of lunar metals and the age and early differentiation of the Moon. *Science*, *310*(5754), 1671-1674.

Knoll, A. H., & Swett, K. (1990). Carbonate deposition during the late Proterozoic Era: an example from Spitsbergen. *American Journal of Science*, *290*, 104-132.

Knoll, A. H., & Beukes, N. J. (2009). Introduction: Initial investigations of a Neoarchean shelf margin-basin transition (Transvaal Supergroup, South Africa). *Precambrian Research*, *169*(1–4), 1–14.

Koehler, M. C., Buick, R., Kipp, M. A., Stüeken, E. E., & Zaloumis, J. (2018). Transient surface ocean oxygenation recorded in the~ 2.66-Ga Jeerinah Formation, Australia. *Proceedings of the National Academy of Sciences*, *115*(30), 7711-7716.

Konhauser, K. O., Hamade, T., Raiswell, R., Morris, R. C., Ferris, F. G., Southam, G., & Canfield, D. E. (2002). Could bacteria have formed the Precambrian banded iron formations?. *Geology*, *30*(12), 1079-1082.

Konhauser, K. O., Lalonde, S. V., Planavsky, N. J., Pecoits, E., Lyons, T. W., Mojzsis, S. J., ... & Bekker, A. (2011). Aerobic bacterial pyrite oxidation and acid rock drainage during the Great Oxidation Event. *Nature*, *478*(7369), 369-373.

Konhauser, K. O., Planavsky, N. J., Hardisty, D. S., Robbins, L. J., Warchola, T. J., Haugaard, R., Lalonde, S. V., Partin, C. A., Oonk, P. B. H., Tsikos, H., Lyons, T. W., Bekker, A., & Johnson, C. M. (2017). Iron formations: A global record of Neoarchaean to Palaeoproterozoic environmental history. *Earth-Science Reviews*, *172*, 140–177.

Kostka, J. E., & Nealson, K. H. (1995). Dissolution and reduction of magnetite by bacteria. *Environmental Science & Technology*, *29*(10), 2535-2540.

Krapež, B., Barley, M. E., & Pickard, A. L. (2003). Hydrothermal and resedimented origins of the precursor sediments to banded iron formation: Sedimentological evidence from the Early Palaeoproterozoic Brockman Supersequence of Western Australia. *Sedimentology*, *50*(5), 979–1011.

Krogh, T. (1973). A low-contamination method for hydrothermal decomposition of zircon and extraction of U and Pb for isotopic age determinations. *Geochimica et Cosmochimica Acta, 37*(3), 485-494.

Kutzbach, J. E. (1994). Idealized Pangean climates: sensitivity to orbital change. *Geological Society of America Special Paper*, *288*, 41-56.

Kutzbach, J. E., Xiaodong, L., Zhengyu, L. & Guangshan, C. (2008). Simulation of the evolutionary response of global summer monsoons to orbital forcing over the past 280,000 years. *Climate Dynamics, 30*, 567–579.

Kuypers, M. M., Lourens, L. J., Rijpstra, W. I. C., Pancost, R. D., Nijenhuis, I. A., & Damsté, J. S. S. (2004). Orbital forcing of organic carbon burial in the proto-North Atlantic during oceanic anoxic event 2. *Earth and Planetary Science Letters*, *228*(3-4), 465-482.

Lambeck, K. (1080). *The Earth's Variable Rotation* (Cambridge University Press).

Lantink, M. L., Davies, J. H. F. L., Mason, P. R. D., Schaltegger, U., & Hilgen, F. J. (2019). Climate control on banded iron formations linked to orbital eccentricity. *Nature Geoscience*, *12*(5), 369–374.

Laskar, J. (1989). A numerical experiment on the chaotic behaviour of the solar system. *Nature*, *338*(6212), 237-238.

Laskar, J. (1990). The chaotic motion of the solar system: A numerical estimate of the size of the chaotic zones. *Icarus*, *88*(2), 266–291.

Laskar, J. (1993). Orbital, precessional, and insolation quantities for the Earth from-20 Myr to+ 10 Myr. *Astronomy and Astrophysics*, *270*, 522–533.

Laskar, J. (2020). Astrochronology. In *Geologic Time Scale 2020*.

Laskar, J., Robutel, P., Joutel, F., Gastineau, M., Correia, A. C. M., & Levrard, B. (2004). A long-term numerical solution for the insolation quantities of the Earth. *Astronomy and Astrophysics*, *428*(1), 261–285.

Laskar, J., Fienga, A., Gastineau, M., & Manche, H. (2011). La2010: A new orbital solution for the long term motion of the Earth. *Astronomy and Astrophysics*, *532*, A89.

Laurin, J., Meyers, S. R., Galeotti, S., & Lanci, L. (2016). Frequency modulation reveals the phasing of orbital eccentricity during Cretaceous Oceanic Anoxic Event II and the Eocene hyperthermals. *Earth and Planetary Science Letters*, *442*, 143-156.

Le Roux, J. P. (1997). Cycle hierarchy of a Neoproterozoic carbonate-siliciclastic shelf: Matjies River formation of the Kango Group, South Africa. *South African Journal of Geology*, *100*(1), 1-10.

Le Treut, H., & Ghil, M. (1983). Orbital forcing, climate interactions, and glaciation cycles. *Journal of Geophysical Research: Oceans*, *88*(C9), 5167–5190.

Lenstra, W. K., Egger, M., Van Helmond, N. A., Kritzberg, E., Conley, D. J., & Slomp, C. P. (2018). Large variations in iron input to an oligotrophic Baltic Sea estuary: impact on sedimentary phosphorus burial. *Biogeosciences*, *15*(22), 6979-6996.

Li, W., Beard, B. L., & Johnson, C. M. (2015). Biologically recycled continental iron is a major component in banded iron formations. *Proceedings of the National Academy of Sciences*, *112*(27), 8193-8198.

Li, M., Hinnov, L., & Kump, L. (2019). Acycle: Time-series analysis software for paleoclimate research and education. *Computers and Geosciences*, *127*(September 2018), 12–22.

Liebrand, D., De Bakker, A.T.M., Beddow, H.M., Wilson, P.A., Bohaty, S.M., Ruessink, G., Pälike, H., Batenburg, S.J., Hilgen, F.J., Hodell, D.A., Huck, C.E., Kroon, D., Raffi, I., Saes, M.J.M., Van Dijk, A.E., and Lourens, L.J. (2017). Evolution of the early antarctic ice ages. *Proceedings of the National Academy of Sciences of the United States of America*, 114(15).

Littler, K., Röhl, U., Westerhold, T., and Zachos, J.C. (2014). A high-resolution benthic stable-isotope record for the South Atlantic: Implications for orbital-scale changes in late Paleocene-early Eocene climate and carbon cycling. *Earth and Planetary Science Letters*, 401, 18-30.

Lomb, N. R. (1976). Least-squares frequency analysis of unequally spaced data. *Astrophysics and Space Science*, *39*(2), 447–462.

Lourens, L. J., Antonarakou, A., Hilgen, F. J., Hoof, A. A. M. Van, & Zachariasse, W. J. (1996). Evaluation of the Plio-Pleistocene astronomical timescale. *Paleoceanography*, *11*(4), 391–413.

Lourens, L. J., Wehausen, R., & Brumsack, H. J. (2001). Geological constraints on tidal dissipation and dynamical ellipticity of the Earth over the past three million years. *Nature*, *409*(6823), 1029-1033.

Lourens, L. J., Sluijs, A., Kroon, D., Zachos, J. C., Thomas, E., Röhl, U., ... & Raffi, I. (2005). Astronomical pacing of late Palaeocene to early Eocene global warming events. *Nature*, *435*(7045), 1083-1087.

Lovley, D. R. (1991). Magnetite formation during microbial dissimilatory iron reduction. In *Iron* *biominerals* (pp. 151-166). Springer, Boston, MA.

Lovley, D. R., & Phillips, E. J. (1986). Availability of ferric iron for microbial reduction in bottom sediments of the freshwater tidal Potomac River. *Applied and Environmental Microbiology*, *52*(4), 751-757.

Lovley, D. R., Stolz, J. F., Nord, G. L., & Phillips, E. J. (1987). Anaerobic production of magnetite by a dissimilatory iron-reducing microorganism. *Nature*, *330*(6145), 252-254.

Lyons, T. W., Reinhard, C. T., & Planavsky, N. J. (2014). The rise of oxygen in Earth's early ocean and atmosphere. *Nature*, *506*(7488), 307-315.

Ma, C., Meyers, S. R., & Sageman, B. B. (2017). Theory of chaotic orbital variations confirmed by Cretaceous geological evidence. *Nature*, *542*(7642), 468–470.

Ma, K., Li, R., Hinnov, L. A., & Gong, Y. (2019). Conodont biostratigraphy and astronomical tuning of the Lower–Middle Ordovician Liangjiashan (North China) and Huanghuachang (South China) marine sections. *Palaeogeography, Palaeoclimatology, Palaeoecology*, *528*(May), 272–287.

Ma, C., Meyers, S. R., & Sageman, B. B. (2019). Testing Late Cretaceous astronomical solutions in a 15 million year astrochronologic record from North America. *Earth and Planetary Science Letters*, *513*, 1-11.

Marino, M., Maiorano, P., Lirer, F., & Pelosi, N. (2009). Response of calcareous nannofossil assemblages to paleoenvironmental changes through the mid-Pleistocene revolution at Site 1090 (Southern Ocean). *Palaeogeography, Palaeoclimatology, Palaeoecology*, *280*(3–4), 333–349.

Martin, D. M., Clendenin, C. W., Krapez, B., & McNaughton, N. J. (1998). Tectonic and geochronological constraints on late Archaean and Palaeoproterozoic stratigraphic correlation within and between the Kaapvaal and Pilbara Cratons. *Journal of the Geological Society*, *155*(2), 311-322.

Martinez, M., & Dera, G. (2015). Orbital pacing of carbon fluxes by a ~9-My eccentricity cycle during the Mesozoic. *Proceedings of the National Academy of Sciences*, *112*(41), 12604–12609.

Mattinson, J. M. (2005). Zircon U–Pb chemical abrasion ("CA-TIMS") method: combined annealing and multi-step partial dissolution analysis for improved precision and accuracy of zircon ages. *Chemical Geology, 220*(1-2), 47-66.

McLean, N. M., Condon, D. J., Schoene, B., & Bowring, S. A. (2015). Evaluating uncertainties in the calibration of isotopic reference materials and multi-element isotopic tracers (EARTHTIME Tracer Calibration Part II). *Geochimica et Cosmochimica Acta, 164*, 481-501.

McLean, N. M., Bowring, J. F., & Bowring, S. A. (2011). An algorithm for U-Pb isotope dilution data reduction and uncertainty propagation. *Geochemistry, Geophysics, Geosystems*, *12*(6).

McLean, N. M., Condon, D. J., Schoene, B., & Bowring, S. A. (2015). Evaluating uncertainties in the calibration of isotopic reference materials and multi-element isotopic tracers (EARTHTIME Tracer Calibration Part II). *Geochimica et Cosmochimica Acta*, *164*, 481-501.

Meyers, S. R., Sageman, B. B., & Hinnov, L. A. (2001). Integrated quantitative stratigraphy of the Cenomanian-Turonian Bridge Creek Limestone Member using evolutive harmonic analysis and stratigraphic modeling. *Journal of Sedimentary Research, 71*(4), 628-644.

Meyers, S. R. (2012). Seeing red in cyclic stratigraphy: Spectral noise estimation for astrochronology. *Paleoceanography*, *27*(3), 1–12.

Meyers, S. R. (2014). *An R package for astrochronology. Available at cran.rproject.org/web/packages/ astrochron/index.html.*

Meyers, S.R., Sageman, B.B., and Pagani, M. (2008). Resolving Milankovitch: Consideration of signal and noise. *American Journal of Science*, 308, 770–786.

Meyers, S.R., Siewert, S.E., Singer, B.S., Sageman, B.B., Condon, D.J., Obradovich, J.D., Jicha, B.R., and Sawyer, D.A. (2012a). Intercalibration of radioisotopic and astrochronologic time scales for the Cenomanian-Turonian boundary interval, Western Interior Basin, USA. *Geology*, 40, 7–10.

Meyers, S. R., Sageman, B. B., & Arthur, M. A. (2012b). Obliquity forcing of organic matter accumulation during Oceanic Anoxic Event 2. *Paleoceanography*, *27*(3).

Meyers, S. R., & Malinverno, A. (2018). Proterozoic Milankovitch cycles and the history of the solar system. *Proceedings of the National Academy of Sciences*, *115*(25), 6363-6368.

Meysman, F. J., Boudreau, B. P., & Middelburg, J. J. (2005). Modeling reactive transport in sediments subject to bioturbation and compaction. *Geochimica et Cosmochimica Acta*, *69*(14), 3601-3617.

Middelburg, J. J., Soetaert, K., & Hagens, M. (2020). Ocean alkalinity, buffering and biogeochemical processes. *Reviews of Geophysics*, *58*(3), e2019RG000681.

Milankovitch, M. (1941). *Kanon der Erdbestrahlung und seine Anwendung auf das Eiszeiten-problem*. Royal Serbian Academy, Belgrade (pp. 633).

Milankovitch, M. (1920). *Théorie mathématique des phénomènes thermiques produits par la radiation solaire*. Gauthier-Villars, Paris (pp. 338).

Mingxiang, M., & Tucker, M. E. (2013). Milankovitch-driven cycles in the Precambrian of China: the Wumishan formation. *Journal of Palaeogeography*, *2*(4), 369-389.

Mitchell, R. N., Bice, D. M., Montanari, A., Cleaveland, L. C., Christianson, K. T., Coccioni, R., & Hinnov, L. A. (2008). Oceanic anoxic cycles? Orbital prelude to the Bonarelli Level (OAE 2). *Earth and Planetary Science Letters*, *267*(1-2), 1-16.

Mitchell, R. N., Gernon, T. M., Cox, G. M., Nordsvan, A. R., Kirscher, U., Xuan, C., ... & He, X. (2021a). Orbital forcing of ice sheets during snowball Earth. *Nature Communications*, *12*(1), 1-9.

Mitchell, R. N., Kirscher, U., Kunzmann, M., Liu, Y., & Cox, G. M. (2021b). Gulf of Nuna: Astrochronologic correlation of a Mesoproterozoic oceanic euxinic event. *Geology*, *49*(1), 25-29.

Morris, R. C. (1993). Genetic modelling for banded iron-formation of the Hamersley Group, Pilbara Craton, Western Australia. *Precambrian Research*, *60*(1-4), 243-286.

Morris, R. C., & Horwitz, R. C. (1983). The origin of the iron-formation-rich Hamersley Group of Western Australia—deposition on a platform. *Precambrian Research*, *21*(3-4), 273-297.

Munk, W. (1968). Once again-tidal friction. *Quarterly Journal of the Royal Astronomical Society*, *9*, 352.

Næraa, T., Scherstén, A., Rosing, M.T., Kemp, A.I.S., Hoffmann, J.E., Kokfelt, T.F., and Whitehouse, M.J. (2012). Hafnium isotope evidence for a transition in the dynamics of continental growth 3.2 Gyr ago. *Nature*, 485(7400), 627-630.Nelson, D. R., Trendall, A. F., & Altermann, W. (1999). Chronological correlations between the Pilbara and Kaapvaal cratons. *Precambrian Research*, *97*(3–4), 165–189.

Noorbergen, L. J., Abels, H. A., Hilgen, F. J., Robson, B. E., de Jong, E., Dekkers, M. J., Krijgsman, W., Smit, J., Collinson, M. E., and Kuiper, K. F. (2018). Conceptual models for short-eccentricity-scale climate control on peat formation in a lower Palaeocene fluvial system, north-eastern Montana (USA). *Sedimentology*, 65(3), 775-808.

Olsen, P. E. (2001). Grand cycles of the Milankovitch band. *AGU Fall Meeting*, U11A-11.

Olsen, P. E., & Kent, D. V. (1996). Milankovitch climate forcing in the tropics of Pangaea during the Late Triassic. *Palaeogeography, Palaeoclimatology, Palaeoecology*, *122*(1-4), 1-26.

Olsen, P. E., & Kent, D. V. (1999). Long-period Milankovitch cycles from the Late Triassic and Early Jurassic of eastern North America and their implications for the calibration of the Early Mesozoic time-scale and the long-term behaviour of the planets. *Philosophical Transactions of the Royal Society A: Mathematical, Physical and Engineering Sciences*, *357*(1757), 1761–1786.

Olsen, Paul E., Laskar, J., Kent, D. V., Kinney, S. T., Reynolds, D. J., Sha, J., & Whiteside, J. H. (2019). Mapping solar system chaos with the geological orrery. *Proceedings of the National Academy of Sciences of the United States of America*, *166*(22), 10664–10673.

Oonk P. B. H. ((2016). *Fraction-Specifc Geochemistry across the Asbestos Hills BIF of the Transvaal Supergroup, South Africa: Implications for the Origin of BIF and the History of Atmospheric Oxygen*. PhD thesis, Rhodes University 1–209.

Oonk, P. B., Tsikos, H., Mason, P. R., Henkel, S., Staubwasser, M., Fryer, L., ... & Williams, H. M. (2017). Fraction-specific controls on the trace element distribution in iron formations: Implications for trace metal stable isotope proxies. *Chemical Geology*, *474*, 17-32.

Ostrander, C. M., Nielsen, S. G., Owens, J. D., Kendall, B., Gordon, G. W., Romaniello, S. J., & Anbar, A. D. (2019). Fully oxygenated water columns over continental shelves before the Great Oxidation Event. *Nature geoscience*, *12*(3), 186-191.

Pälike, H. (2001). *Extending the astronomical calibration of the geological time scale*. PhD Thesis.

Pälike, H., & Shackleton, N. J. (2000). Constraints on astronomical parameters from the geological record for the last 25 Myr. *Earth and Planetary Science Letters*, *182*(1), 1-14.

Passier, H. F., Middelburg, J. J., van Os, B. J., & de Lange, G. J. (1996). Diagenetic pyritisation under eastern Mediterranean sapropels caused by downward sulphide diffusion. *Geochimica et Cosmochimica Acta*, *60*(5), 751-763.

Perry, E. C., Tan, F. C., & Morey, G. B. (1973). Geology and stable isotope geochemistry of the Biwabik Iron Formation, northern Minnesota. *Economic Geology*, *68*(7), 1110-1125.

Petit, J.R., et al. (1999). Climate and Atmospheric History of the Past 420,000 Years from the Vostok Ice Core, Antarctica. *Nature*, 399, 429-436.

Petzold, L. (1983). Automatic selection of methods for solving stiff and nonstiff systems of ordinary differential equations. *SIAM journal on scientific and statistical computing*, *4*(1), 136-148.

Pickard, A. L. (2002). SHRIMP U–Pb zircon ages of tuffaceous mudrocks in the Brockman Iron Formation of the Hamersley Range, Western Australia. *Australian Journal of Earth Sciences*, *49*(3), 491-507.

Pickard, A. L. (2003). SHRIMP U-Pb zircon ages for the Palaeoproterozoic Kuruman Iron Formation, Northern Cape Province, South Africa: Evidence for simultaneous BIF deposition on Kaapvaal and Pilbara Cratons. *Precambrian Research*, *125*(3–4), 275–315.

Pickard, A. L., Barley, M. E., & Krapež, B. (2004). Deep-marine depositional setting of banded iron formation: Sedimentological evidence from interbedded clastic sedimentary rocks in the early Palaeoproterozoic Dales Gorge Member of Western Australia. *Sedimentary Geology*, *170*(1–2), 37–92.

Planavsky, N. J., Rouxel, O. J., Bekker, A., Lalonde, S. V., Konhauser, K. O., Reinhard, C. T., & Lyons, T. W. (2010). The evolution of the marine phosphate reservoir. *Nature*, *467*(7319), 1088-1090.

Pollard, D., & DeConto, R. M. (2009). Modelling West Antarctic ice sheet growth and collapse through the past five million years. *Nature*, *458*(7236), 329-332.

Posth, N. R., Hegler, F., Konhauser, K. O., & Kappler, A. (2008). Alternating Si and Fe deposition caused by temperature fluctuations in Precambrian oceans. *Nature Geoscience*, *1*(10), 703-708.

Postma, G., Hilgen, F. J., & Zachariasse, W. J. (1993). Precession-punctuated growth of a late Miocene submarine-fan lobe on Gavdos (Greece). *Terra Nova*, *5*(5), 438–444.

Potts, P. J., Williams-Thorpe, O., & Webb, P. C. (1997). The bulk analysis of silicate rocks by portable X-ray fluorescence: effect of sample mineralogy in relation to the size of the excited volume. *Geostandards Newsletter*, *21*(1), 29-41.

Poulton, S. W., & Canfield, D. E. (2011). Ferruginous conditions: a dominant feature of the ocean through Earth's history. *Elements*, *7*(2), 107-112.

Poulton, S. W., Bekker, A., Cumming, V. M., Zerkle, A. L., Canfield, D. E., & Johnston, D. T. (2021). A 200-million-year delay in permanent atmospheric oxygenation. *Nature*, *592*(7853), 232-236.

Rasmussen, B., Meier, D. B., Krapež, B., & Muhling, J. R. (2013). Iron silicate microgranules as precursor sediments to 2.5-billion-year-old banded iron formations. *Geology*, *41*(4), 435-438.

Rasmussen, B., Krapež, B., & Muhling, J. R. (2015). Seafloor silicification and hardground development during deposition of 2.5 Ga banded iron formations. *Geology*, *43*(3), 235-238.

Raymo, M. E., & Nisancioglu, K. (2003). The 41 kyr world: Milankovitch's other unsolved mystery. *Paleoceanography*, *18*(1), 1–6.

Redfield, A. C. (1934). *On the proportions of organic derivatives in sea water and their relation to the composition of plankton* (Vol. 1). Liverpool: University Press of Liverpool.

Reed, D. C., Slomp, C. P., & Gustafsson, B. G. (2011). Sedimentary phosphorus dynamics and the evolution of bottom-water hypoxia: A coupled benthic–pelagic model of a coastal system. *Limnology and Oceanography*, *56*(3), 1075-1092.

Reichart, G. J., Lourens, L. J., & Zachariasse, W. J. (1998). Temporal variability in the northern Arabian Sea oxygen minimum zone (OMZ) during the last 225,000 years. *Paleoceanography*, *13*(6), 607-621.

Reinhard, C. T., Planavsky, N. J., Gill, B. C., Ozaki, K., Robbins, L. J., Lyons, T. W., ... & Konhauser, K. O. (2017). Evolution of the global phosphorus cycle. *Nature*, *541*(7637), 386-389.

Reinhard, C. T., & Planavsky, N. J. (2020). Biogeochemical controls on the redox evolution of Earth's oceans and atmosphere. *Elements: An International Magazine of Mineralogy, Geochemistry, and Petrology*, *16*(3), 191-196.

Reinhardt, L. & Ricken, W. Te stratigraphic and geochemical record of Playa Cycles: monitoring a Pangaean monsoon-like system (Triassic, Middle Keuper, S. Germany). Palaeogeogr. Palaeoclimatol. Palaeoecol. 161, 205–227 (2000)

Ripepe, M., & Fischer, A. G. (1991). Stratigraphic rhythms synthesized from orbital variations. *Kansas Geological Survey Bulletin*, *233*, 335–344.

Robbins, L. J., Funk, S. P., Flynn, S. L., Warchola, T. J., Li, Z., Lalonde, S. V., ... & Konhauser, K. O. (2019). Hydrogeological constraints on the formation of Palaeoproterozoic banded iron formations. *Nature Geoscience*, *12*(7), 558-563.

Robbins, L. J., Funk, S. P., Flynn, S. L., Warchola, T. J., Li, Z., Lalonde, S. V., ... & Konhauser, K. O. (2019). Hydrogeological constraints on the formation of Palaeoproterozoic banded iron formations. *Nature Geoscience*, *12*(7), 558-563.

Röhling, E.J., Marino, G., and Grant, K.M. (2015). Mediterranean climate and oceanography, and the periodic development of anoxic events (sapropels). *Earth-Science Reviews, 143*, 62-97.

Rooney, A.D., Strauss, J.V., Brandon, A.D., and Macdonald, F.A. (2015). A Cryogenian chronology: Two long-lasting synchronous Neoproterozoic glaciations. *Geology*, 43(5), 459-462.

Rossignol-Strick, M. (1983). Mediterranean Quaternary sapropels, an immediate climatic response to orbital insolation. *Nature, 303*, 46-49, 1983.

Ruddiman, W. F. (2001). *Earth's Climate: past and future*. Macmillan.

Ruddiman, W. F., Raymo, M. E., Martinson, D. G., & Backman, J. (1989). Pleistocene evolution: northern hemisphere ice sheets and North Atlantic Ocean. *Paleoceanography*, *4*(4), 353–412.

Ruttenberg, K. C., & Berner, R. A. (1993). Authigenic apatite formation and burial in sediments from non-upwelling, continental margin environments. *Geochimica et cosmochimica acta*, *57*(5), 991-1007.

Scargle, J. D. (1982). Studies in astronomical time series analysis. II-Statistical aspects of spectral analysis of unevenly spaced data. *The Astrophysical Journal*, *263*, 835–853.

Schad, M., Halama, M., Bishop, B., Konhauser, K. O., & Kappler, A. (2019). Temperature fluctuations in the Archean ocean as trigger for varve-like deposition of iron and silica minerals in banded iron formations. *Geochimica et Cosmochimica Acta*, *265*, 386-412.

Schaltegger, U., Ovtcharova, M., Gaynor, S. P., Schoene, B., Wotzlaw, J. F., Davies, J. F., ... & Chelle-Michou, C. (2021). Long-term repeatability and interlaboratory reproducibility of high-precision ID-TIMS U–Pb geochronology. *Journal of analytical atomic spectrometry*, *36*(7), 1466-1477.

Sexton, P. F., Norris, R. D., Wilson, P. A., Pälike, H., Westerhold, T., Röhl, U., Bolton, C. T., & Gibbs, S. (2011). Eocene global warming events driven by ventilation of oceanic dissolved organic carbon. *Nature*, *471*(7338), 349–353.

Shackleton, N. J., & Opdyke, N. D. (1973). Oxygen isotope and palaeomagnetic stratigraphy of Equatorial Pacific core V28-238: Oxygen isotope temperatures and ice volumes on a 105 year and 106 year scale. *Quaternary research*, *3*(1), 39-55.

Short, D. A., Mengel, J. G., Crowley, T. J., Hyde, W. T., & North, G. R. (1991). Filtering of Milankovitch cycles by Earth's geography. *Quaternary Research*, *35*(2), 157–173.

Siever, R. (1992). The silica cycle in the Precambrian. *Geochimica et Cosmochimica Acta*, *56*(8), 3265-3272.

Simonson, B. M., & Hassler, S. W. (1996). Was the deposition of large Precambrian iron formations linked to major marine transgressions?. *The Journal of Geology*, *104*(6), 665-676.

Simonson, B. M., Sumner, D. Y., Beukes, N. J., Johnson, S., & Gutzmer, J. (2009). Correlating multiple Neoarchean-Paleoproterozoic impact spherule layers between South Africa and Western Australia. *Precambrian Research*, *169*(1–4), 100–111.

Sinnesael, M., McLaughlin, P. I., Desrochers, A., Mauviel, A., Weirdt, J. De, Claeys, P., & Vandenbroucke, T. R. A. (2021). Precession-driven climate cycles and time scale prior to the Hirnantian glacial maximum. *Geology*, *49*(11), 1295–1300.

Slomp, C. P., Epping, E. H., Helder, W., & Raaphorst, W. V. (1996). A key role for iron-bound phosphorus in authigenic apatite formation in North Atlantic continental platform sediments. *Journal of marine Research*, *54*(6), 1179-1205.

Soetaert, K., Petzoldt, T., & Setzer, R. W. (2010). Package deSolve: solving initial value differential equations in R. *Journal of Statistical Software*, *33*(9), 1-25.

Soetaert, K., Cash, J., & Mazzia, F. (2012). *Solving differential equations in R*. Springer Science & Business

Media.

Sonett, C. P., Zakharian, A., & Kvale, E. P. (1996). Ancient tides and length of day: Correction. *Science*, *274*(5290), 1068-1069.

Sonett, C. P., & Chan, M. A. (1998). Neoproterozoic Earth-Moon dynamics: Rework of the 900 Ma Big Cottonwood Canyon tidal laminae. *Geophysical Research Letters*, *25*(4), 539-542.

Söderlund, U., & Johansson, L. (2002). A simple way to extract baddeleyite (ZrO2). *Geochemistry, Geophysics, Geosystems, 3*(2), 1-of.

Sørensen, A. L., Nielsen, A. T., Thibault, N., Zhao, Z., Schovsbo, N. H., & Dahl, T. W. (2020). Astronomically forced climate change in the late Cambrian. *Earth and Planetary Science Letters*, *548*, 116475.

Spang, A., Stairs, C.W., Dombrowski, N., Eme, L., Lombard, J., Caceres, E.F., Greening, C., Baker, B.J., and Ettema, T.J.G. (2019). Proposal of the reverse flow model for the origin of the eukaryotic cell based on comparative analyses of asgard archaeal metabolism. *Nature Microbiology*, 4(7), 1138-1148.

Sproson, A. D. (2020). Pacing of the latest Ordovician and Silurian carbon cycle by a ~4.5 Myr orbital cycle. *Palaeogeography, Palaeoclimatology, Palaeoecology*, *540*, 109543.

Sprovieri, M., Sabatino, N., Pelosi, N., Batenburg, S. J., Coccioni, R., Iavarone, M., & Mazzola, S. (2013). Late cretaceous orbitally-paced carbon isotope stratigraphy from the bottaccione gorge (Italy). *Palaeogeography, Palaeoclimatology, Palaeoecology*, *379–380*, 81–94.

Sumner, D. Y., & Grotzinger, J. P. (1996). Were kinetics of Archean calcium carbonate precipitation related to oxygen concentration?. *Geology*, *24*(2), 119-122.

Sun, S., Konhauser, K. O., Kappler, A., & Li, Y. L. (2015). Primary hematite in Neoarchean to Paleoproterozoic oceans. *Bulletin*, *127*(5-6), 850-861.

Thomson, D. J. (1982). Spectrum Estimation and Harmonic Analysis. *Proceedings of the IEEE*, *70*(9), 1055–1096.

Timmermann, A., and Friedrich, T. (2016). Late Pleistocene climate drivers of early human migration. *Nature*, 538(7623), 92–95.

Touboul, M., Kleine, T., Bourdon, B., Palme, H., & Wieler, R. (2007). Late formation and prolonged differentiation of the Moon inferred from W isotopes in lunar metals. *Nature*, *450*(7173), 1206-1209.

Trendall, A. F. (1968). Three Great Basins of Precambrian Banded Iron Formation Deposition: A Systematic Comparison. *Geological Society of America Bulletin*, *79*(11), 1527–1544.

Trendall, A. F. (1969). The Joffre Member in the gorges south of Wittenoom. *Geological Survey of Western Australia Annual Report for 1968*, 53-57.

Trendall, A. F. (1972). Revolution in earth history: Presidential address delivered in Brisbane on 25 May 1971. *Journal of the Geological Society of Australia*, *19*(3), 287-311.

Trendall, A. F. (1973). Varve cycles in the Weeli Wolli Formation of the Precambrian Hamersley Group, Western Australia. *Economic Geology*, *68*(7), 1089-1097.

Trendall, A. F. (2002). The significance of iron-formation in the Precambrian stratigraphic record. *Precambrian sedimentary environments: A modern approach to ancient depositional systems*, 33-66.

Trendall, A. F., & Blockley, J. G. (1968). Stratigraphy of the Dales Gorge Member of the Brockman Iron Formation in the Precambrian Hamersley Group of Western Australia. In *Geological Survey of Western Australia Annual Report for 1967* (pp. 48–53).

Trendall, A. F., & Blockley, J. B. (1970). *The iron formations of the Precambrian Hamersley Group, Western Australia with special reference to the associated crocidolite* (Vol. 119). Geological Survey of Western Australia.

Trendall, A. F., Nelson, D. R., Thorne, A. M., Compston, W., Williams, I. S., & Armstrong, R. A. (1990). Precise zircon U-Pb chronological comparison of the volcano-sedimentary sequences of the Kaapvaal and Pilbara Cratons between about 3.1 and 2.4 Ga. In *Third international Archaean symposium*, Perth, 1990.

Trendall, A. F., Nelson, D. R., De Laeter, J. R., & Hassler, S. W. (1998). Precise zircon U-Pb ages from the Marra Mamba Iron Formation and Wittenoom Formation, Hamersley Group, Western Australia. *Australian Journal of Earth Sciences, 45*(1), 137-142.

Trendall, A. F., Compston, W., Nelson, D. R., De Laeter, J. R., & Bennett, V. C. (2004). SHRIMP zircon ages constraining the depositional chronology of the Hamersley Group, Western Australia. *Australian Journal of Earth Sciences*, *51*(5), 621–644.

Tsikos, H., Matthews, A., Erel, Y., & Moore, J. M. (2010). Iron isotopes constrain biogeochemical redox cycling of iron and manganese in a Palaeoproterozoic stratified basin. *Earth and Planetary Science Letters, 298*(1-2), 125-134.

Tuenter, E., Weber, S. L., Hilgen, F. J., & Lourens, L. J. (2003). The response of the African summer monsoon to remote and local forcing due to precession and obliquity. *Global and Planetary Change*, *36*(4), 219–235.

Tyrrel, T. (1999). The relative influences of nitrogen and phosphorus on oceanic primary production. Nature, 400, 525-531.

Tzedakis, P. C., Hooghiemstra, H., & Pälike, H. (2006). The last 1.35 million years at Tenaghi Philippon: Revised chronostratigraphy and long-term vegetation trends. *Quaternary Science Reviews*, 25(23-24), 3416-3430.

van Dam, J.A., Abdul Aziz, H., Sierra, M.A.A., Hilgen, F.J., van den Hoek Ostende, L.W., Lourens, L.J., Mein, P., van der Meulen, A.J., and Pelaez-Campomanes, P. (2006). Long-period astronomical forcing of mammal turnover. *Nature*, 443(7112), 687-691.

van de Velde, S. J., Reinhard, C. T., Ridgwell, A., & Meysman, F. J. (2020). Bistability in the redox chemistry of sediments and oceans. *Proceedings of the National Academy of Sciences*, *117*(52), 33043-33050.

van der Laan, E., Hilgen, F. J., Lourens, L. J., de Kaenel, E., Gaboardi, S., & Iaccarino, S. (2012). Astronomical forcing of Northwest African climate and glacial history during the late Messinian (6.5-5.5Ma). *Palaeogeography, Palaeoclimatology, Palaeoecology*, *313–314*, 107–126.

van Hoof, A. A. M., van Os, B. J. H., Rademakers, J. G., Langereis, C. G., & De Lange, G. J. (1993). A paleomagnetic and geochemical record of the upper Cochiti reversal and two subsequent precessional cycles from southern Sicily (Italy). *Earth and planetary science letters*, *117*(1-2), 235-250.

van Os, B. J. H., Lourens, L. J., Hilgen, F. J., De Lange, G. J., & Beaufort, L. (1994). The formation of Pliocene sapropels and carbonate cycles in the Mediterranean: diagenesis, dilution, and productivity. *Paleoceanography*, *9*(4), 601-617.

Vaughan, S., Bailey, R. J., & Smith, D. G. (2011). Detecting cycles in stratigraphic data: Spectral analysis in the presence of red noise. *Paleoceanography*, *26*(4).

Viehmann, S., Bau, M., Hofmann, J. E. & Münker, C. Geochemistry of the Krivoy Rog Banded Iron

Formation, Ukraine, and the impact of peak episodes of increased global magmatic activity on the trace element composition of Precambrian seawater. Precambrian Res. 270, 165–180 (2015).

Von Dobeneck, T., & Schmieder, F. (1999). Using Rock Magnetic Proxy Records for Orbital Tuning and Extended Time Series Analyses into the Super- and Sub-Milankovitch Bands. In *Use of Proxies in Paleoceanography: Examples from the South Atlantic* (pp. 601–633).

Walker, J. C., & Zahnle, K. J. (1986). Lunar nodal tide and distance to the Moon during the Precambrian. *Nature*, *320*(6063), 600-602.

Waltham, D. (2015). Milankovitch Period Uncertainties and Their Impact On Cyclostratigraphy. *Journal of Sedimentary Research*, *85*(8), 990–998.

Wang, Y., & van Cappellen, P. (1996). A multicomponent reactive transport model of early diagenesis: Application to redox cycling in coastal marine sediments. *Geochimica et Cosmochimica Acta*, *60*(16), 2993-3014.

Wang, Y., Cheng, H., Edwards, R. L., Kong, X., Shao, X., Chen, S., Wu, J., Jiang, X.,Wang, X., and An, Z. (2008). Millennial- and orbital-scale changes in the east Asian monsoon over the past 224,000 years. *Nature*, 451(7182), 1090-1093.

Warke, M. R., Di Rocco, T., Zerkle, A. L., Lepland, A., Prave, A. R., Martin, A. P., ... & Claire, M. W. (2020). The great oxidation event preceded a paleoproterozoic "snowball Earth". *Proceedings of the National Academy of Sciences*, *117*(24), 13314-13320.

Webb, D. J. (1982). Tides and the evolution of the Earth—Moon system. *Geophysical Journal International*, *70*(1), 261-271.

Weedon, G. P. (2003). *Time-series analysis and cyclostratigraphy: examining stratigraphic records of environmental cycles* (pp. 129 - 160).

Wehausen, R., & Brumsack, H. J. (2000). Chemical cycles in Pliocene sapropel-bearing and sapropel-barren eastern Mediterranean sediments. *Palaeogeography, Palaeoclimatology, Palaeoecology*, *158*(3-4), 325-352.

Weltje, G., & De Boer, P. L. (1993). Astronomically induced paleoclimatic oscillations reflected in Pliocene turbidite deposits on Corfu (Greece): Implications for the interpretation of higher order cyclicity in ancient turbidite systems. *Geology*, *21*(4), 307–310.

Weltje, G. J., Bloemsma, M. R., Tjallingii, R., Heslop, D., Röhl, U., & Croudace, I. W. (2015). Prediction of geochemical composition from XRF core scanner data: a new multivariate approach including automatic selection of calibration samples and quantification of uncertainties. In *Micro-XRF studies of sediment cores* (pp. 507-534). Springer, Dordrecht.

Westerhold, A. T., Marwan, N., Drury, A. J., Liebrand, D., Agnini, C., Anagnostou, E., Barnet, J. S. K., Bohaty, S. M., De, D., Florindo, F., Frederichs, T., Hodell, D. A., Holbourn, A. E., Kroon, D., Lauretano, V., Littler, K., Lourens, L. J., & Lyle, M. (2020). An astronomically dated record of Earth ' s climate and its predictability over the last 66 Million Years. *Science*, *369*(6509), 1383–1387.

Westphal, H., Böhm, F., & Bornholdt, S. (2004). Orbital frequencies in the carbonate sedimentary record: Distorted by diagenesis? *Facies*, *50*(1), 3–11.

Widmann, P., Davies, J. H. F. L., & Schaltegger, U. (2019). Calibrating chemical abrasion: Its effects on zircon crystal structure, chemical composition and UPb age. *Chemical Geology*, *511*, 1-10.

Widmann, P., Bucher, H., Leu, M., Schneebeli-Hermann, E., Goudemand, N., Bagherpour, B., & Schaltegger, U. (2019). What triggered the largest Early Triassic extinction? Potential causes for end-

Smithian extinction inferred from a new U/Pb-CA-ID-TIMS calibration. In *Geophysical Research Abstracts* (Vol. 21).

Williams, G. E. (2005). Comment on "Tidal rhythmites and their implications" by R. Mazumder and M. Arima [Earth-Science Reviews, 69 (2005) 79–95]. *Earth-Science Reviews*, *72*(1-2), 113-117.

Williams, G. E. (2000). Geological constraints on the Precambrian history of Earth's rotation and the Moon's orbit. Reviews of Geophysics, 38(1), 37-59.

Williams, J. G., & Boggs, D. H. (2016). Secular tidal changes in lunar orbit and Earth rotation. *Celestial Mechanics and Dynamical Astronomy*, *126*(1), 89-129.

Williams, G. E. (1989). Late Precambrian tidal rhythmites in South Australia and the history of the Earth's rotation. *Journal of the Geological Society, 146*(1), 97-111.

Williams, G. E., Gostin, V. A., McKirdy, D. M., & Preiss, W. V. (2008). The Elatina glaciation, late Cryogenian (Marinoan epoch), South Australia: sedimentary facies and palaeoenvironments. *Precambrian Research*, *163*(3-4), 307-331.

Wu, H., Zhang, S., Hinnov, L. A., Jiang, G., Feng, Q., Li, H., & Yang, T. (2013). Time-calibrated Milankovitch cycles for the late Permian. *Nature Communications*, *4*, 2452.

Zachos, J. C., McCarren, H., Murphy, B., Röhl, U., & Westerhold, T. (2010). Tempo and scale of late Paleocene and early Eocene carbon isotope cycles: Implications for the origin of hyperthermals. *Earth and Planetary Science Letters*, *299*(1–2), 242–249.

Zahnle, K., & Walker, J. C. (1987). A constant daylength during the Precambrian era?. *Precambrian Research*, *37*(2), 95-105.

Zeebe, L. J. Lourens, Solar System chaos and the Paleocene–Eocene boundary age constrained by geology and astronomy. *Science (80-.).* **365**, 926–929 (2019).

Zeebe, R. E. (2017). Numerical Solutions for The Orbital Motion of The Solar System Over The Past 100 Myr: Limits and New Results. *ArXiv*, *154*(5), 193.

Zeebe, R. E., & Lourens, L. J. (2019). Solar System chaos and the Paleocene–Eocene boundary age constrained by geology and astronomy. *Science*, *365*(6456), 926–929.

Zeeden, C., Hilgen, F. J., Hüsing, S. K., & Lourens, L. L. (2014). The Miocene astronomical time scale 9–12 Ma: New constraints on tidal dissipation and their implications for paleoclimatic investigations. *Paleoceanography*, *29*(4), 296-307.

Zerkle, A. L., Poulton, S. W., Newton, R. J., Mettam, C., Claire, M. W., Bekker, A., & Junium, C. K. (2017). Onset of the aerobic nitrogen cycle during the Great Oxidation Event. *Nature*, *542*(7642), 465-467.

Zhang, S., Wang, X., Hammarlund, E. U., Wang, H., Costa, M. M., Bjerrum, C. J., ... & Canfield, D. E. (2015). Orbital forcing of climate 1.4 billion years ago. *Proceedings of the National Academy of Sciences*, *112*(12), E1406-E1413.

Zhelezinskaia, I., Kaufman, A. J., Farquhar, J., & Cliff, J. (2014). Large sulfur isotope fractionations associated with Neoarchean microbial sulfate reduction. *Science*, *346*(6210), 742-744.

Zhu, S., Zhu, M., Knoll, A.H., Yin, Z., Zhao, F., Sun, S., Qu, Y., Shi, M., and Liu, H. (2016). Decimetre-scale multicellular eukaryotes from the 1.56-billion-year-old Gaoyuzhuang Formation in North China. *Nature Communications*, 7.

Zi, J.-W., Sheppard, S., Muhling, J. R., & Rasmussen, B. (2021). Refining the Paleoproterozoic tectonothermal history of the Penokean Orogen: New U-Pb age constraints from the Pembine-Wausau terrane, Wisconsin, USA. *GSA Bulletin*, *July*, 1–15.

Samenvatting in het Nederlands

Quasi-periodieke schommelingen in de baan van de aarde om de zon en de stand van de aardas doen zich voor op tijdschalen van vele duizenden tot miljoenen jaren ten gevolge van de gravitatieve aantrekkingskracht tussen de Aarde en de andere lichamen in het zonnestelsel. Deze bewegingen brengen cyclische veranderingen teweeg in de hoeveelheid zonlicht die de aarde per seizoen en breedtegraad ontvangt (zonne-instraling) en worden wel de "Milankovitch-cycli" genoemd. De drie parameters die daarbij een rol spelen zijn de excentriciteit van de aardbaan, de inclinatie (obliquiteit) van de aardas, en de klimatologische precessie (*Fig. 1 in Hoofstuk 1*). Studies uit het Fanerozoïcum - de laatste 540 miljoen jaar van de geologische geschiedenis - hebben aangetoond dat deze instralingsveranderingen, die tot wel 20-25% kunnen oplopen, van grote invloed zijn geweest op het aardse klimaat in het geologische verleden, een fenomeen dat astronomische of Milankovitch-forcering wordt genoemd. Markante voorbeelden van astronomisch-gestuurde klimaatschommelingen zijn de IJstijden uit het Kwartair, de Hyperthermalen uit het Eoceen, en periodes van wijdverspreide mariene zuurstofloosheid tijdens het Krijt en het Neogeen uit het Middellandse Zeegebied.

In schril contrast met het Fanerozoïcum staat daarentegen onze kennis over de invloed van Milankovitch-forcering tijdens het Precambrium. In deze periode, die de eerste ~4 miljard jaar van de geologische geschiedenis beslaat, waren de condities op aarde in meerdere opzichten (biologisch, tektonisch, chemisch) fundamenteel verschillend van het meer recente verleden en tegenwoordig. Dit geldt met name voor de eerste helft van het Precambrium, vóór het moment dat vrije zuurstof (O_2) permanent zijn intrede deed in de atmosfeer en oceaan, tijdens de zogeheten 'Grote Oxidatie Event' (GOE) die ongeveer 2.4 – 2.2 miljard jaar geleden plaats vond. In het gesteentearchief dat de aanloop naar dit omslagpunt in de redoxgeschiedenis van Systeem Aarde beslaat, komen grote hoeveelheden van een zeer ijzerrijk, marien sedimentair gesteente voor dat bekend staat als 'gestreepte ijzerformaties' of 'banded iron formations' (BIFs). Dit type gesteente, dat uitsluitend in het Precambrium voorkomt, laat een opvallende gelaagdheid zien die op meerdere dikteschalen (micrometer- tot meterschaal) optreedt en waaraan het gesteente zijn naam ontleent. In de vroeg-Paleoproterozoïsche Brockman IJzerformatie (IF) in West-Australië zijn eind jaren '60 en begin jaren '70 bijzonder regelmatige afwisselingen beschreven door de geoloog Alec F. Trendall, die tevens speculeerde over een mogelijk verband met de astronomische sturing van het klimaat. Echter, mede door de afwezigheid van nauwkeurige dateringsmethodes in die tijd, maar ook door een verminderde aandacht voor dit onderwerp in de daaropvolgende jaren, is deze hypothese nooit verder systematisch onderzocht.

In dit proefschrift heb ik mij gericht op de vraag of Milankovitch-forcering van invloed was op de afzetting van de ~2,49 - 2,45 miljard jaar oude BIFs van de Kuruman IF in Zuid-Afrika en de Brockman IF in West-Australië. Dit testen van de Milankovitch-hypothese voor BIF-afzetting is van groot belang voor onze kennis over hoe het vroege

Systeem Aarde reageerde op de astronomische forcering, toen de omstandigheden fundamenteel anders waren dan vandaag de dag. Daarnaast biedt het mogelijkerwijs een fundamentele inkijk in de dynamische geschiedenis van het Zonnestelsel (gekoppeld aan de periodes van de excentriciteitscycli) en het Aarde-Maansysteem (gekoppeld aan de periodes van precessie en obliquiteit). Door middel van cyclostratigrafisch onderzoek naar de onderliggende klimaatveranderingen, gecombineerd met hoge-precisie uranium-lood (U/Pb) dateringen en geochemisch modelleren, heb ik mij daarom op de volgende twee hoofdprobleemstellingen gericht, die in Hoofstukken 2 t/m 5 aan bod komen:

- 1) de mogelijke invloed van astronomische klimaatforcering op BIF-afzetting en het Systeem Aarde tijdens het vroege Paleoproterozoïcum (**Hoofdstukken 2 en 3**). Vanwege het verloop van het onderzoek is **Hoofdstuk 3** speciaal gericht op het verband tussen astronomische klimaatforcering en (cyclische veranderingen in) mariene redoxcondities;

- 2) het gebruik van de cycli in de BIF voor de reconstructie van het Aarde-Maansysteem **(Hoofdstuk 4**) en de ontwikkeling van een astrochronologisch raamwerk (**Hoofdstuk 5**) voor het vroege Paleoproterozoïcum. In dat laatste hoofdstuk wordt tevens geprobeerd om informatie over de dynamische geschiedenis van de planeetbanen in het vroege Zonnestelsel te vergaren.

Overzicht van de hoofstukken

Tijdens de start van het project in 2017 was het onderzoek logischerwijs gericht op het beantwoorden van de eerste vraag, namelijk of astronomische klimaatforcering inderdaad is vastgelegd in de stratigrafie van vroeg-Paleoproterozoïsche BIFs. Hiervoor richtten we ons in **Hoofstuk 2** op de Kuruman IF uit Zuid-Afrika. Tijdens bestudering van satellietbeelden en een verkennend veldwerk in het Griqualand West Bekken (voorjaar ‘17), viel de aanwezigheid op van een hiërarchisch patroon van regelmatige afwisselingen ("bundeling") in de stratigrafie van de Kuruman IF, dat duidelijk zichtbaar was in het verweringsprofiel. Dit patroon kon lateraal over meer dan 250 km vervolg worden van Kuruman Kop in het noorden tot Prieska in het zuiden. Uit cyclostratigrafisch onderzoek bleek dat het patroon grotendeels verklaard kon worden door de aanwezigheid van twee prominente cycli met diktes van ~4 - 6 en ~16 - 22 meter. Lithologische faciësanalyse toonde aan dat de hardere intervallen ("richels") van deze cycli relatief rijker waren aan ijzeroxiden, en werden afgewisseld met zachte intervallen die relatief rijk waren aan ijzercarbonaat. Door de cyclostratigrafische waarnemingen te integreren met de sterk verbeterde U/Pb-ouderdommen, kon vervolgens een Milankovitch-oorsprong voor de cycli worden vastgesteld, waarbij de ~5 meter-cyclus werd gekoppeld aan de lange en stabiele, 405 duizend jaar excentriciteitscyclus (gerelateerd aan de planeetbanen van Venus en Jupiter), en de ~16 - 22 meter-cyclus aan de instabiele, zeer lange excentriciteitscyclus met een verkorte periode van ~1,2 - 1,6 miljoen (deze cyclus, die gerelateerd is aan de planeetbanen van de Aarde en Mars, heeft een huidige duur van 2,4 miljoen jaar, maar kan in periode veranderen als gevolg van chaotische resonantie).

Drie van de vier schalie-intervallen die werden bemonsterd voor de chemische abrasie (CA)-ID-TIMS U/Pb-zirkoondatering waren afkomstig uit een nieuwe kern van de Kuruman IF, die we nog in datzelfde jaar (herfst '17) hadden geboord omdat de aanwezige kernen niet geschikt bleken. Deze kern (UUBH-1) maakte een hoge resolutie, multi-proxystudie van vers, niet verweerd gesteente van de Kuruman IF mogelijk tijdens een latere fase van het onderzoek (op basis van X-ray fluorescentie (XRF) corescanning), waarvan de resultaten zijn opgenomen in **Hoofdstuk 5**.

In **Hoofdstukken 3 en 4** verlegden we onze focus naar de Joffre Member van de Brockman IF in het West-Australische Hamersley Bekken. Veldopnamen van de Joffre Member bij Joffre Falls in het Karijini National Park, waar we tijdens een verkennend veldwerk in de Hamersley Range (zomer '18) op stuitten, lieten een opmerkelijk continue en regelmatige expressie zien van ~5 - 15 cm-dikke afwisselingen die gegroepeerd voorkwamen in ~85 cm-dikke bundels. Een dergelijke bundeling is vaak indicatief voor de modulatie van precessie door de korte, ~100.000 jaar, excentriciteitscyclus. Deze afwisselingen kwamen overeen met de eerder door Trendall op dezelfde locatie beschreven "Knox-cyclothem" en een regelmatige "65 - 150 cm" afwisseling tussen BIF en stilpnomelaan-rijke schalie (*Fig. 10 in Hoofdstuk 1*). De Knox-cyclothemen in het veld werden in het algemeen gekenmerkt door een opvallende dubbele witte vuursteenband (bijgenaamd "tramrails"). Bij latere inspectie van een bestaande kern (DD98SGP001) van de Joffre Member, die ~150 km ten westen van Joffre Falls was geboord en in de kernbibliotheek van Perth lag opgeslagen, werden verschillende lithologische typen Knox-cyclothemen geïdentificeerd. Het meest basale, opvallendste type bestond uit een regelmatige voorkomen van een groenige carbonaatrijke kleilaag van ~1 cm, afgewisseld met vuursteen en een ijzeroxide-rijke lithologie. Bij nadere bestudering bleken er dunne, glinsterende magnetietlaagjes, alsmede duidelijke carbonaat- en pyrietlaagjes, te zijn ontwikkeld aan de boven- en onderkant van de groenige intervallen. Deze kenmerken deden sterk denken aan de chemische reactiefronten zoals die eerder beschreven waren van precessie-gestuurde 'redox-cycli' in mariene sedimenten uit het Plioceen-Pleistoceen van het Mediterrane gebied (*Fig. 3 in Hoofdstuk 1*). Deze fronten zijn ontstaan als gevolg van vroeg-diagenetische afbraak van cyclisch afgezet organisch-rijk sediment.

Om (meer) inzicht te krijgen in de afzettingsgeschiedenis van de precessieschaal-afwisselingen in de Joffre Member, besloten we in **Hoofstuk 3** tot een geochemisch onderzoek van geselecteerde Knox-cyclothemen uit kern DD98SGP001 op basis van o.a. XRF-corescanning op millimeterschaal. Karakteristieke patronen in de Fe- en S-concentratie (dubbele pieken) in de gegevens van de XRF-corescans konden vervolgens kwantitatief worden gesimuleerd met behulp van een reactief-transportmodel. Op basis van deze resultaten en nieuwe U/Pb-zirkoonouderdommen uit kern DD98SGP001, hebben we deze afwisselingen geïnterpreteerd in termen van cyclische veranderingen in de accumulatie van organisch materiaal, Fe^{2+}-gehalte, en de productie van O_2 in de bovenliggende waterkolom in het mariene bereik. Deze processen worden op hun beurt toegeschreven aan precessie-gestuurde veranderingen in door de moesson bepaalde riverafvoer en de bijbehorende toevoer van nutriënten. Onze (model) observaties wijzen op een zeer dynamische redoxevolutie van de vroege oceaan in reactie op de Milankovitch-forcering. We speculeren dat de astronomisch-gestuurde klimaatveranderingen mogelijk een belangrijke rol hebben gespeeld in de dynamiek van de oxygenatie (zuurstofvoorziening) van de atmosfeer in de aanloop naar de GOE 2,4 miljard jaar geleden.

In **Hoofdstuk 4** richtten we ons op de reconstructie van de precessieperiode om de afstand Aarde-Maan te achterhalen, op basis van de verhouding tussen de periode van precessie en de (stabiele) excentriciteitscyclus, die onafhankelijk is van het Aarde-Maan systeem. Aangezien hiervoor een duidelijke en continue expressie van zowel de precessie- als excentriciteitscycli vereist was, richtten we ons voor dit onderzoek op de natuurlijke ontsluitingen bij Joffre Falls. De resultaten van de cyclostratigrafische analyse en sedimentatiesnelheden verkregen uit de DD98SGP001-kern bleken consistent te zijn met de Milankovitch-interpretatie uit Hoofdstuk 3, namelijk dat de ~85 cm-cycli samenhangen met de korte excentriciteitscyclus en de Knox-cyclothemen met de (klimatologische) precessiecyclus. Vanwege de complexe interne opbouw van de Knox-cyclothemen en de grote verschillen in dikte van deze cycli (variërend van minder dan 5 tot meer dan 20 cm binnen één korte excentriciteit-gerelateerde bundel), kozen we niet voor een statistische benadering, maar voor een in onze ogen meer ‘robuuste’ aanpak van het nauwkeurig tellen om het gemiddelde aantal klimatologische precessie-gerelateerde cycli per korte excentriciteit-gerelateerde bundel te bepalen (in plaats dus van de statistische methode gebaseerd op de ratio tussen spektraalpieken). Op basis van de door ons bepaalde ~1:9 dikteverhouding tussen deze twee cycli kon vervolgens een waarde worden bepaald voor de frequentie van de astronomische (d.w.z. axiale) precessiecyclus, de afstand Aarde-Maan en de lengte van de dag, tijdens afzetting van de Joffre circa 2,46 miljard jaar geleden. De door ons berekende Aarde-Maanafstand werd vervolgens vergeleken met andere empirische schattingen en met de uitkomsten van modellen voor de recessie van de Maan uit de literatuur. Ons datapunt en het verloop van de maanrecessie zoals dat gesuggereerd wordt door ons punt te combineren met twee eerdere op cyclostratigrafie gebaseerde schattingen uit het Mesoproterozoïcum en Cambrium, laat een opmerkelijk goede overeenkomst zien met het oceaangetijdemodel van Webb uit 1982. Deze overeenkomst wijst, heel voorzichtig, op een dominante invloed van resonanties voorkomend uit lange-termijnveranderingen in de rotatiesnelheid van de aarde op de gemiddelde getijdendissipatie in de oceaan.

Tenslotte hebben we in **Hoofdstuk 5** onderzocht of het mogelijk was om de Kuruman IF in Zuid-Afrika en de grotendeels even oude Dales Gorge Member van de Brockman IF in West-Australië cyclostratigrafisch met elkaar te correleren. Karakteristieke patronen in grootschalige en lateraal continue afwisselingen in de Dales Gorge Member ("BIF-S macrobanding") suggereerden eenzelfde oorsprong gerelateerd aan lang-periodieke excentriciteitscycli zoals in **Hoofdstuk 2** was aangetoond voor de Kuruman IF. Als zodanig vormden deze twee BIF-eenheden een interessante toets voor het opstellen van een astrochronologisch raamwerk voor het vroege Proterozoïcum, op basis van de stabiele, 405 duizend jaar excentriciteitscyclus. Bovendien zou een dergelijke oefening fundamentele informatie kunnen opleveren over de exacte periode van de geïnterpreteerde zeer lange excentriciteitscyclus (in **Hoofdstuk 2**), alsmede over de aanwezigheid van mogelijk andere lang-periodieke Milankovitch-cycli.

Hierom besloten we tot een vergelijkend cyclostratigrafisch onderzoek van de Dales Gorge Member en Kuruman IF, waarbij gebruik werd gemaakt van verschillende records met een zeer hoge resolutie (verticaliteitsprofielen van veldontsluitingen verkregen uit 3D-modellen, mineraaldata, elementrecords verkregen uit XRF-corescanning, magnetische susceptibiliteit), opnieuw geïntegreerd met U/Pb-zirkoondateringen. De resultaten van **Hoofstuk 5** bleken in grote lijnen overeen te komen met, maar ook enigszins af te wijken van die in **Hoofdstuk 2.** In beide eenheden werd een ~5 m-cyclus gelinkt aan de lange excentriciteitscyclus, maar bleek een ~16 m-cyclus vooral verantwoordelijk te zijn voor de karakteristieke hiërarchische bundeling die in beide BIF-eenheden te zien is; deze cyclus werd nu meer voorzichtig geïnterpreteerd als de zeer lange excentriciteitscyclus, met een nog kortere periode van ~1,3 Myr.

Ondanks de aangetoonde invloed van astronomische forcering en het feit dat de cyclische patronen in elk van de eenheden over honderden kilometers vervolgd konden worden, bleek het niet mogelijk om de Dales Gorge Member en Kuruman IFs op hoge resolutie (d.w.z. op de schaal van de stabiele, 405 duizend jaarcyclus) cyclostratigrafisch overtuigend met elkaar te correleren. De belangrijkste reden hiervoor is waarschijnlijk het verschil in afzettingsmilieu waarin deze BIF-eenheden werden afgezet, wat resulteerde in een verschillende uitdrukking en/of amplitude van bepaalde cycli, waarvan de precieze astronomische oorsprong eveneens onzeker blijft. Hoewel er in dit proefschrift flinke vooruitgang is geboekt, kan (moet?) er dus nog veel nader fundamenteel onderzoek worden verricht naar de invloed van astronomische sturing op vroeg-Paleoproterozoïsche ijzerformaties.

Curriculum Vitae

Margriet Louise Lantink was born on the 16th of March 1992 in Leiden. In 2010 she received her VWO diploma at the Stedelijk Gymnasium Leiden, and in September of that same year she started studying Earth Sciences at Utrecht University. In January 2014 she obtained her Bachelor's degree in Geology, followed by her Master's degree in the Earth, Life and Climate program in August 2016. During her Master's she enjoyed the lectures and fieldwork course given by dr. Frits Hilgen on the subject of astronomical climate forcing and cyclostratigraphy. At the same time, she became interested in the early Earth, and wrote her MSc thesis on the paleoenvironmental origin of the 2.4-billion-year-old Hotazel Iron Formation, under supervision of prof. Paul Mason. For her subsequent PhD project at the Department of Earth Sciences in Utrecht, she was able to combine these two research topics: starting in January 2017, she investigated the influence of astronomical forcing on early Proterozoic banded iron formations. During her PhD she spent several months in South Africa and Western Australia for fieldwork and to drill a new core, and at the Royal Netherlands Institute for Sea Research (NIOZ) on Texel for X-ray fluorescence core scanning. The results of her work are presented in this thesis. From January to March 2022 Margriet was a visiting scientist at the Institute for Celestial Mechanics and Calculation of the Ephemerides (IMCCE) at the Paris Observatory in France, within the AstroGeo project. From September 2022 onwards, she will be working as a postdoctoral researcher at the University of Wisconsin-Madison, USA, as a member of the CycloAstro Cohort team.

Publications

Sinnesael, M., De Vleeschouwer, D., Zeeden, C., Batenburg, S. J., Da Silva, A. C., de Winter, N. J., ..., **Lantink, M. L**., … & Claeys, P. (2019). The Cyclostratigraphy Intercomparison Project (CIP): consistency, merits and pitfalls. E*arth-Science Reviews, 199*, 102965.

Lantink, M. L., Davies, J. H., Mason, P. R., Schaltegger, U., & Hilgen, F. J. (2019). Climate control on banded iron formations linked to orbital eccentricity. *Nature Geoscience, 12*(5), 369-374.

Lantink, M. L., Oonk, P. B., Floor, G. H., Tsikos, H., & Mason, P. R. (2018). Fe isotopes of a 2.4 Ga hematite-rich IF constrain marine redox conditions around the GOE. *Precambrian Research, 305*, 218-235.

Utrecht University
Faculty of Geosciences
Department of Earth Sciences

ISSN 2211-4335